Modelling and Design of Efficient Photomixer Based Terahertz Antennas

By:

Xiaohang Li

A Thesis Submitted to The University of Sheffield for the Degree of Doctor of Philosophy

Department of Electronic and Electrical Engineering

20.05.2021

Contents

ACKNOWLEDGEMENTS

I would like to thank my dedicated supervisor, Dr Salam Khamas, for his patience, guidance and encouragement.

I would like to thank my wife and parents, regardless of the distance they encouraged, supported me all the time and trust me in every second.

I would like to thank all communities in the communication group, who help me whether in life or research.

I would like to thank everyone who helped me during the pandemic of COVID-19 in the past year.

ABSTRACT

The lack of unoccupied and unregulated bandwidth for wireless communication vanished at lower frequency spectrum and the increasing demand of high data transmission rate leads to an intensive interest in the research of THz technologies at 0.3THz to 30THz spectrum. However, the limitation of the low output power and low efficiency of current THz devices obstacles the utilization of THz technologies. Also, compared with microwave antenna, the signal generation and excitation of THz antenna require new simulation approach. Therefore, the motivation of this thesis is theoretically analyse the reason that cause the inefficiency of THz antenna, from which, the performance of such antennas is improved from the aspects of THz source with low efficiency, THz antenna with low match efficiency and THz antenna with low gain. These investigations are necessary for the development of the THz photomixer antenna in various applications .

First of all, an new equation of the generated THz power from photomixer is developed from the equivalent circuit of photomixer fed antenna. Through this equation, various factors that affect the behaviour of photomixer is examined. Furthermore, a computational simulation process that solving both optoelectronic and electromagnetic problem in a full wave electromagnetic solver. This is a prerequisite for the analysis of improving the optical to THz conversion efficiency of photomixer. After that, the optical to THz conversion efficiency of the photomixer has been gradually improved through three different aspects, by optimizing photomixer electrodes, by utilizing reflectors underneath photomixer and by implementing superstrate. As a result, the highest enhancement factor of optical to THz conversion efficiency achieved is 494. Moreover, instead of exciting planar antenna with photomixer, the concept of truncating the photoconductive substrate of photomixer to form a dielectric resonator antenna is proposed. Such design eliminated the substrate effect to improve the radiation efficiency and to avoid using bulky lens. In addition, choke filter network and dielectric superstrate are used to improve the matching and radiation of these DRAs. The proposed DRA improved the matching efficiency and antenna gain by 10 times and 3dBi, respectively. Finally, a realization design that provide physically support to the dielectric superstrate and replace central feeding slot with coplanar waveguide is presented

PUBLICATIONS

[1] X. Li and S. K. Khamas, "Enhance the Optical Intensity of a Photomixer Based THz Antenna Using a Two Dimentional Photonic Crystal," *2019 International Symposium on Antennas and Propagation (ISAP)*, 2019, pp. 1-3.

[2] Xiaohang Li, ; Khamas, S.K.: 'Enhance the Optical Intensity of a THz Photomixer Using a Plasmonic Material Filled Two Dimensional Photonic Crystal', IET Conference Proceedings, 2019, pp.1-4.

[3] X. Li, W. Yin and S. Khamas, "An Efficient Photomixer Based Slot Fed Terahertz Dielectric Resonator Antenna," *2020 International Workshop on Antenna Technology (iWAT)*, 2020, pp. 1-4.

[4] X. Li, W. Yin and S. K. Khamas, "Design of Efficient Photomixer-based Terahertz Dielectric Resonator Antenna," *2020 14th European Conference on Antennas and Propagation (EuCAP)*, 2020, pp. 1-4,

[5] X. Li, W. Yin, and S. Khamas, "An Efficient Photomixer Based Slot Fed Terahertz Dielectric Resonator Antenna," *Sensors*, vol. 21, no. 3, p. 876, Jan. 2021

Chapter 1. Introduction

1.1 The Terahertz Spectrum

The Terahertz radiation covers the frequency range from 0.1 to 10THz with wavelength of 3mm to 30μm, which represents the spectrum between the millimetre and infra-red frequencies [1]. In terms of quantum physics, the corresponding wavelength of THz radiation represent the transition between photonics and electronics. All of these definitions are illustrated in the Figure 1.1. THz band is also known as THz gap, sub-millimetre, far infra-red and near millimetre wave. The term "THz gap" indicates the region of the spectra that, as compared with the adjacent spectrum, is the least investigated because of the lack of efficient compact THz sources [2, 3]. Such efficient compact sources like transistors or RF/MW antennas

work effectively in microwave frequency, and semiconductor laser diodes also have such characteristics for the visible and infrared region [4]. However, as these technologies has been employed in the THz region, a significant reduction in power and efficiency is acquired. The reduction is inevitable because the reactive-resistive effect (such as equivalent first order circuit of solid-state electronics) and long transit-time of the solid-state electronic devices work at the lower boundary of THz spectrum lead to roll-off [5]. In addition, the lack of narrow-gap semiconductor material of optical devices limits the performance of the optical sources to work in the THz range. [4].

In this chapter, an overview of the THz sources using different techniques will be presented. Then, the properties of THz wave and envisioned applications will be demonstrated. Based on these, the research motivations and objectives of this thesis will be outlined.
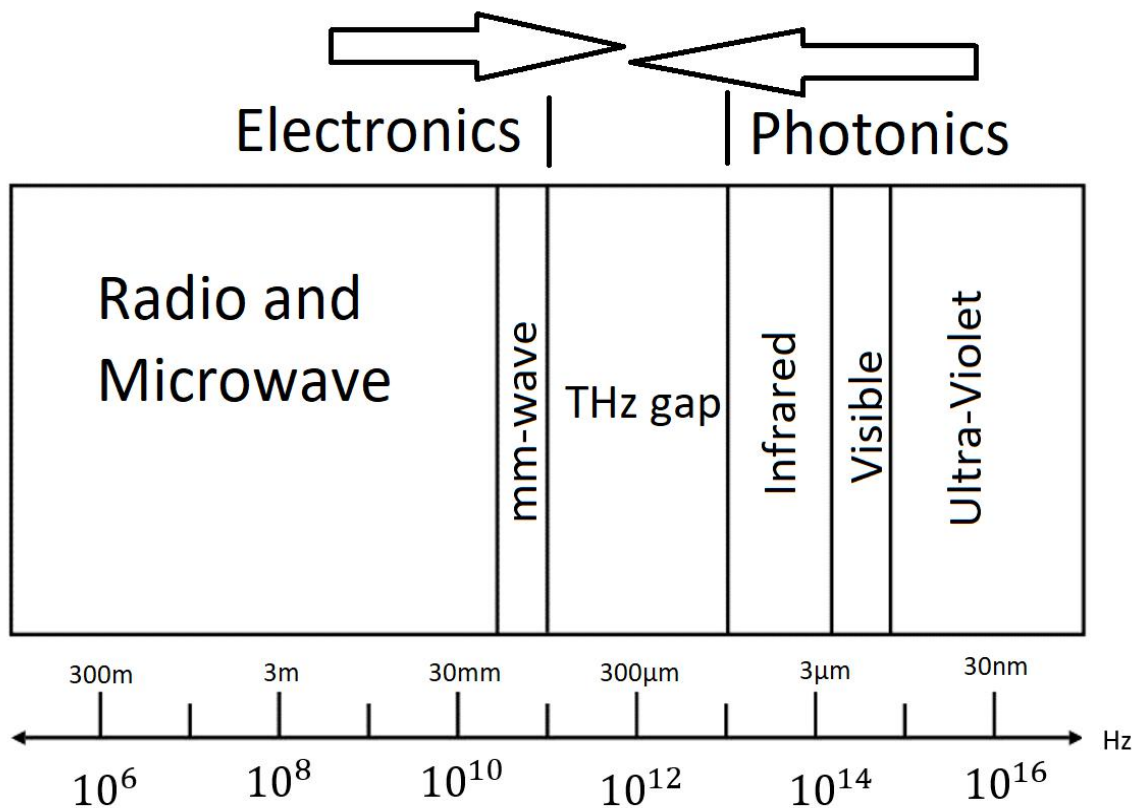

Figure 1.1: Schematic diagram of THz band   [6]

1.2 THz Sources

The main challenge with THz technology is the lack of the efficient and compact sources. This section presents a review and evaluation of existing THz sources from

three different aspects such as extending RF/MW technologies to THz band and down-convert optical technologies to THz band. Finally, trying to combine both of RF/MW and optical technologies to achieve a better performance [7].

1.2.1 THz Sources from RF/MW Techniques

Diodes and THz vacuum tube as THz main sources are introduced in this section.

1.2.1.1 Diodes and frequency Multipliers

At the boundary between mm-wave and THz spectrum, diodes could be used to transfer the electronics with the lower frequency to THz band upon the negative differential resistance property, such as resonant tunnelling diode, Gunn diode and IMPATT diode [8-13]. The negative differential resistance of such electronic device undampens the resonant transmission-line (or a resonant LC) circuit, which in turn yields Terahertz oscillation. However, the main disadvantage of these type of diodes can also be attributed to the negative differential resistance. Such property will lead to a significantly decreased power while at higher frequency, especially THz region [8].

Moreover, frequency multipliers could also be applied rather than other solid-state electronics sources since both the set-up and operation process are simple [9]. Because of the inefficient high order multipliers, a number of doublers and triplers should be connected to drive the multiplication at the THz range. However, the multiplier will not only experience low output power at high frequency, but also have a limited bandwidth [14]. The ratio of the reduction of bandwidth depends on the filter bandwidth of the multiplier and the number of the multiplier been used.

1.2.1.2 THz Vacuum Tube Sources

The traditional THz generation method is THz vacuum tube which utilizes the free electrons emission from a MW tube. Such THz tube includes travelling wave tube (TWT) and backward wave oscillator (BWO). It has been reported that a BWO can generate Thz source at 0.6THz with 52mW output power [15]. The working principle of these sources is based on the interaction between electron beams and electromagnetic wave. Hence, based on this working principle, the main disadvantage

is the fact that large magnetic biases and high voltage power supplies are required than other solid state components to achieve sufficient output power. In addition, the overall size of them is relatively larger than other solid-state devices [8].

1.2.2 THz Sources from Optical Techniques

Lasers with different generation techniques and non-linear crystal are introduced in this section.

1.2.2.1 IR-pumped Gas Laser

The IR-pumped gas laser is used to generate THz signal by discharging the electric current through a gas. Normally, the power level of produced THz signal is 1-20mW based on the gas type and the frequency of the generated signal depends on the gas type and its spectral line. Therefore, not all frequencies within the regime of 0.5-3-THz are covered with strong output power, one of the best performance is produced by methanol at 2.522THz [16]. Moreover, some of the chemically active gases are still not safe to be used under current enviromental safety policies.

1.2.2.2 THz Semiconductor Lasers

Semiconductor diode lasers are popular for the near infra-red and visible frequency applications, however, it only applied to THz when artificial engineered materials with suitable band gap have been considered [4, 17]. Therefore, quantum-cascade lasers (QCL) with GaAs nm-layer separated by AlGaAs barriers has been introduced [3]. The population inversion is achieved by proper design of the thickness of semiconductor layers and biased voltage. Furthermore, the energy of such artificial engineered materials is inversely proportional to the square of the thickness of semiconductor layers. Therefore, series of band with different energy can be created by manipulate the thickness of semiconductor layers. As the electron move from one band to another, THz photon is emitted at each transition. Since the systems depends on the band gap design, same materials can generate photon with a different wavelength. Hence, QCLs is one of the most promising sources for various THz applications in the past decade. It has been reported that the THz QCLs are available from 0.84THz to 5THz [18-21] with peak power of 200mW at 4.5THz [4]. However,

all of the performances above are operated with various cryogenic cooling system, and the power of the THz QCL working at room temperature is 8.5μW at 4THz [22]. In conclusion, QCLs generate higher output power at higher frequency, and the power decreases dramatically as frequency reduces. Though it has such advantages, the cryogenic cooling system limits the laboratory operation of QCLs.

1.2.2.3 Optical Down Converters

The most straightforward way to generate THz band from optical side is using non-linear crystal with large field induced polarisation (second-order susceptibility), therefore the concept of optical down converter is introduced [23]. Near-infrared pump photon generates a photon at THz frequency and a near-infrared idler photon due to the photon like behaviour of polariton. Then, the sum of the frequencies of THz photon and idler photon is the frequency of the pump photon according to energy conservation law. As the momentum remain constant within in the stimulated scattering process, the idler and THz waves exhibit angle-dispersive characteristics. Therefore, as an optical resonator applied to idler wave, a monochromatic THz wave is generated [24]. Optical rectification is another optical method to generate THz wave. However, the first limitation of this technique is that the design of the nonlinear material should be accurate to align the phase of the induced THz band with the phase of the incident optical band. In order to generate sufficient THz power, the power of the incident optical sources should be high enough [2].

1.2.3 THz Sources combining RF/MW and Optical techniques

Based on the concept of combining techniques, THz photoconductive antenna has been introduced [16]. As shown in Figure 1.2, THz photoconductive antenna is made of two main parts, photoconductive substrate and biased antenna. As the incident laser beams illuminate the active region of the photoconductive antenna, the carrier density of the substrate changes rapidly to generates THz wave which is used as the power supply of THz antenna. According to the type of incident laser beams, there are two types of THz antenna that utilizing photoconduction technique. THz photoconductive antenna for pulsed systems and THz photomixer antenna for continuous wave systems.

The physical structure of the THz antenna for pulsed and CW systems can be the same. However, the requirement of different application imply different THz waves, hence, different excitation method and different antenna type. In THz pulsed systems, the current density changes rapidly as the induced photo-carriers in the photoconductive gap generated by a single incident laser beams. Therefore, a THz electromagnetic field is induced by the currents, thus, THz ultra-fast pulses are generated and radiated. In continuous wave systems, the operation principle is identical, however, two co-linear laser beams with beating frequency of THz range are used. The conductivity of the photoconductive substrate is modulated by the absorption of photons and short charge carrier lifetime. Then, the current is converted from the conductivity variation by applying bias electric field. In a continuous wave system, "photomixer" is used to describe the antenna gap, and "photoconductive gap" is used in THz pulsed system.
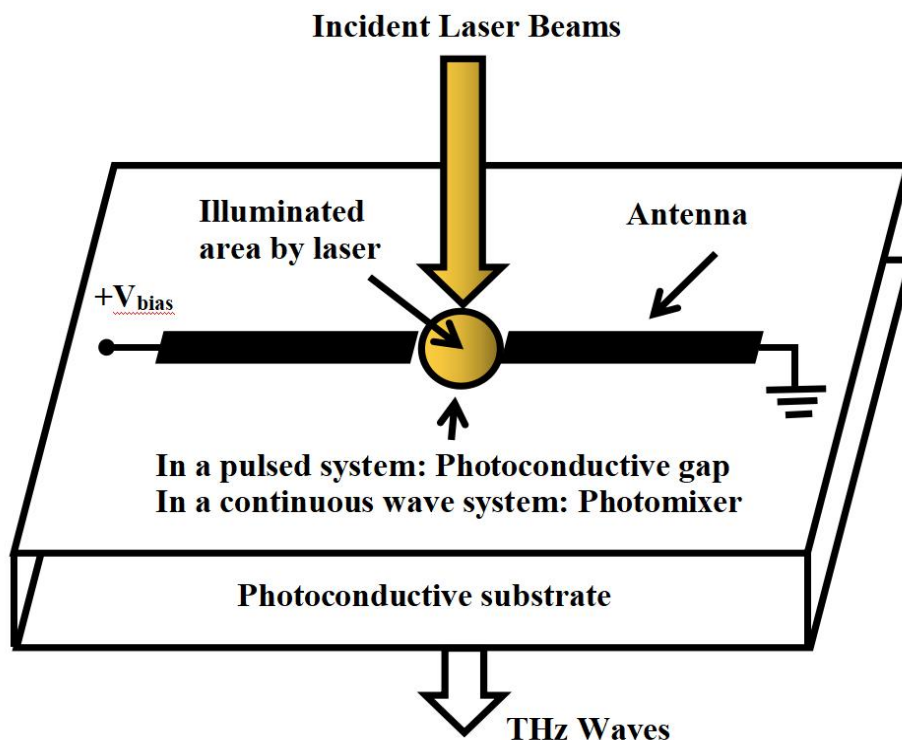
(a)
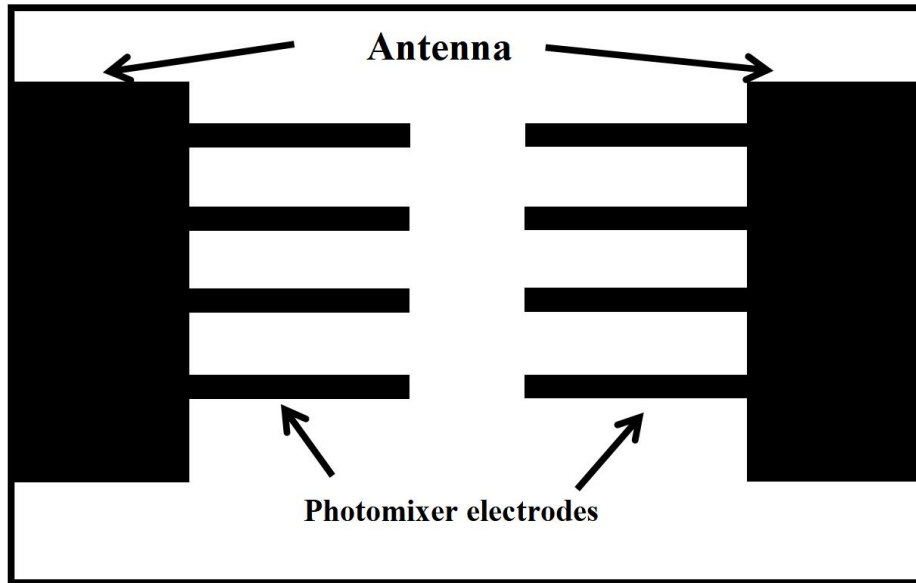
(b)

Figure 1.2: Configuration of (a) THz antenna as an source (b) illuminated area with photomixer electrodes

To sum up, the sources utilizing RF/MW techniques normally operate at lower boundary of the THz spectrum and the output power of such sources decrease with an increase of frequency. The optical source reside in the higher boundary of the THz spectrum and their output power increases with the frequency. Such tendency is summarised from various devices demonstrated in the literature and illustrated in Figure 1.3.
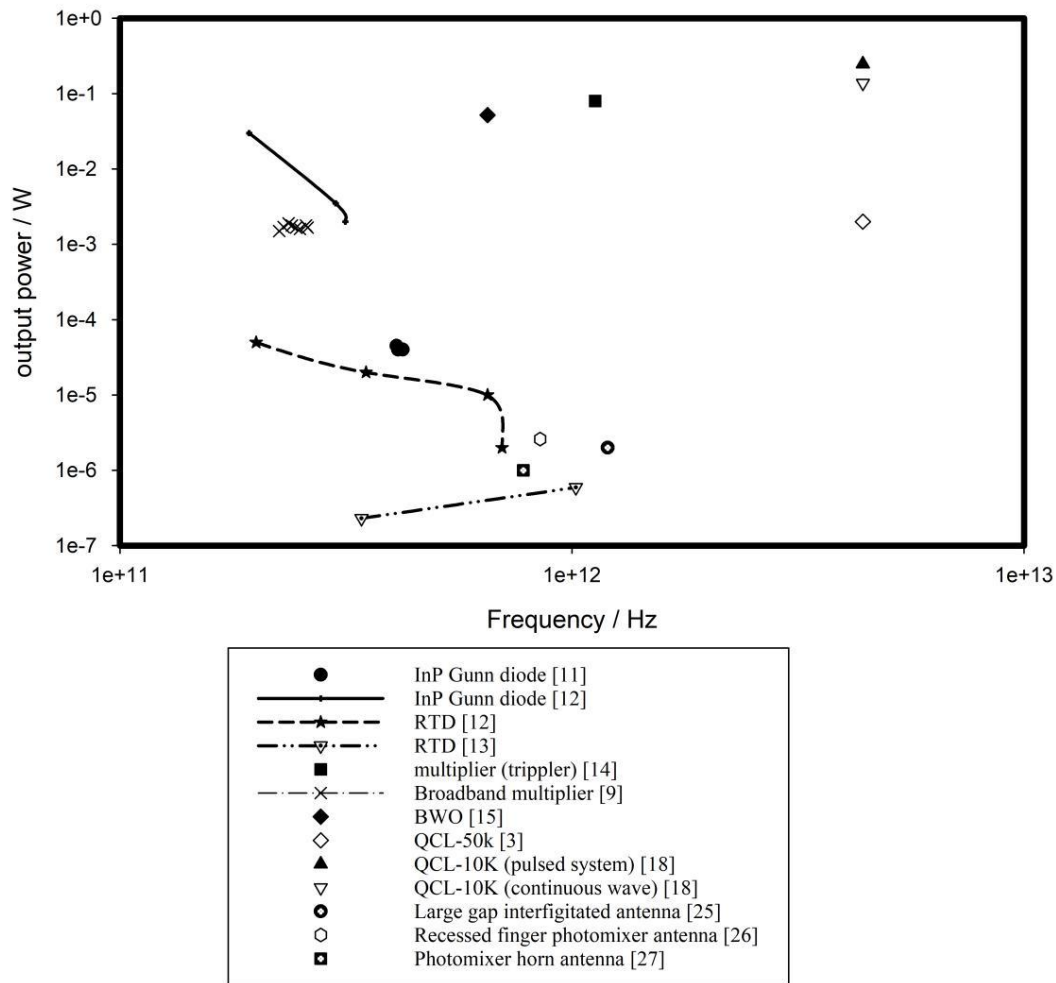
Figure 1.3: An outline of THz sources

1.3 The THz Wave Properties and Applications

The THz region was noticed and interested appeared as early as the 1920s [28], however, more substantial investigations dedicate to THz technology in the past 20 years. The explosion in the THz research in last two decades is due to the extraordinary wave properties and extensive potential applications in THz band. As mentioned previously, THz band resides between millimetre and infrared frequency, consequently, THz band offers some promising properties that borrowed from two adjacent bands.

Penetration: The attenuation of THz radiation is relatively less than the attenuation of infrared, especially, through dry and non-metallic media. The

penetration depth of THz wave is in the order of centimetre and it is micrometre for infrared.

High Resolution imaging: As the wavelength of THz wave is shorter than millimetre wave, sub-millimetre spatial imaging resolution can be generated.

Spectroscopy: The spectral fingerprint of many materials lies in THz band. Since dry and non-metallic material are transparent for THz radiation, these materials can be detected even when they sealed in the container.

Safety: Compared to X-rays, THz radiation is non-ionizing and operated at lower photon energies.

1.3.1 Channel Modelling of THz Communication

Two types of channels are defined for communication system, the indoor channels and outdoor channels. It should be noted that the indoor channel is more sophisticated than the outdoor channel. Since the wavelength of THz radiation is much higher than the microwave radiation which results in different absorption and reflection losses, the channel models for current microwave communication is not applicable for THz communication [29-31].

For indoor channels, the pass loss can be compensated with the highly directive antenna, consequently, the high output power can be achieved as suggested by link budget calculation [32]. The path loss refer to the atmospheric losses while the THz wave travelling between the transmitter and receiver. Friis law summarize such loss and conduct the received power and signal to noise ratio as following equation [33]:

$$\frac{P_r}{P_t} = \frac{G_r G_t (\frac{\lambda}{4\pi d})^2}{L_{ex}\alpha(f)d} \tag{1.1}$$

$$SNR_{dB} = P_r - (N_0 + 10\log(B) + NF + M) \tag{1.1}$$

Where P_r the power at the receiver, P_t is the radiated power from the transmitter, G_r and G_t are the gains of receiving and transmitting THz antennas, respectively. λ is the free space wavelength. d is the distance between the transmitter and receiver. $\alpha(f)$ is the atmospheric attenuation at frequency f and L_{ex} is excess loss. NF is receiver's noise figure, M is the system margin, N_0 is the noise spectral density and B is the

noise bandwidth [34]. The link budget can be calculated using the parameters listed in Table 1.1 and data rates with BER of 10^{-6} at different modulations versus antenna gain is illustrated in Figure 1.4. It should be noted that the value of noise spectral density at 20°C introduced in [34] is -178dBm/Hz. However, since $N_0=30+10\log(kTB)$ where k is Boltzmann constant, T is temperature in kelvin and B is bandwidth, the noise spectral density at 20°C should be -174dBm/Hz which is the value used in this thesis. It can be noticed that for 10Gb/s, antenna gain of approximately 30dBi is necessary. However, due to the physical size of the antenna, it is impractical to utilize microwave antenna with 30dBi gain in a indoor application. Since the effective antenna aperture $A_e=G_r\lambda^2/4\pi$, the effective antenna aperture of THz antenna with 30 dBi gain at 300GHz can be calculated as around 80 mm^2 which won't be a problem at all.

Table 1.1: Parameters for link budget calculation [34]

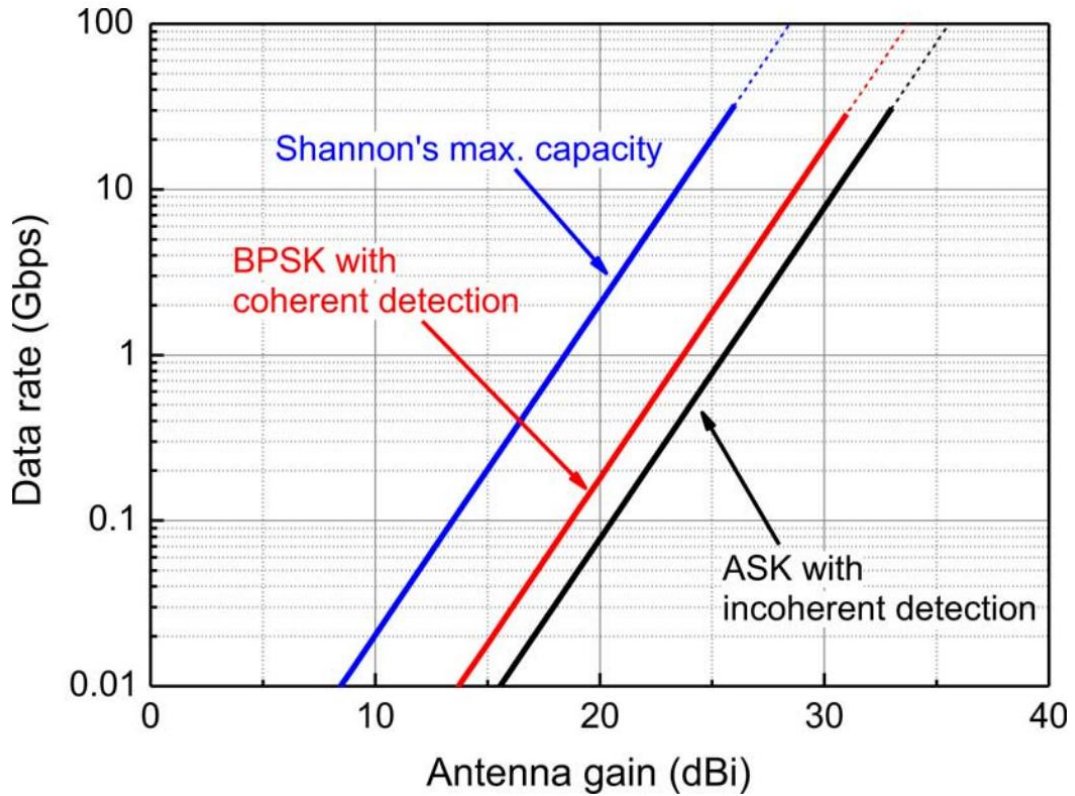| Quantity	Symbol	Value
Transmitting power	P_t	0dBm
Carrier frequency	f	300GHz
Wavelength	λ	1mm
Distance	d	5m
Atmospheric attenuation	$\alpha(f)$	0.01dB/m at 300GHz
Excess loss	L_{ex}	0dB
Noise spectral density	N_0	-174dBm/Hz at 20°C
Spectral efficiency		1bit/s/Hz
Noise bandwidth	B	Data rate×spectral efficiency
Noise figure	NF	15dB
System margin	M	10dB

Figure 1.4: Data rates for ASK and BPSK as a function of antenna gain [34]

Moreover, atmosphere loss becomes more crucial as the transmission distance and frequency increases, which is shown in Figure 1.5 [35]. Therefore, the atmosphere attenuation is worth noticing in THz band system.
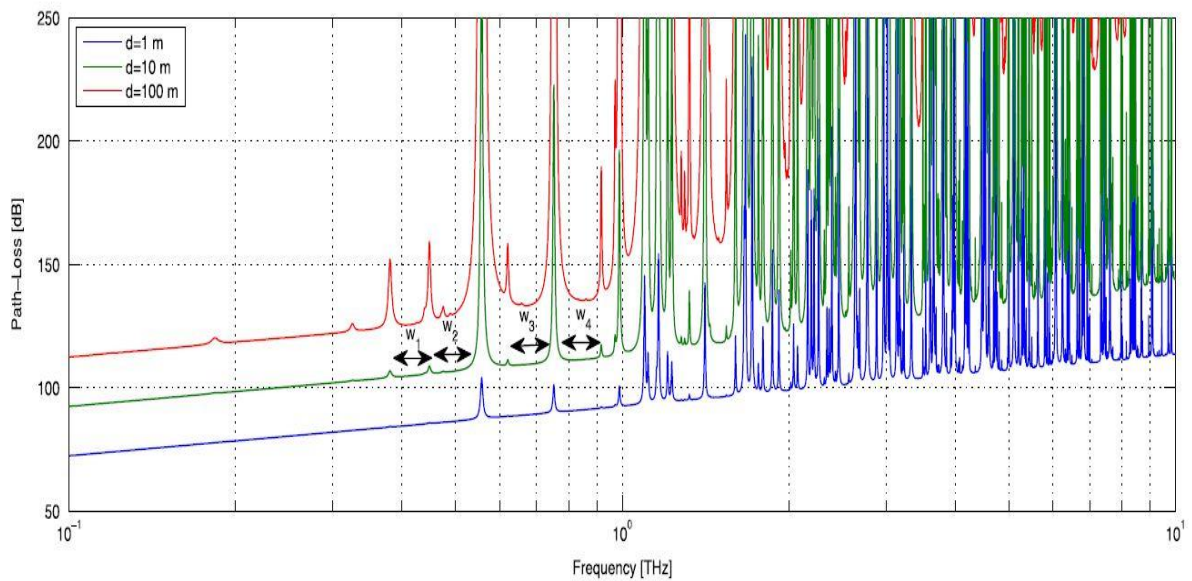

Figure 1.5: Atmosphere loss for different transmission distance [35]

For outdoor channels, the path loss becomes more complex. Figure 1.5 shows the attenuation for six different weather at sea level, and the environment characteristics of the weather conditions are described in Table 1.2 [36]. It can be observed that the windows are board for all the weather conditions below 300GHz, though it is hard to define a window as the attenuation increased with higher frequency.
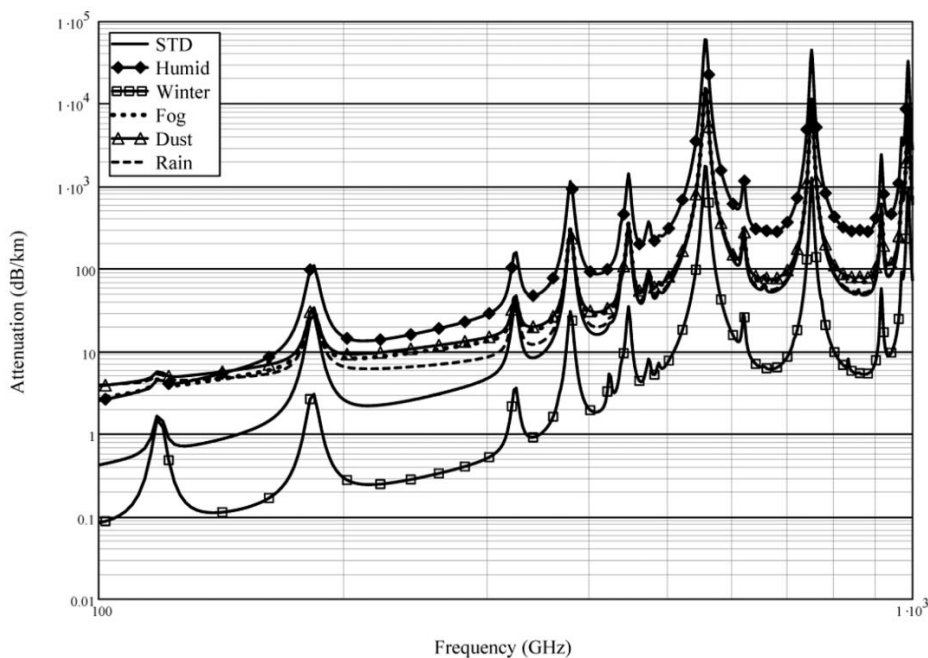

Figure 1.6: Atmospheric attenuation for six weathers at sea level [36]

Table 1.2: Characteristics of Weather conditions used in Figure 1.6 [36]

Weather	Temperature (°C)	Pressure (hPa)	Relative Humidity	Rain (mm/h)	Fog (m)	Dust (m)
Standard(STD)	20	1013	44%	0	0	0
Humid	35	1013	90%	0	0	0
Winter	-10	1013	30%	0	0	0
Fog	20	1013	44%	0	100	0
Dust	20	1013	44%	0	0	10
Rain	20	1013	44%	4	0	0

1.3.2 Application of THz Radiation

Due to the properties of TH band described previously, applications like imaging [7], spectroscopy [37] and wireless communication [38] can utilize THz radiation technology. Commercial THz imaging and spectroscopy system has been marketed by TeraView [39], Advanced Photonix [40] and Topica Photonics [41].

Medical imaging is one of the main application that benefit from the THz imaging research. Since the penetration depth of THz radiation is around few hundred micrometers in human body, the skin cancer [42], breast tumour [43] and dental tissue [44] can be detected. Other than computerised tomography scan, magnetic resonance imaging and biopsy, such imaging method can detect cancerous tissues at early stage and minimize the damage to the healthy organisation. However, the cost and time consuming data acquisition reduce the popularity of THz medical imaging equipment.

Since wood, papers and natural paint is transparent for THz radiation, THz imaging and spectroscopy is ideal for archaeology [45, 46]. Antiquities with multi layers and different materials can be investigated and scanned without destruction [47]. Furthermore, such imaging systems can be applied to the quality control of polymer compounding [48].

THz communication with high carrier frequency and sufficient transmission capacity provide possibility of the development of novel applications in different scenarios, include both marcoscale network applications and nanocale communications.

Outdoor wireless ultra-high-definition video communication can be achieved by utilizing THz technologies as small cells with 10m radius coverage area as illustrated in Figure 1.7(a) [35]. Indoor THz communication applications can be categorised as devices-to-network applications and devices-to-devices applications. Figure 1.7(b) demonstrate the scenario of Terabit Wireless Local Area Networks (T-WLAN), specific application like high-definition holographic video conferencing can be achieved by T-WLAN [35]. On the other hand, Terabit Wireless Personal Area Networks (T-WPAN) is shown in Figure 1.7(c) [35]. The exist applications like wireless screen projection to/from mobile devices can be further boosted. Jamming attacks can be prevented by ultra-broad channel bandwidth achieved by spread spectrum techniques when secure Terabit wireless communication in the military and defence applications (Figure 1.7(d)) [35].
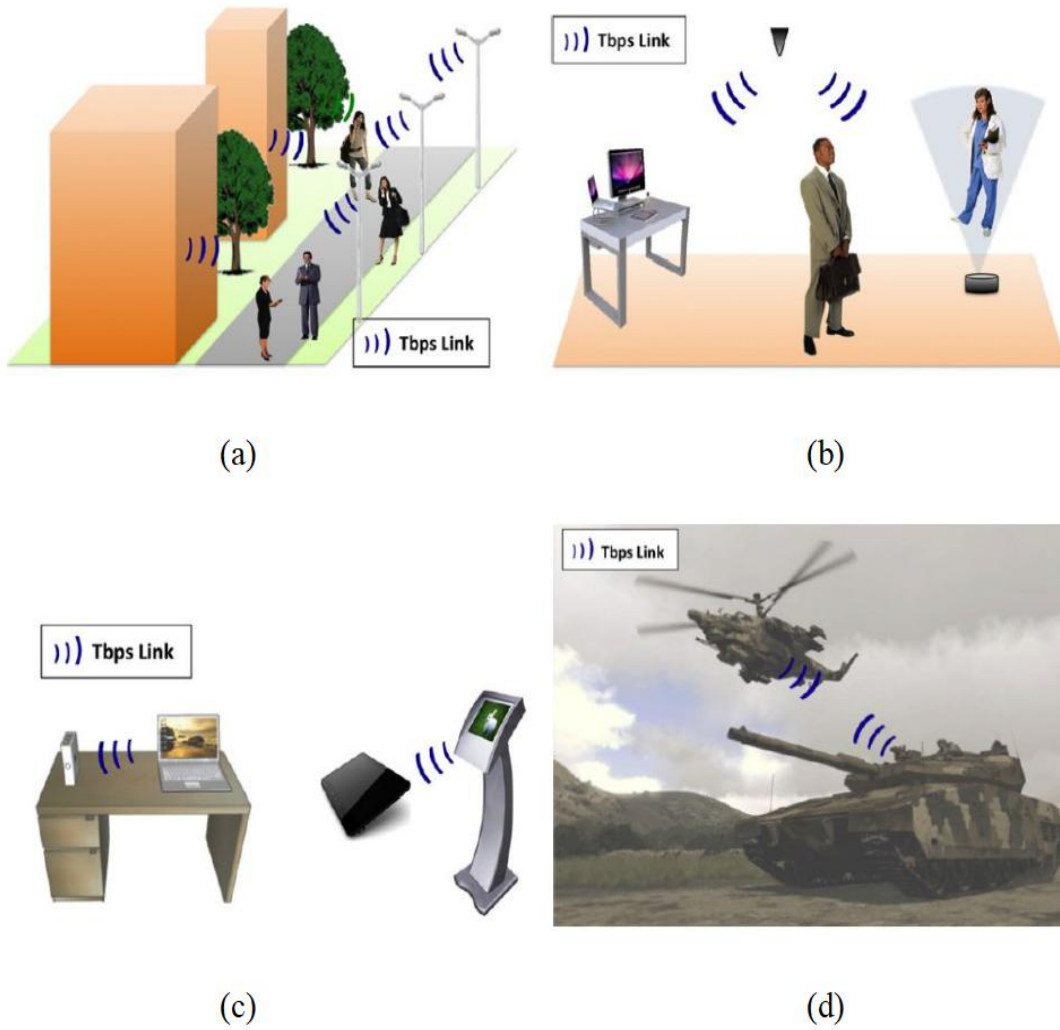
Figure 1.7: THz communication applications at macroscale (a) Future 6G Cellular Networks, (b) Terabit Wireless Local Area Networks, (c) Terabit Wireless Personal Area Networks, (d) secure Terabit Wireless Communication [35].

Portable personal health monitoring systems can be achieved by using nanoscale sensors around body. As a nanoscale personal network established between the sensors, the health condition data can be collected by a micro devices like mobile phone, consequently, these data can be forwarded to the healthcare provider as demonstrated in Figure 1.8 (a)[35]. Planar THz antenna can provide efficient and scalable method to establish a ultra-high-speed on-chip communication at core level as shown in Figure 1.8(b) [35].
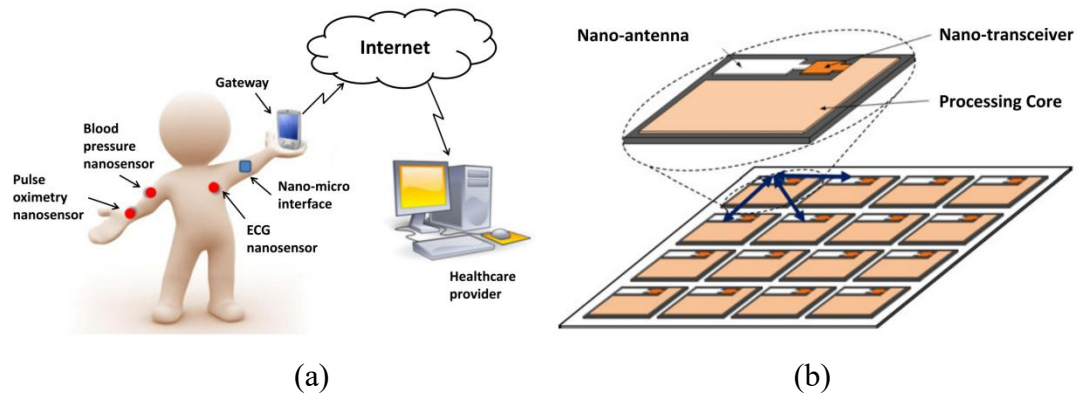
Figure 1.8:THz communication applications at nanoscale: (a) Wireless Nano Sensor (include blood pressure nanosensor, pulse oximetry nanosensor and ECG nanosensor) Networks for health monitoring , (b) Wireless on-chip communication [35].

1.4 Research Motivations and Objects

Although THz spectrum has potential in many industries, the major limitation is the lack of compact, efficient and cheap THz sources. In the 1980s, development of femtosecond laser and photoconductive antenna introduced in [49] led to a revolution in the development in THz devices. Since then, especially in the last decade, several different THz sources have been introduced, but the practical feasibility of applying THz techniques to many systems is still restricted since the THz sources are still facing four main problems as following: low output power, low efficiency, bulky nature and cooling system. Among all the available THz emitters, THz antenna is demonstrated to be an important and common components in THz systems. The prevalence of THz antenna can be attributed to several facts such as these antennas can work as both detector and emitter, they also offer small sizes and the independent on the cryogenic cooling facilities. The efficiency of a THz antenna is small, low of 0.1% in pulsed systems [50], and 1% in continuous wave systems [51], and the difference between the two systems will be explained later. Therefore, it is important to investigate the performance of the THz antenna to maximise the efficiency. The total efficiency of it separated into three components: coupling, matching and radiation efficiencies. The last two are similar to those of radio frequency and microwave antenna, the methods used to enhance these efficiencies of RF/MW antenna can also be applied to THz antenna. The coupling efficiency has triggered noticeable interest in the optical-to-THz conversion efficiency. Therefore, a

fundamental research on the interaction between the optical laser beam and THz antenna will be carried out including photoconduction behaviour and factors affect the optical-to-THz conversion efficiency.

It is common to use commercial simulation tool for the RD antenna analysis, however, the analysis of THz antenna requires extra investigations on the optopelectronic characteristics which cause by the photoconduction effect of the material. Commercial semiconductor solvers like Synopsys Sentaurus TCAD [52] provide advanced modelling of the electric field distribution and charge concentration. However, it is not capable of the THz antenna simulation. It is possible to import the results of field distribution from semiconductor solvers to full-wave electromagnetic solvers to perform the antenna analysis, this method can be a less accurate process. Therefore, a new simulation process that can examine both the field distribution of photoconductive material and antenna performance with a full-wave electromagnetic solver is investigated.

Conventional THz photomixer antenna consists of electrodes, antenna and a lens, where electrodes is the structure that generate THz current to excite the antenna. Geometrical optimization of electrodes can improve the photoductive electric field distribution and generate more THz current as a result. However, the source resistance of the antenna will also affected by the configuration of photomixer, therefore, optimizing optical-to-THz conversion efficiency without changing the configuration of photomixer is very important. Moreover, since the configuration of photomixer affects the source resistance of THz antenna, impedance matching of THz antenna should be studied. In addition, lens is utilised in conventional THz antenna to couple the generated THz filed to air and form a directional radiation. Hence, in order to improve the radiated THz power and abandon the usage of lens, modifications in THz antenna design are required. By considering optical-to-THz efficiency, matching efficiency, radiation efficiency and the physical structure of the THz antenna, an optimized THz photomixer based antenna is proposed and studied.

The main objective of this thesis are summarised as follows:

1. To develop a new equivalent circuit model of THz photomixer based antenna

2. To develop a simulation method that examine both electric field distribution of photomixer and THz antenna with a full wave electromagnetic simulation tool.

3. To optimize the optical-to-THz conversion efficiency of photmixer

4. To improve the matching and radiation efficiency of photomixer based THz antenna

5. To investigate the feasibility of the proposed photomixer based THz antenna's physical construction

1.5 Thesis Overview

In Chapter 1, an introduction of Terahertz band, an overview of THz sources utilizing radio frequency technique, optical technique and the combination of both techniques have been given with the challenges in the channel modelling of terahertz communications. Furthermore, applications utilizing terahertz imaging, spectroscopy and wireless communication have been addressed. Then, the motivation and the objectives of this thesis are outlined.

In Chapter 2, The THz antenna will be compared with RF/MW antennas to highlight the research options of THz antenna. A new model of terahertz photomixer based antenna will be developed. By analysing the new model mathematical, various parameters that affect the performance of THz photomixer antennas will be analysed and discussed.

In Chapter 3, a new design process that evaluate both optoelectronic behaviour of photomixer and THz photomixer based antenna with a full-wave simulation solver will be discussed. Then, the finite difference time domain method for cross validation will be introduced briefly.

In Chapter 4, different approaches of optimizing the optical-to-THz conversion efficiency such as manipulating the configuration of photomixer electrodes, replacing photomixer electrode with plasmonic material, utilizing bragg reflector, implementing two designs of two dimensional photonic crystal as reflector underneath photomixer and employing dielectric superstrate and frequency selective surface above photomixer will be proposed.

In Chapter 5, the limitations of using lens to achieve power capture and directional radiation will be highlighted. In order to avoid lens, THz dielectric resonator antenna based upon the photomixer designed in Chapter 3 will be proposed. The proposed DRA is truncated from the electrically thick photoconductive substrate of photomixer to create a DRA that supports higher order mode in conjunction with a dielectric superstrate for gain enhancement. In addition, source capacitance and

biasing network will be incorporated in the model of DRA. Then, the choke filter is used to minimize the power leakage of generated THz photocurrent and to improve the impedance matching.

In Chapter 6, further research about feasibility of physically supporting superstrate above DRA using multi-layered configuration at millimetre wave frequency with coplanar waveguide port will be proposed. Furthermore, optimizing the feeding method to accomplish a wide band and circular polarization will be discussed.

Finally, Chapter 7 presents the summary of the main objectives, highlights the achievements. Furthermore, the future work suggestions are presented.

Chapter 2: Analysis of Terahertz Photomixer based Antenna

2.1 Introduction

Various THz sources and envisioned THz applications were introduced in the previous chapter. The THz antenna is the final block in all transmitting applications, and it is the first block in receiving applications. Therefore, THz antenna is the foundation of any THz application system. However, compared with RF/ MW antenna, the analysis, simulation and measurement of THz antenna are totally different due to the special excitation method. Therefore, a comparison between THz

antennas and RF/MW antennas is performed to stress research options in THz antennas. Low power level and low optical-to-THz conversion efficiency are the main limitation of the development of THz antenna, and some of the THz photomixer in the literature will be reviewed. In order to analyse and solve these problem, an equivalent circuit modelling is necessary. Two types of equivalent circuit models have been introduced in the literature. One is large-signal circuit model [53]. The gap capacitance of the antenna is modelled as constant capacitance, photoconductive material is modelled as time-dependent resistance and antenna resistance is included in the model. The main lack of the model is that the local electric field cannot be predicated accurately. The other equivalent circuit consists of three element: the photo-switch is modelled as a resistor with time-varying conductance, the space-charge screening is modelled as time-varying voltage source and the antenna impedance [54]. This model improve the accuracy since more physical behaviour of the devices have been considered compared with previous simplified lumped element model. However, the complexity of the physical behaviour complicate the equation deviation. Therefore, involving physical behaviour in the simplified lumped element model is necessary to keep both the accuracy and simplicity of the equivalent circuit model. Therefore, a new equivalent circuit model is developed with the usage of lumped element that derived from complex physical mechanisms in this chapter. In addition, based upon the newly developed equivalent circuit, factors that improve the low efficiency of THz photomixer antenna is studied.

2.2 Comparison of THz photomixer antennas with RF/MW Antennas

Figure 2.1 and Figure 2.2 demonstrate the setups of RF/MW antenna and THz phtomixer antenna during measurement. It can be noticed that the measurement setup of THz photomixer antenna is more complex since the THz antenna operates based upon the laser excitation where the conventional RF/MW antennas is fed by the measurement facility. In this section the differences between THz photomixer antenna and RF/MW antenna are summarised.
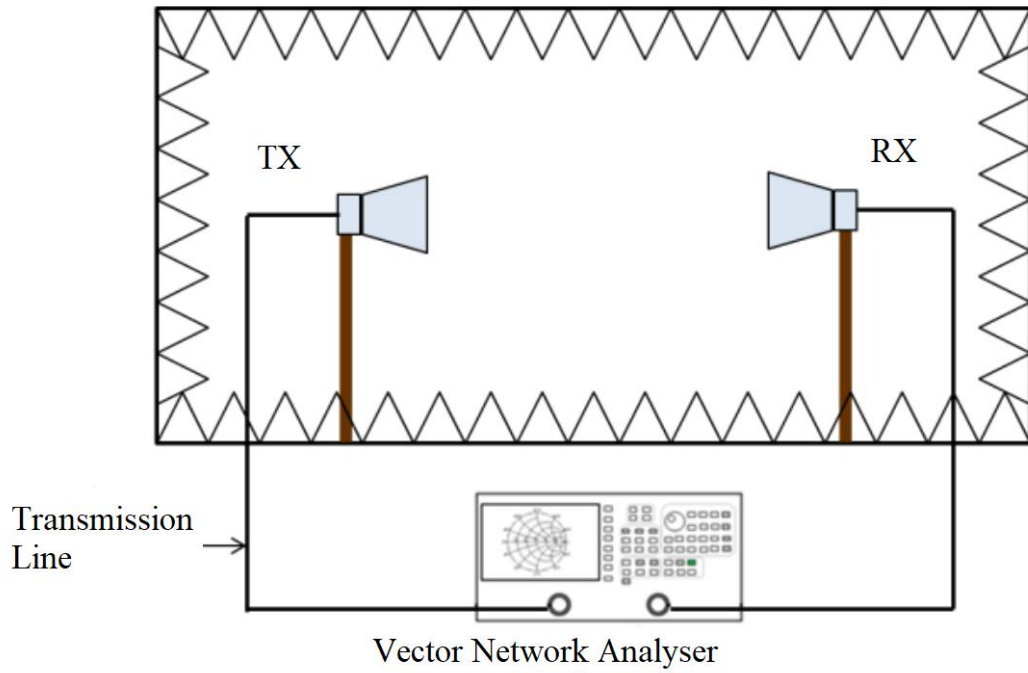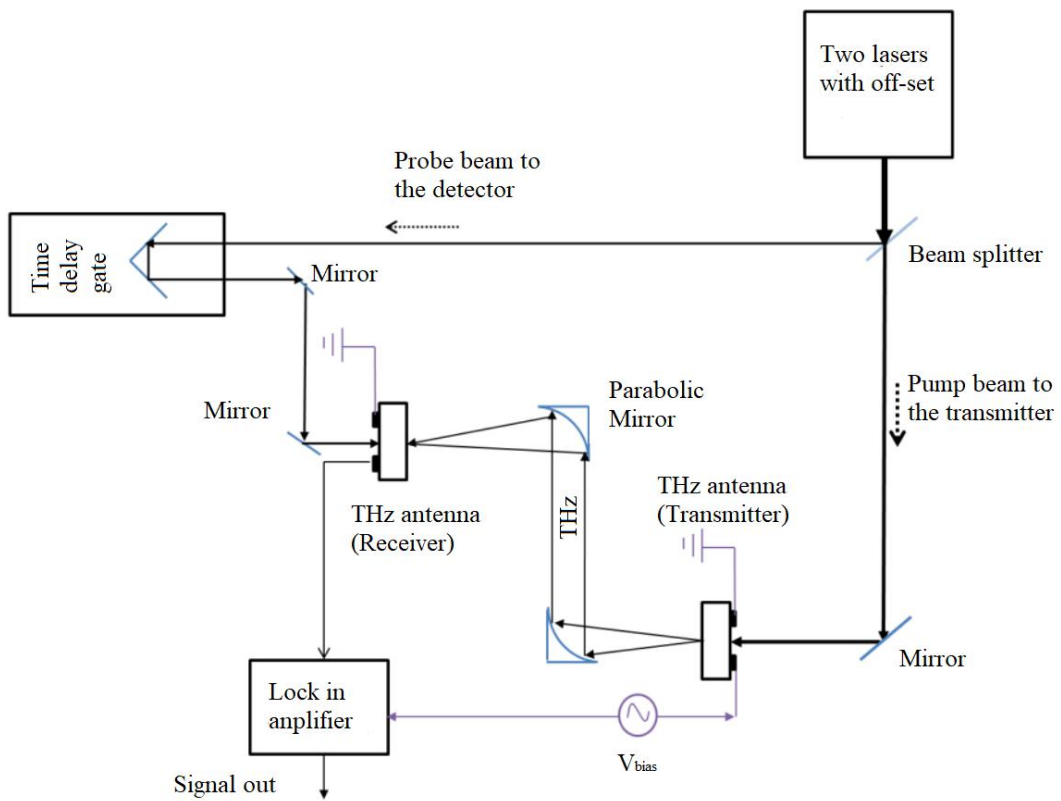
Figure 2.1: Measurement setup of RF/MW antenna

Figure 2.2:   Measurement setup of THz photomixer antenna [55]

2.2.1 Excitation Source, Feeding and Biasing

There are numerous types of feed such as coaxial cable, microstrip and coplanar waveguide available for the conventional antenna. But move onto the THz photomixer antenna, analogous feed lines is not applicable. In practice, the laser can be coupled to the THz antenna either through air or by fibre. Generally, as shown in Figure 2.2, optical waves illuminate the photomixer antenna through air. Exception presence when there is requirement of flexible transmitter and receiver, in this case, optical fibre is employed to achieve so. 800nm and 1550nm laser pulses that coupled through fibre to THz systems have been demonstrated [56, 57, 58]. Since the THz photomixer is fed by two co-linear laser beam, the source impedance of THz photomixer antenna is not a constant value, which is other than the normal 50/75 ohms feed line used for RF/MW antennas. The varying source impedance imposes a new requirement of the THz photomixer antenna's analysis which will be investigated later in this chapter.

Furthermore, bias voltage is required for the THz photomixer antenna, since the generation of THz signal of photomixe antenna on the transmitting side based upon the bias voltage as illustrated in Figure 2.2. However, for normal RF/MW antenna without any semidonductor switches, bias voltage is not necessary.

2.2.2 Substrate Material

The substrate material for the planar RF/MW antenna is required to be low-loss dielectric material. For most PCB based RF/MW antenna, FR4, which is made of glass-reinforced epoxy laminate material, is one of the most popular option. III-V compound semiconductor like GaAs is used as substrate of monolithic microwave integrated circuit antenna due to the property of high carrier mobility [59]. Photoconductive material is the foundation of the THz signal generation for THz photomixer antenna. The materials like Si, GaAs and InGaAs are used in the THz photomixer antenna, from which the most popular material is low temperature grown GaAs. The advantages of using LT-GaAs is firstly fast current variation can be obtained by ultra-short carrier lifetime, secondly, stronger THz signals can be generated due to the relatively high electron mobility, finally, high bias voltage can be applied to the photomixer because of the high intrinsic resistivity and breakdown

voltage characteristics[60, 61]. Because of the advantages of LT-GaAs and the importance of photocnductive materials for the THz wave generation, the characteristics and effective parameters of LT-GaAs will be described in next sub-section.

2.2.2.1 THz Photoconductive Materials

The popularity of THz photoconductive material study not only due to its importance for THz wave generation, but also because there is no natural material capable of emitting THz wave efficiently [62].

The first ever THz antenna reported employed Silicon as the photoconductive materials [49]. Silicon have the bandgap of 1.12eV and intrinsic resistivity of $2.3 \times 10^5 \Omega$.cm. However the optical recombination processes of Silicon photoconductive substrate are relatively low due to the misalignment between low boundary of conduction band and higher boundary of valence band [63]. By contrast, GaAs has direct band and the intrinsic resistivity of it is $10^8 \Omega$.cm. In addition, GaAs is III-V compound semiconductor which means it is possible to optimise the electrical and optical behaviours by manipulate the composition of it.

Since the GaAs is used as photoconductive substrate, ability of growing extra epitaxial layer is important. Consequently, liquid encapsulated Czochralski method is utilized to grow semi-insulating GaAs [64]. Since the carrier life time affect the bandwidth and SNR of THz antennas, intermediate energy band is design in the bandgap by native point defect. However, the mean free path is reduced by the presence of the intermediate energy levels which lead to the reduction of thermal conductivity and the carrier mobility [65, 66]. Therefore, achieving small carrier lifetime, high mobility and high dark resistivity at same time becomes the prior challenge in the ultrafast photoconductive material research.

LT-GaAs produced by low temperature beam epitaxy can achieve intensive point defects. It was used as substrate of THz photoconductive antenna since 1988 [67]. Since then, substantial research on the factors that affect the properties of LT-GaAs dueing the fabrication has been performed [68-71]. Figure 2.3 collects the carrier lifetime of LT-Gas versus the growth temperature of them. It can be noticed that even though the growth temperature is same, the values of carrier lifetime from different literatures are different. The reason is that every MBE chambers are different from

each other, and even using same chamber, it is very difficult to control the exact growth temperature and ambient condition. Therefore, the production of two LT-GaAs wafers with identical characteristics are impossible.
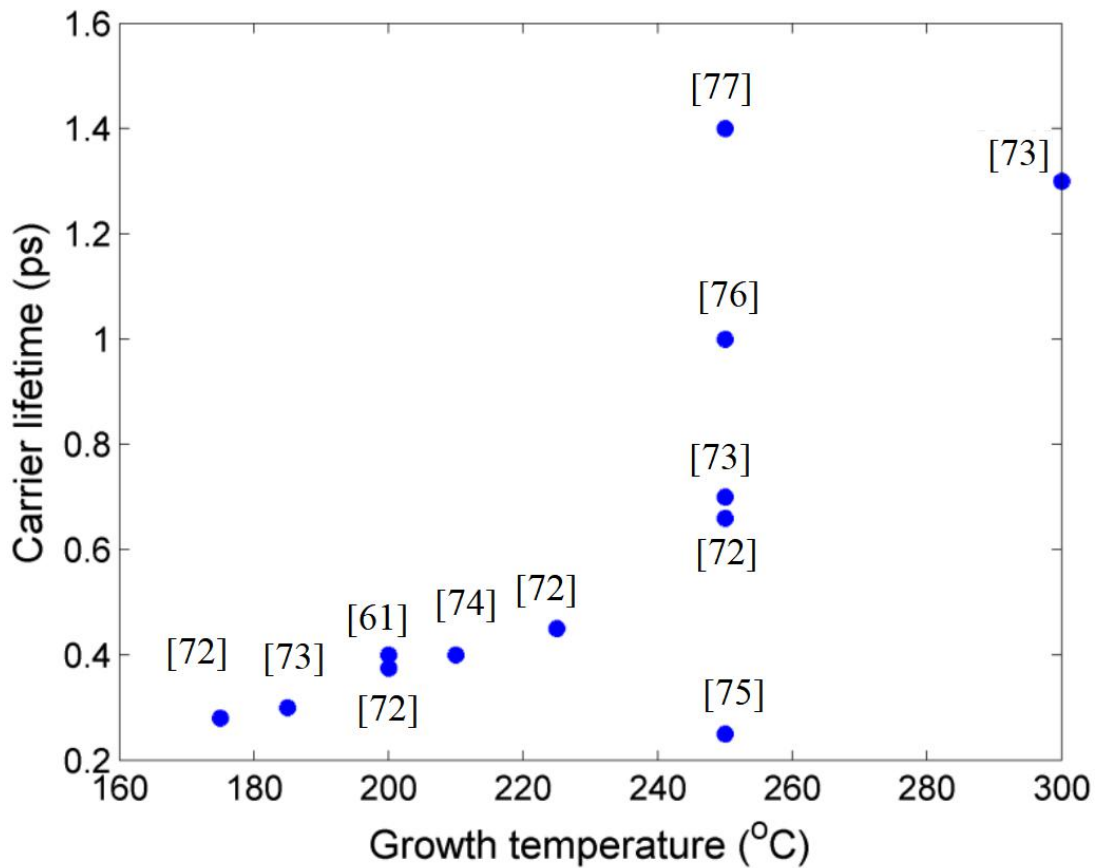

Figure 2.3: Measured carrier liftime of LT-GaAs versus the growth temperature

Other techniques like ion-implantation [76] and self-assembled ErAs island in GaAs [73,75] can be used to optimize the characteristics of GaAs. As a result, similar carrier lifetime to the LT-GaAs can be achieved. However, the outcome of low intrinsic resistivity from ion-implantation and drawback of low mobility from ErAs:GaAs limits their utilization. Therefore, LT-GaAs still be the best option for the photoconductive material of THz antenna [78].

Table 2.1 summarises the properties of SI-GaAs and LT-GaAs and LT-InGaAs which are used as photoconductive substrate at 800nm and 1550nm, respectively. SI-GaAs offers high mobility, but the bias voltage could be applied to it is low which is because of the lower breakdown voltage. Moreover, the lower resistivity of SI-GaAs produces greater amount of dark current compared to LT-GaAs which causes the system to heat up and terminate faster than the LT-GaAs. Another problem with SI-GaAs is that limited spectrum can be achieved and more noise will be

generated by the large carrier lifetime of it. There are a variety of fabrication methods for InGaAs, which results in variations in the material's properties. LT-InGaAs has the worst properties among the three material listed, however, it can siginficantly minimize the expense of the THz system since its consistency with well established communication optical sources. In general, due to their excellent combined characteristics, LT-GaAs is the most popular material in THz antenna research.

Table 2.1: Properties of various THz photoconductive materials

Material	Carrier liftime (ps)	Mobility $(cm^2.V^{-1}.s^{-1})$	Resistivity $(\Omega.cm)$	Breakdown field $(V.cm^{-1})$
SI-GaAs	Several hundred [79]	8500 [80]	$\sim10^7$[81]	4×10^5 [80]
LT-GaAs	<1 [82]	200 [79]	$>10^7$ [67]	5×10^5 [79]
LT-InGaAs	Larger than LT-GaAs [83]	26 [84]	760 [84]	$\sim6\times10^4$ [84]

2.2.3 Antenna Electrode Material

Copper and other extremely conductive metals are often used in RF/MW antennas. The electrode material in THz antennas is an AuGe alloy or Ti/Au (Titanium/Gold) layer [85]. The stacked Titanium and gold structure is more often used [86-89], in which a Ti sheet is incorporated to maximize the stickiness of the Au, therefore, the electrode is mounted tightly on the substrate[8]. Compared between Ti/Au and the AuGe alloy, Ti/Au is a better choice as it does not require annealing after deposition [90].

The conductivity, σ ,of Au is 45.2×10^6S/m [1]. Since the skin depth, $\delta=(1/\pi f\mu\sigma)^{1/2}$, it is 74.9nm for Au at 1THz. As the current flow near the metal surface, the surface resistance of 0.29Ω for a square shaped gold by using $R=1/(\sigma\times depth)$. Practically, the electrodes are consist of a 10-20nm layer Ti and a Au with few tens of nm thickness.

Graphene is another material that has been investigated as an antenna electrode material [91]. The Young's modulus, carrier density and absorption coefficient of graphene is 1.5Tpa, 200000$cm^2.V^{-1}.s^{-1}$ and $24\times10^4cm^{-1}$, respectively [92, 93]. Since the conductivity of graphene depends on the temperature and the chemical potential, a reconfigurable graphene antennas can be achieved by manipulating such parameters [94].

2.2.4 Type of Current

Conduction current is the main current type of RF/MW antennas, which is caused by the movement of conduction electrons. As for the THz antenna, two types of current are generated, drift current caused by the biased electron-hole pairs and displacement current induced in photoconductive which is substrated by second order nolinear optical characteristics. However, the displacement current could be neglected as the bias voltage getting higher, hence, drift current is the main current type when the biased field is more than 10^5 V.cm^{-1} [95, 96].

2.2.5 Fabrication and Measurement

Due to the limited size of the THz antenna and the need for a specific fabrication environment, fabricating a THz antenna is a difficult and costly process. The photoconductive substrate fabrication, as well as deploying the THz antenna on the substrate, are the two steps in the fabrication of a THz antenna. In section 2.1.2.1, the preparation of photoconductive substrate was briefly introduced. Photolithography and electron beam lithography are the two main method to implementing the THz antenna on the photoconductive substrate. Electron beam lithography is capable of fabricating sub-micron dimensions which is more precise than the Photolithography, hence, it is more expensive.

The measurement setup and techniques of THz antenna is more complex than them of RF/MW antenna. As demonstrated in Figure 2.1, both treanmitter and receiver antennas can be excited by a vector network analyser in RF/ MW antennas, then vector network analyser can compute various parameters. Moreover, the anechoic chambers is widely used to determine the radiation pattern of RF/MW antennas. In THz antenna measurement setup, the THz antenna is excited by laser beams through air as shown in Figure 2.2. Since there is no physical connection between the laser beam and transmitting/receiving antenna as well as the usage of different mirrors to guide the signal during transmission, it is possible that the THz wave is attenuated and diverged during transmission. Moreover, since the THz antenna only work when the laser beams is illuminated, misalignment of incident laser beam and THz antenna will lead to inaccurate results. Therefore, fibre coupled detector is introduced to avoid the lose of laser illumination [97, 98]. In addition, as

described in section 1.3.1, the THz communication is sensitive to the humidity, the THz measurement equipment is packaged and filled with dry nitrogen.

2.2.6 Computer Aided Design

Computer Aided Design (CAD) tools like CST, HFSS and FEKO is now a common simulation software for antenna design. However, all of the aforementioned design tools can only simulate the electromagnetic part of THz antenna design, where the optoelectronic part requires another design tool to examine. Hence, it is necessary to develop a new method that can incorporate the numerical analysis with CAD tools to merge the two parts of THz antenna design in a full wave electromagnetic solver. This is one of the contributions that will be explained later on.

2.3 Equivalent Circuit Modelling of THz Photomixer based Antenna

The photoconduction effect of the THz photomixer based antenna was described in section 1.2.3. A more detailed description of the mechanism of THz wave generation will be provided in this section. The importance of various parameters that affect the performance of THz antenna will be emphasised by equivalent circuit analysis.

2.3.1 Generation of THz wave from a THz Photomixer Antenna

Figure 2.4 depicts a typical photoconductive photomixing scheme. When two femtosecond laser beams with beating frequencies falling in the THz spectrum, electron-hole pairs are generated at the THz spectrum in the photoconductive substrate when the energy offered by incident laser beams is large enough to drive them from valence band to conduction band. Then, the presence of the bias voltage provides electric filed across the antenna electrodes, then, the photo-induced carriers are accelerated by the electric field to produce an AC current. This current is used to excites an antenna and hence generate THz radiation.
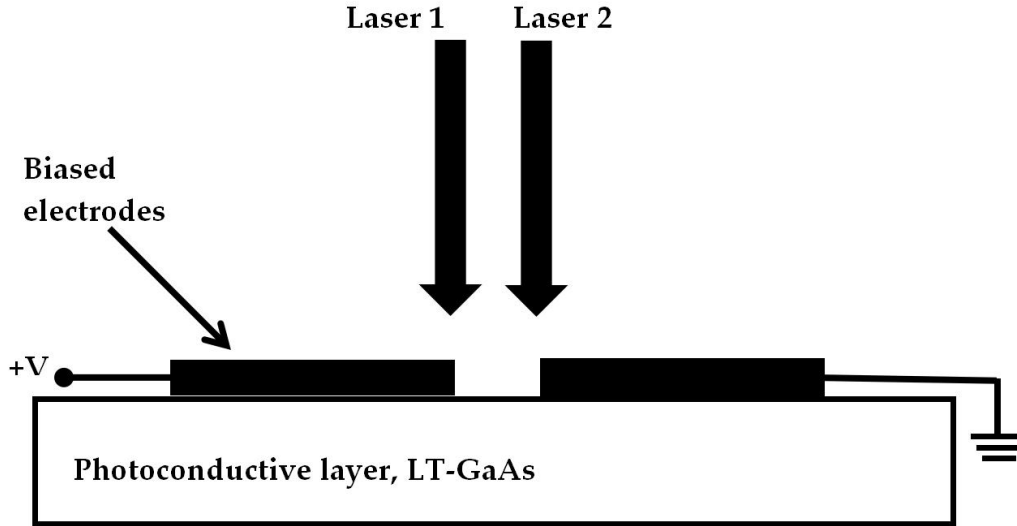
Figure 2.4: Schematic diagram of THz photomixer antenna

2.3.2 Derivation of Generated THz power from the Equivalent Circuit of THz Photomixer Antenna

As the absorption coefficient, mobility and recombination time of the low temperature grown GaAs, LT-GaAs photoconductive layer are independent of the applied bias voltage, the electrodes of the photomixer can be considered as an ohmic conductances. While the time varying source conductance is electrically modelled as a photoconductance because the photocarrier collection process described previously is photoconductive rather than photovoltaic. Consequently, the photomixer based THz antenna can be represented using the equivalent circuit illustrated in Figure 2.5. It can be noted that the photomixer is represented by a photoconductance, $G_s^{-1}(\Omega,t)$ in parallel with a capacitance, $C_{electrodes}$. The configuration of the photomixer electrodes and the dielectric constant of the photoconductive layer contribute to this capacitance. The biased voltage drives the generated photocarrier which result in the generated photocurrent that excite the THz radiating antenna, and the ohmic loss of the antenna is represented in Figure 2.5 by a resistance of $R_{antenna}$ [99].
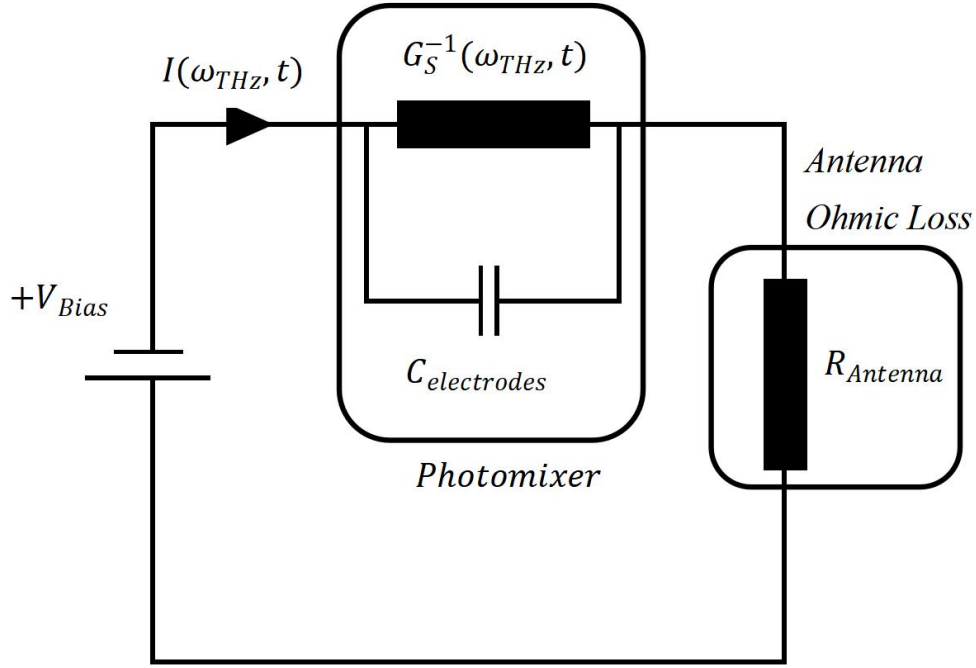
Figure 2.5:Equivalent circuit of photomixer based THz antenna

The electric fields of the two incident laser beams on the LT-GaAs' surface can be expressed as:

$$E = |E_i| e^{j\omega_i t} \tag{2.1}$$

where ω is the angular speed of incident laser and $i = 1,2$, represents laser 1 and laser 2, respectively. The laser intensity been absorbed by the LT-GaAs is proportional to the square of the total incident electric field on the LT-GaAs' surface:

$$I(\Omega,t) = (1-\Gamma) \lozenge_i |E|^2 = I_0 (1-\Gamma)[1 + 2 \frac{\sqrt{m I_1 I_2}}{I_0} \cos(\Omega t)] \tag{2.2}$$

where I_0 is the maximum optical intensity illuminated on the LT-GaAs, Γ is the reflection coefficient at the LT-GaAs -air interface, m is the mixing efficiency which describes the overlap of the laser beams, I_1 and I_2 are the intensity of the two incident laser beam and Ω is angular beat frequency, $(\omega_1 - \omega_2)$.

The induced photo-carriers generated from the incident laser beams as a function of time is:

$$\frac{dn(t)}{dt} = -\frac{n(t)}{\tau_c} + \frac{\alpha(Tmp)}{hf_l} I(\Omega,t) \tag{2.3}$$

in which h is the Plank's constant, f_l is the average frequency of Laser 1and Laser 2 and τ_c is the carrier lifetime. In addition, $\alpha(Tmp)$ is the temperature-dependent

absorption coefficient of LT-GaAs and *Tmp* is the temperature in kelvin. For a LT-GaAs layer with a direct band gap, *α(Tmp)* can be expressed as[100]:

$$\alpha(Tmp) \approx K_{abs} \sqrt{\frac{hf_l - E_g(Tmp)}{q}} \tag{2.4}$$

where K_{abs} is a certain frequency-independent constant which is approximately 9.7×10^{15} for LT-GaAs [100], and the temperature dependent band gap energy of LT-GaAs, $E_g(Tmp)$ is defined as:

$$E_g(Tmp) = E_g(0) - \frac{\alpha_E T^2}{T + \beta_E} \tag{2.5}$$

in which $E_g(0)$ is the gap energy of LT-GaAs at 0 °K which is about 1.519 eV, α_E and β_E are material constants of GaAs which are approximately 5.41×10^{-4} eV/K and 204 K, respectively [101].

By assuming $I_1 = I_2 = I_0$ and $t/\tau_c \gg 1$, then substituting (2.2) into (2.3), the generated carrier density can be obtained as:

$$n(\Omega, t) = \frac{\alpha(Tmp)}{hf_l} I_0 (1 - \Gamma) \tau_c (1 + \sqrt{m} \frac{\cos(\Omega t) + \Omega \tau_c \sin(\Omega t)}{1 + (\Omega \tau_c)^2}) \tag{2.6}$$

The conductance of the photomixer can be expressed as:

$$G_s(t) = \int dG_s(t) = \int_0^{T_{sub}} \sigma(t) e^{-\alpha(Tmp)z} \frac{W}{L} dz = \frac{W}{\alpha(T)L} \sigma(t)(1 - e^{-\alpha(Tmp)T_{sub}}) \tag{2.7}$$

where T_{sub} is the photoconductive region depth, W is the electrode width, L is the electrode length and $\sigma(t)$ is the conductivity. The electrical conductivity is defined as:

$$\sigma(t) = e\mu_e n(t) = \frac{\alpha(Tmp)e\mu_e}{hf_l} I_0 (1 - \Gamma) \tau_c (1 + \sqrt{m} \frac{\cos(\Omega t) + \Omega \tau_c \sin(\Omega t)}{1 + (\Omega \tau_c)^2}) \tag{2.8}$$

In which e is the electron charge and μ_e is the electron mobility. Therefore, the photomixer's conductance can be derived by substituting (2.8) into (2.7):

$$G_s(\Omega, t) = \frac{We\mu_e I_0 \tau_c}{hLf_l} (1 - \Gamma)(1 - e^{-\alpha(Tmp)T_{sub}})(1 + \sqrt{m} \frac{\cos(\Omega t) + \Omega \tau_c \sin(\Omega t)}{1 + (\Omega \tau_c)^2}) \tag{2.9}$$

The impedance of the system can be given by analyzing the equivalent circuit shown in the Figure 2.5:

$$Z_t(\Omega,t) = \frac{1}{j\Omega C_{electrodes} + G_s(\Omega,t)} + R_{antenna} \tag{2.10}$$

and the radiation power can be defined as:

$$P_{THz}(\Omega,t) = R_{antenna}(\frac{V_{biased}}{Z_t(\Omega,t)})^2 \tag{2.11}$$

Therefore, as $R_{antenna}G_s \ll 1$ and by replacing system impedance by (2.10), as well as neglecting the imaginary part, the radiation power can be expressed as:

$$P_{THz}(\Omega,t) \approx R_{antenna} \frac{V_{biased}^2 G_s^2(\Omega,t)}{1+(\Omega R_{antenna}C_{electrodes})^2} \tag{2.12}$$

In addition, by employing (2.9), the mean generated THz power can be expressed as:

$$P_{THz} \approx [\frac{We\mu_e\tau_c}{hLf_l}(1-\Gamma)(1-e^{-\alpha(\mathrm{Tmp})\mathrm{T_{sub}}})]^2 (\frac{mR_{antenna}V_{biased}^2}{[1+(\Omega R_{antenna}C_{electrodes})^2][1+(\Omega\tau_c)^2]})I_0^2 \tag{2.13}$$

2.3.3 Parameter Analysis

In order to demonstrate the time varying characteristic of the source conductance, $G_s(\Omega, t)$, based upon the equation (2.9), an example of photomixer using the parameters listed in Table 2.2 is calculated.

Since the wavelength of the incident laser beam is presumed to be 800nm, λ_1, and the wavelength of the second laser beam, λ_2, is tuned to achieve a THz beating frequency by $f_{THz}=c|\lambda_1-\lambda_2|/(\lambda_1\lambda_2)$ [102]. In the case of a THz photomixer operate at 1THz, $\lambda_2 \approx 802$nm. By applying the parameters listed in Table 2.2, the time varying source conductance of the THz photomixer antenna is shown in Figure 2.6. The periodic variation of the source conductance is consistent with the envelope of the beating waveform. The mean source resistance can be calculated by taking the reciprocal of the mean source conductance between the trough, 6.64$\mu\Omega^{-1}$, and crest, 9.1$\mu\Omega^{-1}$. As a result, the mean source resistance is ~128kΩ, which matches the evaluation of the photoconductive resistance is much larger than 10kΩ [88].

Table 2.2: Parameters used in the source conductance calculation

Parameters	Value
Γ	0.318 for LT-GaAs-air interface
μ_e	1000 cm^2.V^{-1}.s^{-1}
$\alpha(T)$	6000 cm^{-1}
m	1
τ_c	1 ps
L	10 µm
W	10µm
T_{sub}	1µm
f_l	374.5 THz
Average power of one laser	15 mW
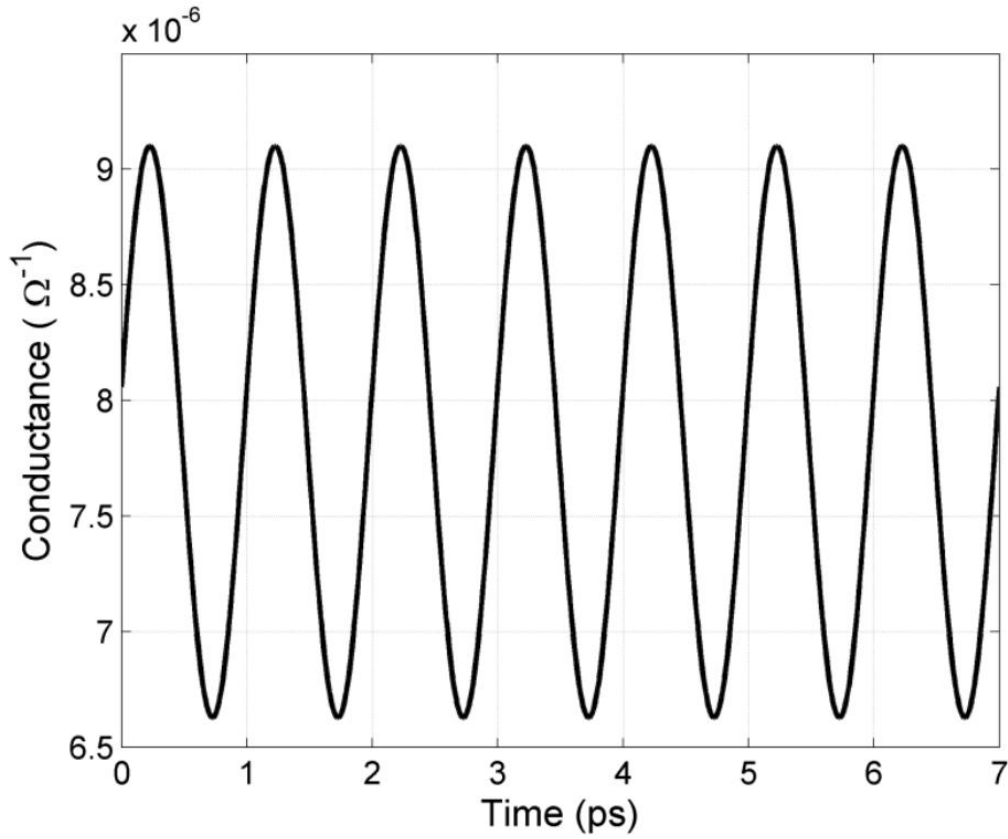
Figure 2.5: The time-dependent source conductance calculated from the parameters listed in Table 2.2

Moreover, the source resistance calculated above stressed the main challenges in the improvement of matching efficiency of THz photomixer antenna is appropriate design with higher impedance. Therefore, the effect of various parameters such as total average optical power, the length of electrodes, carrier lifetime, carrier mobility and optical absorption coefficient on the source resistance of a THz photomixer antenna is investigated. The other parameters are kept as the value listed in Table 2.2 while the one is investigated.

Figure 2.6 demonstrate the impact of the total average laser power on the source resistance. As higher laser power is used, the generated photo-carrier density in the photoconductive substrate as well, in the other word, the photoconductive substrate becomes more conductive, therefore, the source resistance falls at higher average laser power, consequently, moderate the problem of impedance mismatching.

The electrodes' length of THz photomixer represents the illumination area of the laser beams. Therefore, as it is shown in Figure 2.7, the source resistance rises with longer electrodes which is the consequence of the reduction of the generated photo-carrier density.
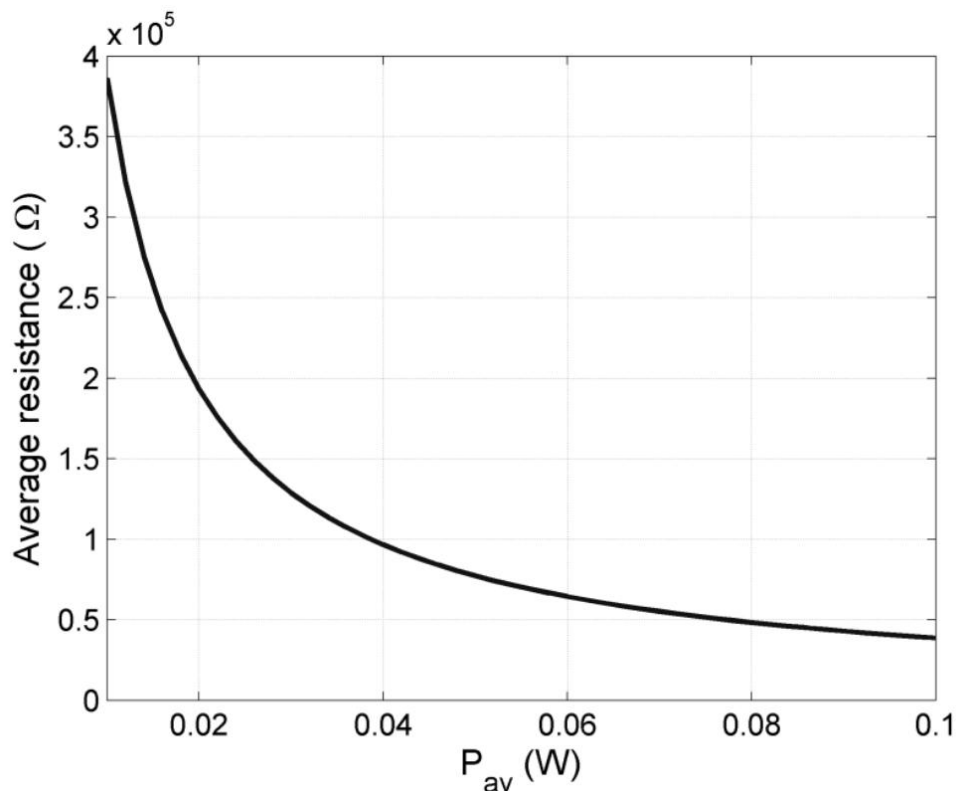
Figure 2.6: Source resistance versus the average laser power
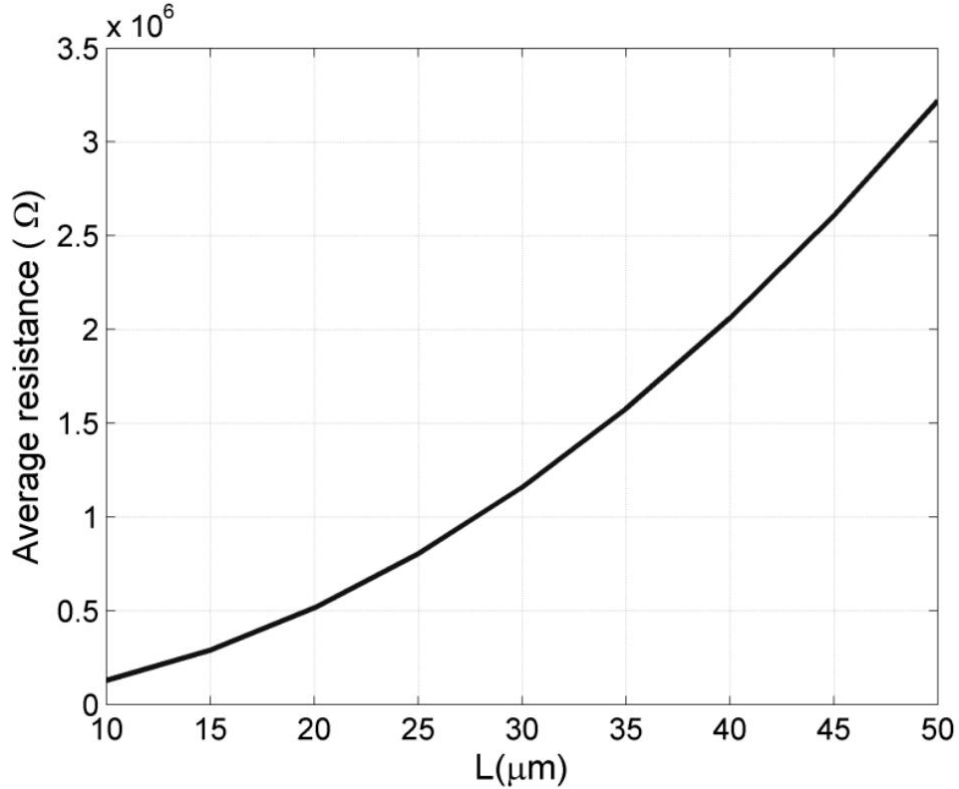
Figure 2.7: Source resistance versus the length of photomixer electrodes

The dependency of average source resistance on the carrier lifetime is studied. It can be observed from Figure 2.8 that the source impedance becomes extremely high with shorter carrier lifetime and becomes flat with longer carrier lifetime. These is because longer carrier lifetime leads to longer recombination period of free photo-carriers, which behaves like conductor. In contrast, shorter carrier lifetime result in less generation of carrier and hence unable to generate photocurrent. For instance, $\tau_{c\text{-}opt}=1/2\pi f_{THz}$ is used to determine the optimum carrier lifetime for THz photomixer antenna [89].

Moreover, Figure 2.9 depicts the impact of carrier mobility of photoconductive material on the source resistance. It shows a similar tendency to the Figure 2.8, smaller carrier mobility leads to extremely high source impedance and almost constant small source resistance can be achieved with larger carrier mobility.

Finally, the effect of optical absorption coefficient on average source resistance is illustrated in Figure 2.10. As the optical absorption coefficient increases, more photo-carriers are generated due to more laser powers absorbed by the photoconductive substrate, consequently, smaller source resistance is achieved.
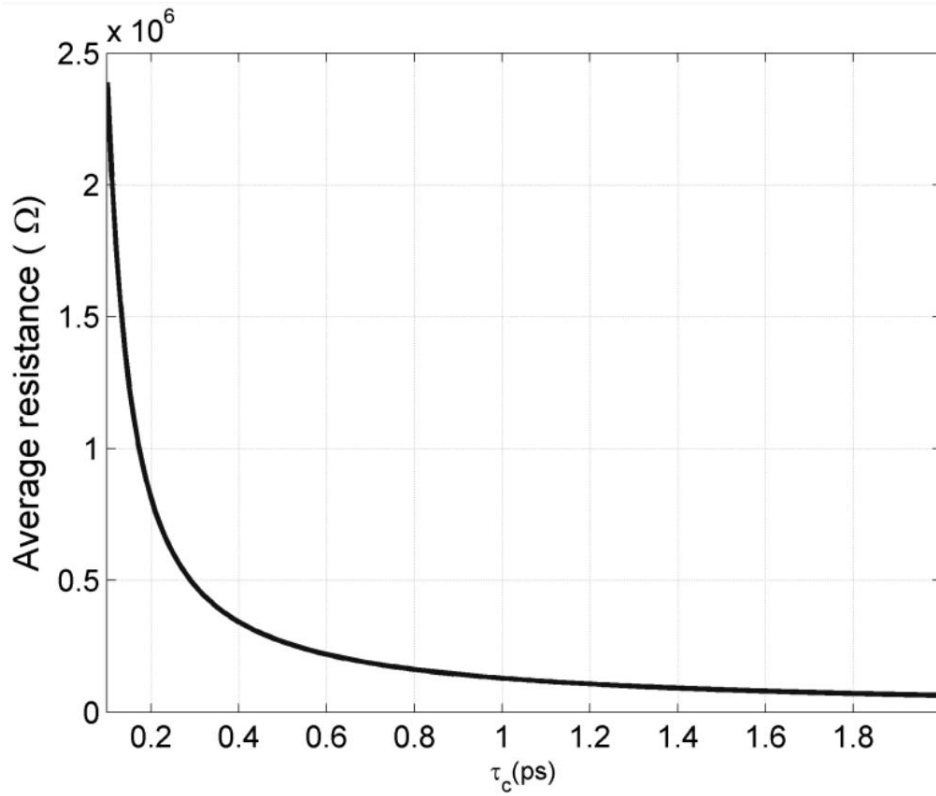
Figure 2.8: Source resistance versus the carrier life time of photoconductive material
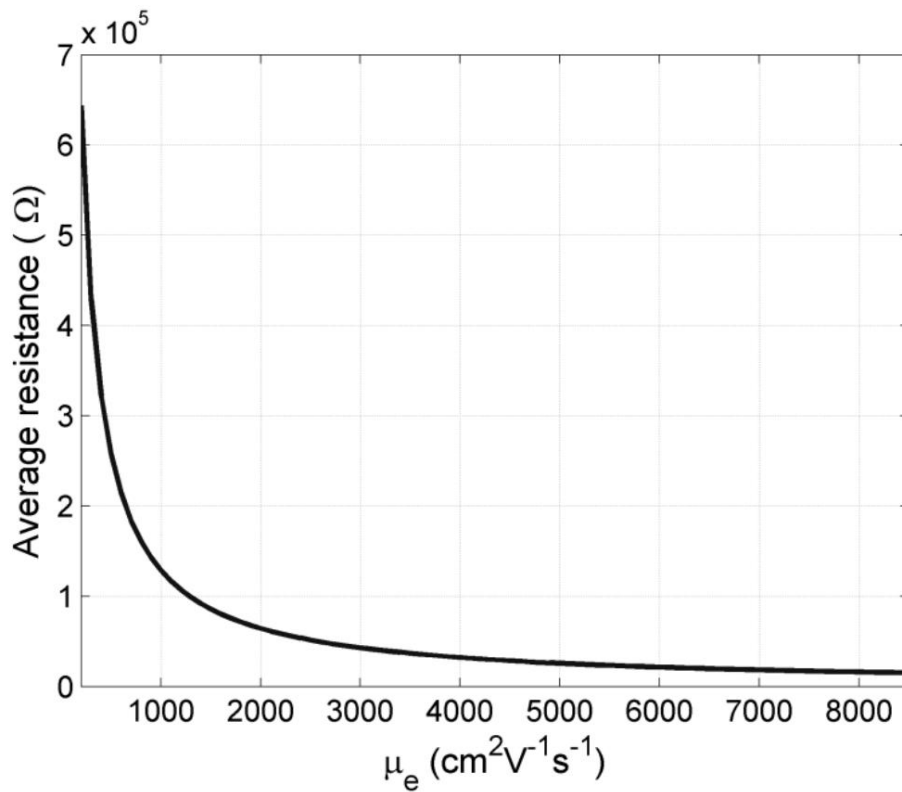
Figure 2.9: Source resistance versus the carrier mobility of photoconductive material
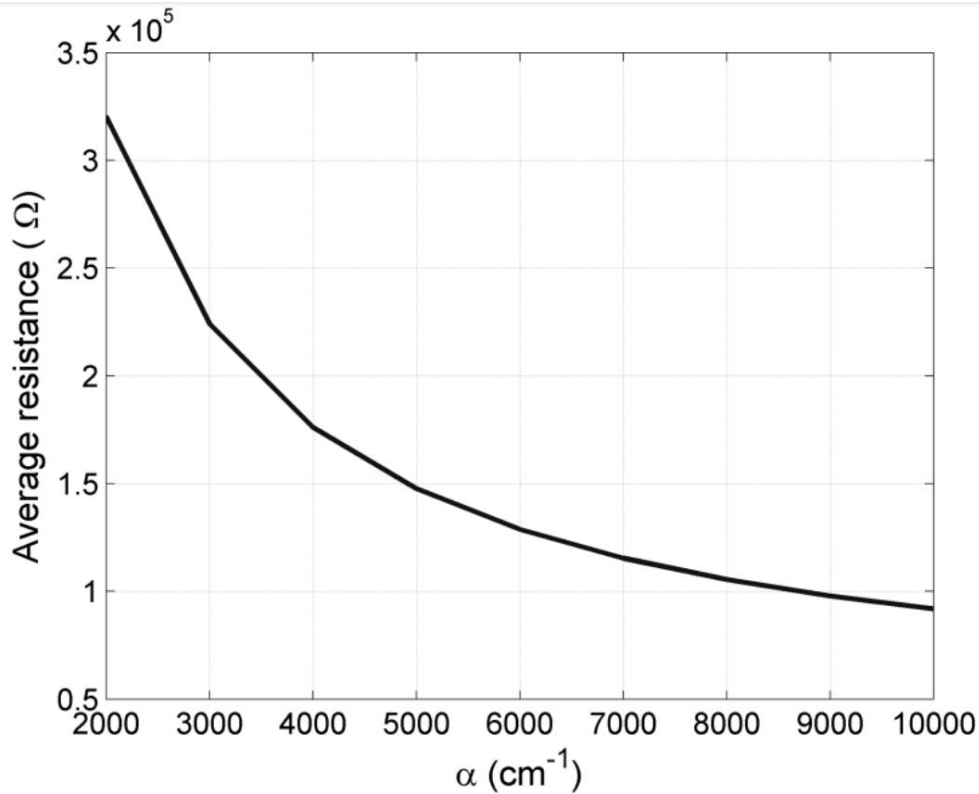
Figure 2.10: Source resistance versus the optical absorption coefficient

2.4 Summary

In this chapter, an overview of THz antennas was provided. The necessity of having THz antenna have been emphasised. Then, it has been addressed that new methods in THz antenna analysis and simulation are required by comparing the THz antenna with RF/MW antenna in various aspects. The working principle of the photomixer has been elaborated. A new equivalent circuit model use lumped element that derived from complex physical mechanisms is introduced. The new equivalent circuit improved the accuracy of large-signal circuit model by involving the physical behaviour and simplified the complexity of numerical deviation by using lumped element. Then, a equation of time variant source conductance has been derived, hence based upon the equivalent circuit, the equation of generated THz power has been derived. Finally, various parameters considered in the equations have been analysis, the results highlighted the problem of impedance matching for THz photomixer antenna.

Chapter 3. New Simulation Process and Cross Validation Method

3.1 Introduction

As compared in chapter 2, different from the simulation of RF/MW antenna, THz photomixer antenna simulation is divided into two parts, optoelectronic simulation and electromagnetic simulation because of the unique excitation method of photomixer. The optical-to-THz conversion efficiency can be analysed by optoelectronic simulation and both of matching and radiation efficiency can be investigated by electromagnetic simulation. Since then, current research of THz photomixer antenna always required two simulation package, for example, Synopsys

Sentaurus TCAD for optoelectronic simulation [52] and CST Microwave Studio for electromagnetic simulation [103]. However, the Maxwell's wave equation is solved using the finite-difference time-domain (FDTD) methods in Synopsys Sentaurus TCAD, and it is solved using finite integration technique (FIT), finite element method (FEM) and transmission line matrix method (TLM) in CST Microwave Studio. This inconsistency highlights the necessity of the development of new simulation process that enable both optoelectronic and electromagnetic simulation in one simulation solver. Therefore, a new simulation process will be discussed in this chapter. Then, in order to validate the results generated from commercial simulation package, Matlab code using FDTD method is utilized. Finally, a brief introduction of Maxwell's equations and FDTD method used for plasmonic simulation and antenna simulation will be presented in this chapter.

3.2 New Simulation Process

According to equation (2.13), the generated THz power meanly depends on three terms, ($\Omega\, R_{antenna}\, C_{electrode}$), ($\Omega\tau_c$) and I_0^2. Therefore, in order to improve the generated THz power, 3 different conditions are required and summarised as follows.

Firstly, the photoconductive material with small carrier life time should be used. Next, in order to achieve small carrier life time, different fabrication technique [68, 104] and appropriate photomixer electrode design [105, 106] had been proposed . In addition the carrier lifetime is a function of the applied bias voltage [101,107,108], however, high bias voltage result in breakdown of photoconductive material.

Secondly, the capacitance should be small to achieve higher generated THz power. Same as the method used for the reduction of carrier lifetime, appropriate photomixer electrode design can modify the capacitance [106, 109].

Then, higher optical power incident on the photomixer can improve the generated THz power. In order to maximize this value, the optimization of photomixer electrode design is applicable and it will be verified in next chapter. In addition, higher optical illumination power can lead to smaller source resistance of photomixer and consequently, offers better matching efficiency as presented in previous section. However, though the optical illumination power play an important role in THz power generation, not much effort has been put into developing new method of illumination power improvement. Therefore, new methods of improving

the optical intensity that has been illuminate on the photoconductive region is one of the main objectives of this thesis.

Since the generated THz power is can be improved by the enhancing the illuminated optical intensity on the photoconductive substrate, when same photoconductive material and photomixer configuration are used with the same biased voltage, the equation (2.13) can be simplified to:

$$P_{THz} \propto I_0^2 \tag{3.1}$$

As the intensity is proportional to the square of the electric field amplitude, the equation (3.1) can be further expressed as:

$$P_{THz} \propto \left| E_0 \right|^4 \tag{3.2}$$

In this case, the improvement factor of generated THz power can be determined by monitoring the electric field magnitude. Therefore, the complex optoelectronic interaction problem has been transformed into an electromagnetic radiation problem. In consequence, optical-to-THz conversion efficiency, matching efficiency and radiation efficiency can be obtained by a single electromagnetic simulation package, i.e., CST Microwave Studio.

CST Microwave Studio is an electromagnetic simulation software with a number of tools that are designed for the modelling, analysis and optimization of devices over a wide range of different frequencies. CST Microwave Studio is designed for high frequency simulation of the 3D EM elements, in particular for antennas, optical applications, planar and multi layer structures as well as EMC. For both low-and high-frequency simulations, CST MWS provides multiple solvers such as time domain solver, frequency domain solver, eigenmode solver and integral equation solver.

Generally, 5 steps is required to complete a design, model construction, source implementation, configuration meshing, defining numerical solution and result presentation. For both photomixer and antenna simulation, the geometrical model can be constructed by the built-in 3D CAD tool. However, the source implementation for them are different. Laser beams are required in the simulation of photomixer design, and it can be defined as a linearly polarized plane wave with 1V/m electric field vector and normal incident angle towards the photomixer. On the other hand, the source implementation of antenna depends on the feed, and various options like discrete port and waveguide are available. Then, the model is discretized. In terms of

numerical solution, both of the two designs will used time domain solver which utilizing finite integration technique. Finally, only electric field is interested and monitored in photomixer simulation, and gain, input impedance as well as field distribution are studied in the antenna simulation.

3.2 Maxwell's Equations

Maxwell's equations summarizes the electromagnetic behaviour in all media based on minor modification of Gauss's law, Gauss's law for magnetism, Faraday's law and Ampere's law. In this section, it is assumed that the transmission medium of the electromagnetic wave is isotropic,homogeneous and non frequency dispersive.

The differential equation of the Maxwell's equation are given by following:

$$\nabla \times E = -\frac{\partial B}{\partial t} - M \tag{3.3}$$

$$\nabla \times H = \frac{\partial D}{\partial t} + J \tag{3.4}$$

$$\nabla \bullet D = \rho \tag{3.5}$$

$$\nabla \bullet B = 0 \tag{3.6}$$

where, E is the electric field, H is the magnetic field, D is the electric flux density, B is the magnetic flux density, M is the mathematical constructed fictitious magnetic current density, J is the conduction electric current density. M and J represent the source of the electromagnetic field.

The relationship between the field and flux density can be used to describe the properties of propagation medium:

$$D = \varepsilon_0 \varepsilon_r E \tag{3.7}$$

$$B = \mu_0 \mu_r H \tag{3.8}$$

where ε_0 and μ_0 are the free space electric permittivity and free space magnetic permeability with value of, $\varepsilon_0=8.854 \times 10^{-12} \text{F.m}^{-1}$ and $\mu_0=4\pi \times 10^{-7} \text{H.m}^{-1}$, respectively. ε_r and μ_r are relavtive electric permittivity and relative magnetic permeability. In addition, by using above two equations, the phase velocity v_p becomes:

$$\mathbf{v}_p = \frac{1}{\sqrt{\mu_0\mu_r\varepsilon_0\varepsilon_r}} = \frac{c}{n} \tag{3.9}$$

where n is the refractive index of the transmitting medium, and c is the speed of electromagnetic wave which is approximately $3\times10^8 \mathrm{ms}^{-1}$.

When Ohm's law is considered, the conduction electric current density becomes:

$$J = \sigma E \tag{3.10}$$

where the conductivity σ is introduced to measure the ability of accommodate electric current in the medium. Since there is no perfect electric conductors or perfect dielectrics in nature, the relative permittivity can be derived as:

$$\begin{aligned}
\nabla \times H &= \frac{\partial \mathrm{D}}{\partial \mathrm{t}} + J = \frac{\partial \varepsilon_r \varepsilon_0 E}{\partial \mathrm{t}} + \sigma E = (\varepsilon_r \varepsilon_0 \frac{\partial}{\partial \mathrm{t}} + \sigma)E \\
&= (j\omega \varepsilon_r \varepsilon_0 + \sigma)E = j\omega \varepsilon_0 (\varepsilon_r + \frac{\sigma}{j\omega \varepsilon_0})E = j\omega \varepsilon_0 \varepsilon_r' E \\
&= \frac{\partial \varepsilon_0 \varepsilon_r' E}{\partial t} = \frac{\partial \mathrm{D}}{\partial t}
\end{aligned} \tag{3.11}$$

where the partial time derivative was used in phasor form, $\partial/\partial t = j\omega$. Therefore, the new relative permittivity is given by

$$\varepsilon_r' = \varepsilon_r + \frac{\sigma}{j\omega \varepsilon_0} = \varepsilon_r - j\frac{\sigma}{\omega \varepsilon_0} \tag{3.12}$$

And loss tangent of the conductive material is equal to:

$$\tan \delta = \frac{\sigma}{\omega \varepsilon_0 \varepsilon_r} \tag{3.13}$$

3.2 Finite Difference Time Domain Method

Finite difference time domain method (FDTD), the first numerical time-domain method that describes the Maxwell's curl equations, is proposed by Yee in 1966 [110]. By using Taylor series, the partial derivatives in Maxwell's equations are replaced by finite difference approximations. Hence, Equations (3.3)-(3.8) can be considered as a hyperbolic partial differential equations. In this case, the electromagnetic propagation can be calculated straightforwardly by numerical substitution. And Yee space lattice

shown in Figure 3.1 is used to discretize the space and time dimensions, therefore, space and time dimension properties are saved in the discrete point.
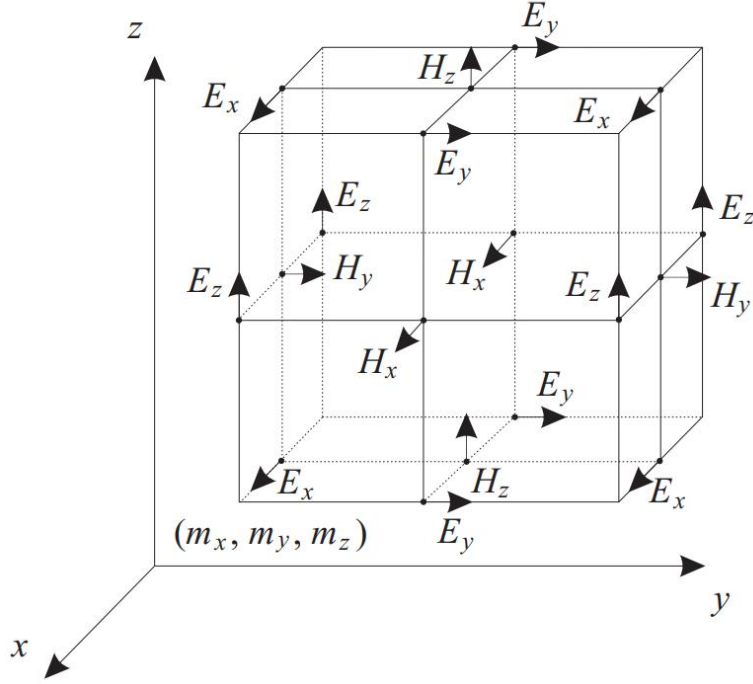
Figure 3.1: Yee Space lattice with the position of electric and magnetic field vector components [110]

In the following mathematical analysis of FDTD, it is assumed that the space is source free and lossless, which means M and J and ρ in equations (3.3) to (3.6) are set to zero. Then, by substituting all the vector with their orthogonal components and substituting curl vector operator with 3 dimensional cross product, equations (3.3) and (3.4) are given by the following:

$$\nabla \times E = (\frac{\partial E_z}{\partial y} - \frac{\partial E_y}{\partial z})\vec{e}_x + (\frac{\partial E_x}{\partial z} - \frac{\partial E_z}{\partial x})\vec{e}_y + (\frac{\partial E_y}{\partial x} - \frac{\partial E_x}{\partial y})\vec{e}_z$$

$$= -\frac{\partial \vec{B}}{\partial t} = -\mu(\frac{\partial B_x}{\partial t}\vec{e}_x + \frac{\partial B_y}{\partial t}\vec{e}_y + \frac{\partial B_z}{\partial t}\vec{e}_z) \quad (3.14)$$

$$\nabla \times H = (\frac{\partial H_z}{\partial y} - \frac{\partial H_y}{\partial z})\vec{e}_x + (\frac{\partial H_x}{\partial z} - \frac{\partial H_z}{\partial x})\vec{e}_y + (\frac{\partial H_y}{\partial x} - \frac{\partial H_x}{\partial y})\vec{e}_z$$

$$= \frac{\partial \vec{D}}{\partial t} = \varepsilon(\frac{\partial D_x}{\partial t}\vec{e}_x + \frac{\partial D_y}{\partial t}\vec{e}_y + \frac{\partial D_z}{\partial t}\vec{e}_z) \quad (3.15)$$

Then, the scalar form of equation (3.14) can be expressed as:

$$\frac{\partial E_z}{\partial y} - \frac{\partial E_y}{\partial z} = -\frac{\partial B_x}{\partial t} \tag{3.16}$$

$$\frac{\partial E_x}{\partial z} - \frac{\partial E_z}{\partial x} = -\frac{\partial B_y}{\partial t} \tag{3.17}$$

$$\frac{\partial E_y}{\partial x} - \frac{\partial E_x}{\partial y} = -\frac{\partial B_z}{\partial t} \tag{3.18}$$

In the same manner, equation (3.15) can be written as:

$$\frac{\partial H_z}{\partial y} - \frac{\partial H_y}{\partial z} = -\frac{\partial D_x}{\partial t} \tag{3.19}$$

$$\frac{\partial H_x}{\partial z} - \frac{\partial H_z}{\partial x} = -\frac{\partial D_y}{\partial t} \tag{3.20}$$

$$\frac{\partial H_y}{\partial x} - \frac{\partial H_x}{\partial y} = -\frac{\partial D_z}{\partial t} \tag{3.21}$$

Next, equations (3.16) to (3.21) are discretized in time and space by the finite difference method [110]:

$$
\begin{aligned}
B_x^{n+1}(i, j, k) = & B_x^n(i, j, k) \\
& + \frac{\Delta t}{\Delta z}[E_y^n(i, j, k) - E_y^n(i, j, k-1)] \\
& - \frac{\Delta t}{\Delta y}[E_z^n(i, j, k) - E_z^n(i, j-1, k)]
\end{aligned} \tag{3.22}
$$

$$
\begin{aligned}
B_y^{n+1}(i, j, k) = & B_y^n(i, j, k) \\
& + \frac{\Delta t}{\Delta x}[E_z^n(i, j, k) - E_z^n(i-1, j, k)] \\
& - \frac{\Delta t}{\Delta z}[E_x^n(i, j, k) - E_x^n(i, j, k-1)]
\end{aligned} \tag{3.23}
$$

$$B_z^{n+1}(i, j, k) = B_z^n(i, j, k)$$

$$+\frac{\Delta t}{\Delta y}[E_x^n(i, j, k) - E_x^n(i, j-1, k)]$$

$$-\frac{\Delta t}{\Delta x}[E_y^n(i, j, k) - E_y^n(i-1, j, k)]$$

(3.24)

$$D_x^{n+1}(i, j, k) = D_x^n(i, j, k)$$

$$+\frac{\Delta t}{\Delta y}[H_z^n(i, j+1, k) - H_z^n(i, j, k)]$$

$$-\frac{\Delta t}{\Delta z}[H_y^n(i, j, k+1) - H_y^n(i, j, k)]$$

(3.25)

$$D_y^{n+1}(i, j, k) = D_y^n(i, j, k)$$

$$+\frac{\Delta t}{\Delta z}[H_x^n(i, j, k+1) - H_x^n(i, j, k)]$$

$$-\frac{\Delta t}{\Delta x}[H_z^n(i+1, j, k) - H_z^n(i, j, k)]$$

(3.26)

$$D_z^{n+1}(i, j, k) = D_z^n(i, j, k)$$

$$+\frac{\Delta t}{\Delta x}[H_y^n(i+1, j, k) - H_y^n(i, j, k)]$$

$$-\frac{\Delta t}{\Delta y}[H_x^n(i, j+1, k) - H_x^n(i, j, k)]$$

(3.27)

The equation (3.22) to (3.27) provide a recursive procedure with respect to time and space for the computation of electronic and magnetic field values in free space with conventional dielectric or magnetic materials. Then, by using equations (3.7) and (3.8), equations (3.22) to (3.27) can be written as:

$$H_x^{n+1}(i, j, k) = H_x^n(i, j, k)$$

$$+ \frac{\Delta t}{\mu_0 \mu(i, j, k) \Delta z} [E_y^n(i, j, k) - E_y^n(i, j, k-1)] \tag{3.28}$$

$$- \frac{\Delta t}{\mu_0 \mu(i, j, k) \Delta y} [E_z^n(i, j, k) - E_z^n(i, j-1, k)]$$

$$H_y^{n+1}(i, j, k) = H_y^n(i, j, k)$$

$$+ \frac{\Delta t}{\mu_0 \mu(i, j, k) \Delta x} [E_z^n(i, j, k) - E_z^n(i-1, j, k)] \tag{3.29}$$

$$- \frac{\Delta t}{\mu_0 \mu(i, j, k) \Delta z} [E_x^n(i, j, k) - E_x^n(i, j, k-1)]$$

$$H_z^{n+1}(i, j, k) = H_z^n(i, j, k)$$

$$+ \frac{\Delta t}{\mu_0 \mu(i, j, k) \Delta y} [E_x^n(i, j, k) - E_x^n(i-1, j, k)] \tag{3.30}$$

$$- \frac{\Delta t}{\mu_0 \mu(i, j, k) \Delta x} [E_y^n(i, j, k) - E_y^n(i-1, j, k)]$$

$$E_x^{n+1}(i, j, k) = E_x^n(i, j, k)$$

$$+ \frac{\Delta t}{\varepsilon_0 \varepsilon(i, j, k) \Delta y} [H_z^n(i, j+1, k) - H_z^n(i, j, k)] \tag{3.31}$$

$$- \frac{\Delta t}{\varepsilon_0 \varepsilon(i, j, k) \Delta z} [H_y^n(i, j, k+1) - H_y^n(i, j, k)]$$

$$E_y^{n+1}(i, j, k) = E_y^n(i, j, k)$$

$$+ \frac{\Delta t}{\varepsilon_0 \varepsilon(i, j, k) \Delta z} [H_x^n(i, j, k+1) - H_x^n(i, j, k)] \tag{3.32}$$

$$- \frac{\Delta t}{\varepsilon_0 \varepsilon(i, j, k) \Delta x} [H_z^n(i+1, j, k) - H_z^n(i, j, k)]$$

$$E_z^{n+1}(i, j, k) = E_z^n(i, j, k)$$

$$+ \frac{\Delta t}{\varepsilon_0 \varepsilon(i, j, k) \Delta x} [H_y^n(i+1, j, k) - H_y^n(i, j, k)]$$

$$- \frac{\Delta t}{\varepsilon_0 \varepsilon(i, j, k) \Delta y} [H_x^n(i, j+1, k) - H_x^n(i, j, k)]$$

(3.33)

Indices i, j, k are derived by the spatial discretisation in following equations:

$$i = \frac{x}{\Delta x} \Rightarrow x = i\Delta x$$

(3.34)

$$j = \frac{y}{\Delta y} \Rightarrow y = j\Delta y$$

(3.35)

$$k = \frac{z}{\Delta z} \Rightarrow z = k\Delta z$$

(3.36)

In the same manner, index n is calculated by time discretisation as given by:

$$n = \frac{t}{\Delta t} \Rightarrow t = n\Delta t$$

(3.37)

Generally, the computation of FDTD algorithm can be divided into three steps. Firstly, all the field and variables are initialised where variables are usually set to zero. Then, by using equations (3.28) to (3.30), values of electric field are computed from the values of magnetic field that is calculated from the value of magnetic field at previous time step, and identical algorithm is computed for magnetic field by using equations (3.31) to (3.33) as well. Finally, the boundary condition should be checked to decide whether the computation should be terminated or not.

As the design include the interaction between the incident laser beam and the plasmonic material which can be modelled as dispersive material, it is necessary to involve dispersive material modelling in FDTD algorithm. In order to achieve so, auxiliary differential equation (ADE) method is used [111]. Moreover, since the FDTD is time domain, it is important to convert the relationship between the property of material and frequency to time domain by using Lorentz dispersive model.

Initially, relative permittivity and permeability in equations (3.7) and (3.8) can be expressed by Lorentz dispersive model [112]:

$$\varepsilon_{\mathrm{r}} = \mu_{\mathrm{r}} = 1 - \frac{\omega_p^2}{\omega^2 - j\omega\gamma - \omega_0^2} \tag{3.38}$$

Where ω_0 and ω_p are plasma and resonant frequencies, respectively, and γ is the collision frequency. Plasma frequency is the frequency where the electrons fluid of the material oscillate longitudinally. Then, the relative permittivity and permeability in equations (3.7) and (3.8) are substituted by Lorentz dispersive model, and they are given by:

$$(\omega^2 - j\omega\gamma_e - \omega_{0e}^2)D_{x,y,z} = \varepsilon_0[\omega^2 - j\omega\gamma_e - (\omega_{0e}^2 + \omega_{pe}^2)]E_{x,y,z} \tag{3.39}$$

$$(\omega^2 - j\omega\gamma_m - \omega_{0m}^2)B_{x,y,z} = \mu_0[\omega^2 - j\omega\gamma_m - (\omega_{0m}^2 + \omega_{pm}^2)]H_{x,y,z} \tag{3.40}$$

Where the subscripts e and m represents the electric and magnetic component of the variables, respectively. After that, inverse Fourier transform is applied to equations (3.39) and (3.40) to transform them from frequency domain to time domain which is implemented by FDTD method. The following transformations are used in incerse Fourier transform:

$$j\omega \rightarrow \frac{\partial}{\partial t}, \omega^2 \rightarrow -\frac{\partial^2}{\partial t^2} \tag{3.41}$$

As a result, equations (3.39) and (3.40) can be rewritten in the time domain as:

$$\left(\frac{\partial^2}{\partial t^2} + \frac{\partial}{\partial t}\gamma_e + \omega_{0e}^2\right)D_{x,y,z} = \varepsilon_0\left[\frac{\partial^2}{\partial t^2} + \frac{\partial}{\partial t}\gamma_e + (\omega_{0e}^2 + \omega_{pe}^2)\right]E_{x,y,z} \tag{3.41}$$

$$\left(\frac{\partial^2}{\partial t^2} + \frac{\partial}{\partial t}\gamma_m + \omega_{0m}^2\right)B_{x,y,z} = \mu_0\left[\frac{\partial^2}{\partial t^2} + \frac{\partial}{\partial t}\gamma_m + (\omega_{0m}^2 + \omega_{pm}^2)\right]H_{x,y,z} \tag{3.42}$$

Equations (3.41) and (3.42) are performed with a second-order discretisation with the time domain central finite difference operator and central average operators:

$$\frac{\partial^2}{\partial t^2} \rightarrow \frac{\delta_t^2}{\Delta t^2}, \frac{\partial}{\partial t} \rightarrow \frac{\delta_t}{\Delta t}\mu_t, \omega_0^2 \rightarrow \omega_0^2\mu_t^2, (\omega_0^2 + \omega_p^2) \rightarrow (\omega_0^2 + \omega_p^2)\mu_t^2 \tag{3.43}$$

The central finite difference operator δ_t, δ_t^2 and the central average operators μ_t, μ_t^2 are given by [113]:

$$\delta_t F^n(i, j, k) \equiv F^{n+\frac{1}{2}}(i, j, k) - F^{n-\frac{1}{2}}(i, j, k),$$

$$\delta_t^2 F^n(i, j, k) \equiv F^{n+1}(i, j, k) - 2F^n(i, j, k) + F^{n-1}(i, j, k),$$

$$\mu_t F^n(i, j, k) \equiv \frac{F^{n+\frac{1}{2}}(i, j, k) + F^{n-\frac{1}{2}}(i, j, k)}{2},$$ (3.44)

$$\mu_t^2 F^n(i, j, k) \equiv \frac{F^{n+1}(i, j, k) + 2F^n(i, j, k) + F^{n-1}(i, j, k)}{4}$$

where F is the arbitary field components and (i, j, k) are given by equations (3.34) to (3.36).

Therefore, equations (3.41) and (3.42) can be discretised as:

$$(\frac{\delta_t^2}{\Delta t^2} + \frac{\delta_t}{\Delta t} \mu_t \gamma_e + \omega_{0e}^2 \mu_t^2) D_{x,y,z}$$

$$= \varepsilon_0 [\frac{\delta_t^2}{\Delta t^2} + \frac{\delta_t}{\Delta t} \mu_t \gamma_e + (\omega_{0e}^2 + \omega_{pe}^2) \mu_t^2] E_{x,y,z}$$ (3.45)

$$(\frac{\delta_t^2}{\Delta t^2} + \frac{\delta_t}{\Delta t} \mu_t \gamma_m + \omega_{0m}^2 \mu_t^2) B_{x,y,z}$$

$$= \mu_0 [\frac{\delta_t^2}{\Delta t^2} + \frac{\delta_t}{\Delta t} \mu_t \gamma_m + (\omega_{0m}^2 + \omega_{pm}^2) \mu_t^2] H_{x,y,z}$$ (3.46)

As the operators been applied to equations (3.45) and (3.46), they can now be rewritten in the form:

$$\frac{D_{x,y,z}^{n+1}(i, j, k) - 2D_{x,y,z}^n(i, j, k) + D_{x,y,z}^{n-1}(i, j, k)}{\Delta t^2}$$

$$+ \gamma_e \frac{D_{x,y,z}^{n+1}(i, j, k) - D_{x,y,z}^{n-1}(i, j, k)}{2\Delta t}$$

$$+ \omega_{0e}^2 \frac{D_{x,y,z}^{n+1}(i, j, k) + 2D_{x,y,z}^n(i, j, k) + D_{x,y,z}^{n-1}(i, j, k)}{4}$$

$$= \varepsilon_0 [\frac{E_{x,y,z}^{n+1}(i, j, k) - 2E_{x,y,z}^n(i, j, k) + E_{x,y,z}^{n-1}(i, j, k)}{\Delta t^2}$$ (3.47)

$$+ \gamma_e \frac{E_{x,y,z}^{n+1}(i, j, k) - E_{x,y,z}^{n-1}(i, j, k)}{2\Delta t}$$

$$+ (\omega_{0e}^2 + \omega_{pe}^2) \frac{E_{x,y,z}^{n+1}(i, j, k) + 2E_{x,y,z}^n(i, j, k) + E_{x,y,z}^{n-1}(i, j, k)}{4}]$$

$$\frac{B_{x,y,z}^{n+1}(i,j,k) - 2B_{x,y,z}^{n}(i,j,k) + B_{x,y,z}^{n-1}(i,j,k)}{\Delta t^2}$$

$$+ \gamma_m \frac{B_{x,y,z}^{n+1}(i,j,k) - B_{x,y,z}^{n-1}(i,j,k)}{2\Delta t}$$

$$+ \omega_{0m}^2 \frac{B_{x,y,z}^{n+1}(i,j,k) + 2B_{x,y,z}^{n}(i,j,k) + B_{x,y,z}^{n-1}(i,j,k)}{4} \qquad (3.48)$$

$$= \mu_0 [\frac{H_{x,y,z}^{n+1}(i,j,k) - 2H_{x,y,z}^{n}(i,j,k) + H_{x,y,z}^{n-1}(i,j,k)}{\Delta t^2}$$

$$+ \gamma_m \frac{H_{x,y,z}^{n+1}(i,j,k) - H_{x,y,z}^{n-1}(i,j,k)}{2\Delta t}$$

$$+ (\omega_{0m}^2 + \omega_{pm}^2) \frac{H_{x,y,z}^{n+1}(i,j,k) + 2H_{x,y,z}^{n}(i,j,k) + H_{x,y,z}^{n-1}(i,j,k)}{4}]$$

Finally, the FDTD equations that derived from electric field component and from magnetic field component are the following

$$E_{x,y,z}^{n+1}(i,j,k) = \{[\frac{1}{\varepsilon_0 \Delta t^2} + \frac{\gamma_e}{2\varepsilon_0 \Delta t} + \frac{\omega_{0e}^2}{4\varepsilon_0}]D_{x,y,z}^{n+1}(i,j,k)$$

$$- (\frac{2}{\varepsilon_0 \Delta t^2} - \frac{\omega_{0e}^2}{2\varepsilon_0})D_{x,y,z}^{n}(i,j,k)$$

$$+ [\frac{1}{\varepsilon_0 \Delta t^2} - \frac{\gamma_e}{2\varepsilon_0 \Delta t} + \frac{\omega_{0e}^2}{4\varepsilon_0}]D_{x,y,z}^{n-1}(i,j,k) \qquad (3.49)$$

$$+ [\frac{2}{\Delta t^2} - \frac{\omega_{0e}^2 + \omega_{pe}^2}{2}]E_{x,y,z}^{n}(i,j,k)$$

$$- [\frac{1}{\Delta t^2} - \frac{\gamma_e}{2\Delta t} + \frac{\omega_{0e}^2 + \omega_{pe}^2}{4}]E_{x,y,z}^{n-1}(i,j,k)\}$$

$$\Big/ [\frac{1}{\Delta t^2} + \frac{\gamma_e}{2\Delta t} + \frac{\omega_{0e}^2 + \omega_{pe}^2}{4}]$$

$$H^{n+1}_{x,y,z}(i, j, k) = \{[\frac{1}{\mu_0 \Delta t^2} + \frac{\gamma_m}{2\varepsilon_0 \Delta t} + \frac{\omega^2_{0m}}{4\mu_0}]B^{n+1}_{x,y,z}(i, j, k)$$

$$-(\frac{2}{\mu_0 \Delta t^2} - \frac{\omega^2_{0m}}{2\mu_0})B^n_{x,y,z}(i, j, k)$$

$$+[\frac{1}{\mu_0 \Delta t^2} - \frac{\gamma_m}{2\mu_0 \Delta t} + \frac{\omega^2_{0m}}{4\varepsilon_0}]B^{n-1}_{x,y,z}(i, j, k) \quad\quad (3.50)$$

$$+[\frac{2}{\Delta t^2} - \frac{\omega^2_{0m} + \omega^2_{pm}}{2}]H^n_{x,y,z}(i, j, k)$$

$$-[\frac{1}{\Delta t^2} - \frac{\gamma_m}{2\Delta t} + \frac{\omega^2_{0m} + \omega^2_{pm}}{4}]H^{n-1}_{x,y,z}(i, j, k)\}$$

$$\Big/ [\frac{1}{\Delta t^2} + \frac{\gamma_m}{2\Delta t} + \frac{\omega^2_{0m} + \omega^2_{pm}}{4}]$$

The dispersive FDTD algorithm consists of Equations (3.22) to (3.27), (3.49) and (3.50). It should be noted that there is no difference between dispersive FDTD and free space FDTD when plasma. Collision and resonant frequencies are equal to zero.

3.4 Summary

Maxwell's equations provide a mathematical model to predict the propagation of electromagnetic wave. The finite difference time domain method is introduced to discrerise the Maxwell's equations. As a result, the simulation of electromagnetic waves can be studied using a computer algorithm when the environment is too complex to calculate. A classical FDTD method that can model the propagation of electromagnetic waves in free space is introduced. Then, since the dispersive materials, which have frequency dependent properties, becomes popular, the frequency dependent FDTD method achieved by Drude or Lorentz dispersion models is reviewed.

Chapter 4. Improving the Laser-to-THz Conversion Efficiency of Photomixer

4.1 Introduction

With the demand of higher resolutions and higher scanning speed in low cost and portable devices, THz photomixer which also known as Optical Heterodyne Generation [114] becomes one of the attractive source. The properties offered by THz photomixer such as room temperature operation (unlike QCLs) [3], smaller size (unlike BWOs) [15] and tunable frequencies (unlike diodes) [11,12] highlight the necessity of research of it. However, the low optical-to-THz conversion efficiency was addressed as one of the reasons that limits the application of THz photomixers. The optical-to-THz conversion efficiency that have been reported is less than 1‰ for the conventional photomixer [51]. Therefore, according to the parameter reviews and analysis of equivalent circuit model in Chapter 2, various approaches, include

optimizing photomixer electrodes configuration, utilizing reflector, implementing substrate, are proposed in this chapter to improving the optical-to-THz conversion efficiency. Since the generated THz power is proportional to the 4th power of the optical surface electric field when same photoconductive material and photomixer configuration are used with the same biased voltage, by monitoring the optical surface electric field, the enhancement of generated THz power can be investigated. Moreover, since all the designs proposed in this chapter is within the near field of the incident laser beam, the incident laser beams can be approximated as an incident plane wave with the E-field vector of 1V/m in the direction of the tips with a normal incident angle in this chapter [141]. In addition, design of radiating antenna and feeding network are not considered in the design demonstrated in this chapter, since all the proposed design is in optical scales.

4.2 Improving the Optical-to-THz Conversion Efficiency by Optimizing Photomixer electrodes

It has been discussed in Chapter 2 that the material used for photomixer and the configuration of the photomixer electrode affect the output power from THz photomixer.

4.2.1 Improving the Optical-to-THz Conversion Efficiency by Optimizing the Dimensions of Photomixer Electrodes

Figure 4.1 demonstrate 4 different configurations of photomixer electrode, and the dimensions of them are listed in Table 4.1.

(a)
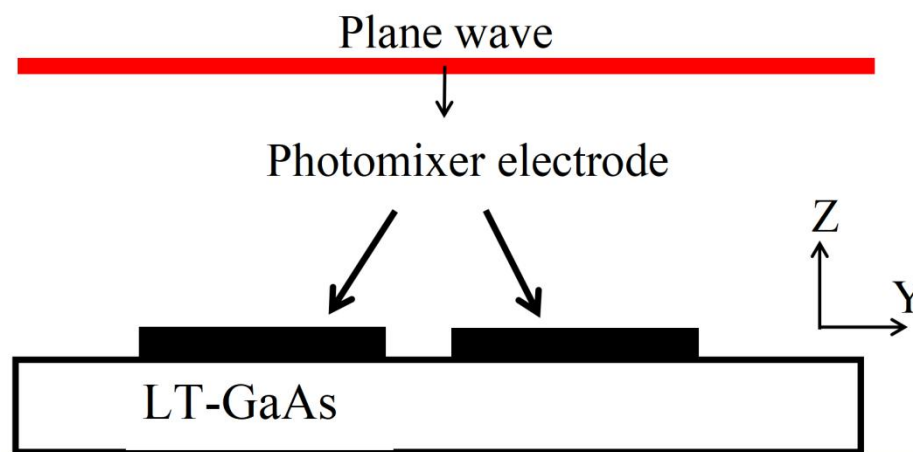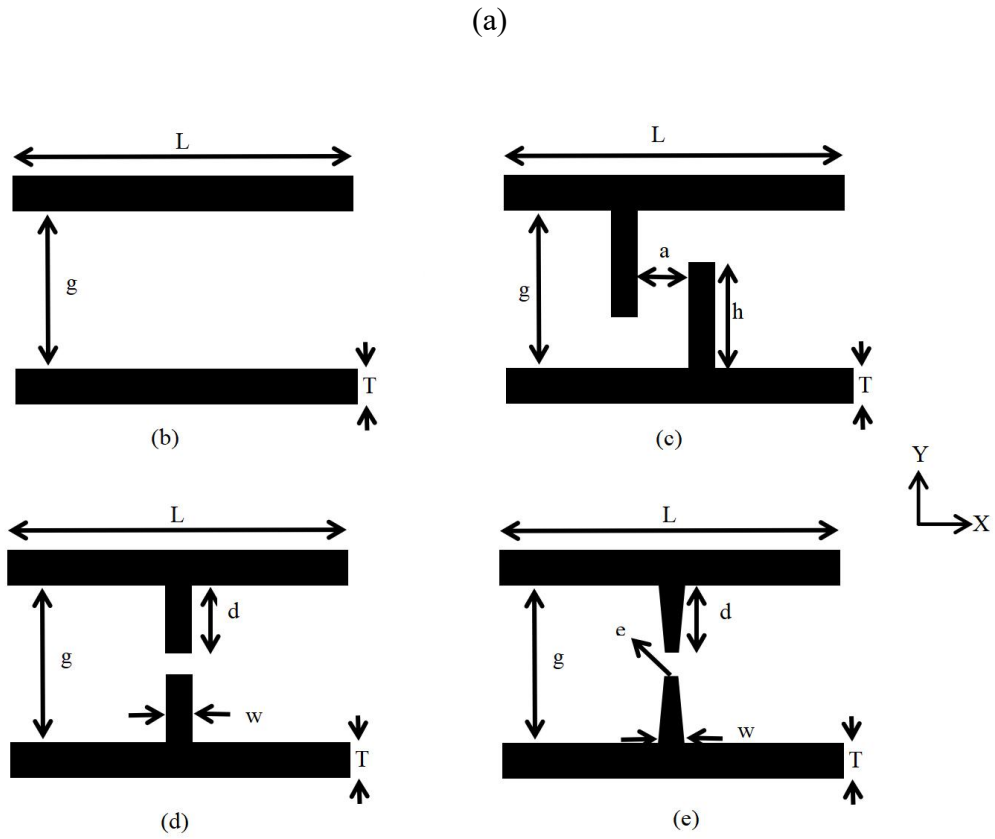
Figure 4.1: (a) Side view of the configuration (b)top view of bare gap photomixer electrode , (c) top view of interdigital photomixer, (d) top view of rectangular tip-to-tip photomixer, (e) top view of trapezoidal tip-to-tip photomixer [115]

Table 4.1: Dimensions of the four photomixers

Parameters	Description	Values
L	Length of photomixer electrodes	4μm
g	Gap between electrodes	2.3μm
T	Width of photomixer electrodes	0.8μm
a	Space between interdigital tips	0.5μm
h	Length of interdigital tips	1.4μm
d	Length of paired tips	1.13μm
w	Bottom width of trapezoidal tips/ Width of rectangular tips	0.2μm
e	Top width of Trapezoidal tips	0.1μm

All of the photomixer electrodes in Figure 4.1 is made of gold with a thickness of 0.1μm and mounted on a LT-GaAs photoconductive substrate with thickness and dielectric constant of 0.44μm and 12.9, respectively. The processing time for each design takes appropriately 5 minutes.

Figures 4.2-4.5 illustrate the E-field distribution for all the four electrode configurations. In order to compare these results quantitatively, the E-field distributions at the central line cross all the tips for all the photomixers are presented in Figure 4.6. It can be observed from these results that X and Z component of the E field can be neglect and the maximum Y component of the E-fields are 1.01V/m, 1.1V/m, 1.25V/m and 1.42V/m for the bare gap, interdigital, rectangular tip-to-tip and trapezoidal tip-to-tip photomixers, respectively. The trapezoidal tip-to-tip photomixer has the largest magnitude and highest concentration of E-field in the gap due to the sharper tip ends, which leads to higher surface charge density. It can be noticed that these results agree with the conclusion made in [116], where a dipole with sharper tip ends offers the best performance.
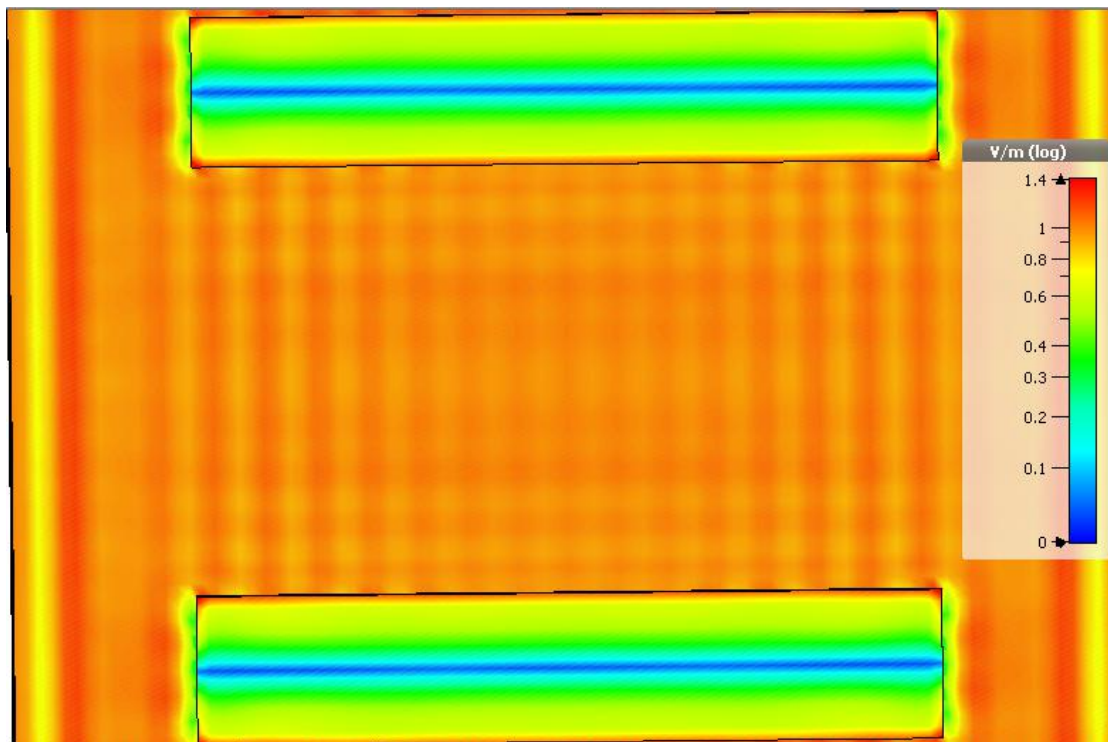
Figure 4.2:E-field distribution on the surface of the bare gap photomixer electrode
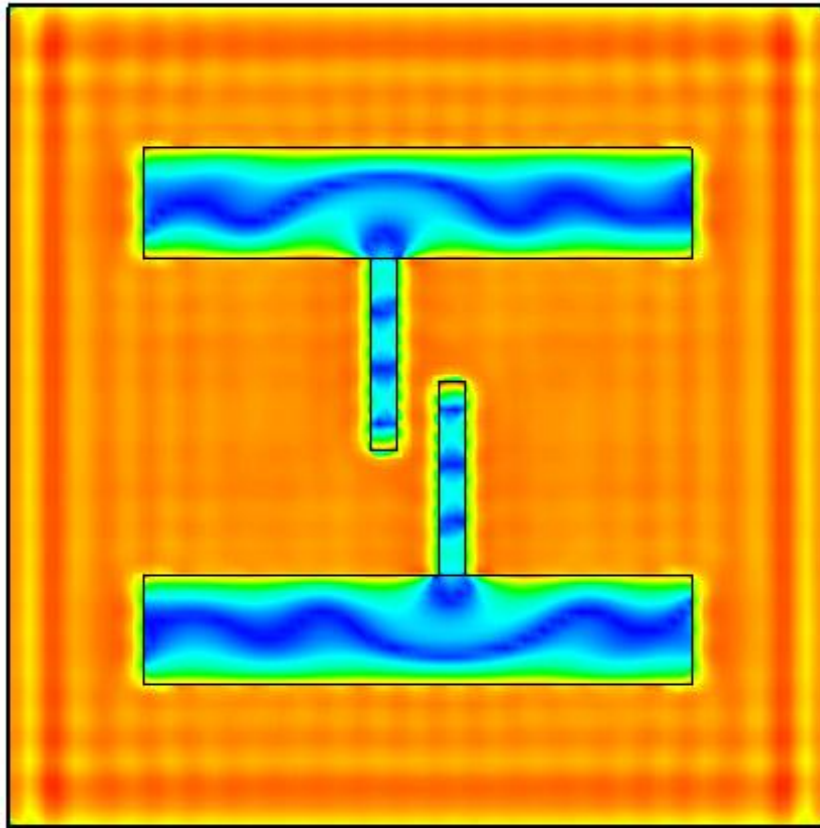
(a)
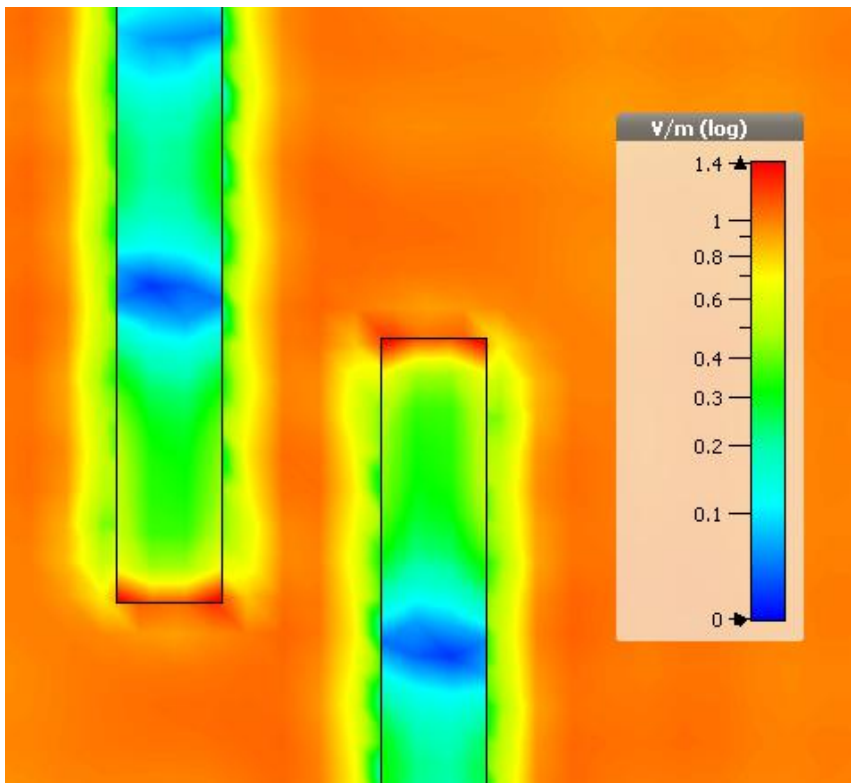
(b)

Figure 4.3:E-field distribution on the surface of the interdigital photomixer (a) full electrodes (b) zoom in view at the tips
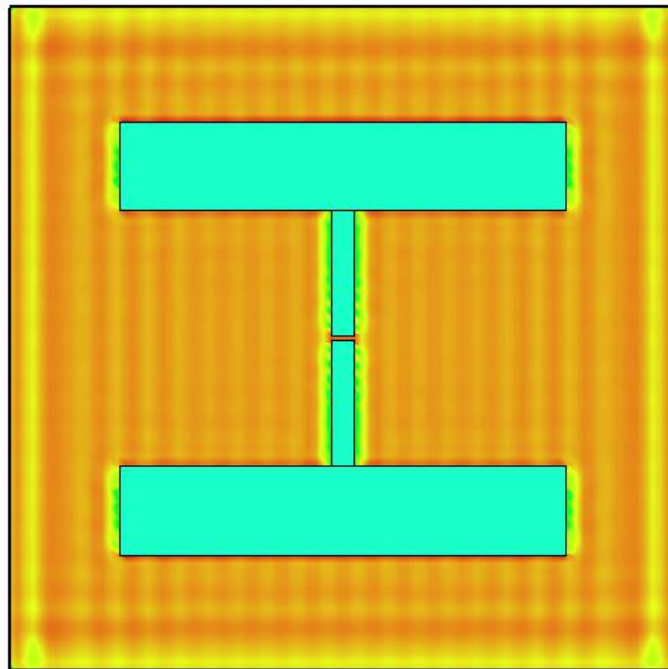
(a)
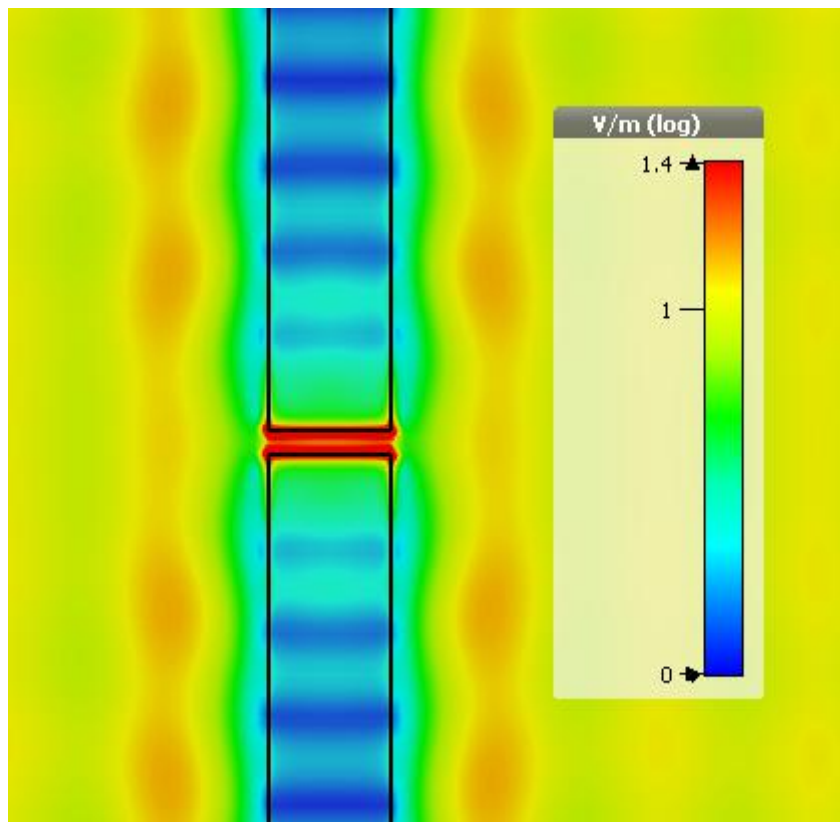
(b)

Figure 4.4:E-field distribution on the surface of the rectangular tip-to-tip photomixer

(a) full electrodes (b) zoom in view at the tips
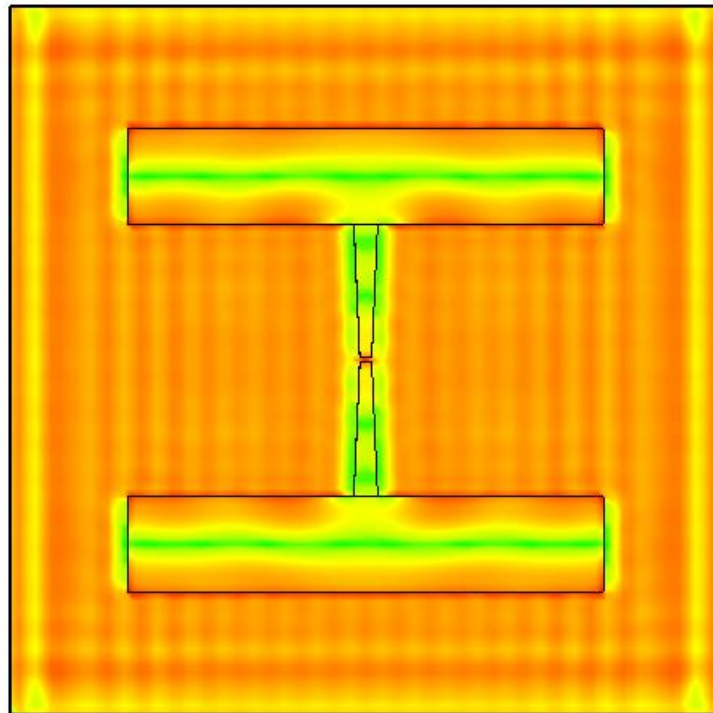
(a)
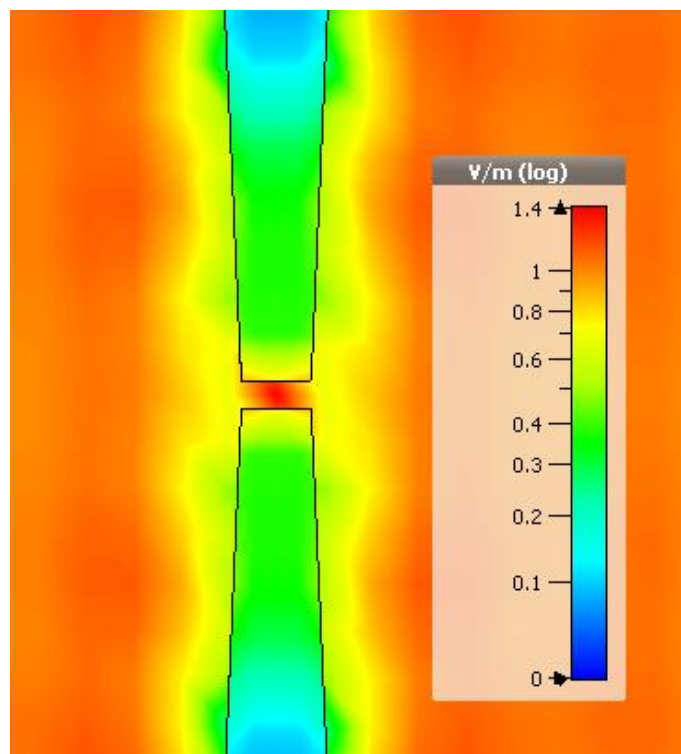
(b)

Figure 4.5:E-field distribution on the surface of the trapezoidal tip-to-tip photomixer

(a) full electrodes (b) zoom in view at the tips
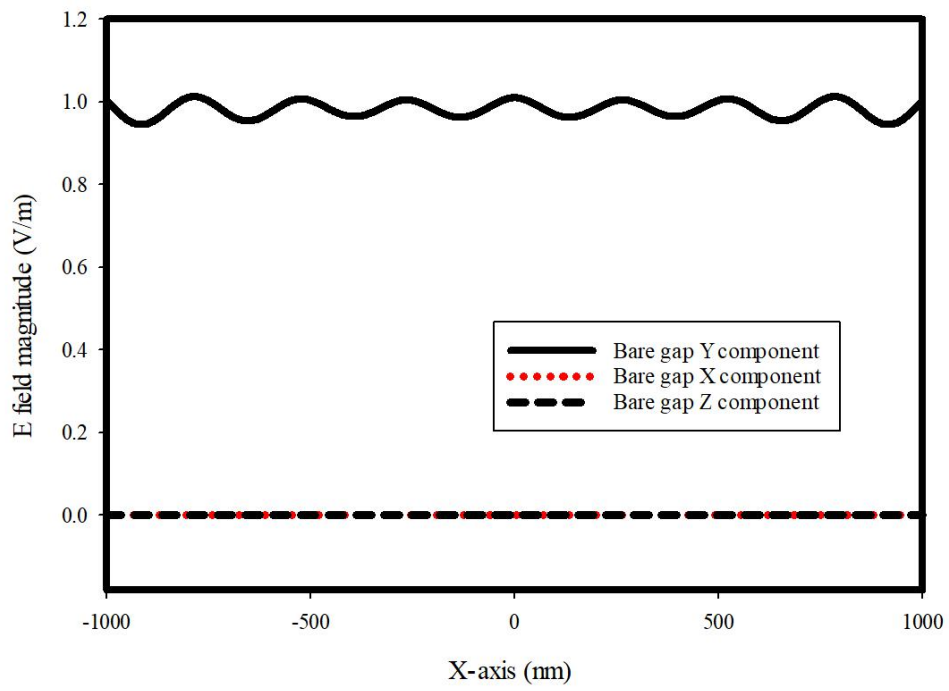
(a)
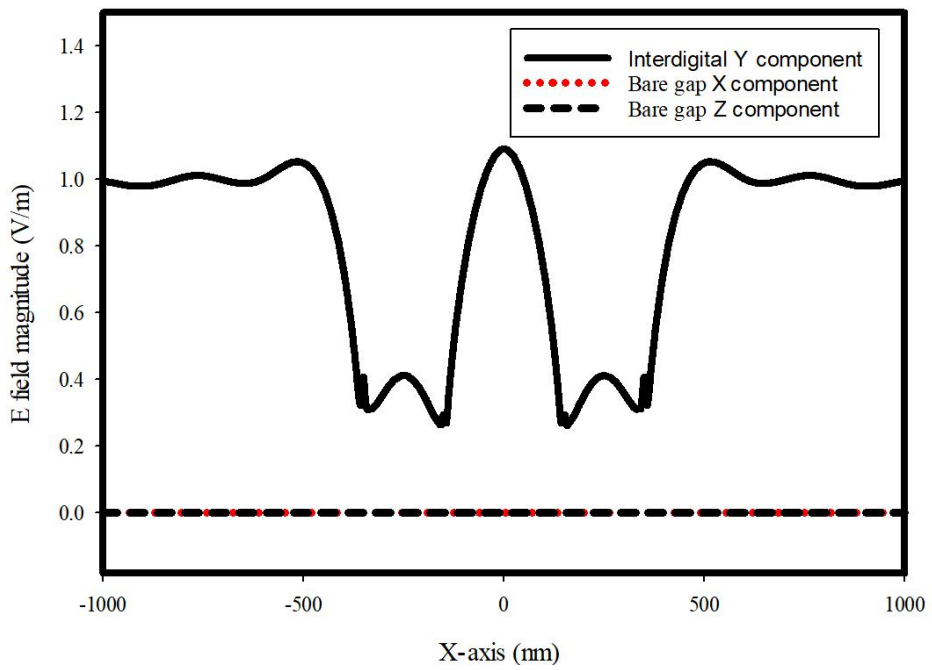
(b)
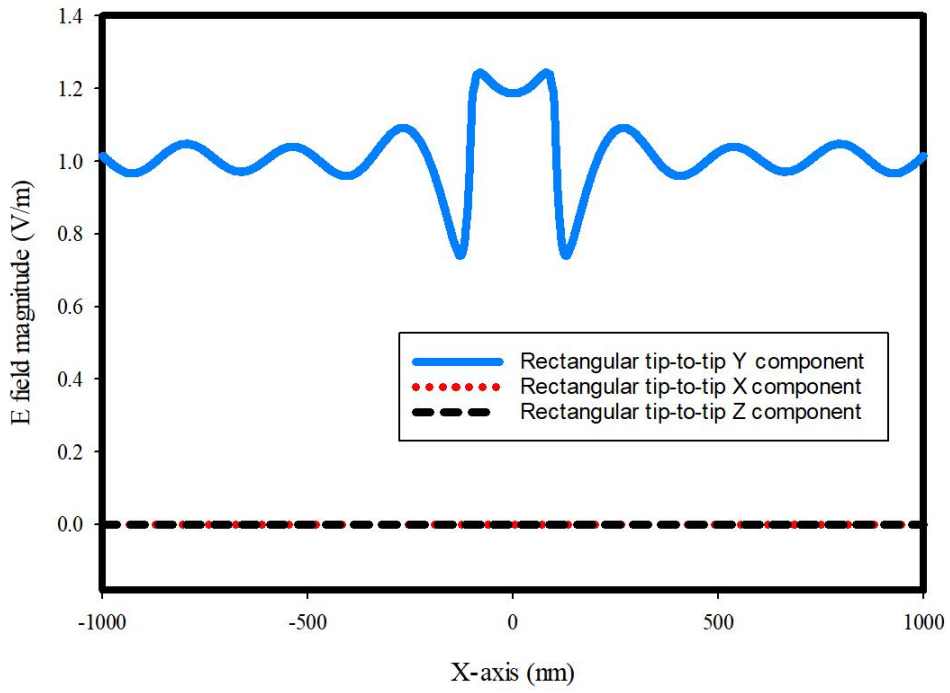
(c)
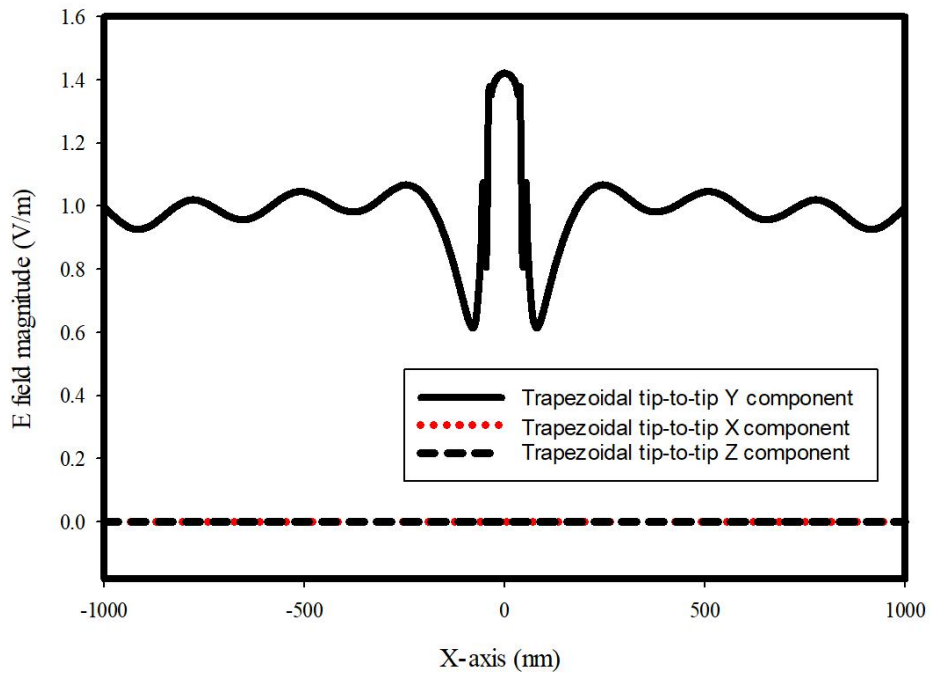
(d)
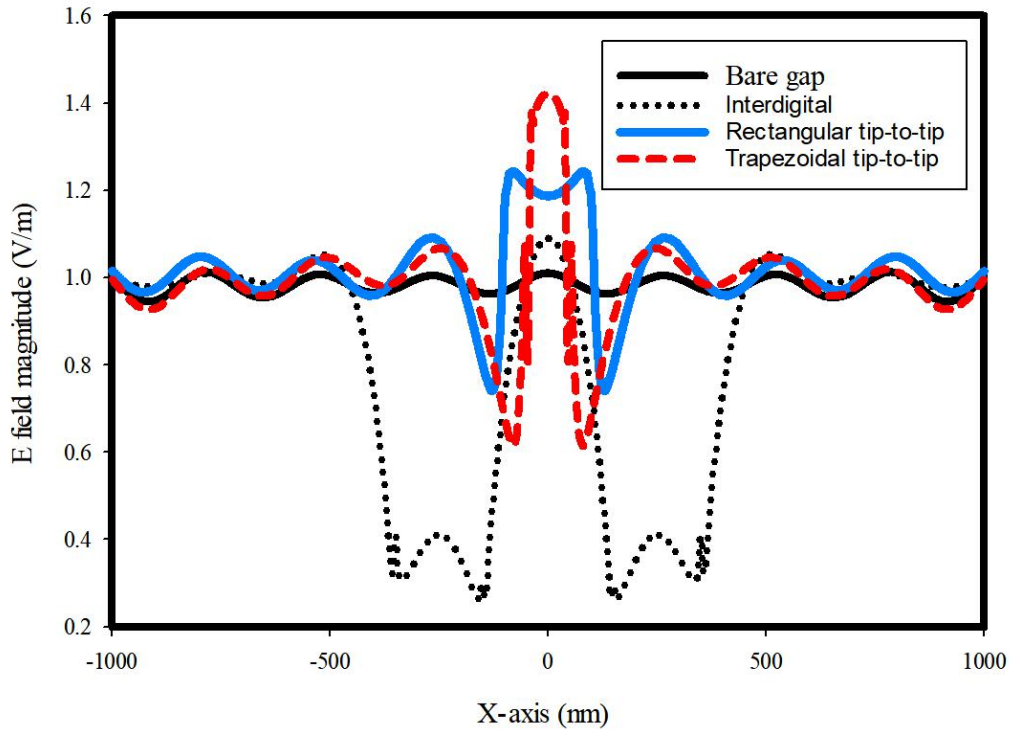
(e)

Figure 4.6: E-field distribution at the central line of each photomixer along the X-axis of the model (a) three dimensional components of bare gap electrode (b) three dimensional components of interdigital electrode (c) three dimensional components of rectangular tip-to-tip electrode (d)   three dimensional components of trapezoidal tip-to-tip electrode (e) comparison of Y component of all electrodes

4.2.2 Photomixer Electrodes using Plasmonic Material

The plasmonic effect represents the interaction between the incident electromagnetic field and free electrons in metal nanoparticles, which depends on several factors such as the shape, size and spacing of the metal structure as well as the permittivity of the surrounding material [117]. The interaction between a metal nanoparticle and the electromagnetic field can generate surface plasmon resonance which will lead to a stronger localised electric field. When the two plasmonic objects are close enough, the interaction between them can squeeze the field and concentrate the localized field [118,119].

Since then, normal gold photomixer electrodes is replaced by plasmonic material , i.e., Palik optical gold [120]. The Palik optical gold is built-in dispersive material in CST microwave studio and it will be modelled using Lorentz dispersive

model in the FDTD. The dimension of trapezoidal tip-to-tip electrodes introduced in section 4.2.1 is used. In this case, the tip width is 100 nm, and the wavelength of incident laser beams lies in the range of 750 nm to 1000 nm, therefore, the width of the tip ends is much smaller than the wavelength of the laser beam, plasmonic effect can be introduced to enhance the electric field distribution in proximity to the photomixer electrodes.

After approximately 8 minutes simulation, the electric field between the electrodes' tip on the surface of LT-GaAs increased to 2.1 V/m as shown in Figure 4.7. Figure 4.8 demonstrates the surface electric field in proximity to the photoconductive active region from two different simulation methods. Both of the results agreed to the positive impact of using plasmonic material as electrodes on the surface electric field in the active region of photomixer. The difference is possibly caused by the discrepancy in the mesh generation. Since the generated THz power is proportional to the 4th power of magnitude of the electric field on the surface of LT-GaAs between electrodes, it can be calculated that the improvement factor of 4.78 have been achieved by using plasmonic photomixer electrodes.
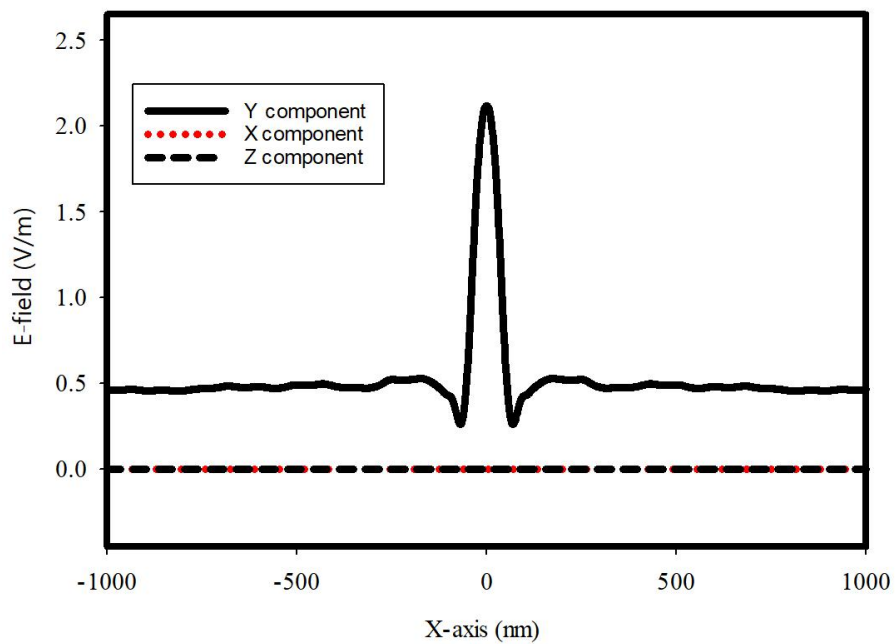
(a)
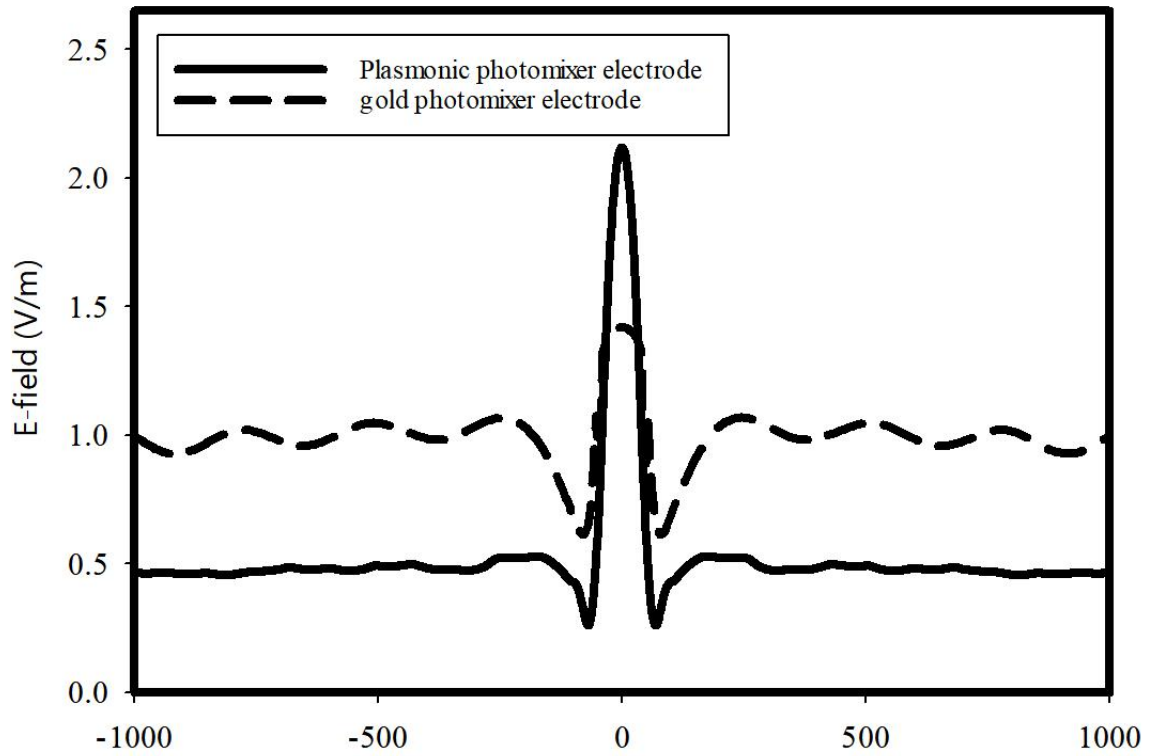
(b)

Figure 4.7: Optical E-field on the surface of LT-GaAs along the central line between electrodes (a) three dimensional component of plasmonic photomixer electrode (b) comparison of Y component between plasmonic photomixer electrodes and gold photomixer electrode
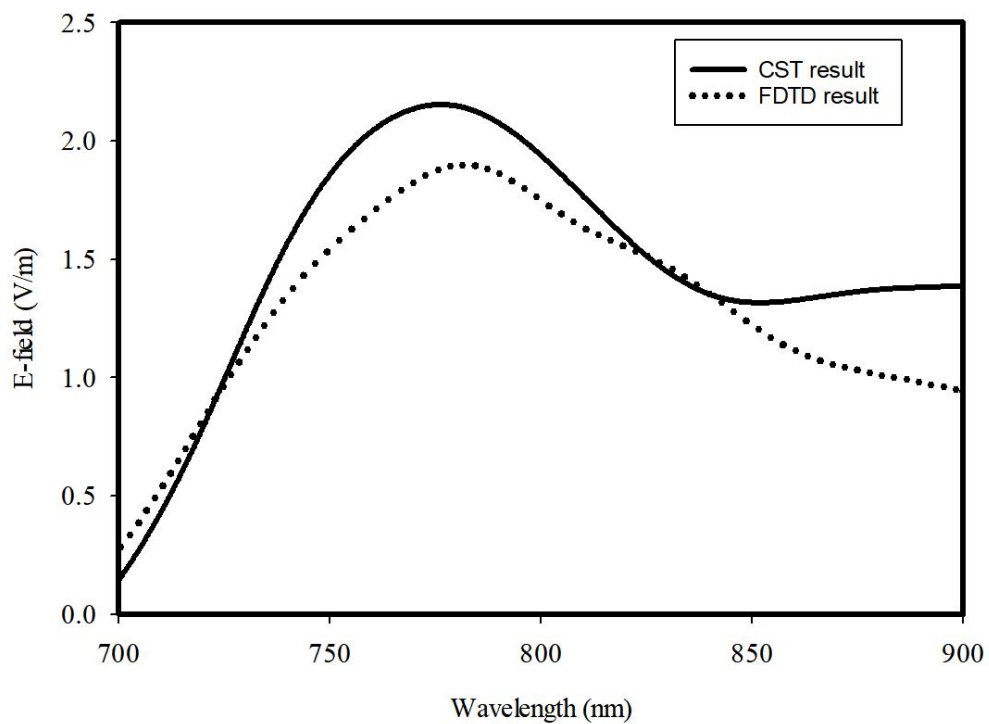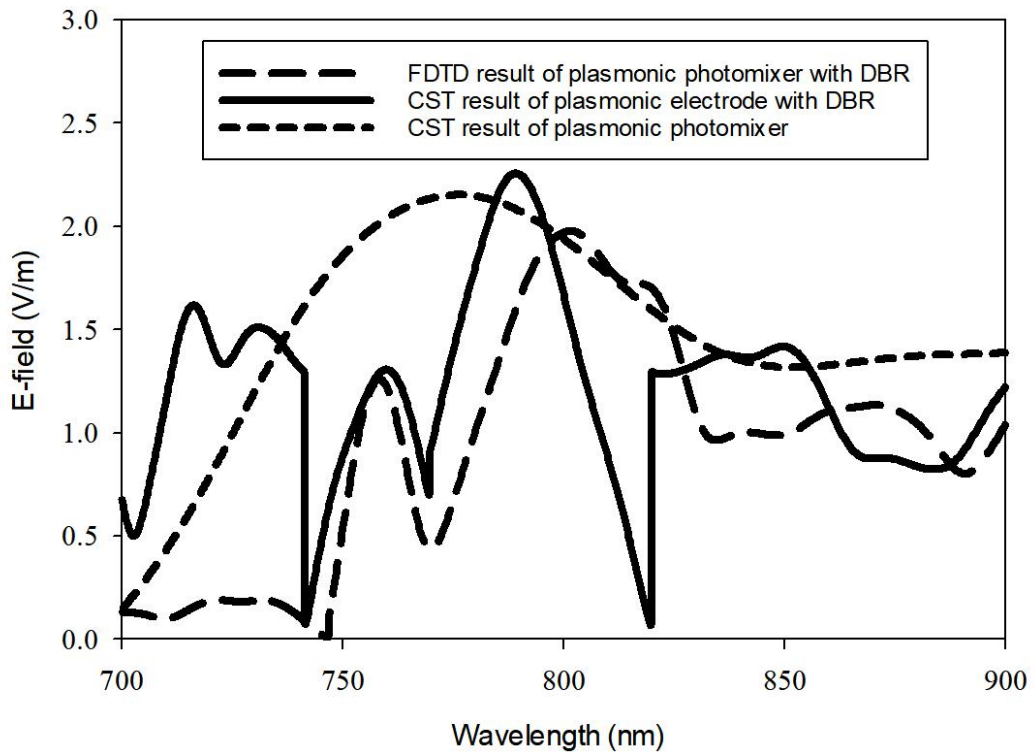
Figure 4.8: Optical E-field on the surface of LT-GaAs between plasmonic electrodes as a function of the wavelength

4.3 Improving the Optical-to-THz Conversion Efficiency by Reflector

As the power from incident laser beams been absorbed by the photoconductive material, photo-carriers were generated in the photoconductive substrate's active region and driven by bias voltage to excite the THz antenna. However, it is impossible to absorb all the incident optical power, therefore, reflecting the leaking optical power back to the active region of photoconductive substrate becomes possible mechanism to improve the generated THz power. Since then, photonic crystal (PhC) has been introduced.

Two types of PhC will be implemented with THz photomixer in this section, Distributed Bragg reflector (one dimensional PhC) and two dimensional PhC. Both of them will be placed underneath the photomixer electrodes to confine the incident optical power in the active region.

4.3.1 Distributed Bragg Reflector Coupled Plasmonic Photomixer

Distributed Bragg Reflector (DBR) is a periodically structured reflector. Basically, two different materials with different permittivity form each pair of layers as shown in Figure 4.9. The thickness of each layer is $T=\lambda/4\varepsilon_r^{-1/2}$, where λ is the wavelength at the desired operating frequency of the DBR, ε_r is the relative permittivity of the material.
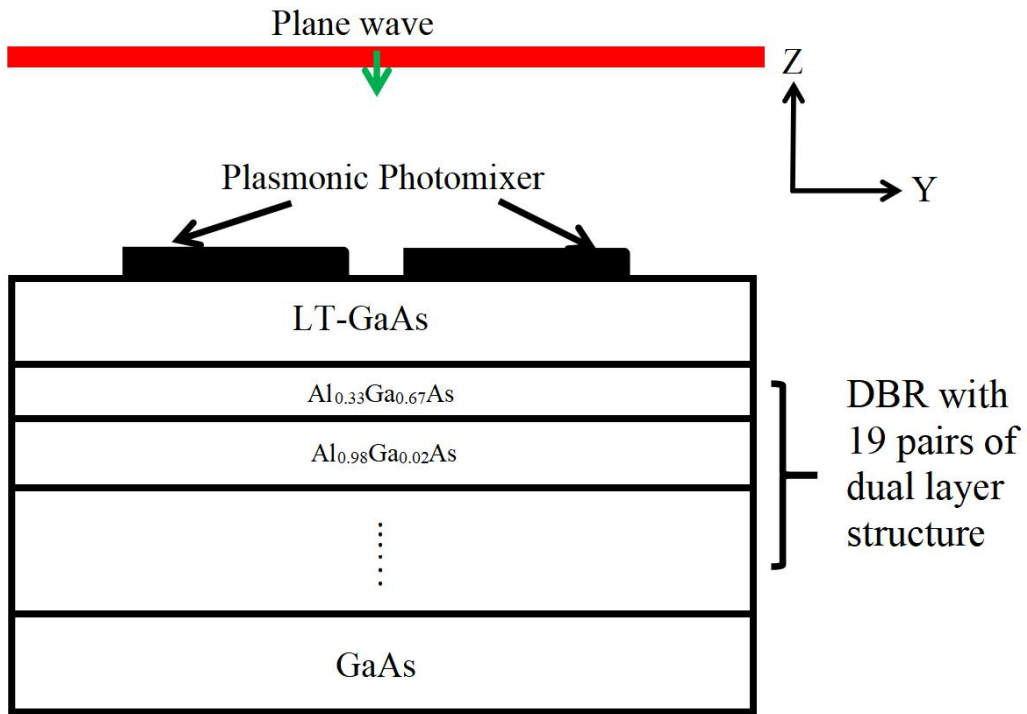
Figure 4.9: Schematic diagram of the DBR coupled plasmonic photomixer

In this case, $Al_{0.33}Ga_{0.67}As$ and $Al_{0.98}Ga_{0.02}As$ with dielectric constant of 9.9891 and 8.2146, respectively, was used to constitute a DBR at the optical band with wavelength of 785 nm. Figure 4.10 demonstrates the reflection coefficient of the DBR, and it is measured by placing a waveguide port on top of the configurations. It can be notice from Figure 4.10 that the stopband located between 765nm and 800nm. In addition, only the trapezoidal tip pair is used, instead of the whole electrodes and the thickness of LT-GaAs and support GaAs layer is 440nm and 300nm, respectively, to simplify and accelerate the simulation as shown in Figure 4.11. . As the thickness of the layer is a quarter wavelength, the phase difference between two adjacent layers is $\pi/2$, therefore, the intensity of the E-field in the DBR periodically varies from maximum to 0, or from 0 to maximum, at the two layers interface as shown in Figure 4.12. By 60 minutes simulation, it can be observed from Figure 4.13 and Figure 4.14 that the surface electric field between electrode tips rise to 2.25V/m. In consequence, the generated THz power has been improved by 30% when DBR was implemented which is consistent with the performance reported in the literature [121].
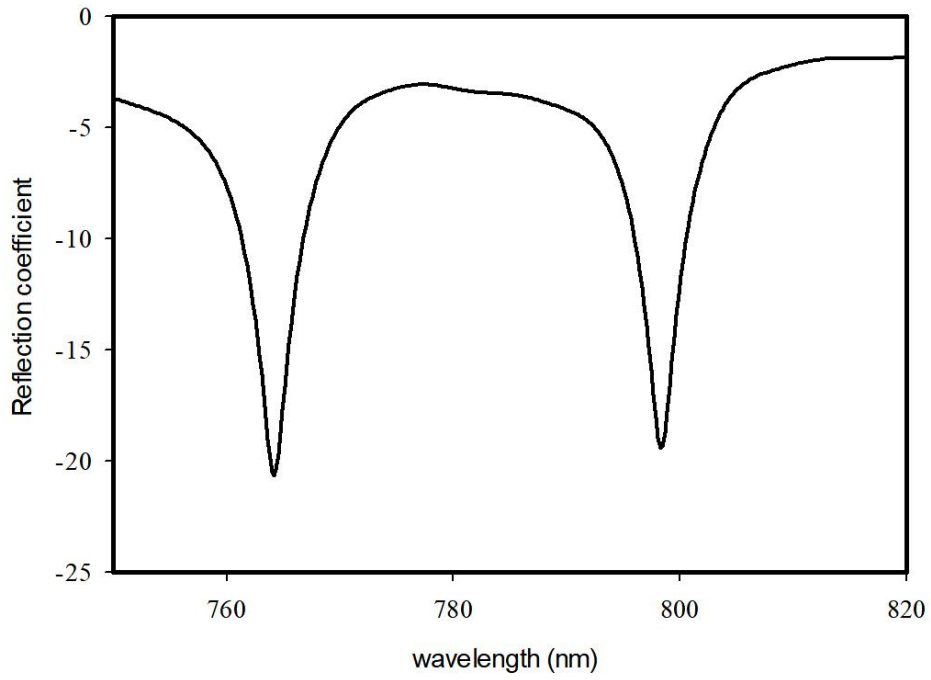
Figure 4.10: Reflection coefficient of DBR
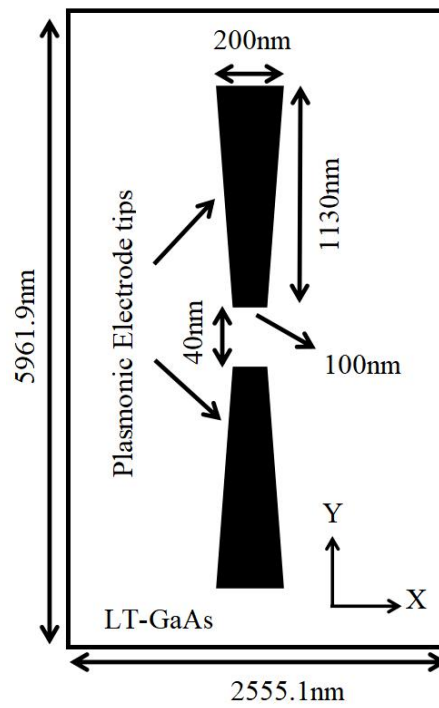
Figure 4.11: Top view of plasmonic electrode tips mounted on LT-GaAs

photoconductive substrate
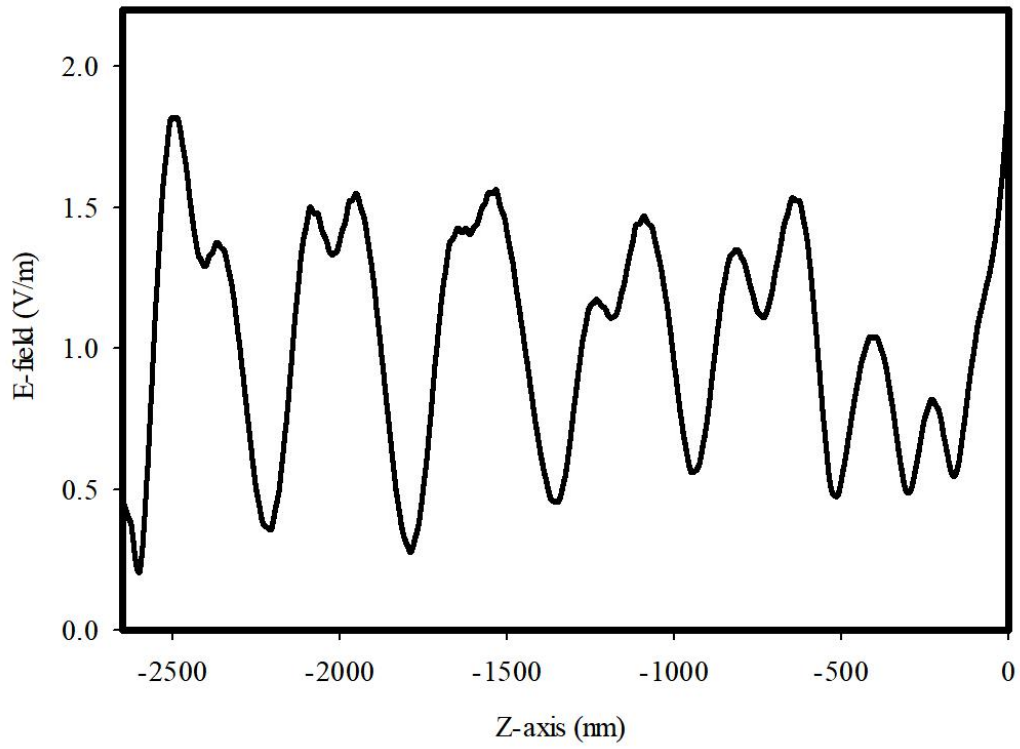
Figure 4.12: Electric field across z axis of DBR
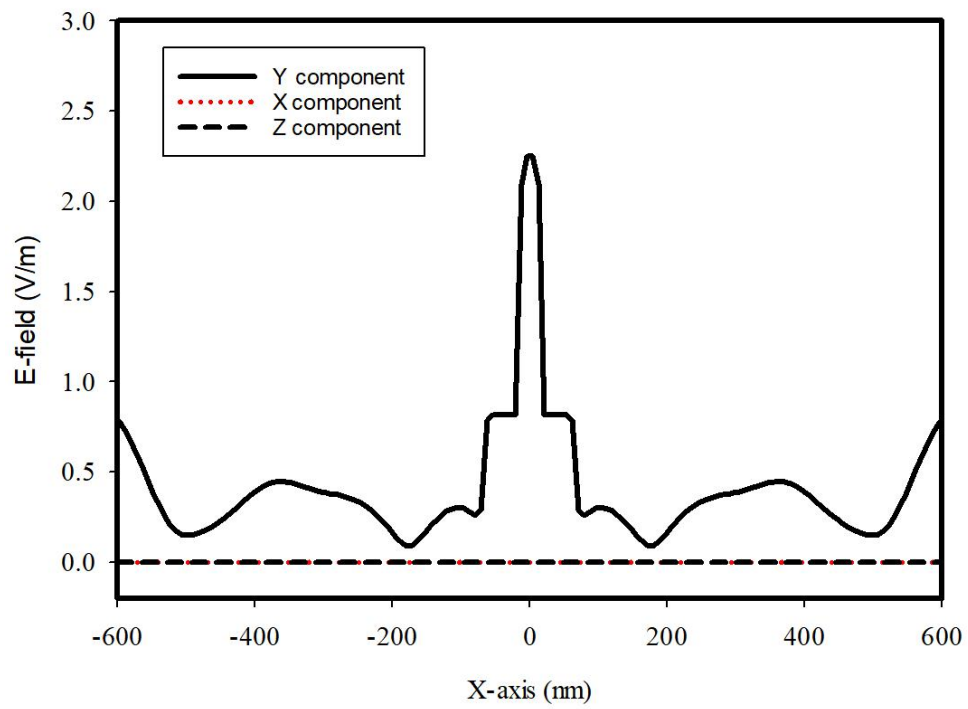
(a)
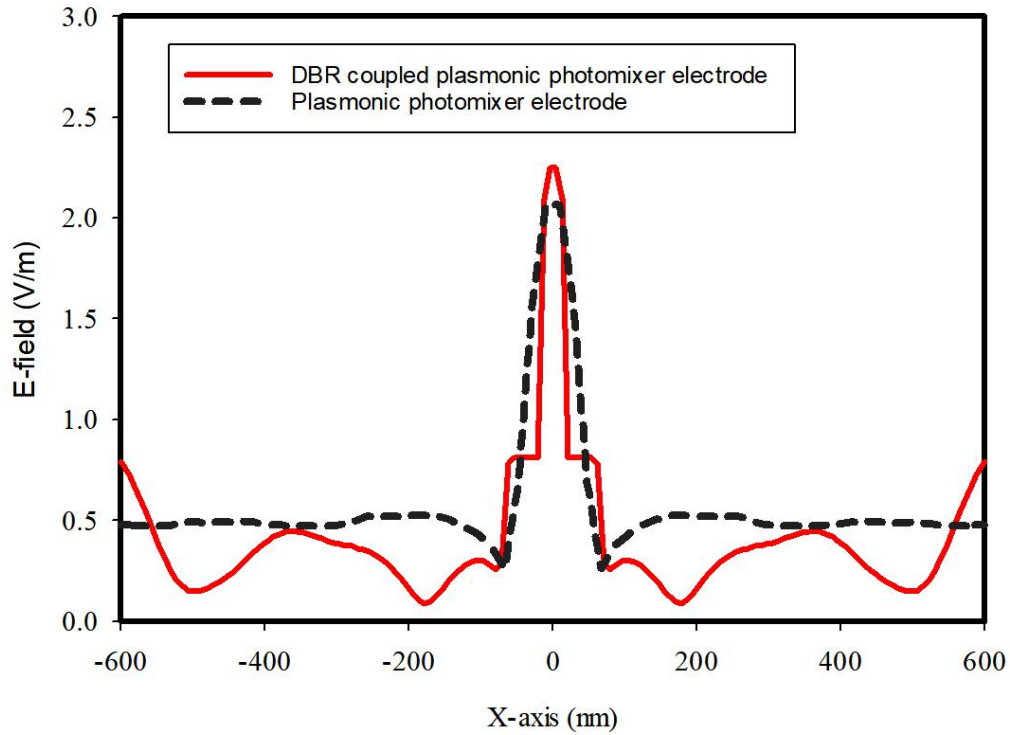
(b)

Figure 4.13:Optical E-field on the surface of LT-GaAs along the central line between plasmonic electrodes (a) three dimensional component of DBR coupled photomixer (b) comparison of Y components between photomixer with and without DBR

Figure 4.14: Optical E-field on the surface of LT-GaAs between plasmonic electrodes as a function of the wavelength for the design of utilizing DBR

4.3.2 Plasmonic Photomixer incorporated with Two Dimensional Photonic Crystal

It has been conducted in section 4.2.2 that the localized electric field can be enhanced by the surface plasmon resonance. The energy of surface plasmon resonance will be lost due to the metal absorption and scattering. Though, the propagation length of surface plasmon polariton is in scale of skin depth in the metal, the field decline far more slow when propagating in the dielectric [122,123]. Therefore, two dimensional photonic crystal (2D-PhC) is introduced to reflect the scattering energy from surface plasmon resonance within the photoconductive substrate. In the meanwhile, the incident power from laser beam can be confined within the photoconductive active region since the 2D-PhC can be designed as a dielectric bandstop frequency selective surface [124]. The unit cell of the 2D-PhC is shown in Figure 4.15 with periodicity, radius of central cylinder and thickness of a, r and t, respectively. The central cylinder should be different material in term of dielectric constant or conductivity. Therefore, for the desired design of 2D PhC, its transverse stopband and its longitudinal stopband should be around 785nm.
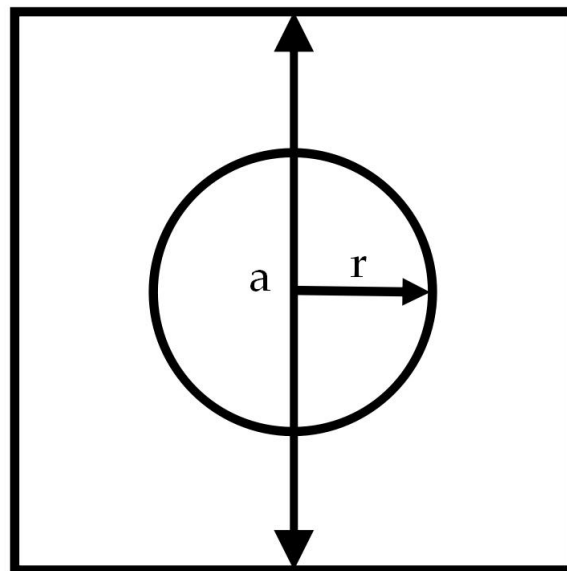
Figure 4.15: Unit cell of 2D-PhC

4.3.2.1 Two Dimensional Photonic Crystal with Air Hole

In this section, a design of 2D-PhC LT-GaAs layer with central air hole with periodicity, radius of central cylinder and thickness of $a=851.7$, $r=0.33a$ and $t=0.27a$ is presented to enhance the electric field at the active region on the surface of photoconducitve substrate. Figures 4.16 demonstrate the parameter analysis of the transverse reflection coefficient of of the 2D-PhC by using two waveguide port at each side of the 2D-PhC layer. It should be noted that the size of the waveguide port should be the same as the 2D-PhC, and the two waveguide ports are propagate toward each other. These results demonstrate that the performance of 2D-PhC as reflector in the transversal plane. Then, it can be observed that the period and radius of central air hole significantly affect the performance of 2D-PhC in XY plane. It is because, in the aspect of XY plane, 2D-PhC can be considered as two identical overlapped Distributed Bragg Reflectors that designed for X direction and Y direction, hence the transverse reflection coefficient depends on the thicknesses of different materials in X and Y directions. Moreover, the designated 2D-PhC demonstrate a stopband between 780nm and 815nm, which satisfied the requirement. The longitudinal reflection coefficients of the designated 2D-PhC are shown in Figure 4.17 by using a waveguide port above the 2D-PhC. It can be noticed that the stopband is between 775nm and 805nm which satisfied the requirement of reflect the incident laser power.
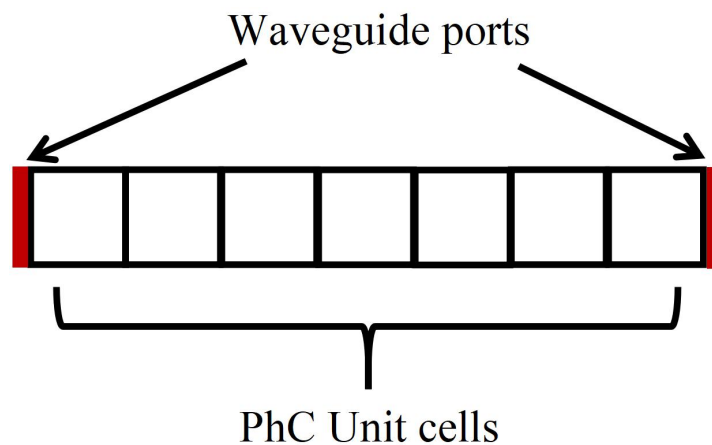
(a)
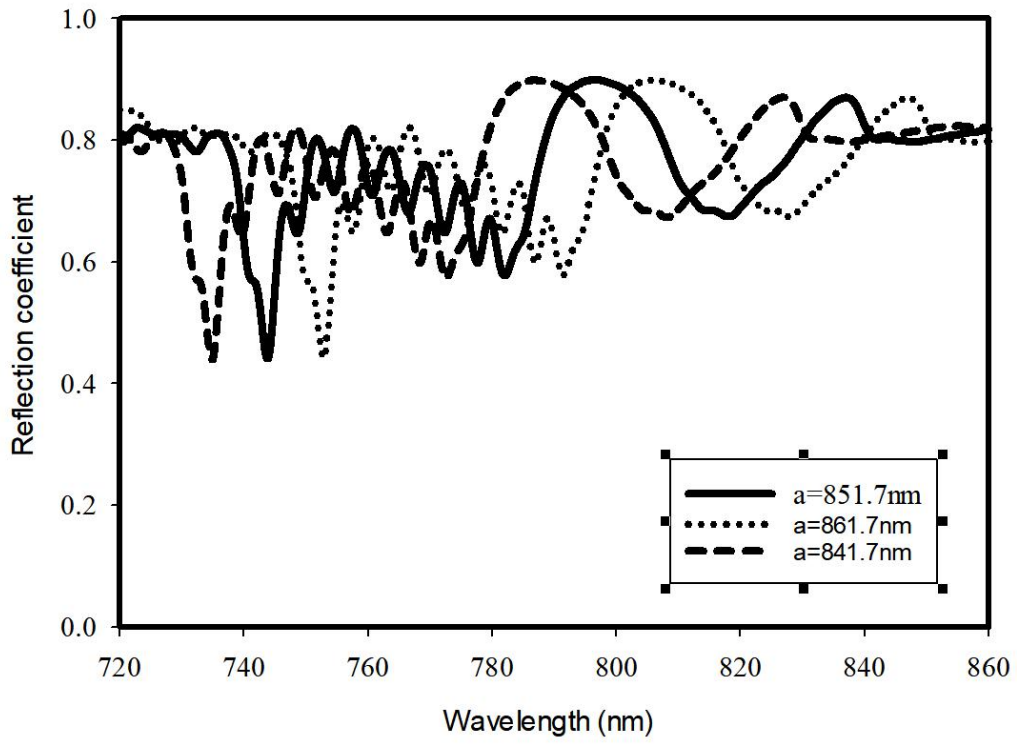
(b)
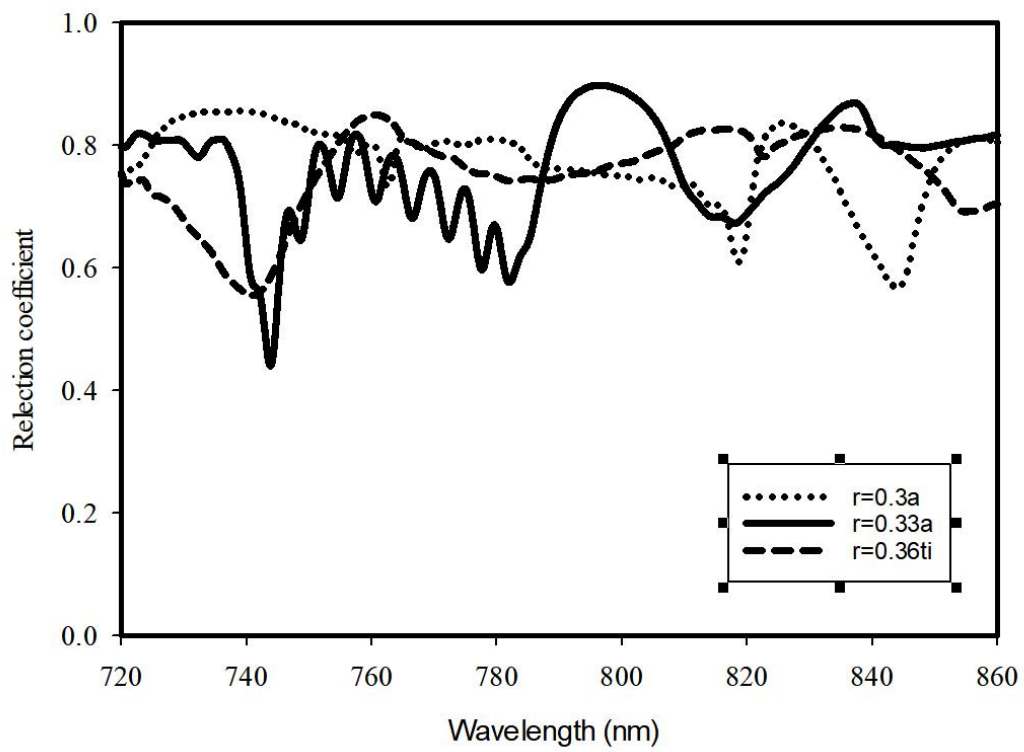
(c)
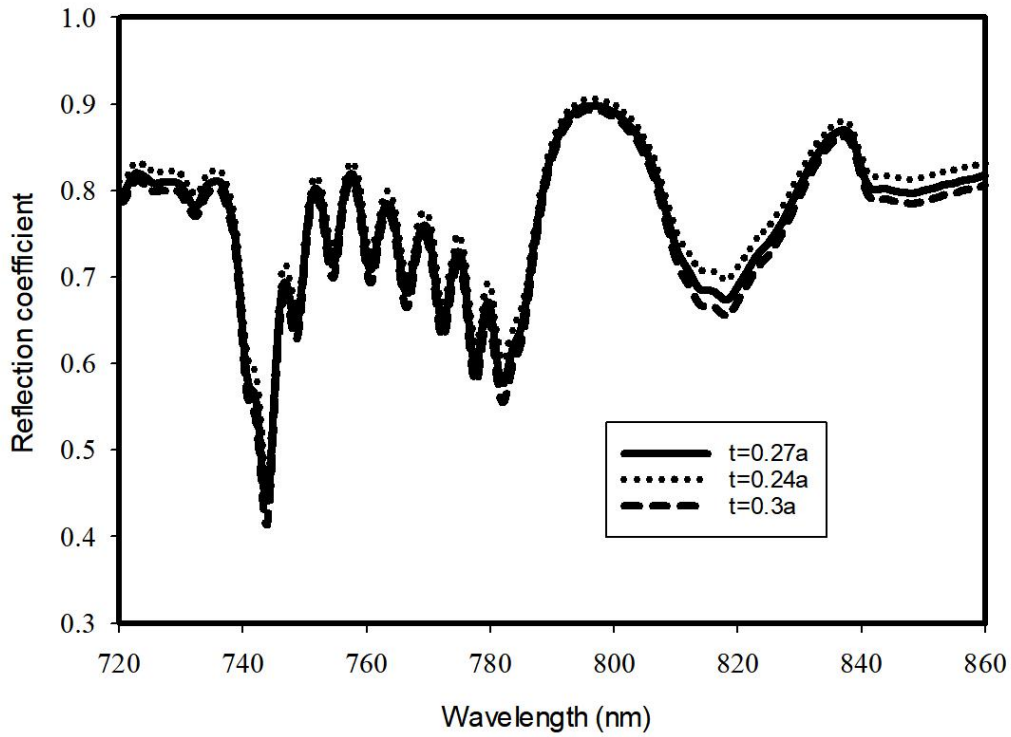
(d)

Figure 4.16 The parameter analysis of the transverse reflection coefficient of 2D-PhC with *a*=851.7nm, *r*=0.33*a*, *t*=0.27*a*: (a) measurement setup (b) various period values, (c) various central hole radius, (d) various thickness values.
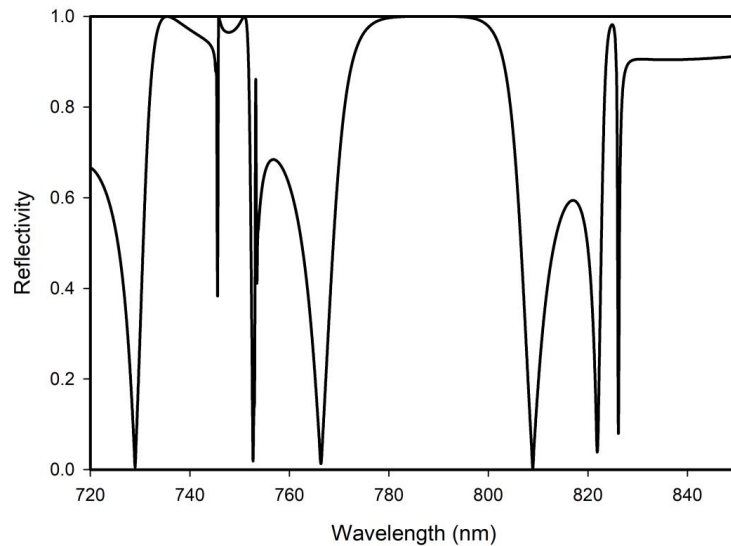
Figure 4.17: Reflectivity of PhC unit cell with *a*=851.7nm, *r*=0.33*a*, *t*=0.27*a*

Therefore, 7×3 unit cells of the 2D-PhC with central air hole are implemented with the trapezoidal tip-tot-tip electrode shown in Figure 4.11. The cross section of the configuration of the photomixer electrode on the 2D-PhC with central air hole is

illustrated in Figure 4.18. Then, the electric field distribution as a function of X-axis and as a function of wavelength after 30 minutes simulation are depicted in Figure 4.19 and 4.20, respectively. It can be noticed that the electric field increased from 2.1V/m to 3.4V/m by implementing 2D-PhC with air hole as reflector. Hence, as indicated by equation (3.4), the enhancement factor of the generated THz power using 2D-PhC as reflector underneath the plasmonic photomixer electrode is 6.87 which represents a significant improvement as compared to the design utilizing Distributed Bragg reflector introduced in section 4.3.1.
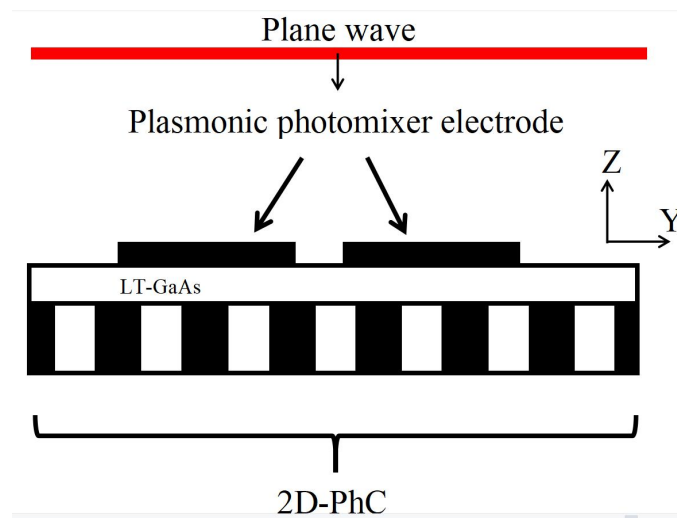
Figure 4.18: Cross section of plasmonic photomixer with 2D-PhC with air hole
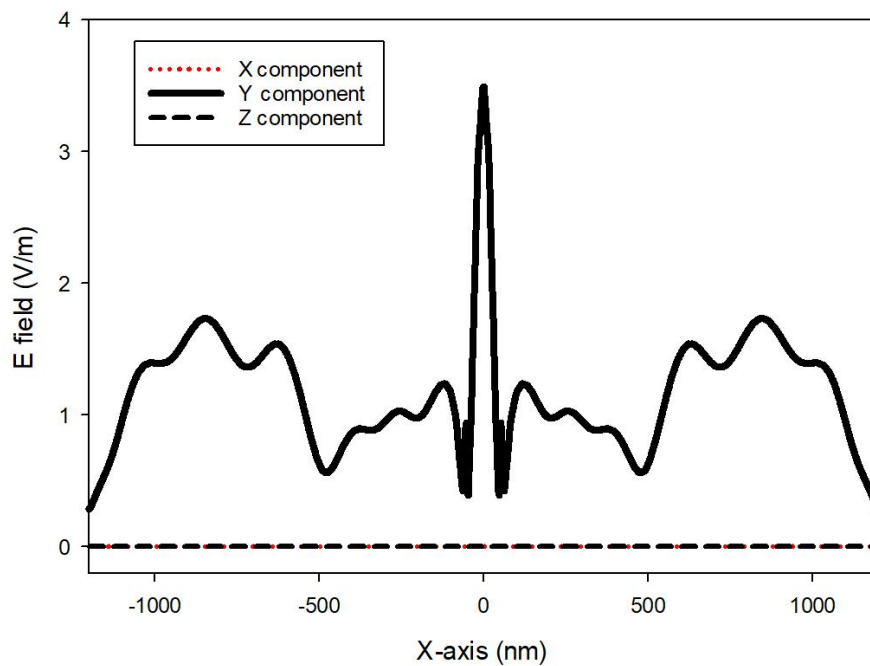
(a)
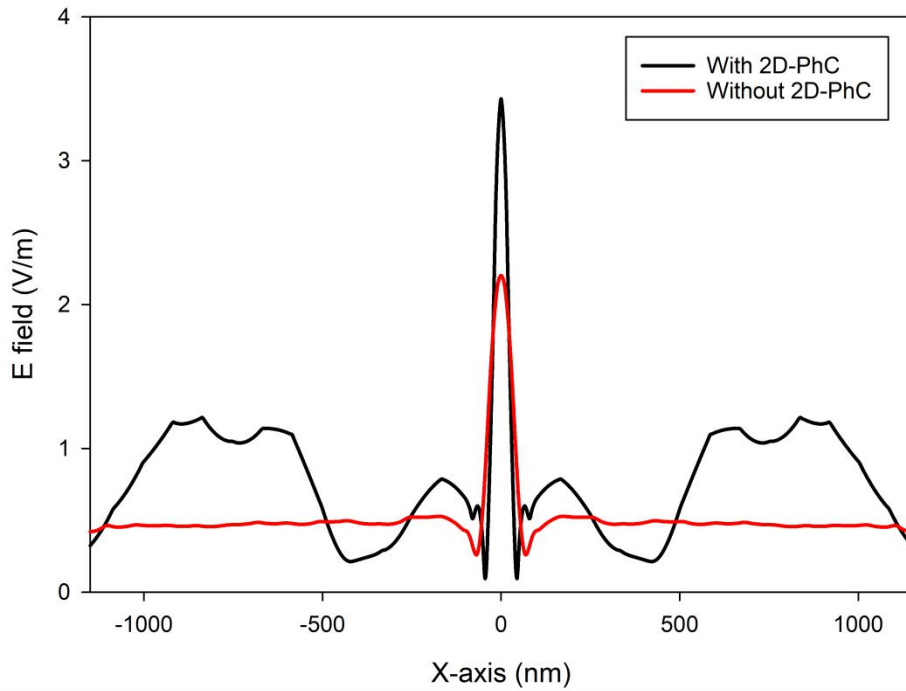
(b)

Figure 4.19: Optical E-field on the surface of LT-GaAs along the central line between plasmonic electrodes (a) three dimensional components at wavelength of 780nm (b) comparison between with and without 2D-PhC at wavelength of 780nm
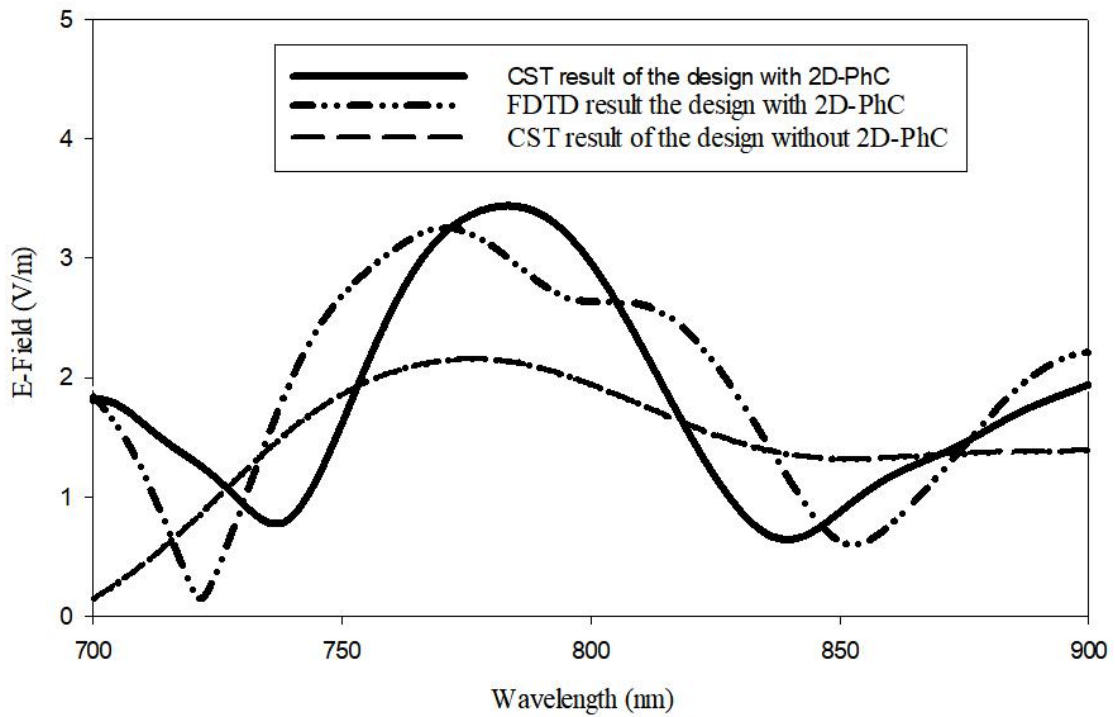
Figure 4.20: Optical E-field on the surface of LT-GaAs between plasmonic electrodes as a function of the wavelength for the design of utilizing 2D-PhC

4.3.2.2: Two Dimensional Photonic Crystal with Plasmonic rod

As introduced in section 4.2.2, the local electric field can be enhanced by the surface plamonic resonance, hence, in order to enhance the photoconductive substrate's surface electric field further on top of the 2D-PhC design, the plasmonic rod is used to fill in the gap of 2D-PhC introduced in section 4.3.2.1. In this case, since there is extra plasmonic material within the 2D-PhC, apart from the plasmonic resonance interaction between two plasmonic electrodes, two more interactions are generated. They are, the interaction between plasmonic rods and plasmonic electrode as well as the interaction between the adjacent plasmonic rods. As a result of more interactions, the localised electric field is further concentrated and enhanced. The dimension of the plasmonic rods filled 2D-PhC are chosen as a=851.7nm, r=0.39a and t=0.22a. The transverse transmission coefficient of the plasmonic rods filled 2D-PhC is shown in Figure 4.21 and the longitudinal reflection coefficient is illustrated in Figure 4.22.
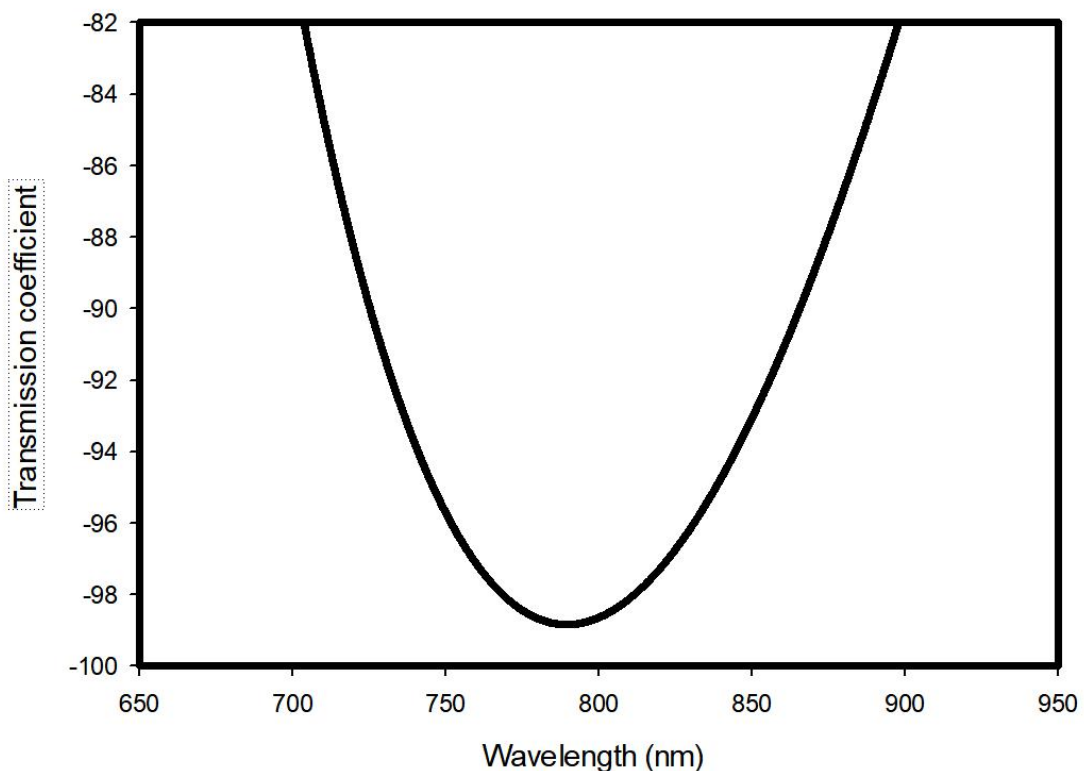
Figure 4.21: The transverse transmission coefficient of plasmonic rods filled PhC unit cell with a=851.7nm, r=0.39a, t=0.22a
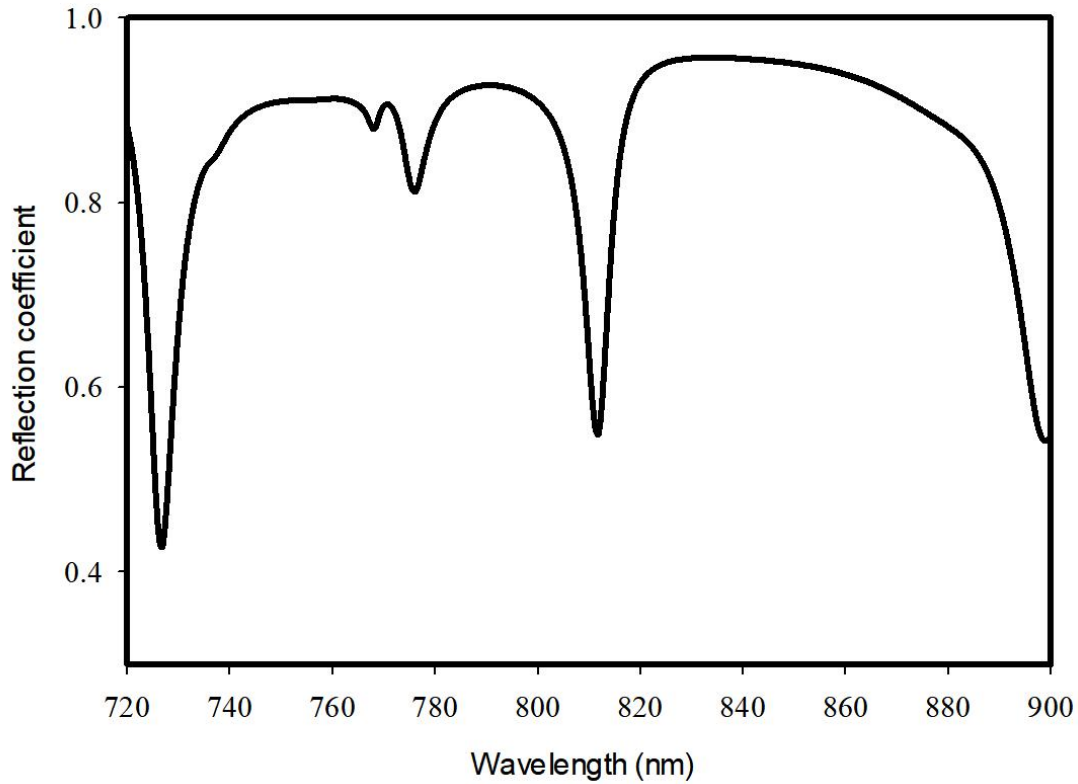
Figure 4.22: The longitudinal reflection coefficient of plasmonic rods filled PhC
unit cell with a=851.7nm, r=0.39a, t=0.22a

Same configuration of the plasmonic electrodes as section 4.3.2.1 is used, except that the 2D-PhC is replaced by the plasmonic rods filled 2D-PhC. By 35 minutes simulation, it can be seen from the electric field distribution shown in Figure 4.23 that the electric field is much stronger when plasmonic rods are implemented compared to that at the same position albeit with the air hole design. Figure 4.24 and Figure 4.25 depict that the optical electric field at the active region of plasmonic electrodes has been increased from 3.4V/m to 4.35V/m by filling the air hole with plasmonic rods. By comparing with the case without any 2D-PhC, 2.07 enhancement factor has been achieved by implementing plasmonic rods filed 2D-PhC, consequently, the generated THz power has been enhanced by 18.4 times as suggested by equation (3.4).
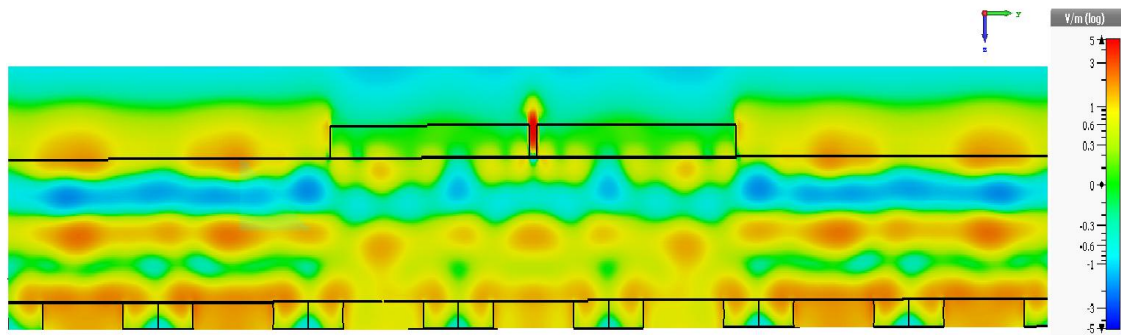
(a)
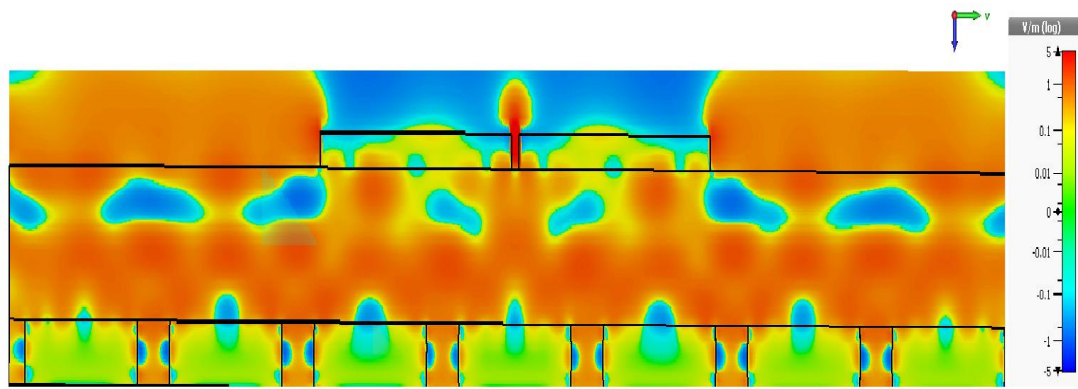
(b)

Figure 4.23: Cross-section cut plane of the optical E-field distribution incorporating different 2D-PhC (a) air hole (b) plasmonic rods
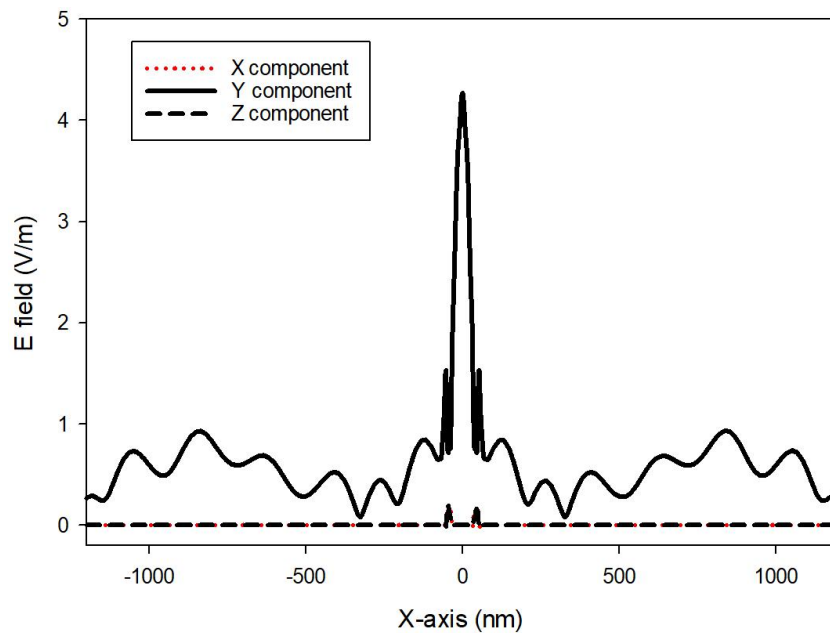
(a)
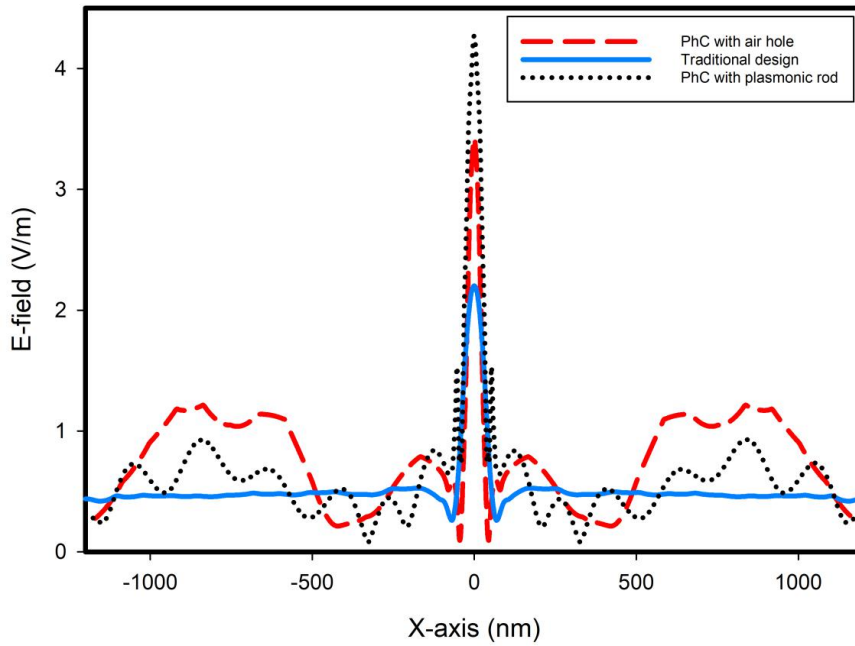
(b)

Figure 4.24: Optical E-field magnitude on the surface of LT-GaAs along the central line between electrodes at wavelength of 780nm (a) three dimensional components (b)comparison between the PhC with and without plasmonic rod along with the traditional design
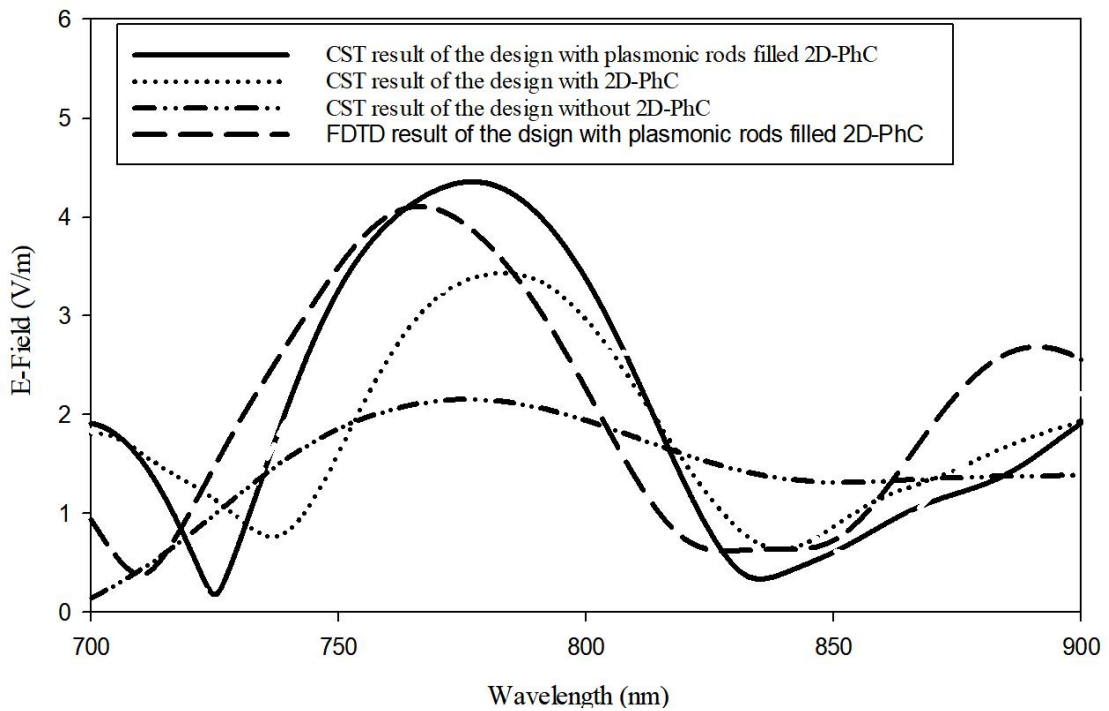
Figure 4.25:Optical E-field magnitude on the surface of LT-GaAs at the centre of active region

4.4 Improving the Optical-to-THz Conversion Efficiency by Implementing superstrate

The design introduced previously in section 4.3 assumed that the incident laser beams have already reach the photoconductive substrate, enhancement should be done locally. On the other hand, it is possible to boost the electric field before the illumination.

Two designs implementing superstrate with THz photomixer will be proposed in this section. They are the plasmonic photomixer incorporated with dielectric superstrate layer and plasmonic rods filled 2D-PhC as well as the plasmonic photomixer implemented with metal ground plane and frequency selective surface (FSS) superstrate.

4.4.1 Dielectric superstrate

On top of previous design that utilizing the plasmonic rods filled 2D-PhC, superstrate, a method that improve the antenna gain, is considered to further improve the generated THz power. In this section, a design that utilizing dielectric superstrate and plasmonic rods filled 2D-PhC is introduced. The configurations of the design is illustrated in Figure 4.26, where the superstrate is suspended above the plasmonic trapezoidal photomixer electrodes, and the identical plasmonic rods filled 2D-PhC introduced in section 4.3.2.2 is employed underneath. The simulation time for each run takes approximately 50 minutes.
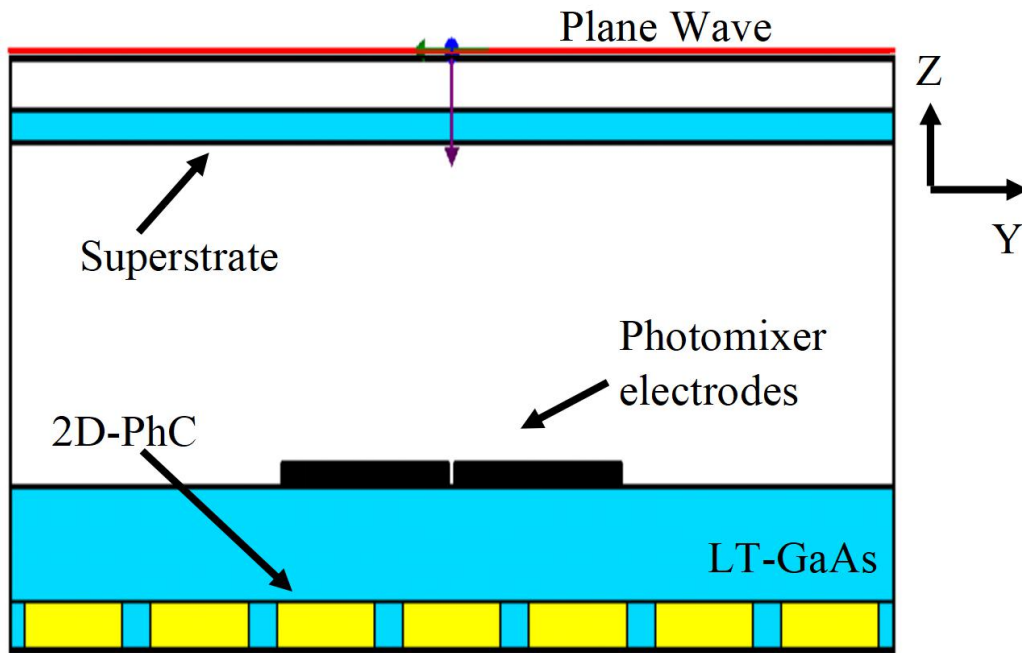
Figure 4.26: Illustration of the design that utilizing plasmonic rods filled 2D-PhC and dielectric superstrate

Figure 4.27 demonstrates the illuminating electric field of the proposed photomixer electrodes with dielectric superstrate, from which it can be noticed that the distance between the dielectric superstrate and the photoconductive substrate as well as the thickness of the dielctric superstrate represent the parameters that determine the illuminating electric field between electrodes, which increases to 8.4V/m as the distance and thickness become 1350 nm and 125nm, respectively. Moreover, the comparison of the surface electric field in active region between the design with and without dielectric superstrate as well as the initial design of plasmonic photomixer is depicted in Figure 4.28. It can be observed that, the surface electric field in active region increased from 4.35V/m to 8.4V/m by implementing dielectric superstrate. Hence, compared with the illuminating electric field of the plain plasmonic electrode design, 2.1V/m, the corresponding enhancement factor of employing dielectric superstrate and plasmonic rods filled 2D-PhC is 256.
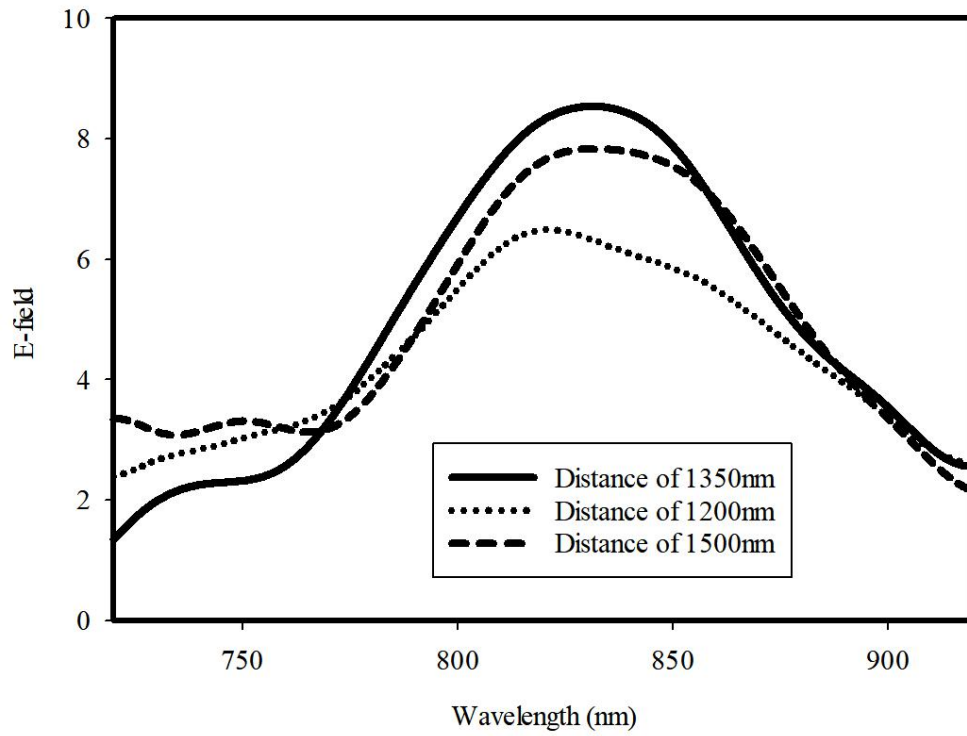
(a)
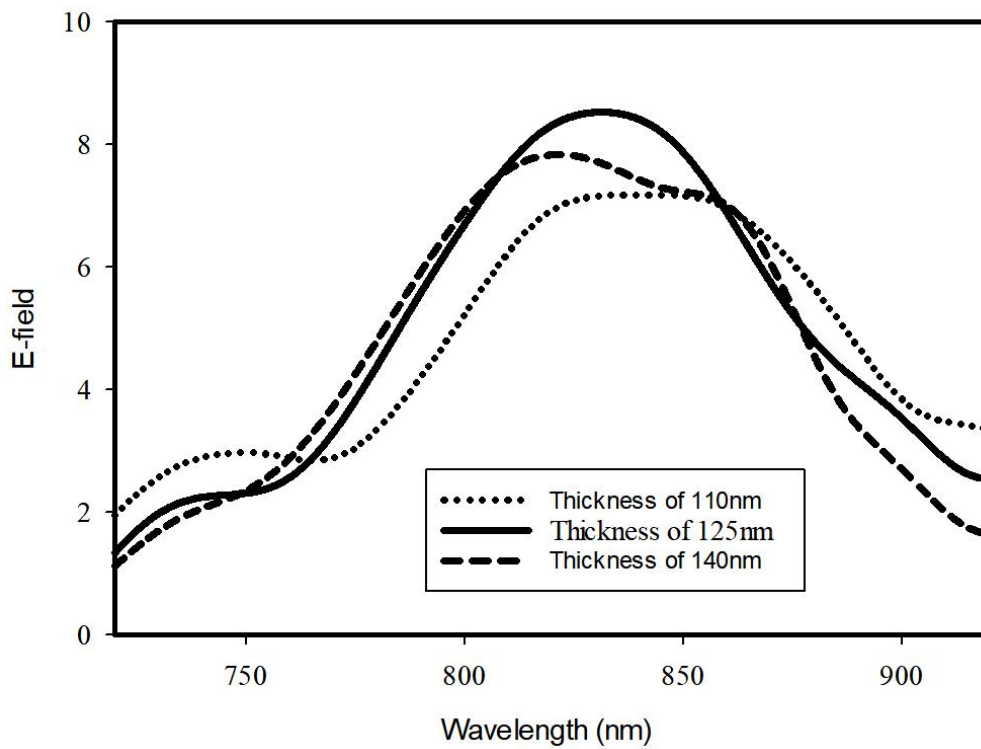
(b)

Figure 4.27:Optical E-field magnitude on the surface of LT-GaAs at the centre of active region by implementing superstrate with distance of 1350nm and thickness of 125 nm (a)various distance values (b) various thickness values
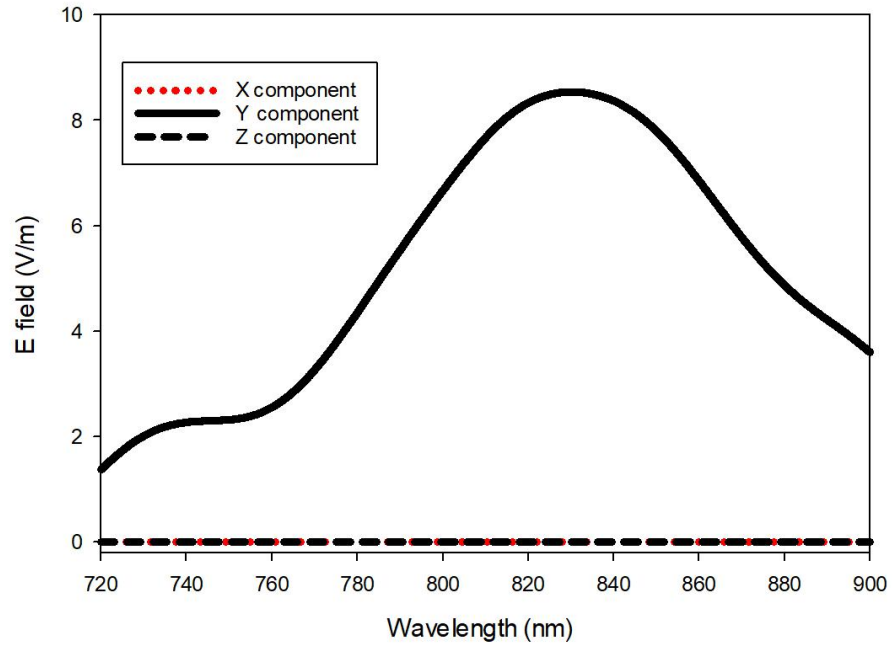
(a)
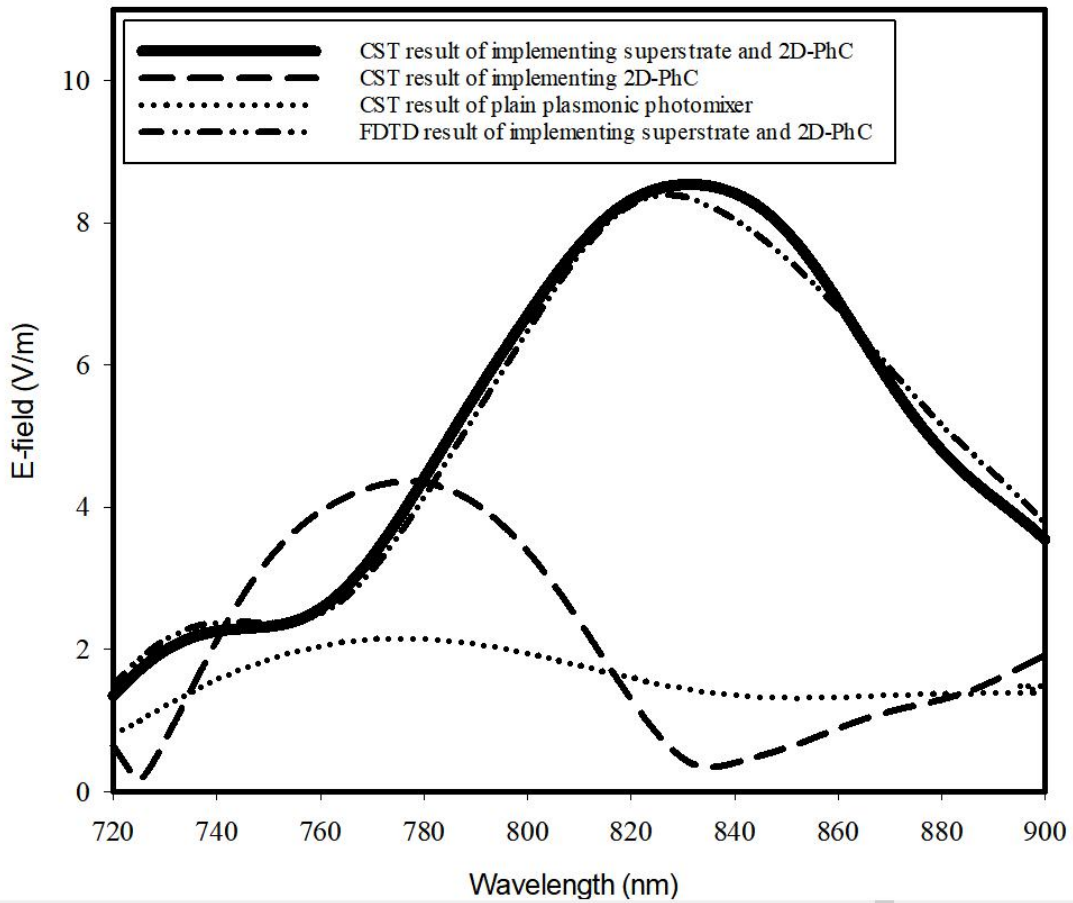
(b)

Figure 4.28: Optical E-field magnitude on the surface of LT-GaAs at the centre of active region (a) three dimensional components (b) comparison between with and without superstrate as well as plain plasmonic photomixer

4.4.2 Plasmonic Photomixer incorporated with Dielectric Frequency Selective Surface Superstrate

Frequency selective surface (FSS) is a repetitive structure that can be used as a optical filter, by which is achieved by the periodic pattern of FSS. FSS is also known as a partial reflection surface and introduced by [125,126], where the infinite boundary condition has been assumed to apply array theory methodology. As shown in Figure 4.29, in order to achieved maximum power, the distance between the FSS superstrate and metal ground plane should be:

$$l_2 = (N+1)\frac{\lambda_{eff}}{2} \tag{4.1}$$

where l_2 is the resonant length, N is integer number and λ_{eff} is effective wavelength.
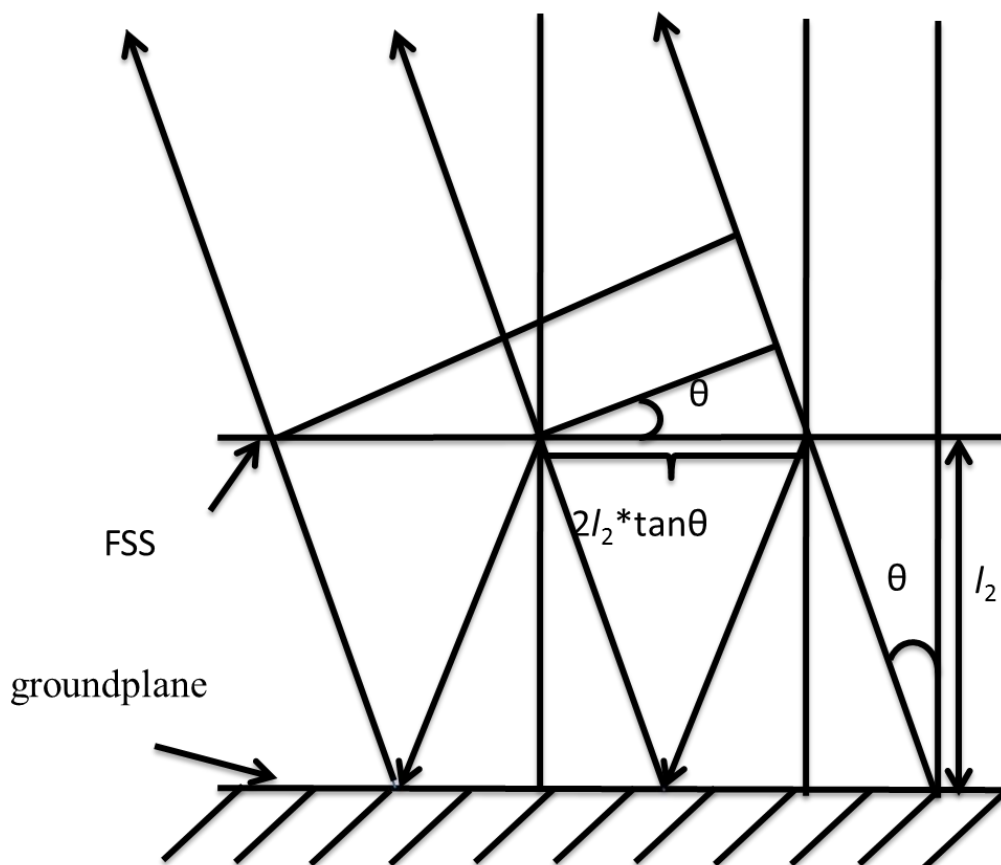
Figure 4.29:Working principle of FSS

The 2D-PhC with air hole is used as FSS in this section. By applying unit cell boundary condition in the simulation, the reflection coefficients of the proposed FSS unit cell are illustrated in Figure 4.30, from which the dimension of the unit cell has

been chosen as a=760 nm, r=0.3a and t=0.2a. Since the photomixer is surrounded by metal ground plane and the size of the central slot within the ground plane depends on the size of photomixer, photomixer electrodes with 5 tip pairs were used in the model as shown in Figure 4.31. The dimensions of the photomixer and slot were chosen as : M = 0.5 µm, B = 0.2 µm, W = 0.1 µm, e = 0.5 µm, P = 2.3 µm, L = 1.13 µm, D = 0.8 µm, T_{end} = 4 µm, H = 1 µm, G = 13.68 µm, and thickness of 0.1 µm. Since then, 19×19 2D-PhC unit cells made of GaAs were used as dielectric FSS superstrate. By employing the linearly polarised plane wave, the illuminated electric field field between the central electrode tips are demonstrated in Figure 4.32 with various distance between FSS superstrate and ground plane. The simulation time for each run takes approximately 60 minutes.
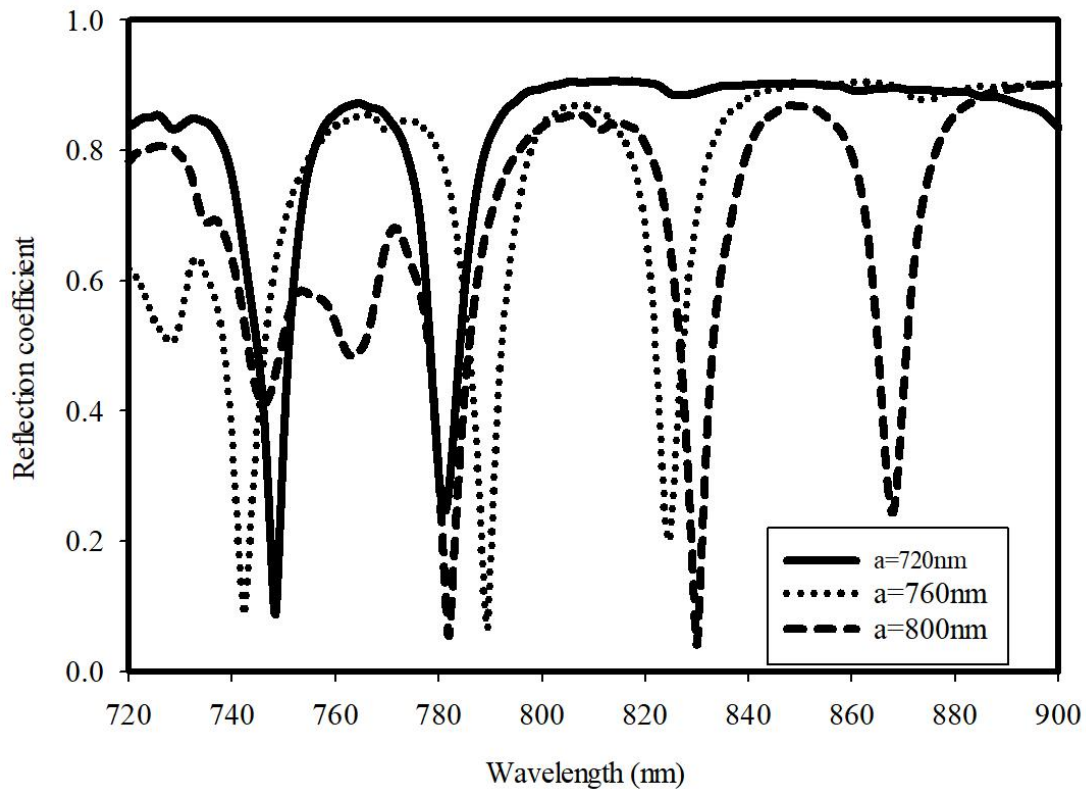
(a)
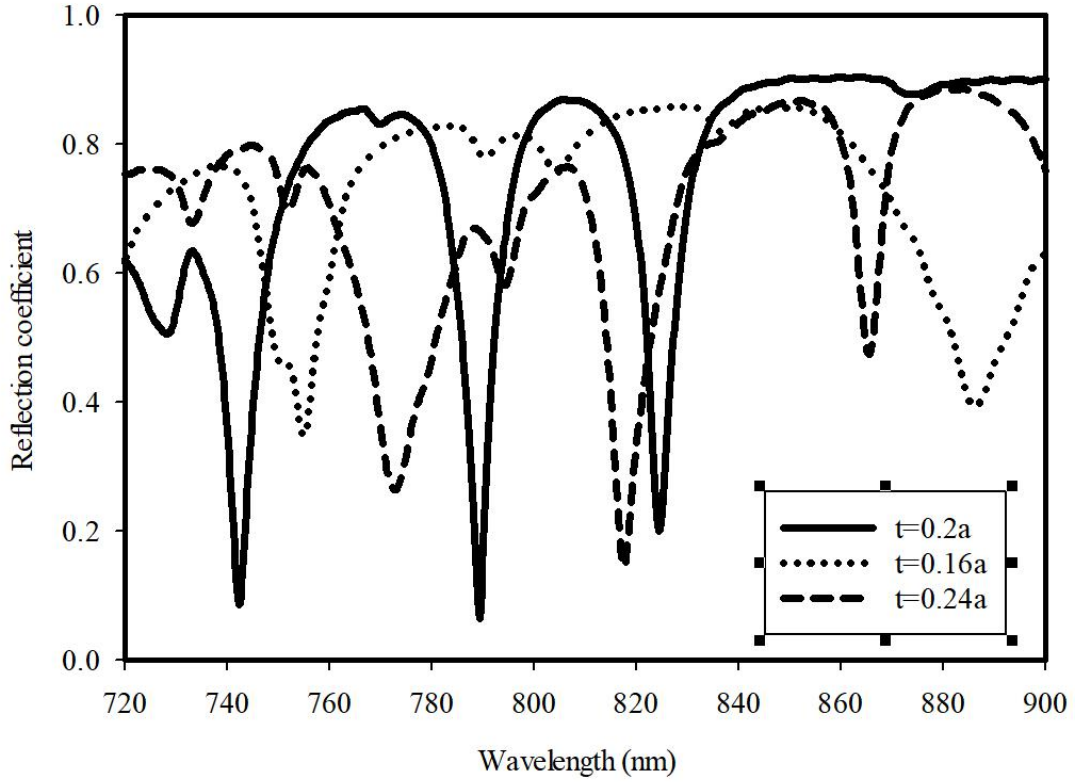
(b)
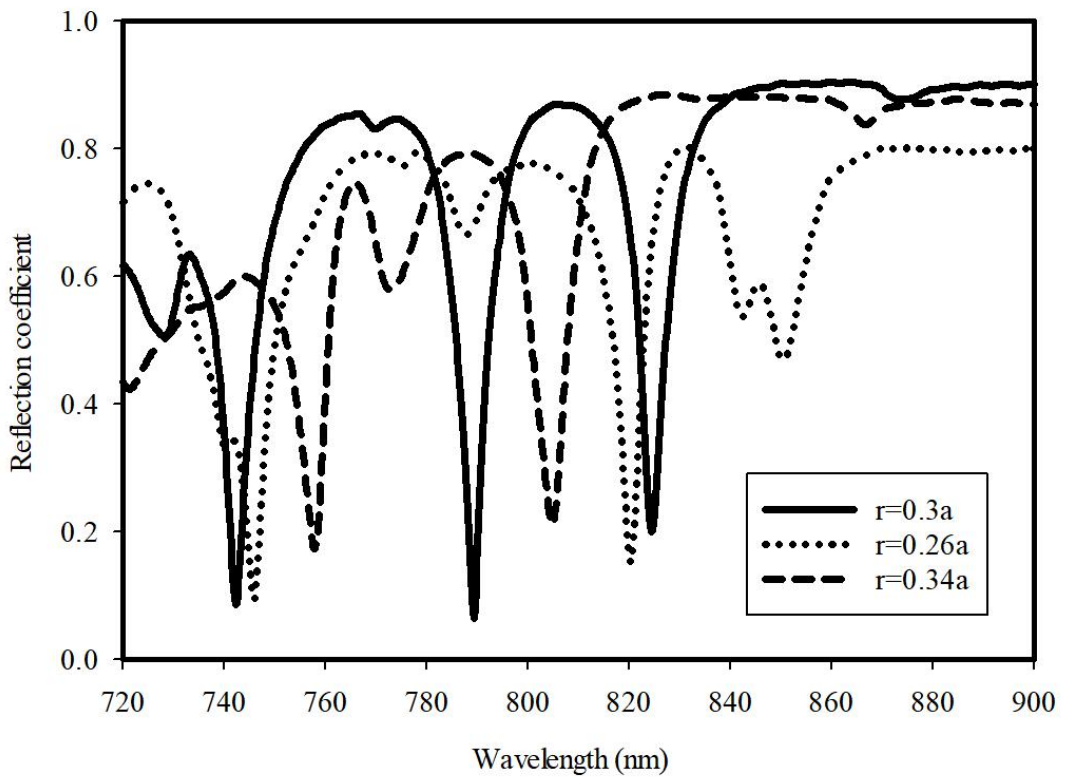
(c)

Figure 4.30: Reflection coefficient of 19×19 unit cells with(a) various

periodicities, (b) various thicknesses, (c) various radius
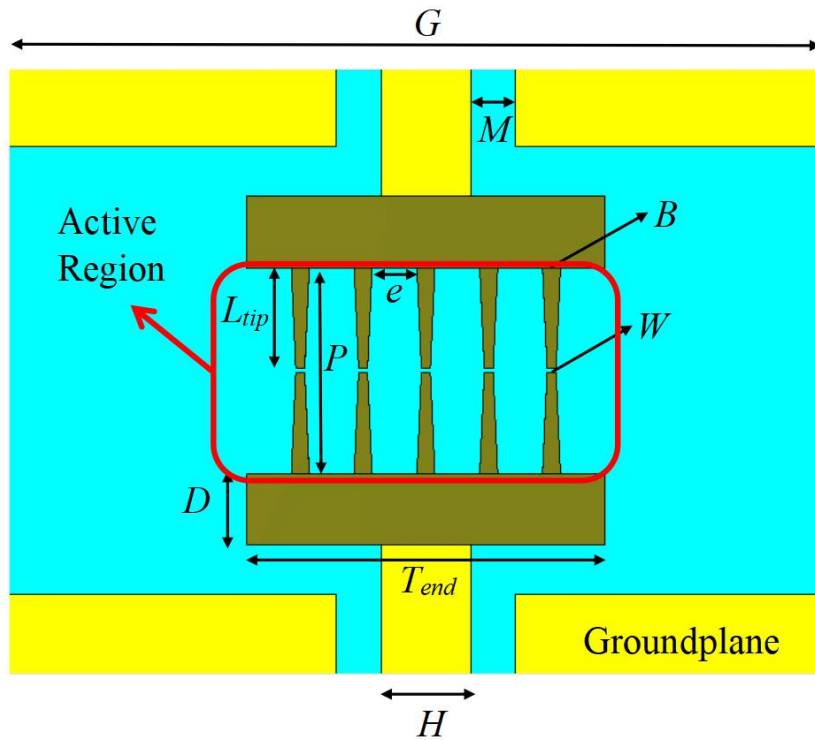
Figure 4.31:Top view of the photomixer based slot
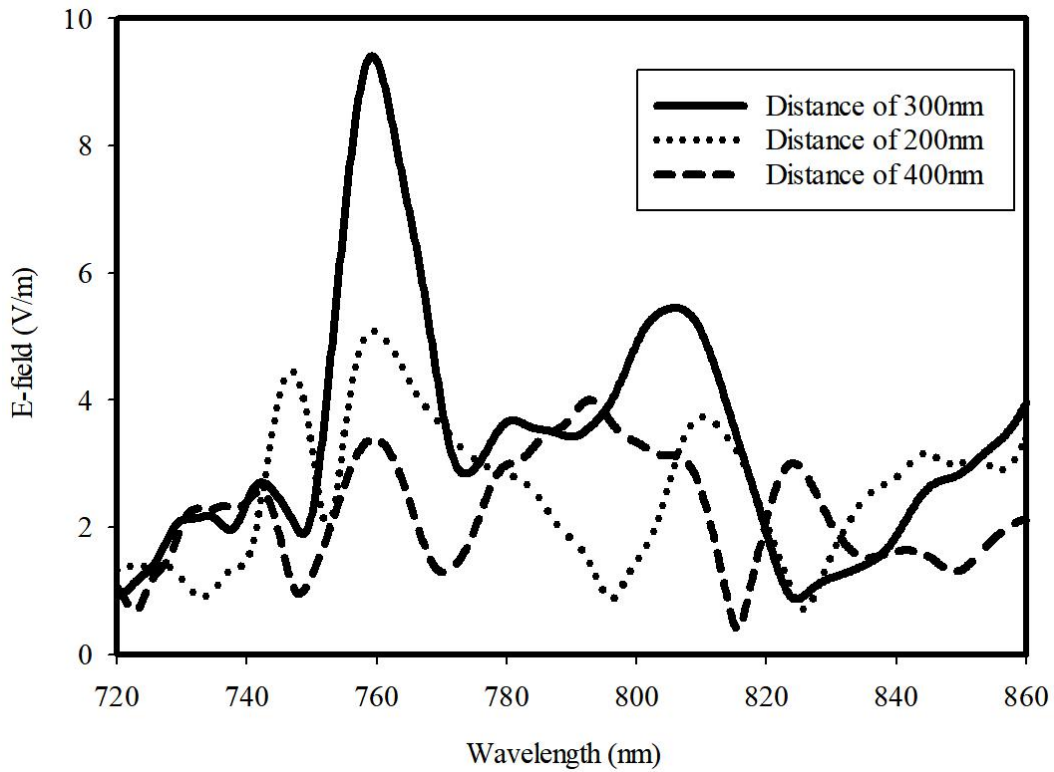
Figure 4.32:Optical E-field magnitude on the surface of LT-GaAs at the centre of active region by implementing FSS with various distances
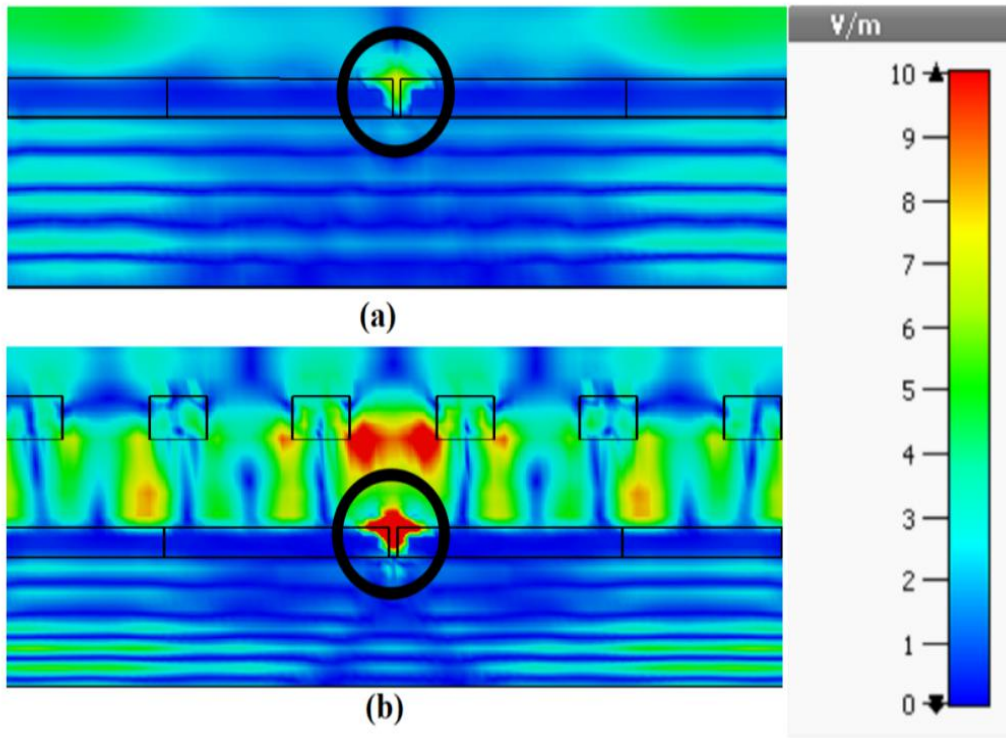
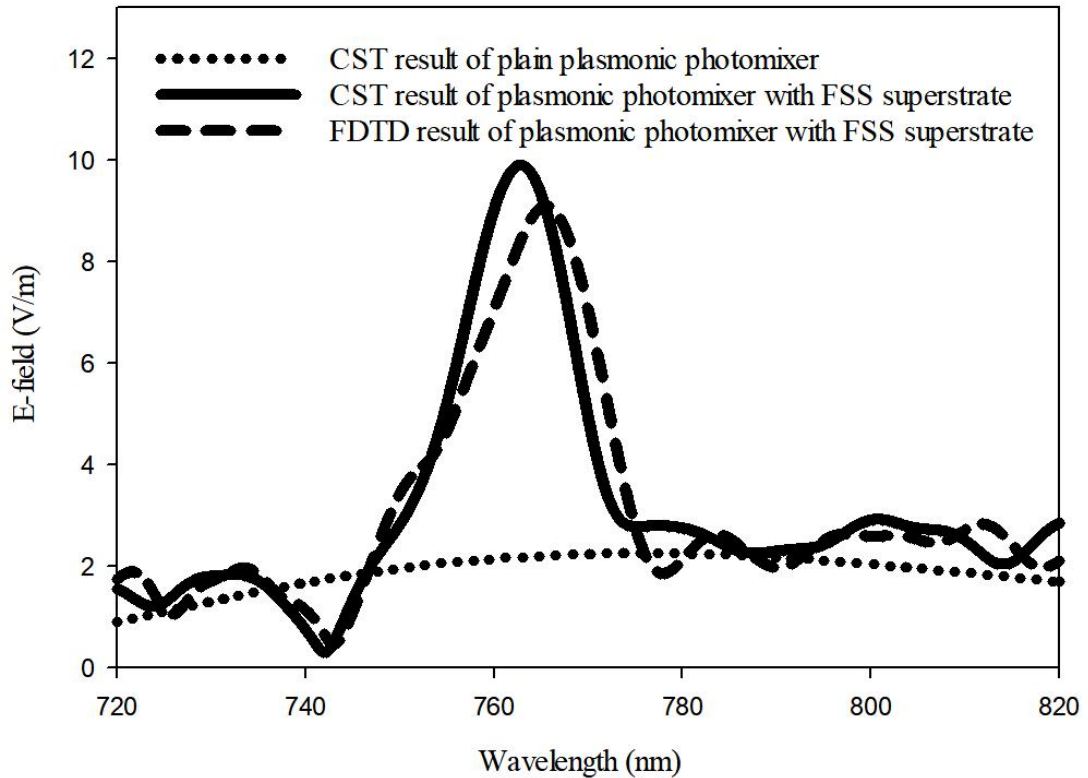Figure 4.33:Cross-section cut plane of the optical E-field distribution (**a**) without FSS (**b**) with FSS
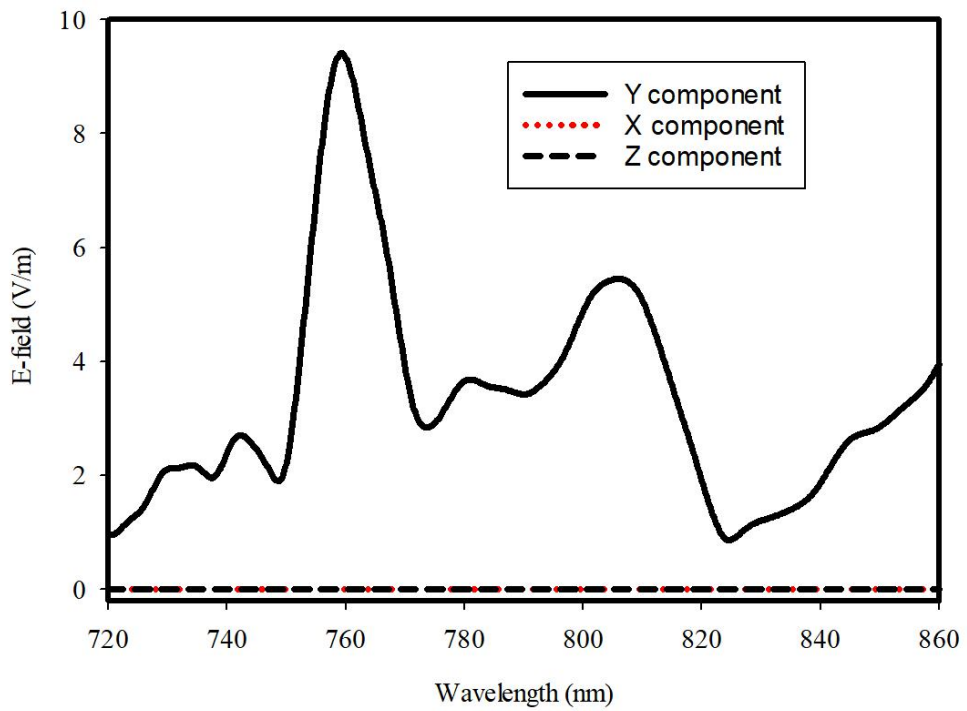
(a)

(b)

Figure 4.34: Optical E-field magnitude on the surface of LT-GaAs at the centre of active region (a) three dimensional components (b) comparison between with and without FSS superstrate

It can be observed from Figure 4.32 that the distance between FSS superstrate and ground plane is the primary factor of the electric field at active region. The maximum electric field is found with distance of 300nm, which result in a local electric field of 9.9 V/m between central plasmonic electrode tips. Strong concentration of the electric field can be found in the proximity of active region between electrode tips by utilizing FSS as shown in Figure 4.33. As demonstrated by Figure 4.34, the illuminating electric field has increased from 2.1V/m to 9.9V/m by employing dielectric FSS superstrate, as a consequence, the generated THz power has been sustainably enhanced by 494 times.

Furthermore, the same methodology has been applied to an identical photomixer albeit with a InGaAs photoconductive layer, where the electric field on the InGaAs's surface has increased form 2.42 to 11.5 V/m by utilizing an FSS superstrate with unit cell's dimension of $a = 0.72$ μm $r = 0.27$ a and $h = 0.19$ a at a height of 0.23 μm above the photomixer. The results are presented in Figure 4.35, where it can be noted

that approximately same enhancement factor has been achieved compared to the LT-GaAs photoconductive layer.
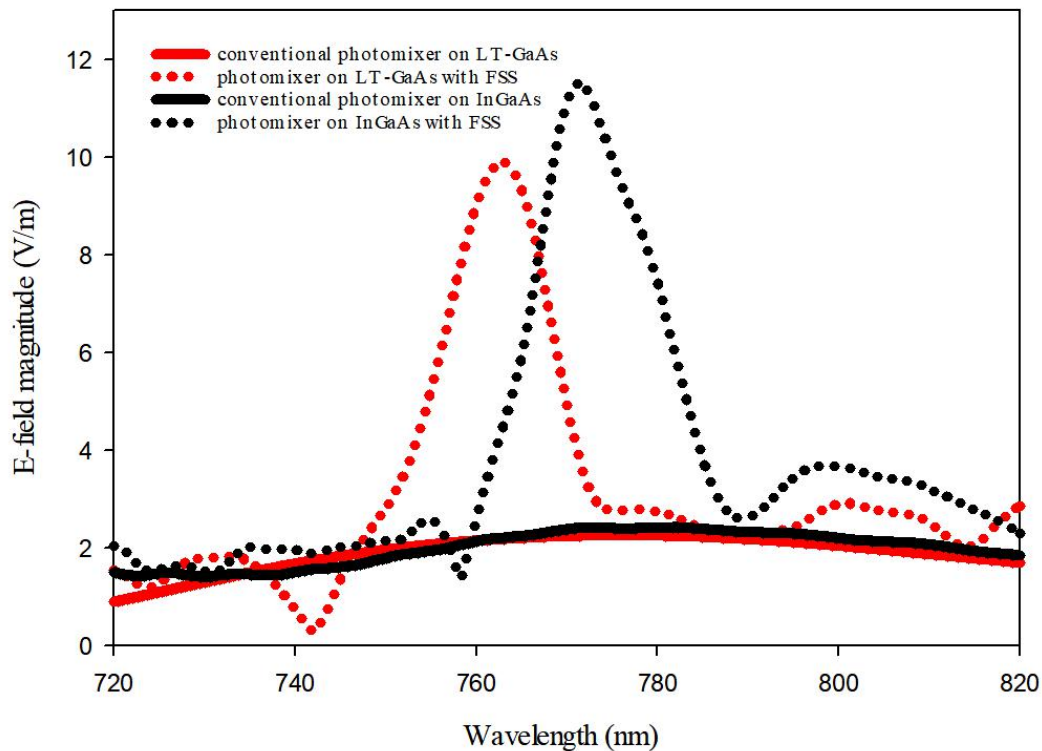

Figure 4.35: Optical E-field magnitude between the central electrodes of a photomixer on the surfaces of LT-GaAs and I GaAs photoconductive layers.

4.5 Summary

Various methods of improving the local electric field on the surface active region, hence, improving the generated THz power have been proposed in this chapter. It has been demonstrated that, optimizing the configuration of the photomixer electrodes can improve the localised electric field slightly, however, the source capacitance of photomixer has changed accordingly. Then, plasmonic material was introduced to replace metal to form the photomixer electrode. In consequence, the interaction between plasmonic electrodes yields a much higher localised electric field. Next, three different photonic crystal are presented to reflect the unabsorbed laser power back to the active region. The Distributed Bragg Reflector, also known as one dimensional photonic crystal, is used to improve the generated THz power by 30%, which agreed with the result from literature. On the other hand, the multiple layered structure of DBR result in a bulky device. Two designs of two dimensional photonic crystal have been proposed. The 2D-PhC with central air hole incorporated plasmonic

photomixer achieved an enhancement factor of 6.87 by reflecting the transversal plasmonic resonance field. Moreover, the enhancement factor has been further improved to 18.4 by introducing plasmonic rods to replace the air hole within the 2D-PhC, which is because more plasmonic interactions between the plasmonic rods and plasmonic photomixer electrodes as well as between the adjacent plasmonic rods. Finally, superstrate techniques are employed to improve the illuminating electric field. Dielectric superstrate is implemented with plasmonic rods filled 2D-PhC reflector to confine the electric field within the active region of photomixer. Consequently, the generated THz power has enhanced by 256 times. Last but not least, 2D-PhC with air hole is used as dielectric frequency selective surface superstrate to be coupled with plasmonic photomixer surrounded by ground plane. The cavity created between the ground plane and FSS superstrate maximize the localised field to 9.9V/m, which corresponding to enhancement of 494. Therefore, it can be concluded that the optical-to-THz power conversion efficiency has been significantly enhanced by a factor of 494 in this chapter.

Chapter 5: Photomixer based THz Dielectric Resonator Antenna

5.1 Introduction

As has been explained previously, the investigation of the THz photomixer can be categorised into two parts, the optoelectronic part which corresponding to the optical-to-THz conversion efficiency, and the antenna design part which affect the matching as well as radiation efficiency. The optical-to-THz conversion efficiency have been studied in chapter 4, therefore, it is necessary to improve the coupling of THz wave from antenna to air as well as design a THz antenna with good antenna impedance matching.

For a THz photomixer, the excitation source is generated from the photocarrier induced within the photoconductive substrate, therefore, the dielectric substrate is indispensable for the photomixer based THz antenna. However, as shown in Figure

5.1, by using a substrate, the radiation pattern of a dipole antenna change from omni-directional to asymmetric and the enhancement is towards the substrate [127]. Back lens is a common and well studied method to alleviate the substrate effect and couple the THz wave to air [128, 129]. However, lens not only bulk the devices but also require high spatial alignment. Therefore, in order to overcome the drawback caused by substrate effect and avoid using bulky lens, the idea of truncating photoconductive substrate to construct a dielectric resonator antenna (DRA) has been introduced. 40% or less radiation efficiency can be achieved by a dipole antenna above a thick dielectric substrate [130]. On the other hand, since there is no surface waves and ohmic losses for DRA, the radiation efficiency can be enhanced considerably.

(a)

(b)
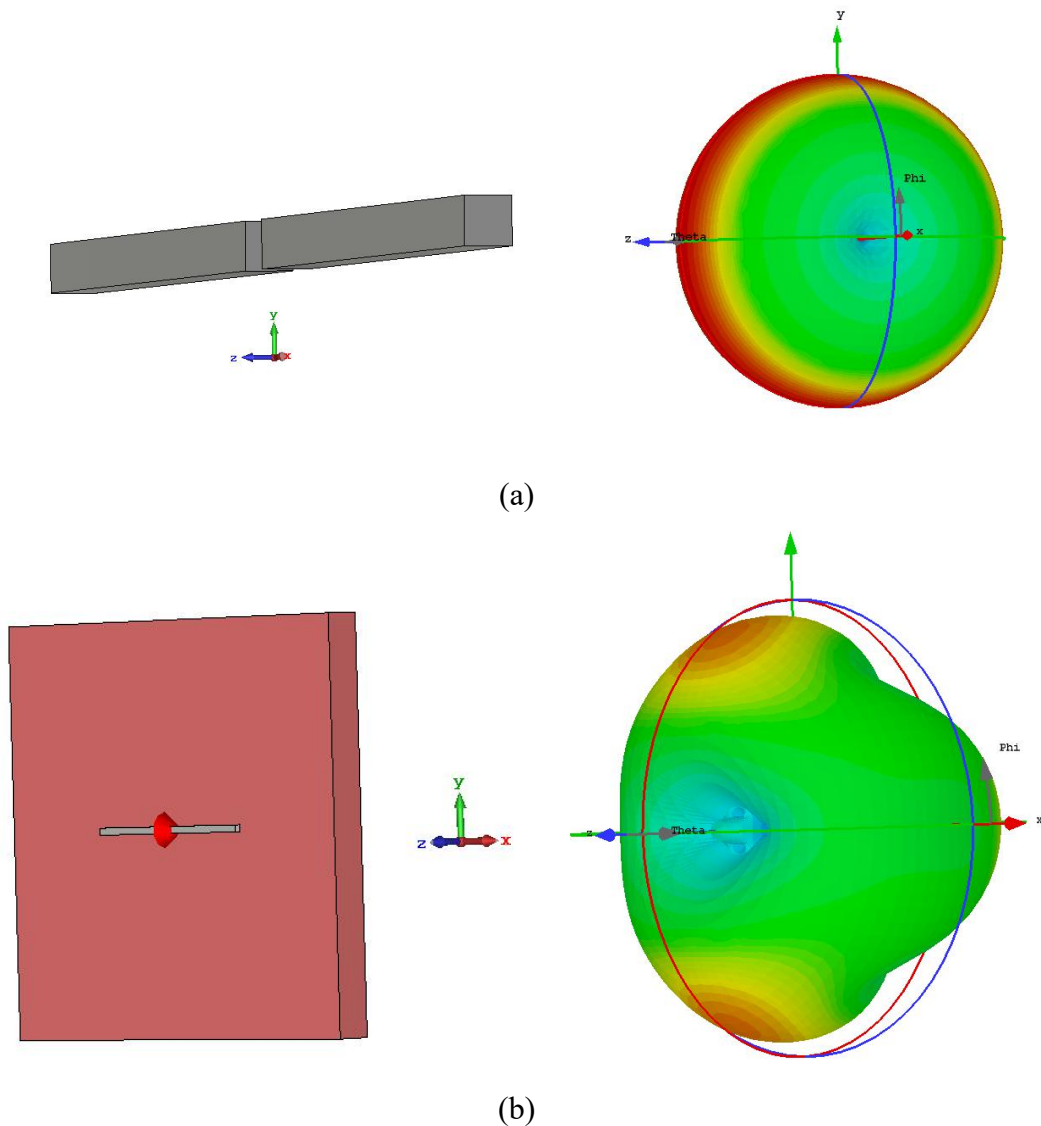
Figure 5.1 (a) Dipole antenna in air and its radiation pattern (b)Dipole antenna on a GaAs substrate and its radiation pattern

Moreover, it has been highlighted and analysed in chapter 2 that, the source impedance is another main challenge of THz antenna design. Unlike RF/MW antenna which connect to a constant 50Ω or 75 Ω input, the source impedance of THz photomixer affected by many parameters as explained in section 2.3.3. It has been proposed that choke filter can be implemented with many type of antennas to improve the matching efficiency, such as dual dipole and slot antenna [131], four-leaf-clover-shaped antenna [132], and Yagi antenna [133].

Therefore, dielectric resonator antenna driven by photomixer with 2D-PhC and optical dielectric superstrate coupled dipole and dielectric resonator antenna driven by photomixer with optical FSS superstrate coupled slot will be presented in this chapter. Then, the chock filters are designed accordingly to improve the matching efficiency of the THz DRA. Finally, the antenna gain will be further improved by proper designed dielectric superstrate. In this case, the antenna resistance and radiation pattern will be studied for each design.

5.2 Dipole Fed Photomixer based THz Dielectric Resonator Antenna

In this section, the photomixer proposed in section 4.4.1 is assumed to be the source of the THz DRA. According to the analysis in chapter 2, this photomixer has approximately 10kΩ source resistance and 3 fF source capacitance. The proposed geometry is illustrated in Figure 5.2, in which the photomixer is assumed to be mounted on a dielectric resonator antenna and placed between the dipoles. The dielectric resonator antenna is truncated from the thick LT-GaAs photoconductive substrate, therefore, its relative dielectric constant is 12.9. The dimensions of the DRA resonant at 1 THz is chosen as L_w =435μm and L_h=155μm. Moreover, the DRA is driven by a dipole antenna with following dimensions: length d_l=45μm, width, d_w=5μm, thickness of 1μm and central gap of d_{gap}=5μm that accommodates the photomixer. It should be noted that in order to model this photomixer, lumped component with 3fF in parallel with the discrete port with 10kΩ impedance are used. They are placed in the gap that used to accommodate photomixer, and dipole antenna is connected by the them in the model.
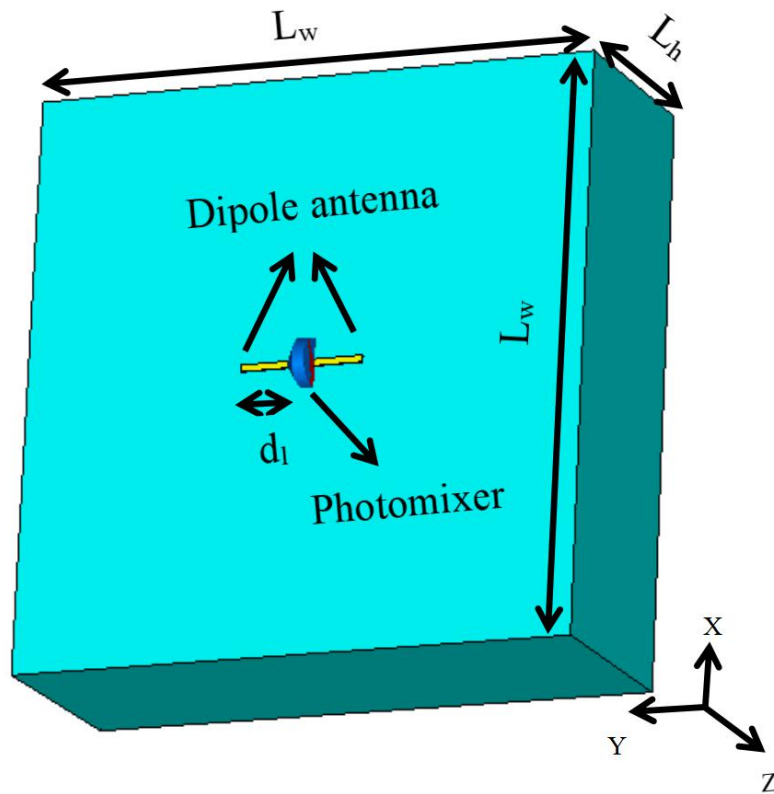
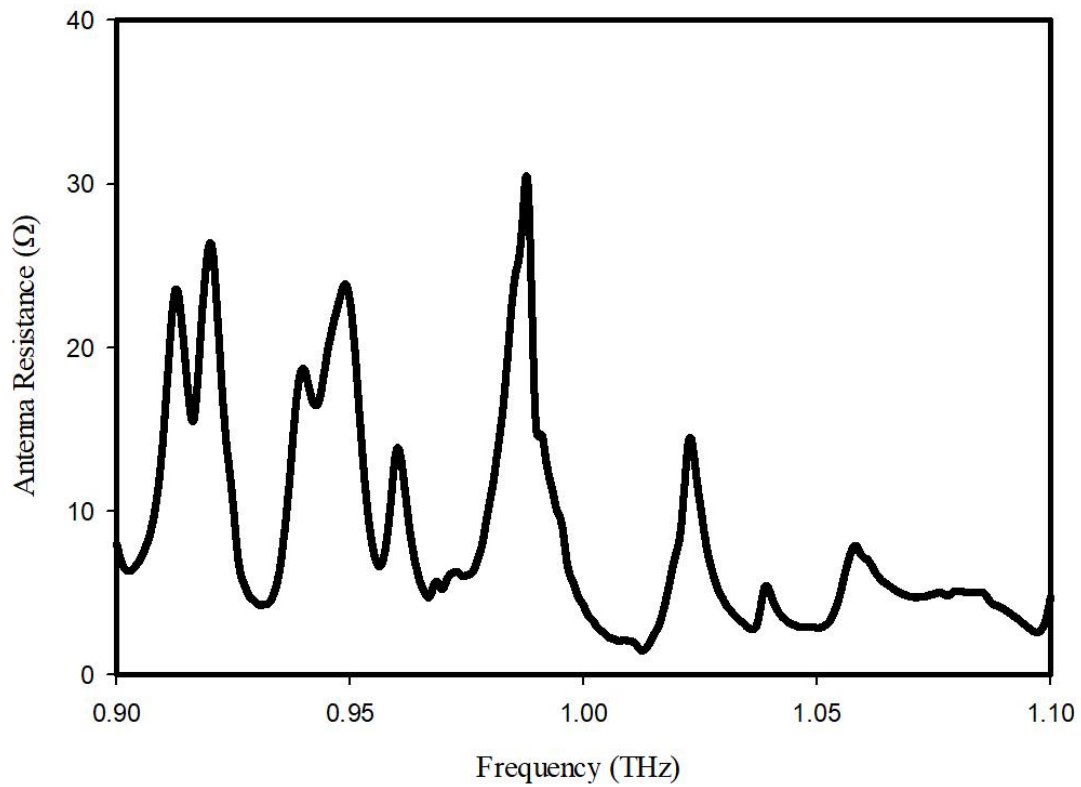Figure 5.2: Geometry of the dipole fed DRA

Figure 5.3: Antenna resistance of photomixer based dipole fed DRA

The antenna resistance has been shown in the Figure 5.3, where it can be noticed that it is too low to match the 10kΩ source resistance caused by the photomixer. In addition, as suggested by the equation (2.13), the optical-to-THz conversion efficiency has roll-off of $\frac{1}{1+\Omega R_{antenna}C_{electrode}}$, hence, its is necessary to minimize the capacitance.
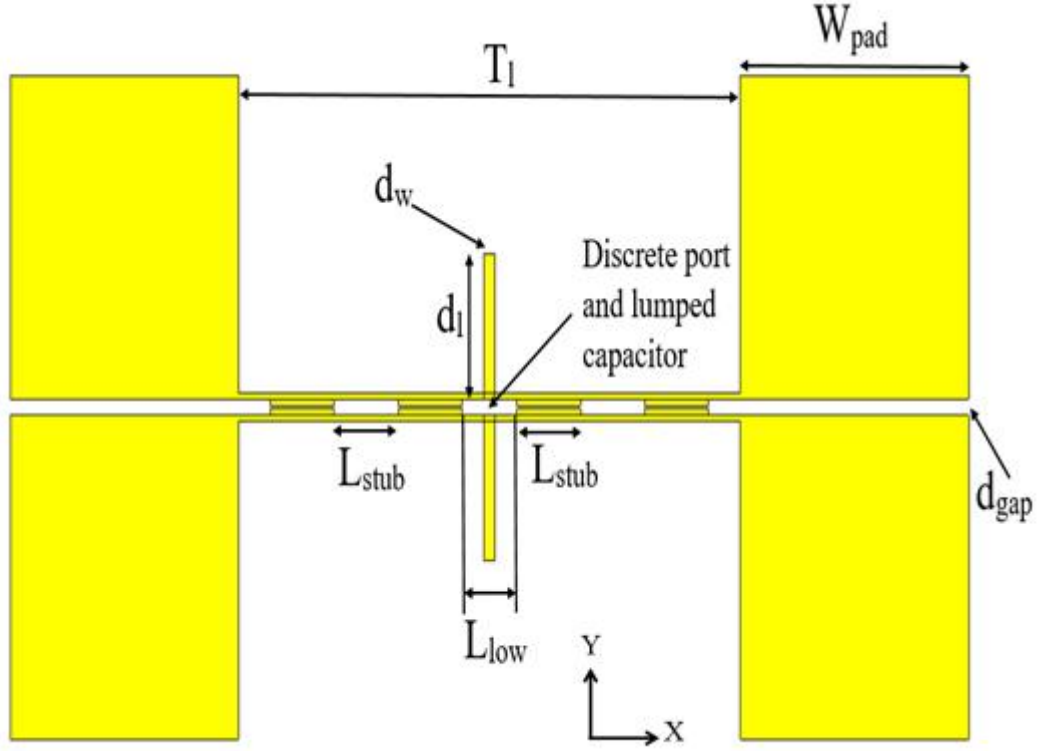

Figure 5.4: Top view of the choke filter and DC pad that connected to the feeding dipole

The choke filter has been introduced to eliminate the source capacitance by applying terminal effect on the power generation [131]. The dimensions of the proposed choke filter and the DC bias pad that connected to the feeding dipole are illustrated in Figure 5.4, and all of these networks are mounted on the GaAs DRA. The gap at the centre with length of L_{low}=38μm offers inductive capacitance that can be used to offset the capacitance from photomixer. Consequently, the generate higher THz power. Moreover, the repetitive stubs with length of $L_{stub} \approx \lambda_{eff}/4$ and the transmission line with length of $3\lambda_{eff}/4$, offers very low impedance (virtual ground) at the point where the stub is attached. In contrast, at the other end of the transmission line, the THz signal experience high impedance (open circuit). Therefore, the antenna resistance has been improved from 4.2 Ω to 436Ω by using the choke filter as shown

in Figure 5.5, and the corresponding matching efficiency increased from 0.16% to 16%. Furthermore, the generation of THz wave from photomixer requires a DC bias voltage, in this case, DC bias pads are connected at the end of transmission line. Therefore, it is possible that the generated THz power leak out through the transmission line. Transmission line with proper designed stub can be used as a choke filter to reflect the THz signal leakage as shown in Figure 5.6. The reflection coefficient of the choke filter is demonstrated in Figure 5.7 by using two waveguide port at each side of transmission line with propagation normal toward each other. This reflection coefficient demonstrate the ratio between reflected power and the input power of choke filter, from which it can be noticed that the stopband of proposed choke filter covers 1THz.
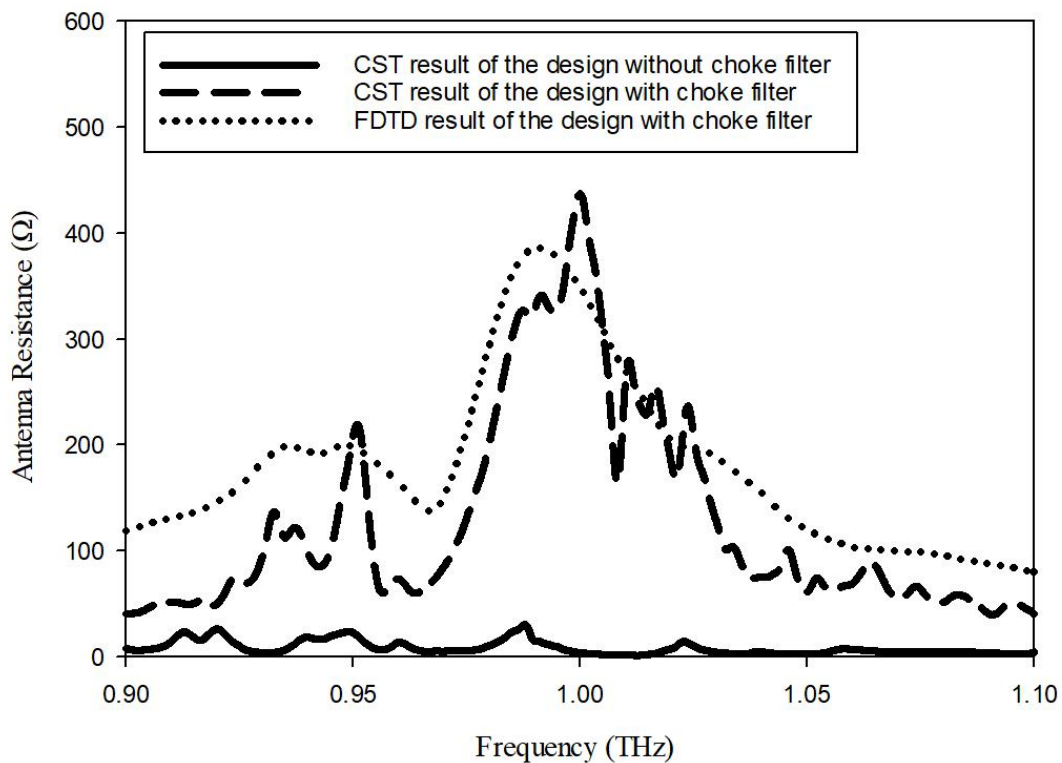
Figure 5.5: Antenna resistance of photomixer based dipole fed DRA with and without choke filter
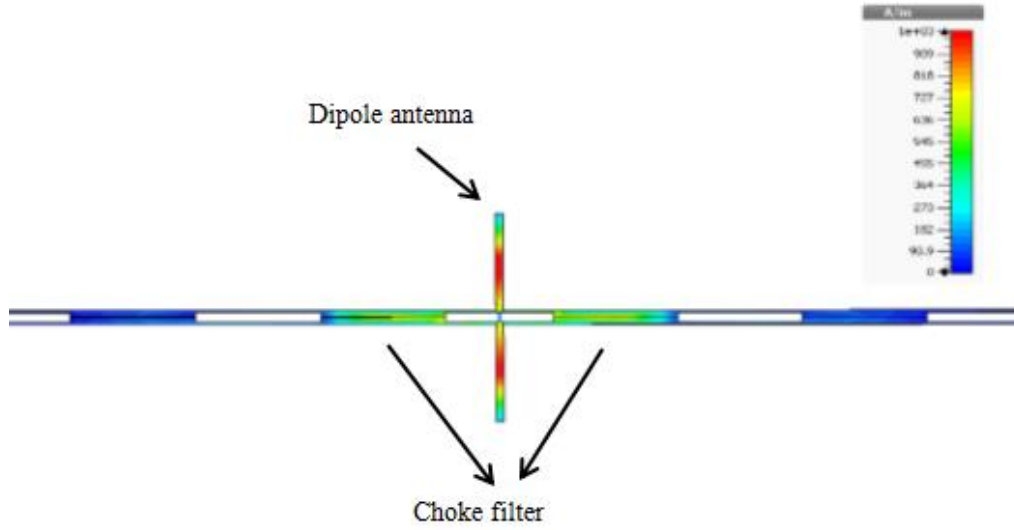
Figure 5.6: Surface current on the choke filter and dipole antenna

(a)

(b)
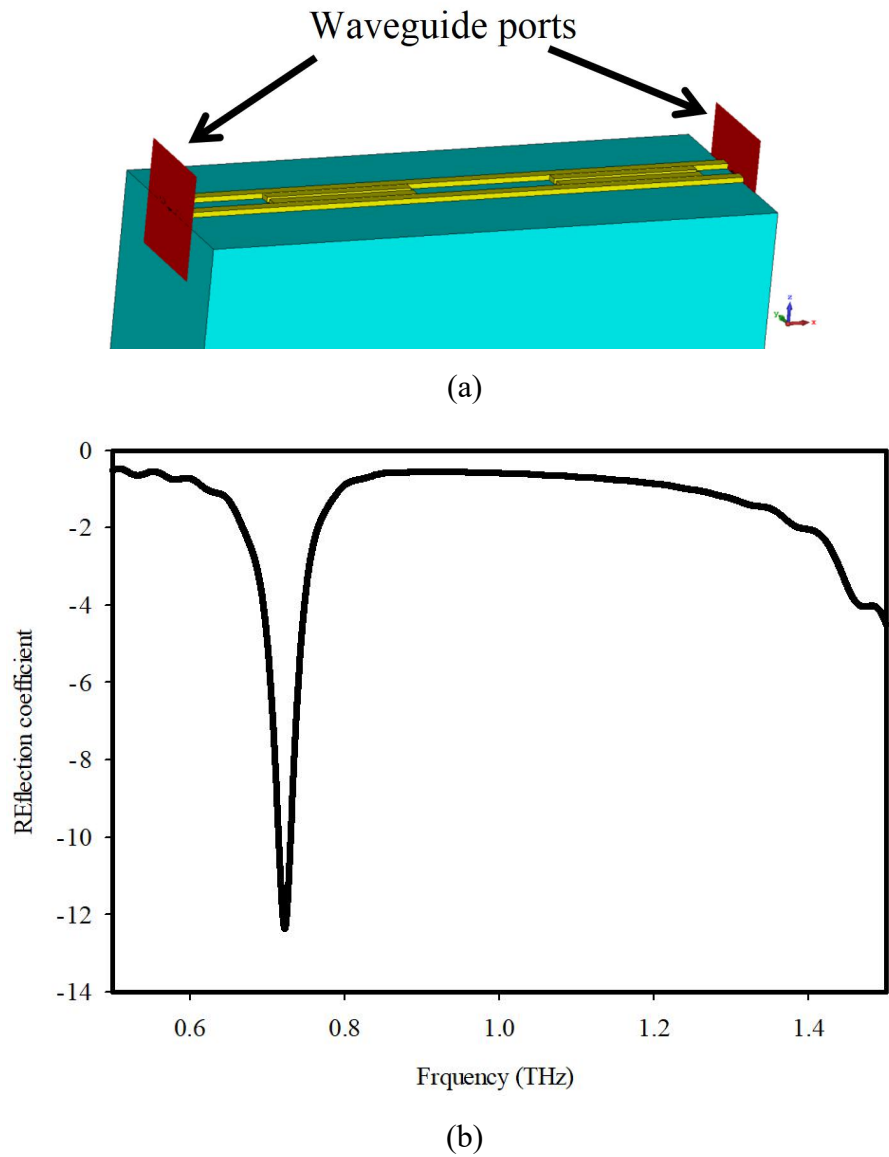
Figure 5.7 Reflection coefficient of the choke filter for dipole fed DRA

Though, choke filter optimized the source capacitance and antenna resistance as well as eliminated the leaking signal, the drawback of higher ohmic losses caused by is inevitable. It can be noticed from Figure 5.8 that, the broadside gain at Z direction of DRA reduced from 10.7dB to 7.55dB by implementing choke filter network.
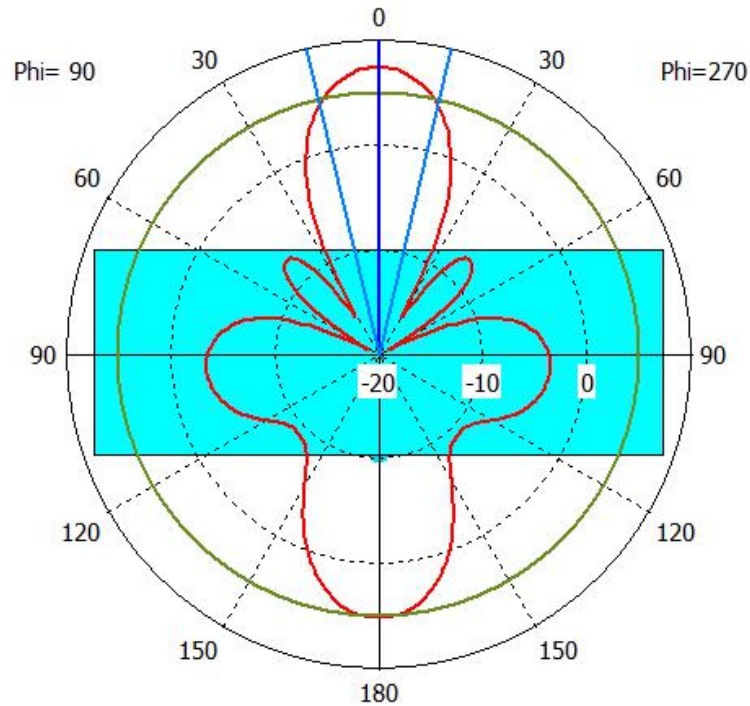
(a)
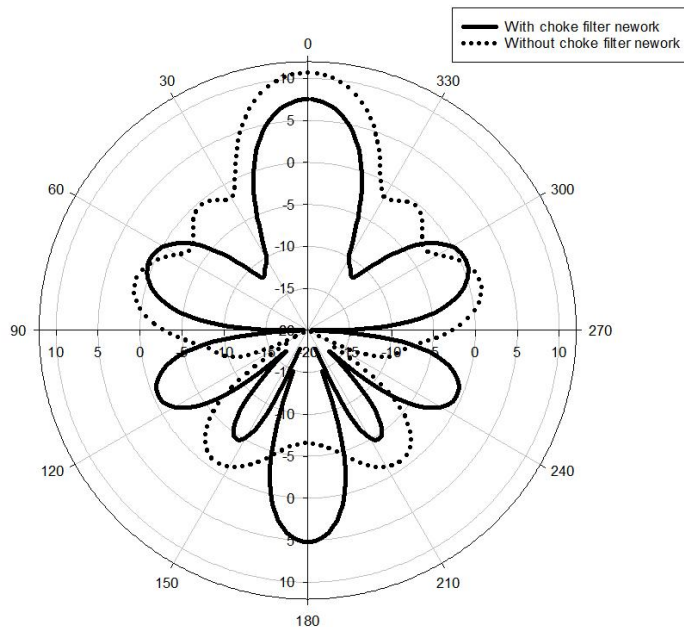
(b)

Figure 5.8: Radiation pattern of photomixer based dipole fed DRA (a) with the structure (b) with and without choke filter network

In order to optimize the radiation efficiency of the proposed DRA, a GaAs dielectric superstrate is employed as shown in Figure 5.9. Since the maximum enhancement can be achieved at $h=(0.25\times((\varphi_1+\varphi_2)/\pi))+0.5)\lambda$ [134], where φ_1 and φ_2 are the reflection phase of antenna and superstrate, λ is the desired wavelength, the distance between the DRA and superstrate is chosen as 65μm. The radiation pattern of dielectric superstrate coupled DRA is shown in Figure 5.10. It can be seen that the broadside gain of the proposed DRA have been optimized from 7.25dBi to 10.18dBi. It should be noted that the bandwidth can be improved by employing dielectric superstrate [130]. All the parameters illustrated in Figure 5.2, 5.4 and 5.9 are listed in Table 5.1.
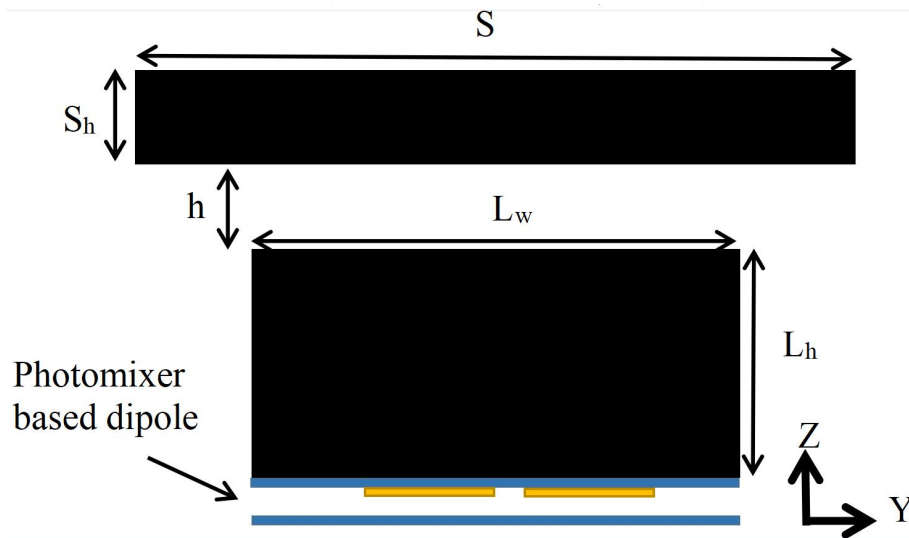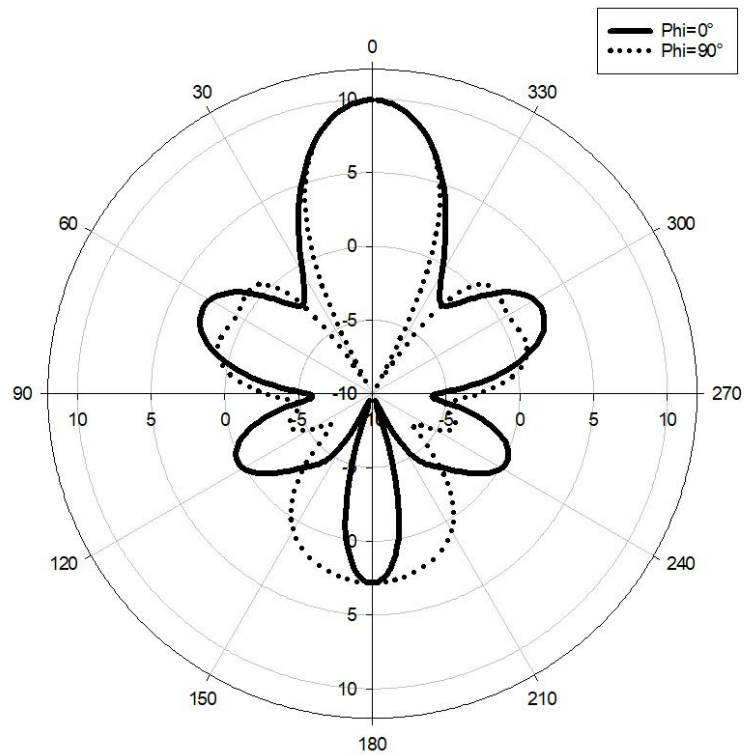

Figure 5.9: Configuration of photomixer based dipole fed DRA with dielectric superstrate
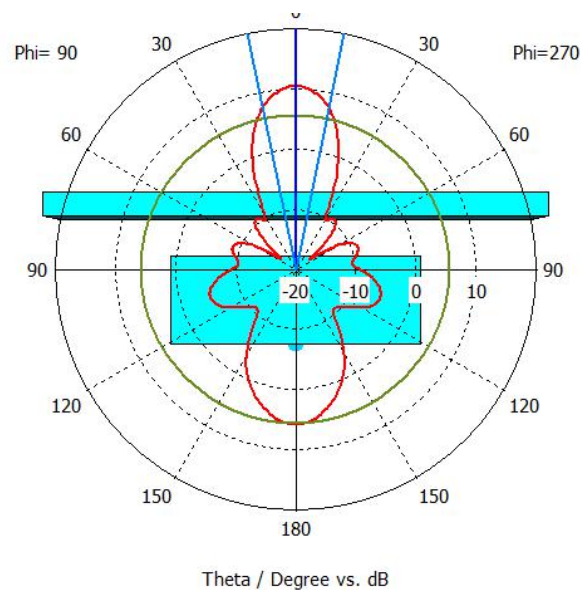
(a)
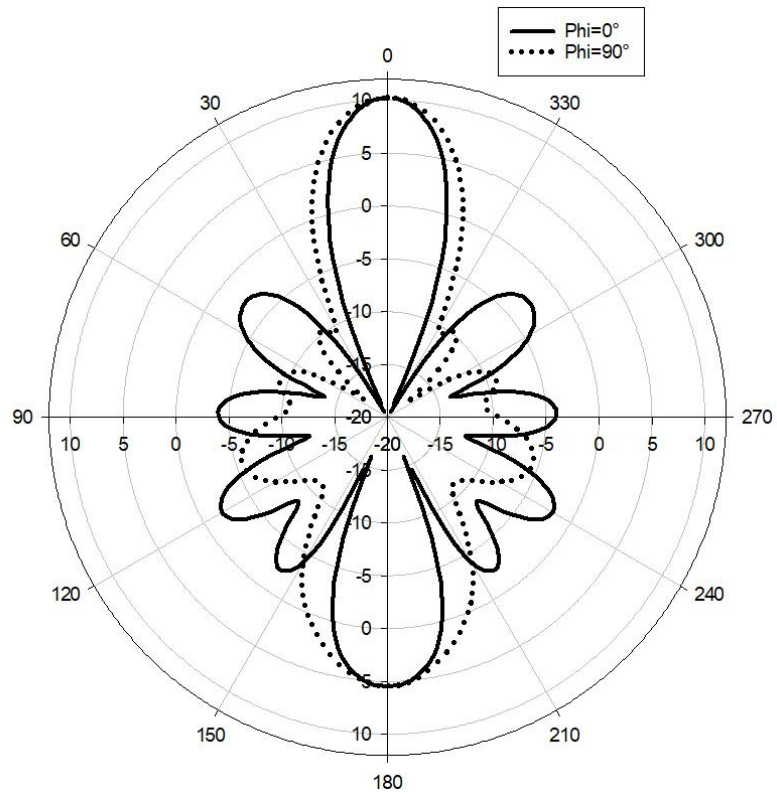
(b)

(c)

Figure 5.10: The far field radiation pattern of proposed DRA with superstrate (a)
the with structure (b) from CST (c) from FDTD

Table 5.1: Parameters of photomixer based dipole fed DRA with dielectric superstrate

Parameters	Values
L_w	435μm
L_h	155μm
S_h	41μm
S	870μm
h	65μm
d_l	45μm
d_w	5μm
d_{gap}	5μm
T_l	220μm
T_w	2μm
L_{low}	28μm
L_{stub}	28μm
W_{stub}	2μm
W_{pad}	100μm

5.3 Slot Feed Photomixer based THz Dielectric Resonator Antenna

In this section, the photomixer introduced in section 4.4.2 is considered to be the power source of the DRA. Since a groundplane with central slot which is used to accommodate the photomixer is offered by the design, the proposed DRA will utilizing slot feeding. Slot feeding can be recognized as a short magnetic dipole, and DRA operating at higher order mode can be recognized as a magnetic dipole array, where the mode number indicate the number of equivalent short magnetic dipoles within the DRA. Therefore, DRA truncated from the photoconductive substrate can not only avoid using bulky lens but also yield a high antenna gain. It is worth to mention that, the width to height aspect ratio of truncated DRA should be greater than 3 for the fabrication purposes. The configuration of the proposed slot fed DRA is illustrated in Figure 5.11. The optical FSS and photomixer located at the back of DRA

will not impact the performance of the antenna, since they are design in the scale of optical wavelength, they are invisible for the THz spectrum. In order to generate photocurrent from photomixer, bias voltage should be applied. However, the DRA is implemented on gold ground plane, there is no sufficient space for a bias pad. In this case, the ground plane is separated by a narrow slot that extended from the ends of central slot feeding as shown in Figure 5.12, hence, two separated ground planes are used as biasing pad. Then, as explained in previous section, choke filter is applied to eliminate source conductance, prevent from power leakage and optimize the antenna resistance. The reflection coefficient of the choke filter is depicted in Figure 5.13, where a stop band between 0.6THz to 1.1THz has been offered. Finally, a GaAs dielectric superstrate shown in Figure 5.11 is utilized to compensate the drawback of low radiation efficiency caused by choke filter network. All the parameters introduced in Figure 5.11 and 5.12 are listed in Table 5.2.
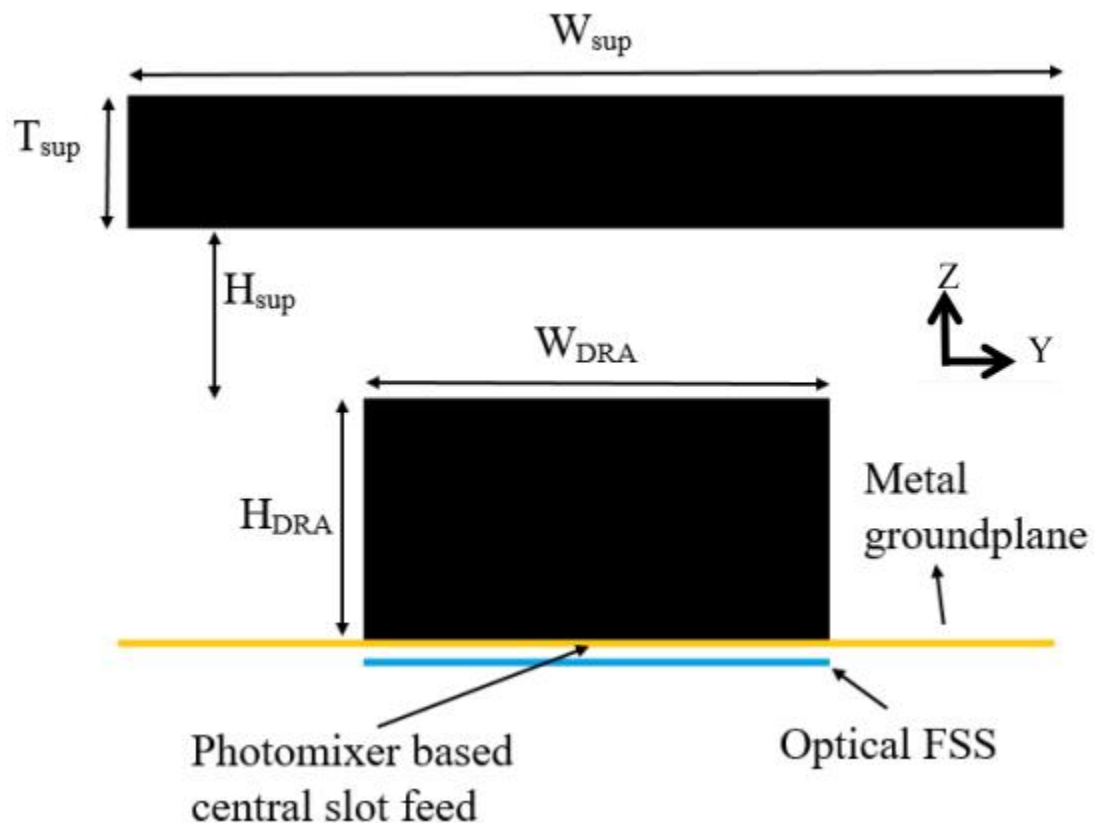
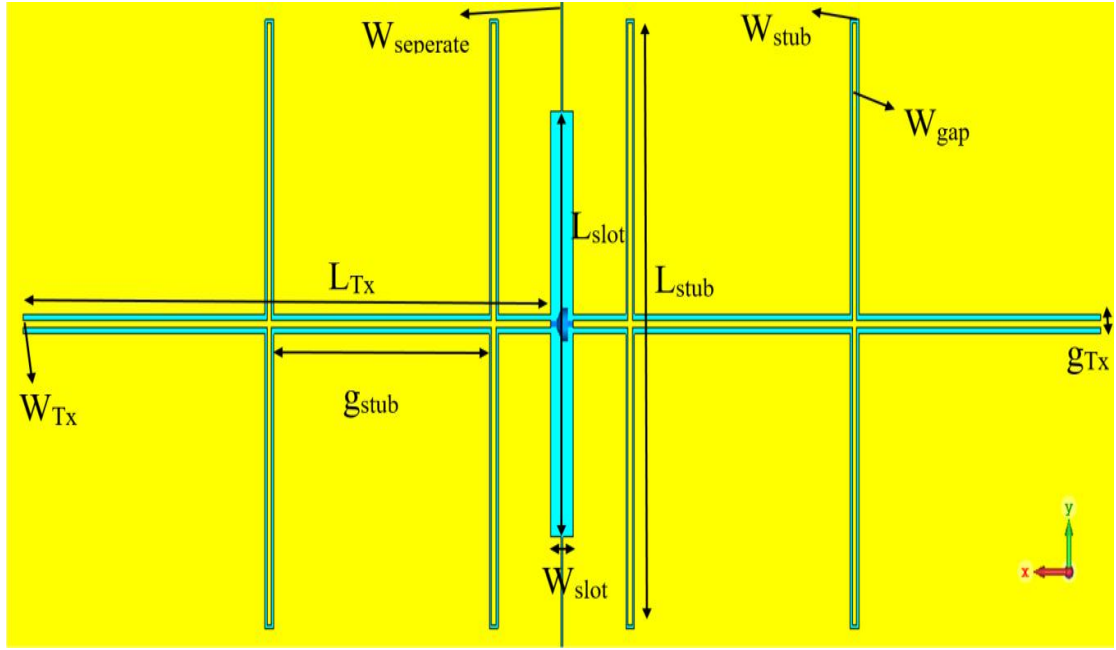Figure 5.11: THz slot fed DRA and superstrate

Figure 5.12: Top view of feeding slot and choke filter network.

Table 5.2: Parameters of photomixer based slot fed DRA with dielectric superstrate

| Parameters	Values
W_{sup}	400µm
T_{sup}	60µm
H_{sup}	30µm
W_{DRA}	250µm
H_{DRA}	60µm
$W_{separate}$	0.5µm
L_{Tx}	120µm
W_{Tx}	1µm
g_{stub}	50µm
W_{slot}	5µm
L_{stub}	91µm
W_{stub}	0.5µm
W_{gap}	0.5µm
g_{Tx}	3µm
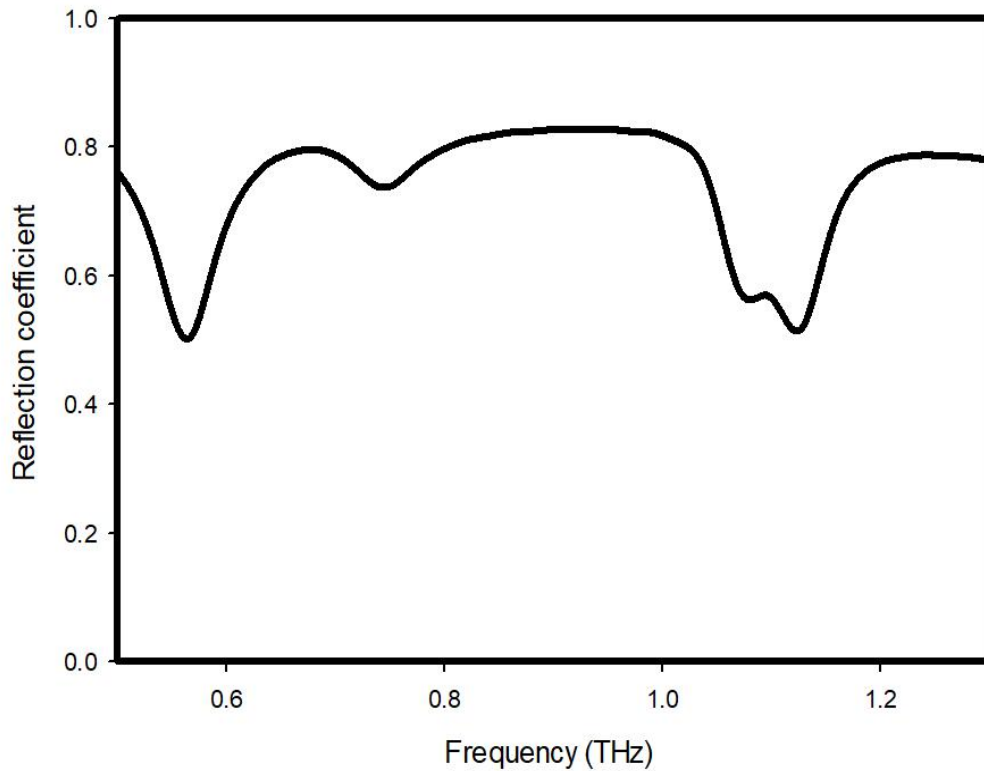
Figure 5.13: Reflection coefficient of choke filter for slot fed DRA

As mentioned in last section, the photomixer is modelled as discrete port with 10kΩ input impedance in parallel with a lumped component of 3fF. Since then, by applying choke filter, the antenna resistance improved from 430Ω to 700Ω as demonstrated by Figure 5.14. Hence, the corresponding matching efficiency has improved from 15.8% to 24.5%. Furthermore, the H field distribution within the proposed DRA is shown in Figure 5.15, it can be observed that the DRA is operating in the TE_{711} mode. The far field radiation pattern of the proposed slot fed DRA with dielectric superstrate is shown in Figure 5.16, which indicate that the broadside gain of the DRA increased to 9dBi from 6.5 dBi by employing dielectric superstrate.
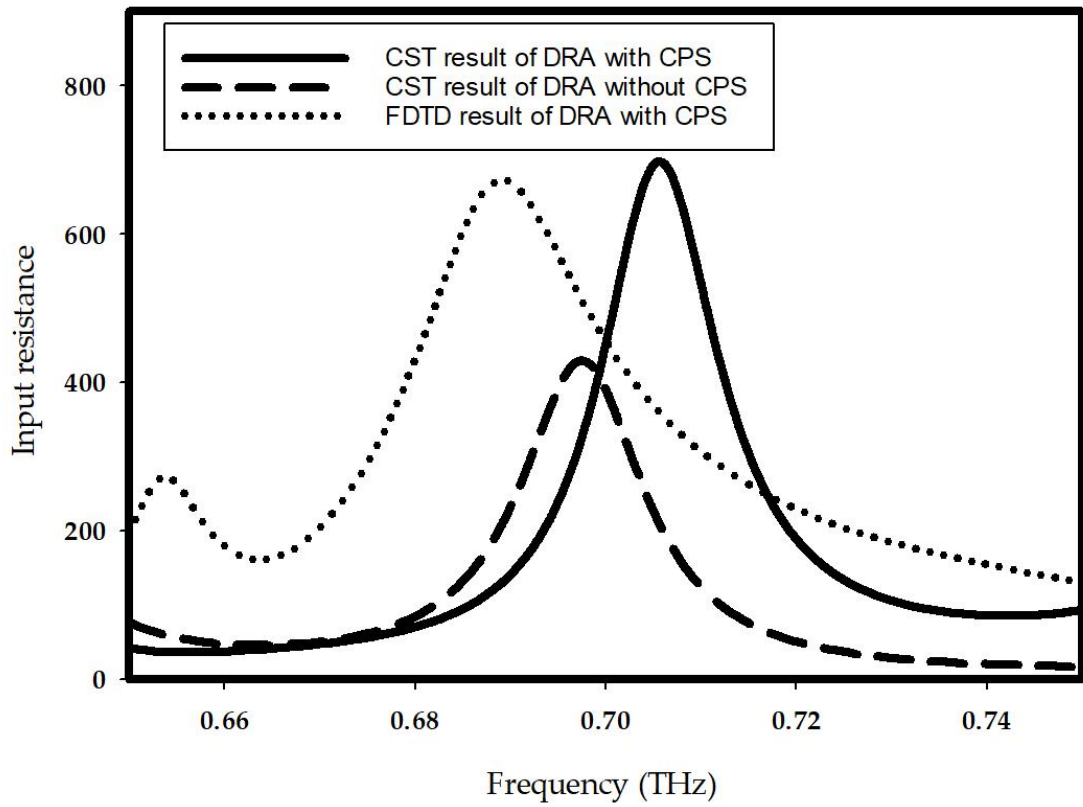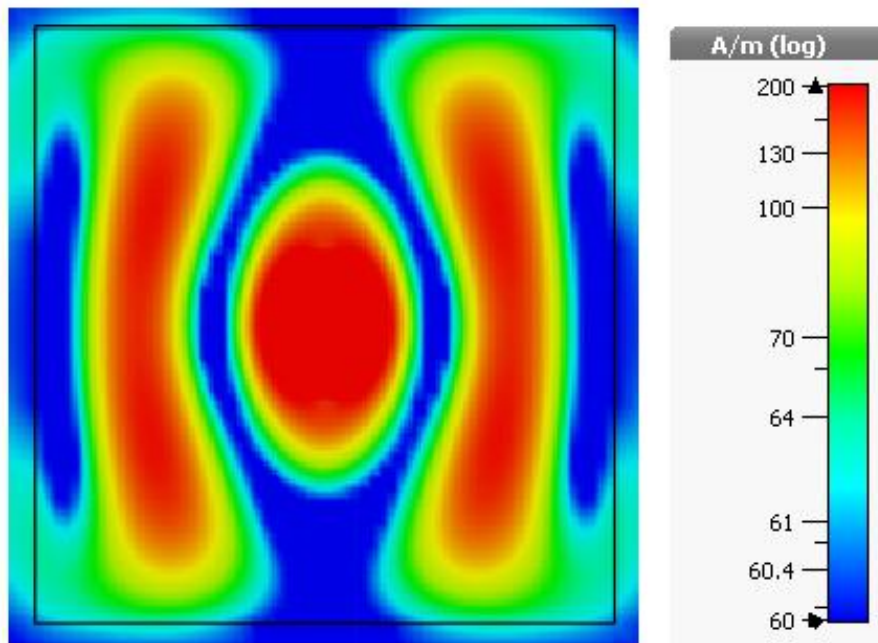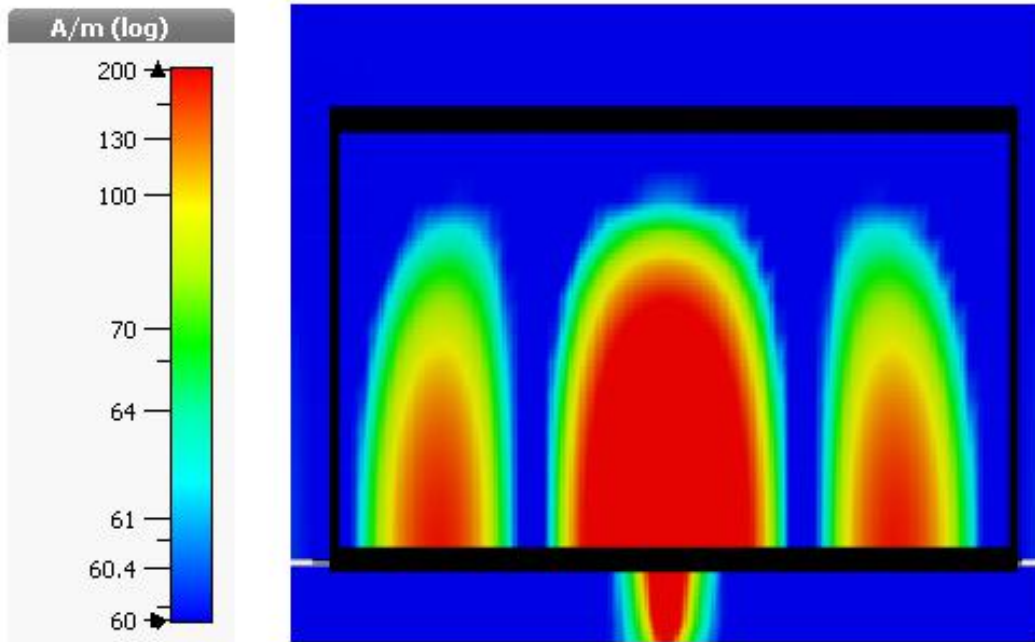
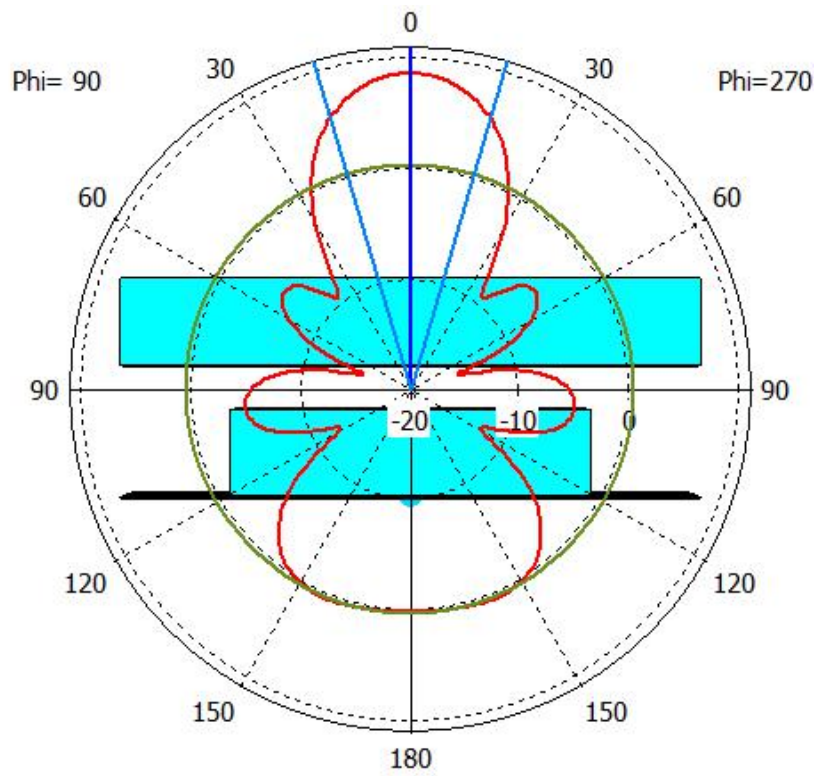Figure 5.14:Reflection coefficient of the choke filter for slot fed DRA

(a)

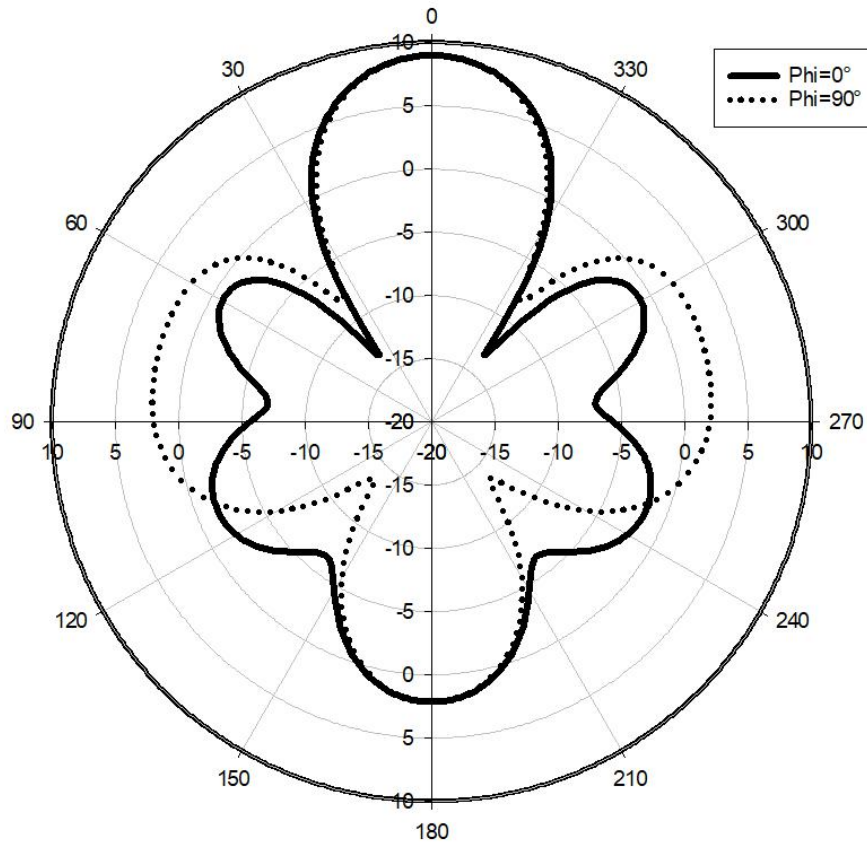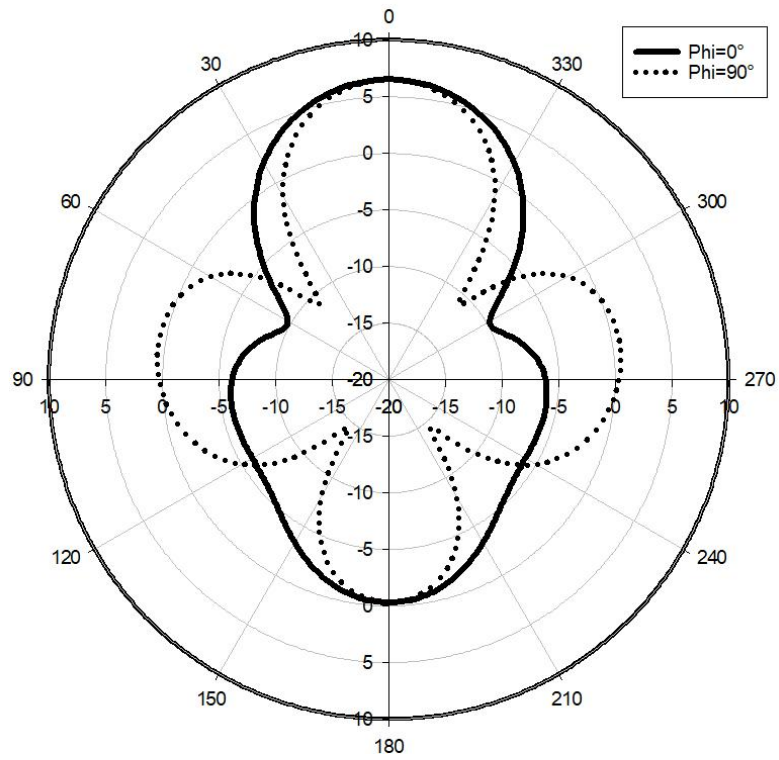(b)

Figure 5.15: H field distribution within DRA operated in TE$_{711}$ mode in (a)XY plane,
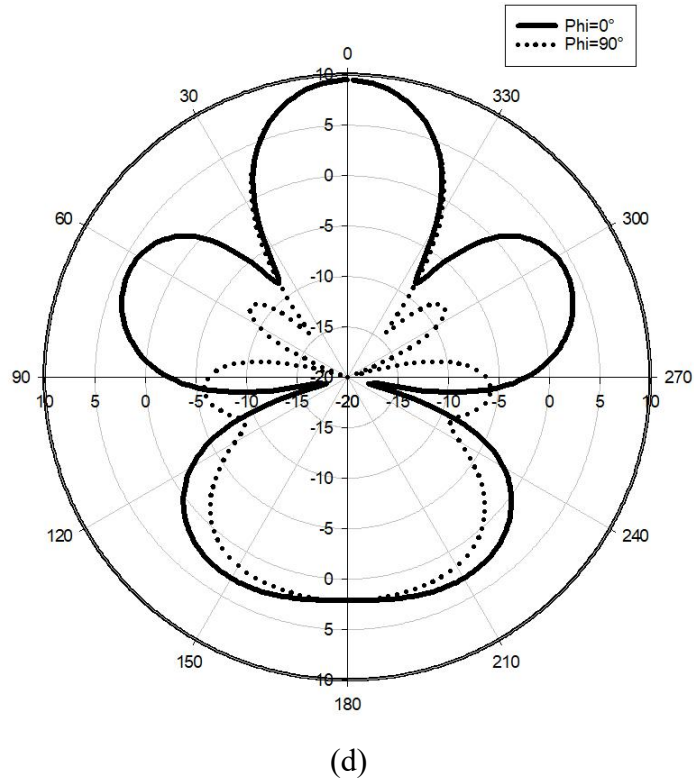
(b)XZ plane

(a)

(b)

(c)

(d)

Figure 5.16: Far field radiation pattern of proposed DRA (a) with the structure (b) with superstrate obtained from CST, (c)without superstrate obtained from CST, (d)with superstrate obtained from FDTD

The performance of the proposed design have been compared with published THz antennas and THz DRAs, and the result is summarised in Table 5.3. It can be observed that, the proposed DRA design offers higher antenna gain than the other THz DRAs with slightly larger size. However, the size of the presented DRA is much smaller than the other types of antenna, while antenna gain of them are similar.

Reference	[135]	[136]	[137]	[138]	This Work
Antenna Type	Small lens with Leaky-wave Slit Dipole Antenna	Dipole Antenna with Horn Cavity	Slot Fed stacked DRA	Patch Fed Higher Order Mode DRA	Slot Fed GaAs Substrate Truncated DRA
Frequency (THz)	0.2	1	0.13	0.34	0.7
Antenna Gain	10.3	9.07	4.7	7.9	9
DR Material/ε_r	-	-	Alumina/10	Silicon/11.9	GaAs/12.9
DR type	-	-	Rectangular	Rectangular	Rectangular
Antenna Aperture (λ^2)	1.44	4.55	0.72	0.2	0.87
Antenna Height (λ)	1.2	1.16	1.28	0.5	0.35

5.4 Summary

In this chapter, the photoconductive substrate is truncated into dielectric resonator antenna to avoid using bulky lens. Then, according to the photomixers designed in section 4.4.1 and 4.4.2, two designs of DRA that utilizing different feeding methods, dipole feeding and slot feeding, are proposed. Choke filter network is employed by both of the designs, by which source conductance is reduced, power leakage through DC bias pad is eliminated and the antenna resistance is enhanced. However, the radiation efficiency is reduced by using choke filter. Therefore, a dielectric superstrate is introduced to improve the antenna gain. As a result, the antenna resistance of dipole fed DRA increased from 4.2Ω to 436Ω by implementing choke filter, the broadside antenna gain of dipole fed DRA improved to 10.5dBi by using dielectric superstrate. Moreover, the slot fed DRA offers 720Ω antenna resistance and 9dBi broadside antenna gain by employing choke filter and dielectric superstrate, which are 430Ω and 6.5dBi with the absence of choke filter and dielectric superstrate.

Chapter 6: Multi-layered Dielectric Resonator Antenna

6.1 Introduction

As mentioned in chapter 1, in order to satisfy the demand of high data rate by utilizing THz communication technique, high gain antenna is required to overcome the environment attenuation. Dielectric resonator antenna which made of high permittivity material can offer high gain with small size and light weight [139], Meanwhile, III-V semiconductor is necessary for the optical heterodyne generation in photomixer, and the permittivity of III-V semiconductor can be manipulated by altering the composition of III-V semiconductor [140]. In this case, the idea of truncating the photoconductive substrate into a dielectric resonator antenna is introduced.

Two designs of dielectric resonator antenna that are truncated from LT-GaAs have been proposed in chapter 5. Moreover, in order to compensate the drawback of reduced radiation efficiency caused by choke filter, dielectric superstrate is employed.

However, the dielectric superstrate presented in chapter 5 is suspended in the air without any physical support which is not possible in the real life. Therefore, a multi layered DRA that combined the DRA with superstrate is proposed.

In this chapter, a multi-layered DRA with slot feeding resonant at THz spectrum is introduced. Then, by considering from the fabrication and measurement point of view, this THz multi-layered DRA is down-converted to operate at mmwave band with coplanar waveguide. Finally, the feeding network of coplanar waveguide is optimized to achieve wideband and circular polarization. In this case, the return loss, radiation pattern and axial ratio will be studied in this chapter.

6.2 THz Multi-layered DRA

A THz rectangular DRA with dielectric constant of 10 is mounted on a gold ground plane with central slot. The width and length of the slot are 140μm and 8μm, respectively as shown in Figure 6.1(a). On top of the dielectric resonator antenna, a top metal plate is used, therefore, the thickness of the dielectric resonator antenna is halved due to imagine theory. In this case, the width to height aspect ratio of DRA is greater than 3, otherwise, it is difficult to fabricate such fragile antenna. Then, the DRA is covered by a supportive coating layer with dielectric constant of 2.25. Finally, a superstrate layer with dielectric constant of 10 is placed on top of the coating layer. The configuration of the proposed THz DRA is illustrated in Figure 6.1(b). And Figure 6.2 and Figure 6.3 demonstrate the parameter studies of the return loss and broadside gain with different slot length, coating height and superstrate thickness, from which the dimensions of the multi-layered DRA are listed in Table 6.1.
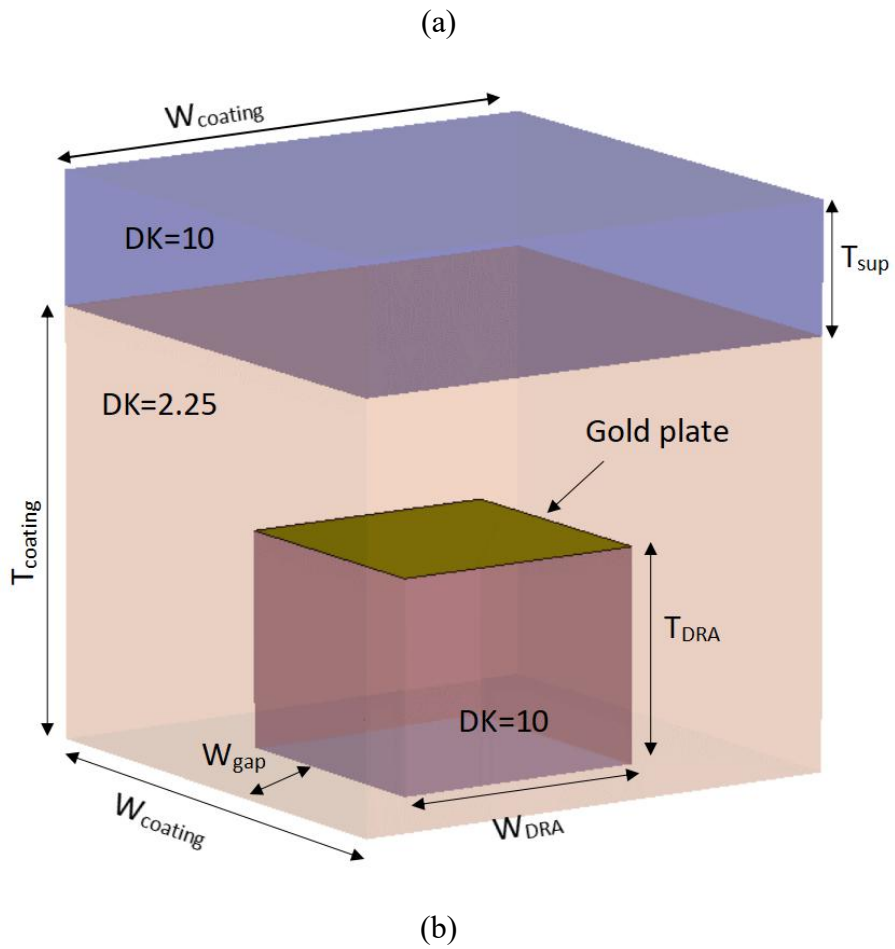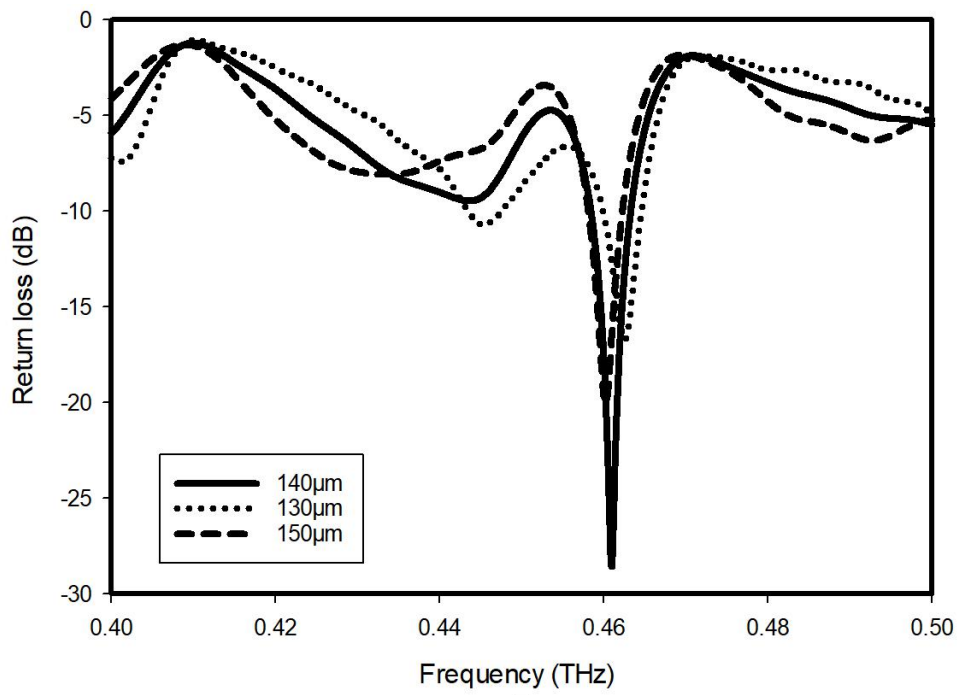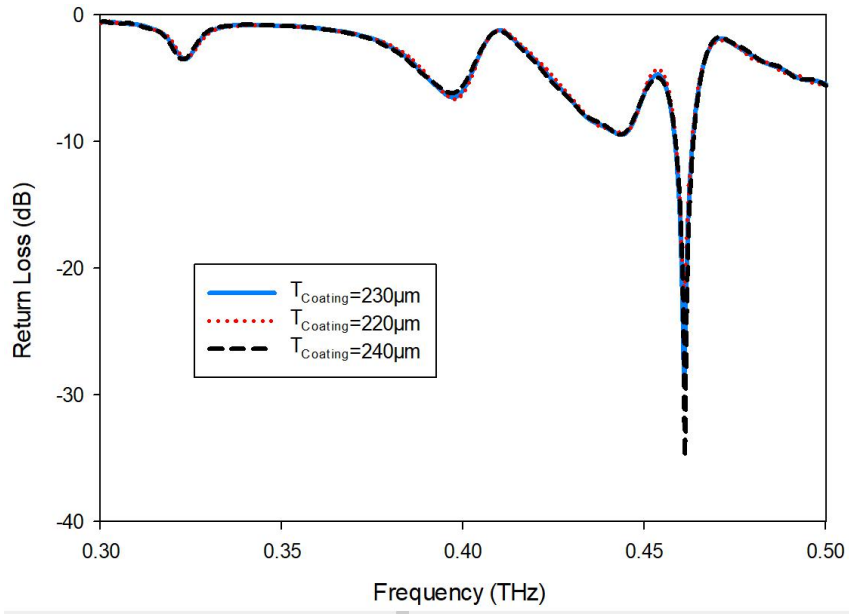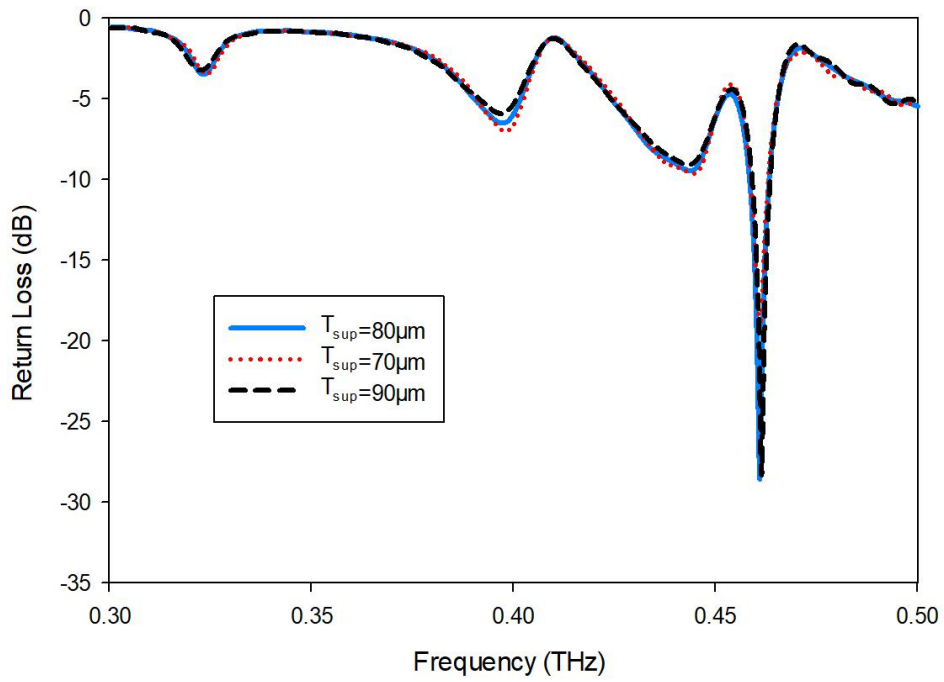

$W_{Coating}$
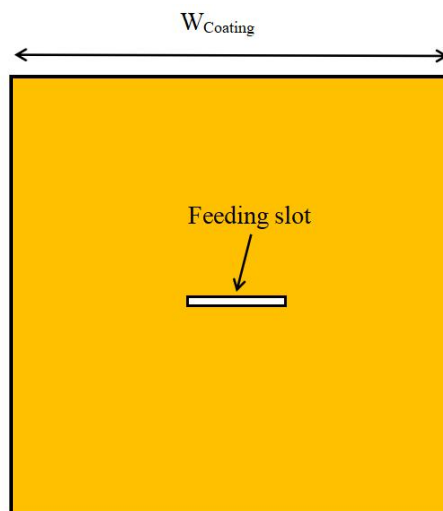
Feeding slot

Figure 6.1: Configuration of (a) ground plane and feeding slot (b) THz multi-layered DRA
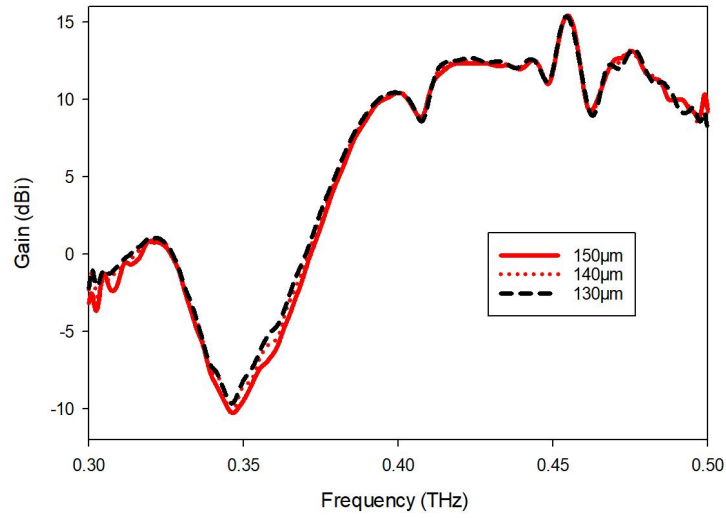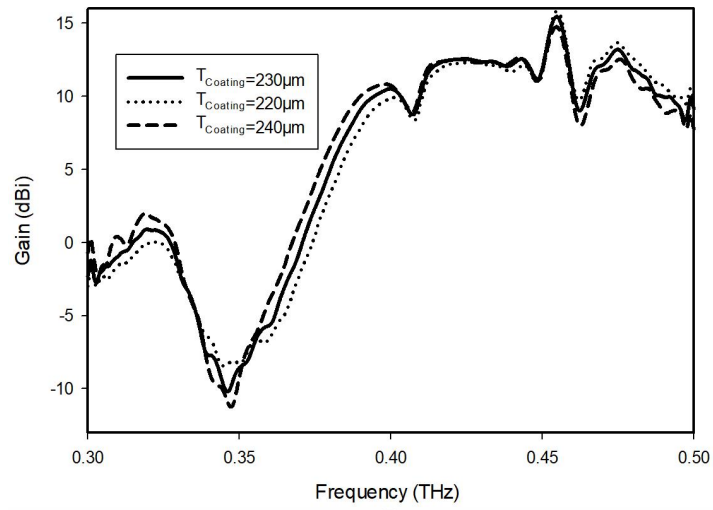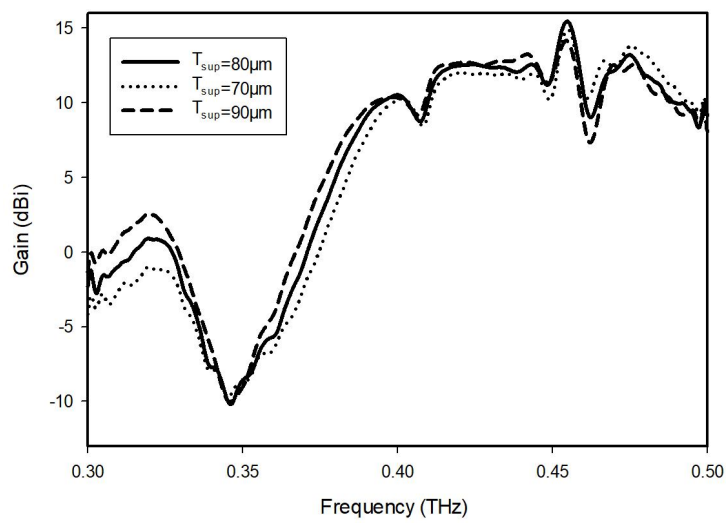

(a)

(b)

(c)

Figure 6.2: Return loss of slot fed DRA (a) with different slot lengths (b) with
different coating heights (c) with different superstrate thickness

(a)

(b)

(c)

Figure 6.3: Broadside gain of slot fed DRA (a) with different slot lengths (b) with
different coating height (c)with different superstrate thickness

Table 6.1: Dimensions of THz multi-layered DRA

Parameters	values
$W_{coating}$	1120μm
T_{sup}	80μm
$T_{coating}$	230μm
W_{gap}	280μm
W_{DRA}	560μm
T_{DRA}	120μm

As the feeding slot excited by a discrete port, the return loss of the proposed THz multi-layered DRA is illustrated in Figure 6.4, which indicate that the resonant frequency of the proposed THz DRA is 0.461THz. The XY plane cross section and YZ plane cross section of the H field distribution of the proposed DRA is illustrated in Figure 6.5. It can be noticed that the DRA operate at TE_{153} higher-order mode. Then, the far field radiation pattern shown in Figure 6.6 demonstrate that the gain of the proposed THz DRA is 14.2dBi.
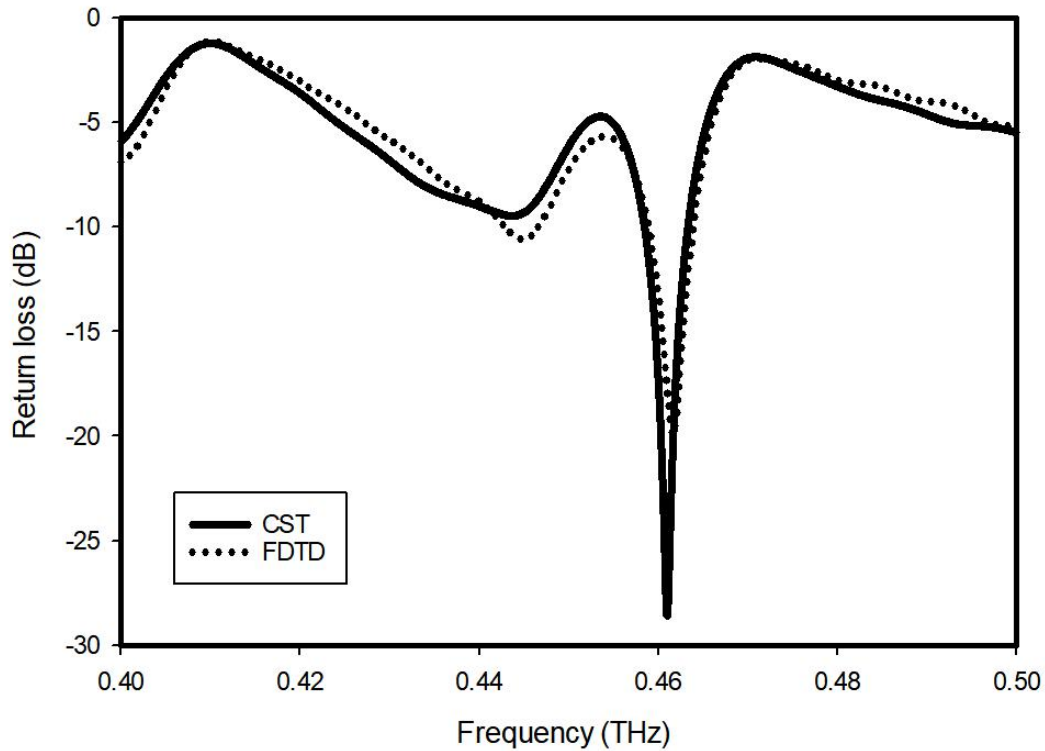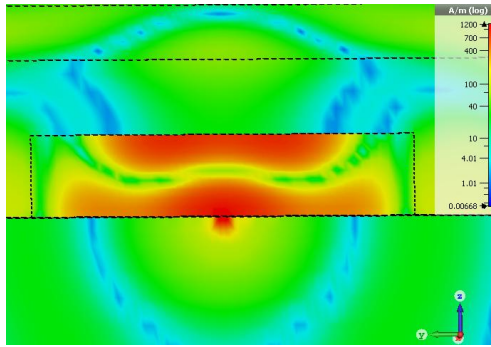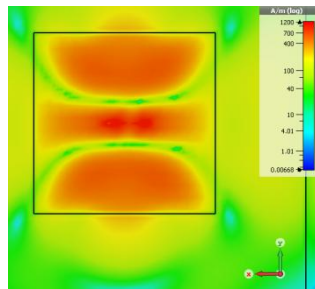

Figure 6.4: Return loss of proposed slot fed DRA with dimensions listed in Table 6.1
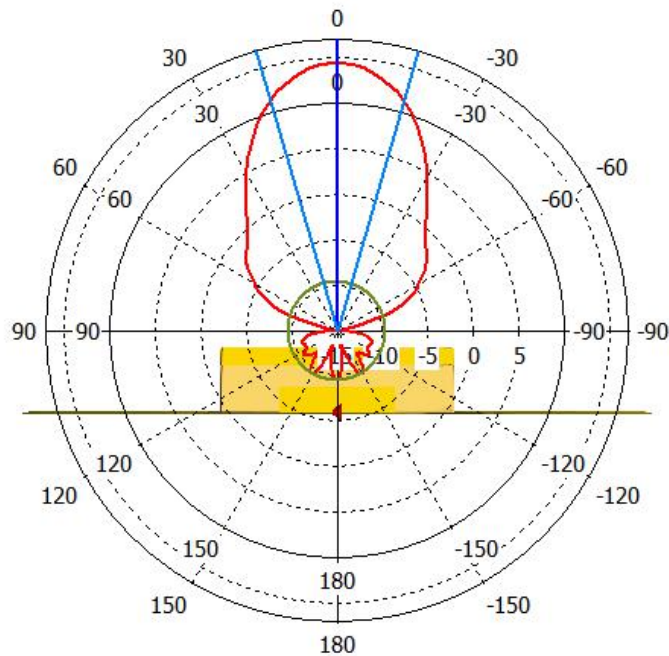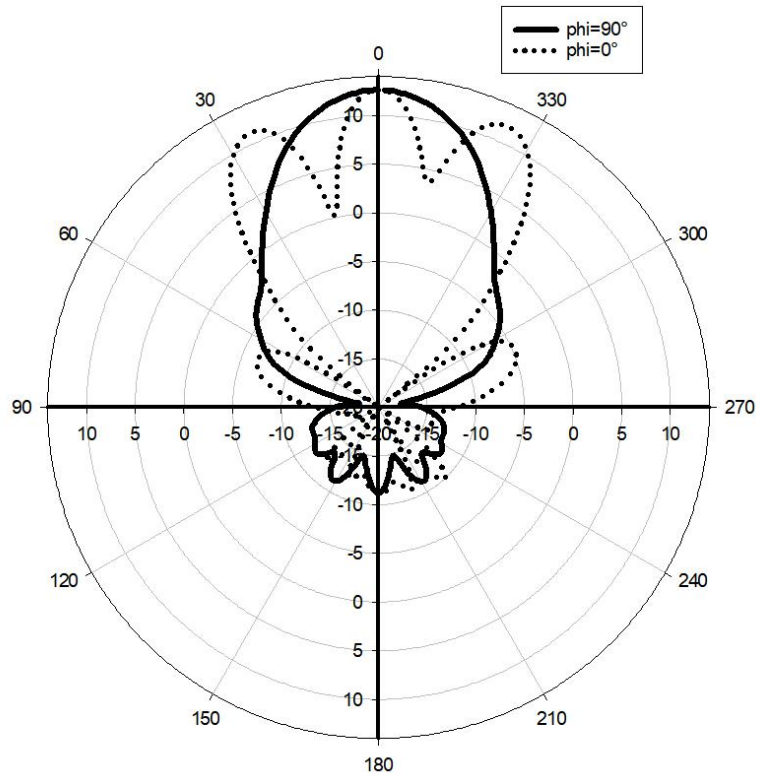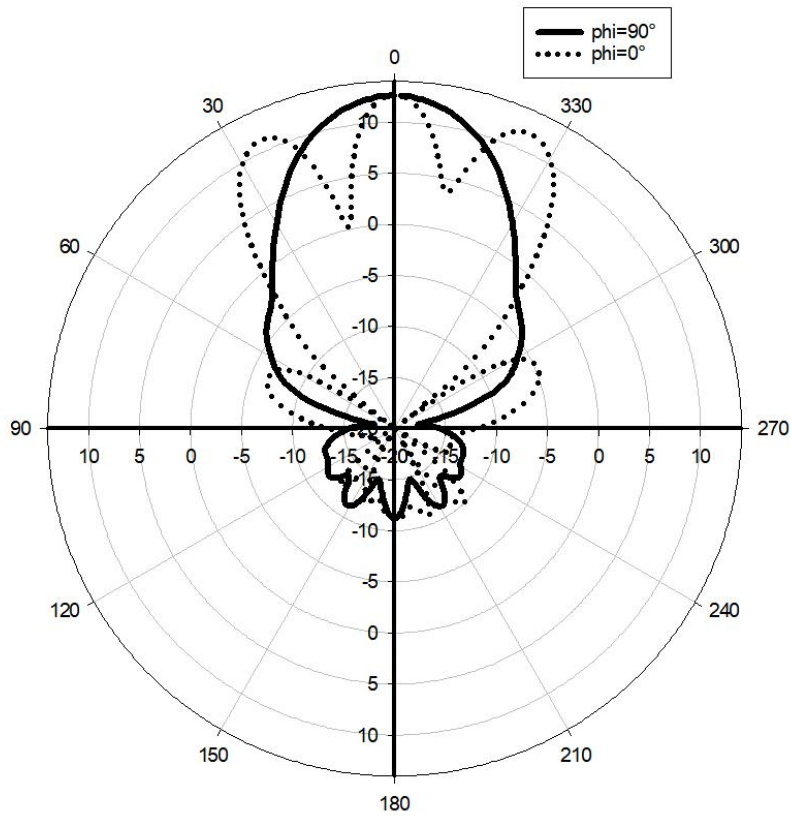
(a)

(b)

Figure 6.5 Cross section of the H field distribution of the multi-layered DRA at 0.46THz (a) YZ plane (b)XY plane

(a)

(b)

(c)

Figure 6.6: Far field radiation pattern (a) with the structure (b) from CST (c) from FDTD

6.3 Down-converted Multi-layered DRA with Wideband

The multi-layered DRA proposed in section 6.2 is down-converted to operate at millimetre wave band with wideband. The DRA is made of Si with dielectric constant of 10. The the central slot feeding is replaced by coplanar waveguide slot. Then the copper ground plane is supported by a low loss dielectric substrate with dielectric constant of 3.66. The metal plate on top of the DRA is utilised to satisfied the fabrication requirement. Then, the DRA is coated by SiO_2 with dielectric constant of 2.7 to provide physical support to the superstrate. Finally, a Si superstrate with dielectric constant of 10 is mounted on the SiO_2 coating. Hence, the configuration of mlti-layered DRA at millimetre with wideband is shown in Figure 6.7. The coplanar waveguide feeding network is illustrated in Figure 6.8.
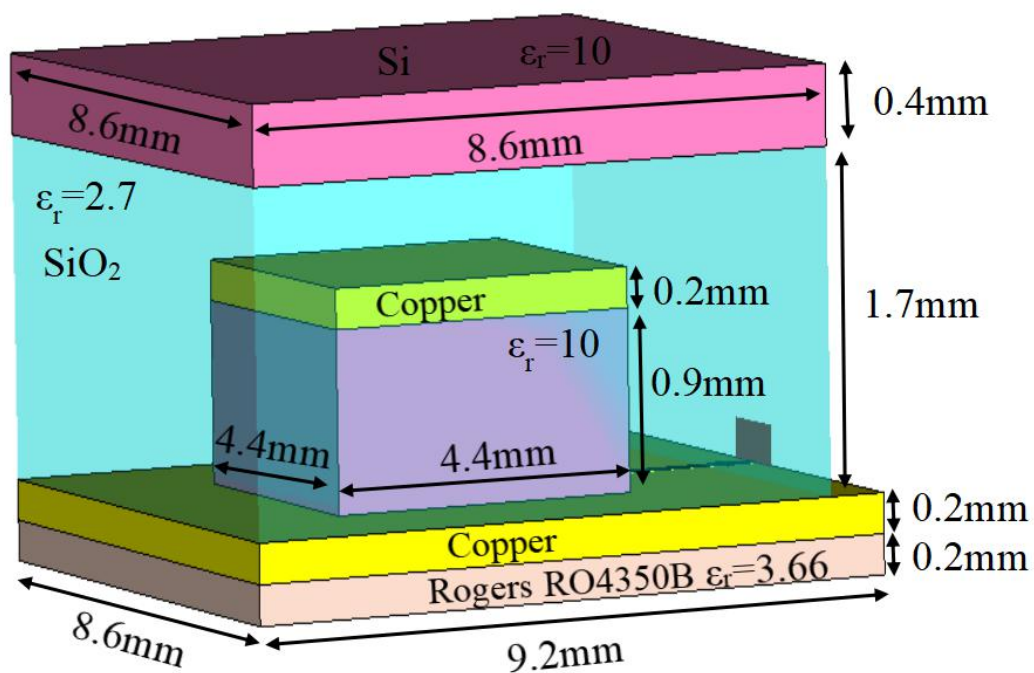

Figure 6.7: Configuration of the multi-layered DRA with wideband at millimetre band
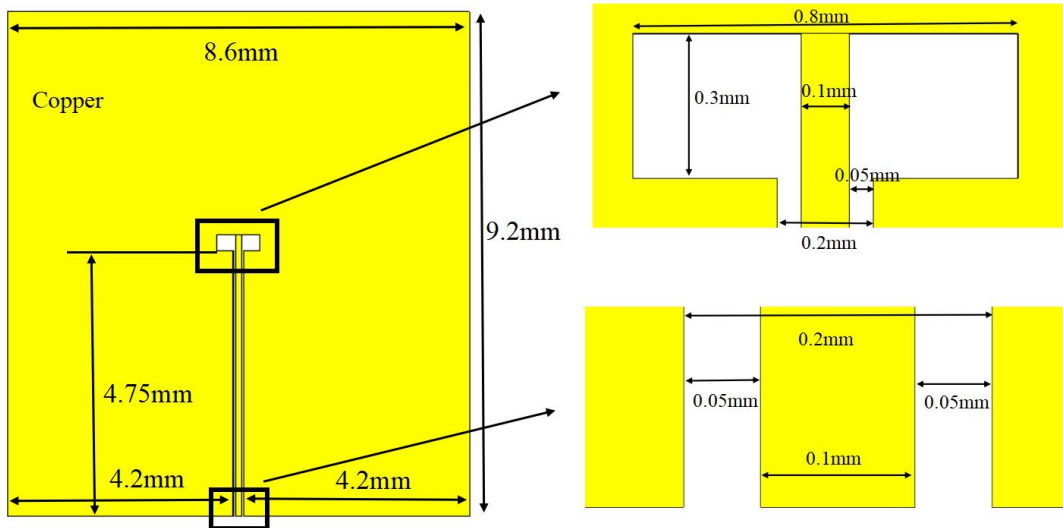
Figure 6.8: Dimensions of coplanar waveguide feeding network

As the power source of coplanar waveguide is modelled as a waveguide port, a parameter studies of the return loss and antenna gain are illustrated in Figure 6.9 and Figure 6.10. According to the parameter study the dimension of the proposed DRA is chosen as the dimension shown in Figure 6.7 and Figure 6.8. The return loss of the proposed multilayer DRA with CPW coupled slot feeding is presented in Figure 6.11, from which it indicates that the resonant frequency of the proposed DRA is from 60.4GHz to 66.9GHz, as a consequence, the corresponding bandwidth is 10.2%. The H field distribution of the proposed wideband antenna at 60.8 GHz shown in Figure 6.12 demonstrate that the antenna operated at TE_{153} high-order mode. Then, Figure 6.13 demonstrate the maximum far field radiation pattern within the resonance band at 60.8GHz, it can be observed that the proposed DRA offers 13.2dBi gain.
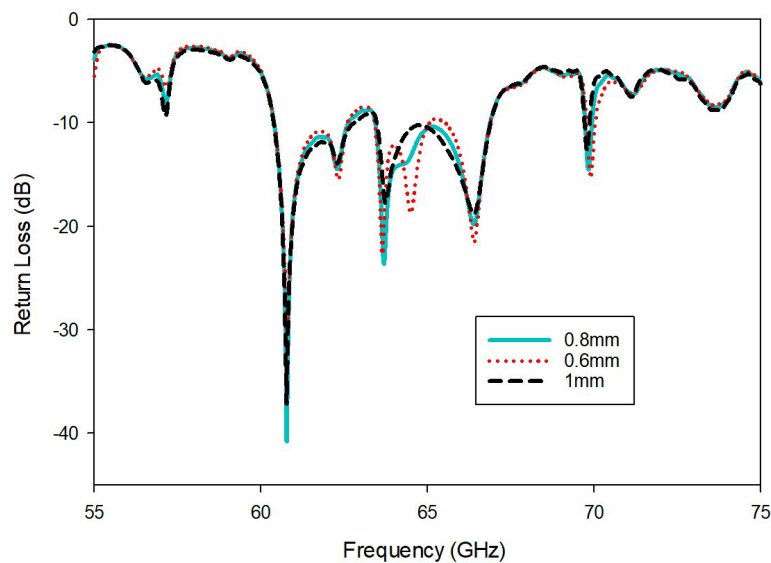
(a)
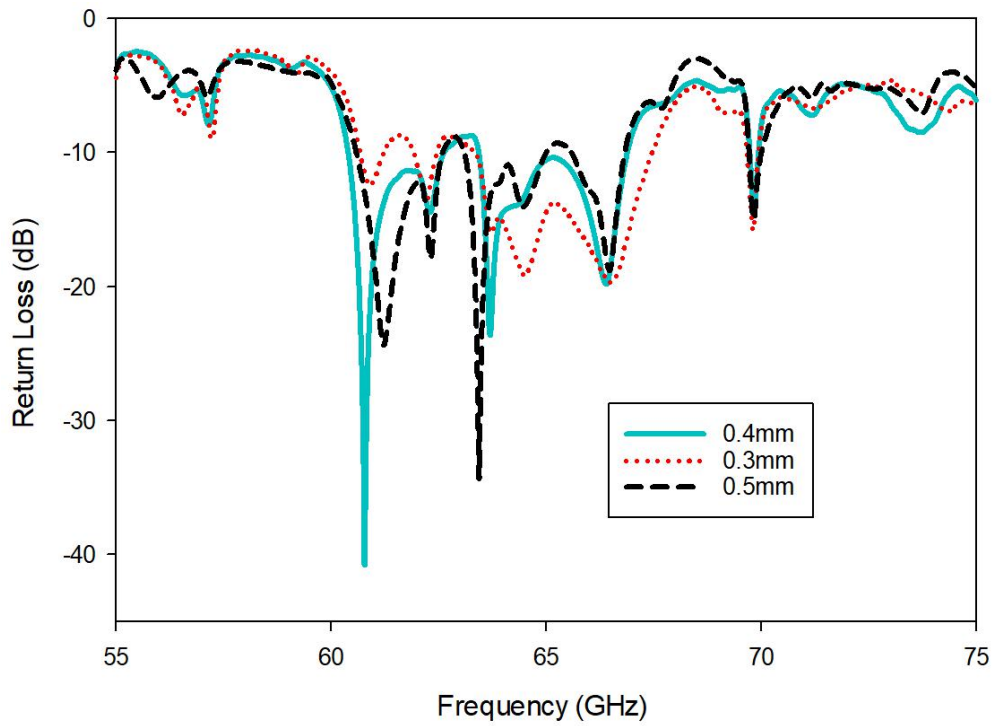
(b)
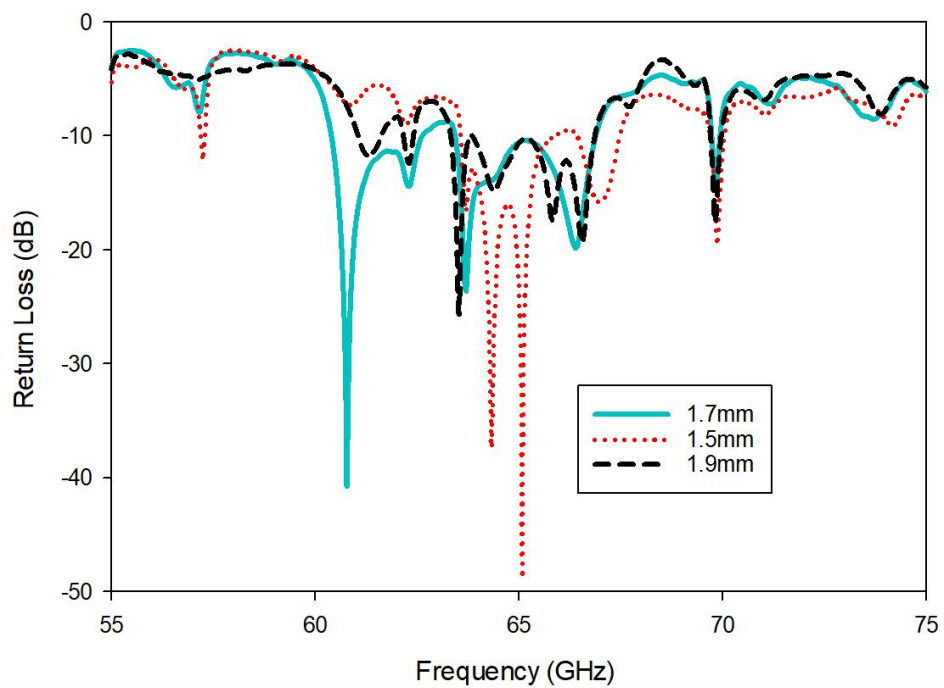
(c)

Figure 6.9: Return loss of CPW coupled slot fed DRA (a) with different slot lengths
(b) with different coating heights (c) with different superstrate thickness
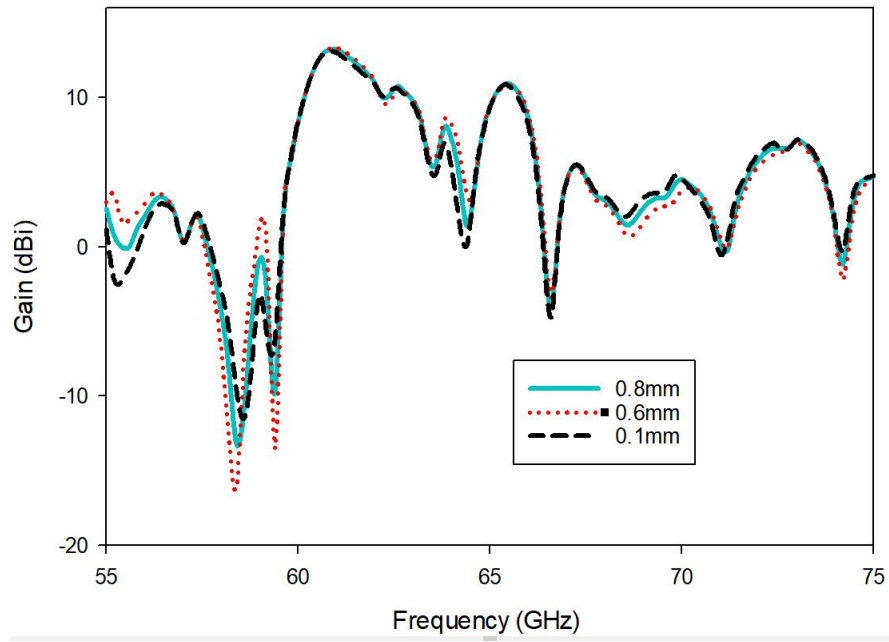
(a)
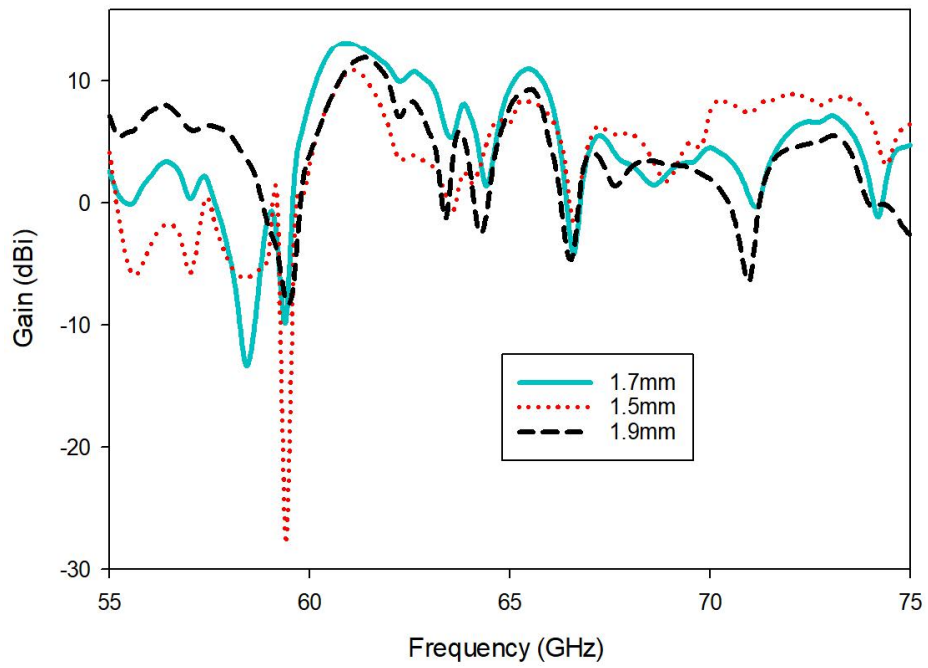
(b)
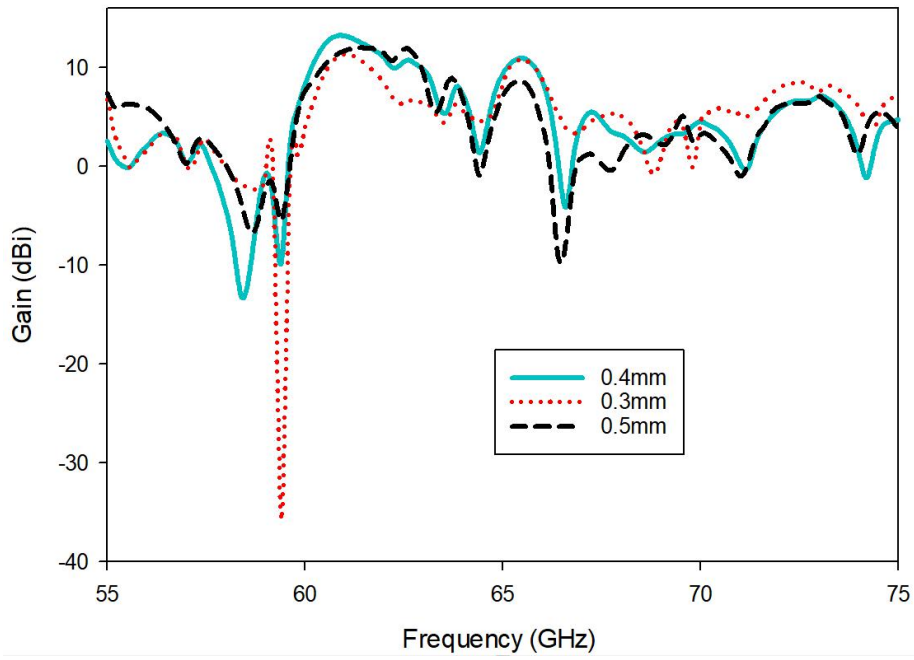
(c)

Figure 6.10: Gain of CPW coupled slot fed DRA (a) with different slot lengths (b) with different coating heights (c) with different superstrate thickness

Figure 6.11: Return loss of multi-layered DRA with wideband
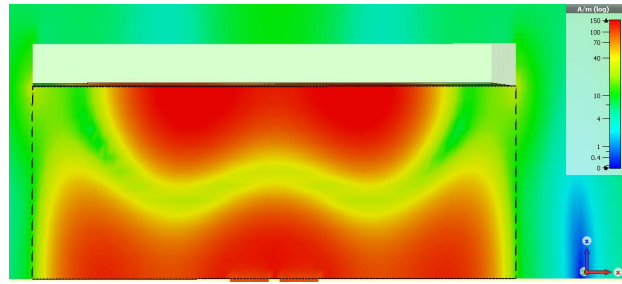
(a)
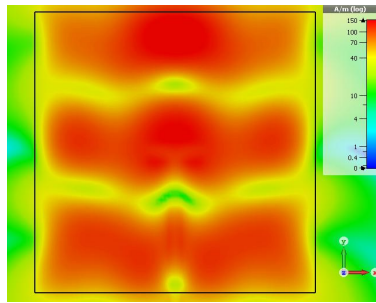
Figure 6.12 Cross section of the H field distribution of the multi-layered DRA at 60.8THz (a) YZ plane (b)XY plane
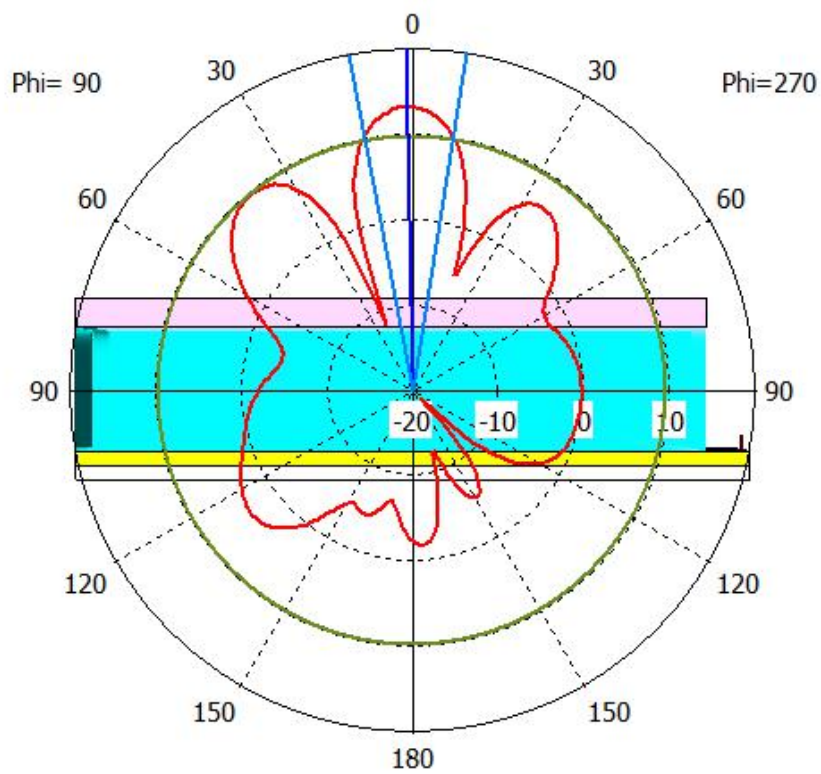
(a)
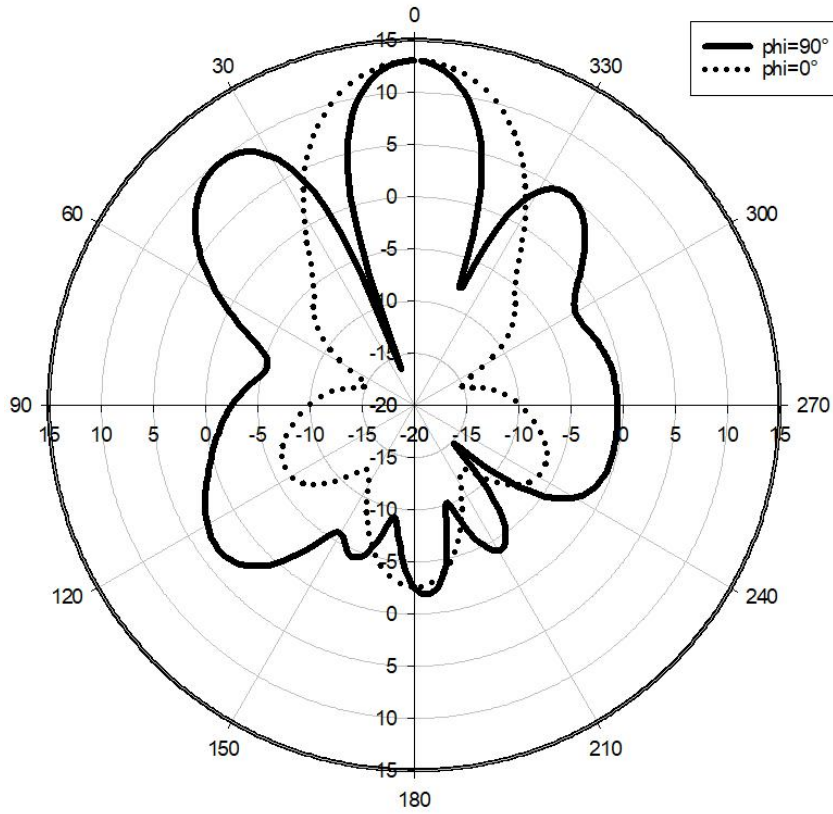
(b)
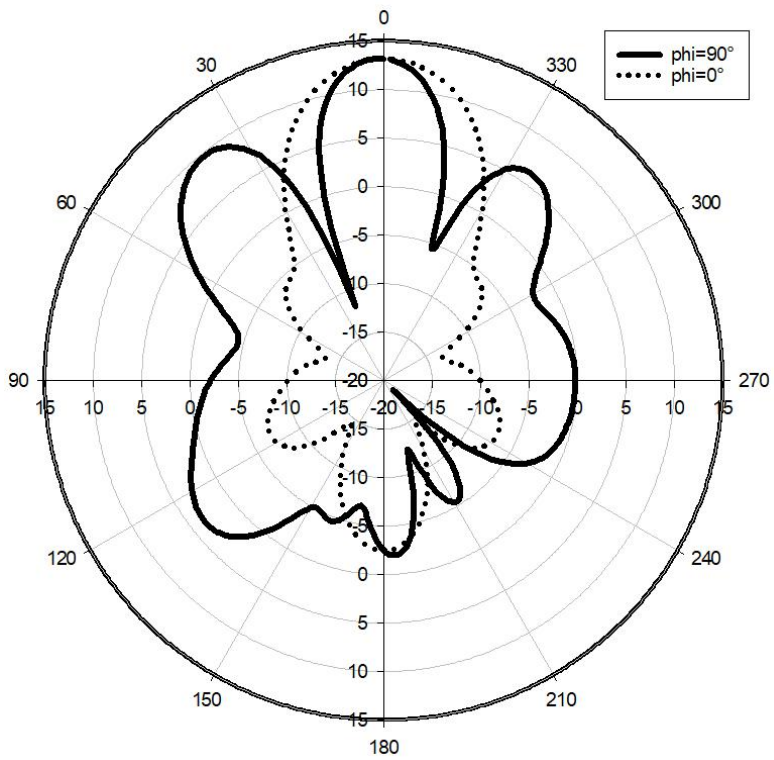
(c)

Figure 6.13: Far field radiation pattern at 60.8GHz (a) with the structure (b) from CST

(c) from FDTD

6.4 Down-converted Multi-layered DRA with Dual Polarisation

The configurations of the multi-layered DRA with dual band and dual polarisation is presented in Figure 6.14, it can be seen that the layout of the antenna is identical to the antenna introduced in section 6.3 except the size. Therefore, dual band and dual polarisation is achieved by open loop feeding slot and stub on transmission network, as shown in Figure 6.15. According to the parameter studies of the return loss, gain and axial ratio shown in Figure 6.16, Figure 6.17 and Figure 6.18. The dimensions of proposed open loop slot feeding multi-layered DRA are chosen as the dimensions shown in Figure 6.14 and 6.15.
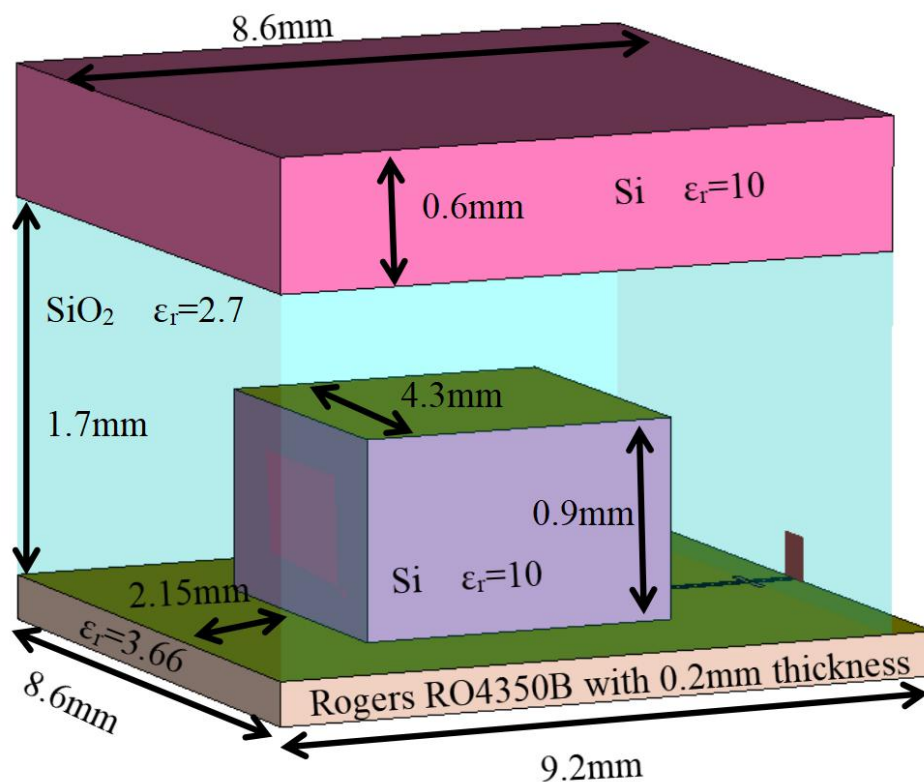
Figure 6.14: Configuration of the multi-layered DRA with dual band and dual polarisation at millimetre band
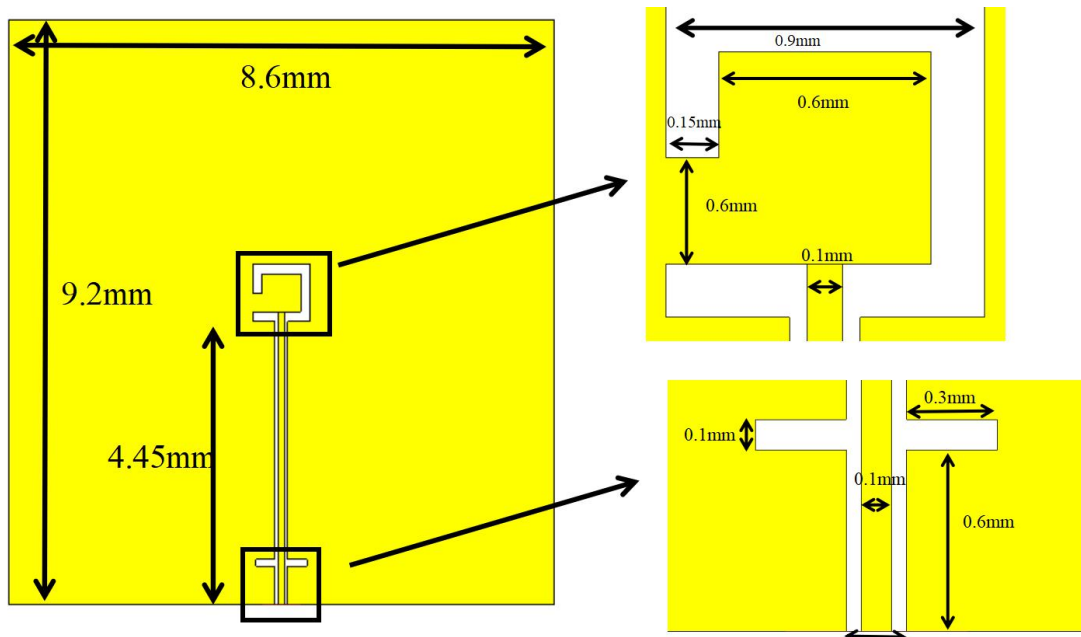
Figure 6.15: Dimensions of coplanar waveguide feeding network
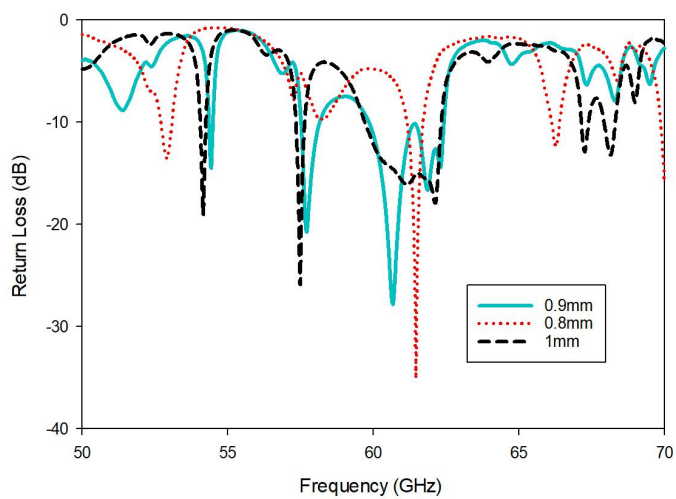
(a)
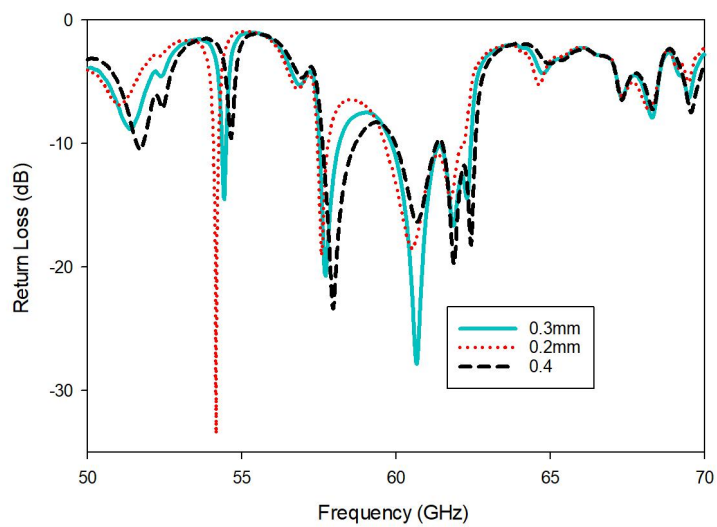
(b)
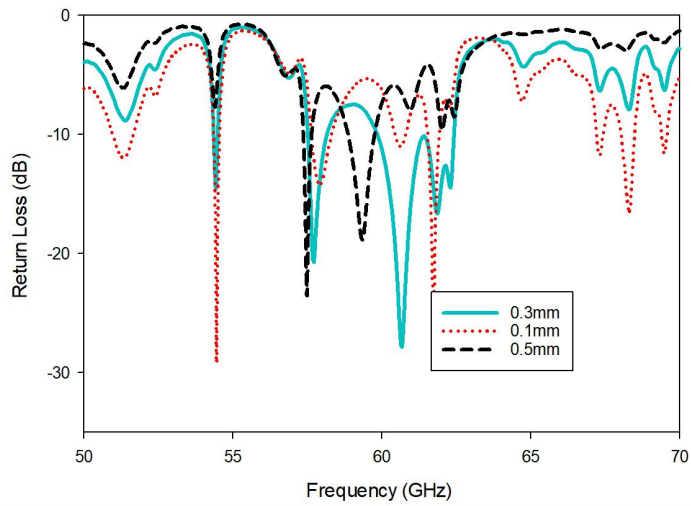
(c)
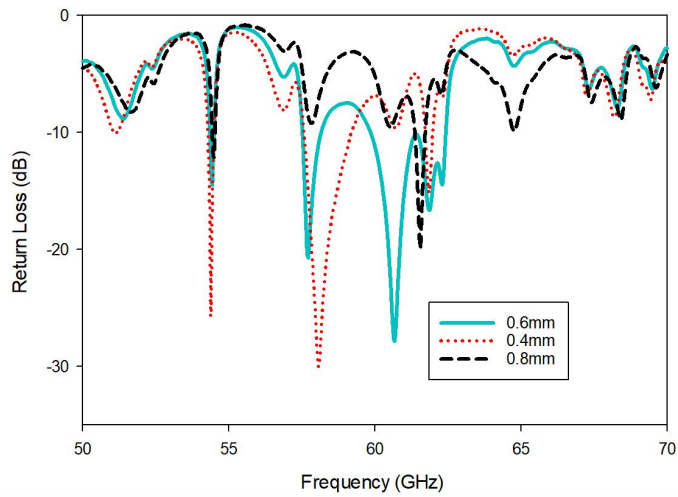
(d)

Figure 6.16: Return loss of CPW coupled open loop slot fed DRA (a) with different loop slot width (b) with different open gap (c) with different stub length (d) with different distance between stub and waveguide port

(a)

129
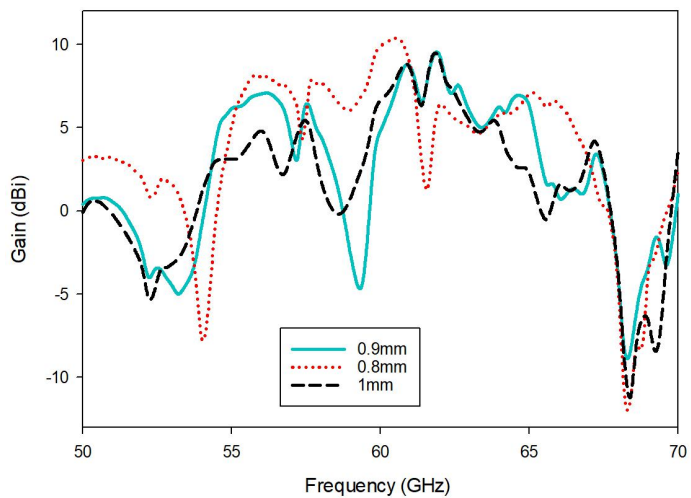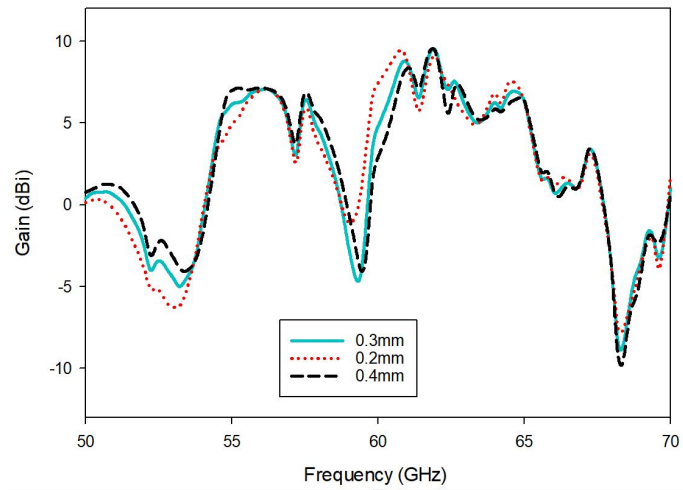
(b)
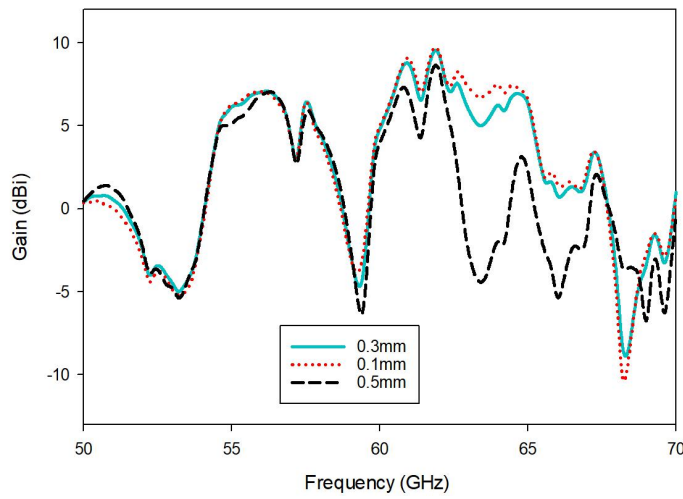
(c)
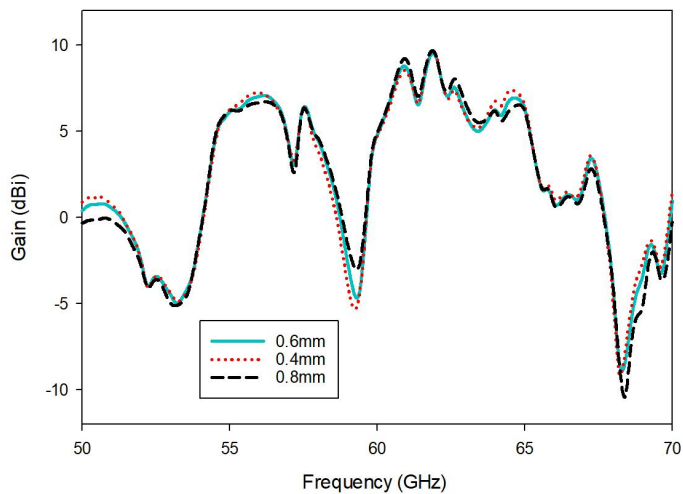
(d)

Figure 6.17: Gain of CPW coupled open loop slot fed DRA (a) with different loop slot width (b) with different open gap (c) with different stub length (d) with different distance between stub and waveguide port
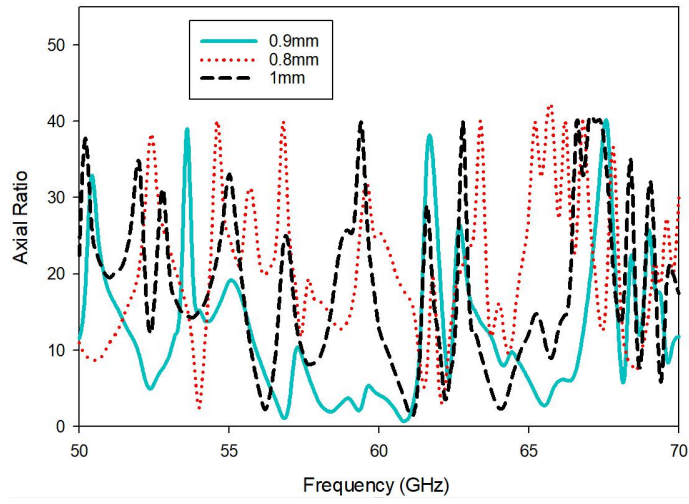
(a)
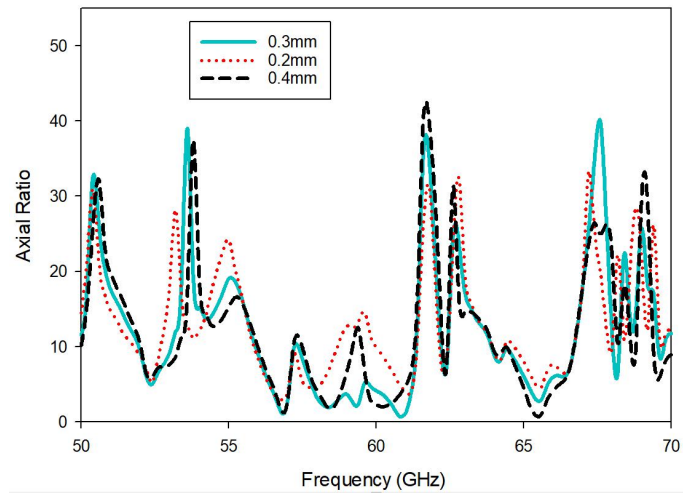
(b)
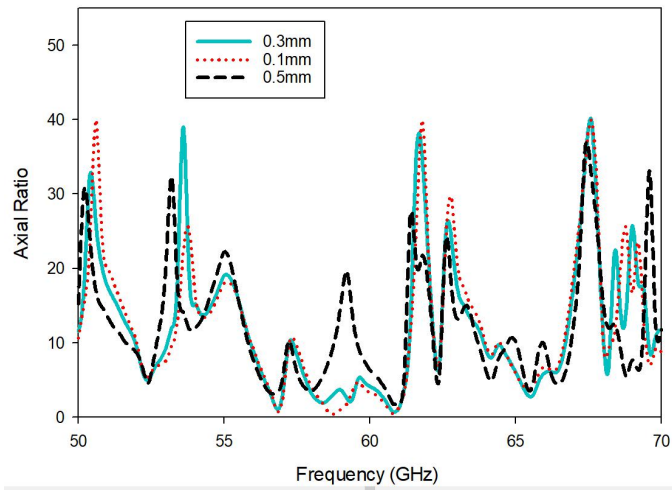
(c)
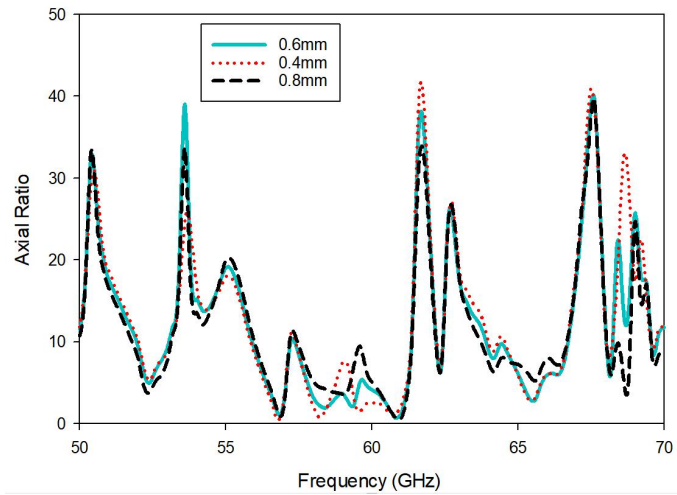
(d)

Figure 6.18: Axial ratio of CPW coupled open loop slot fed DRA (a) with different loop slot width (b) with different open gap (c) with different stub length (d) with different distance between stub and waveguide port
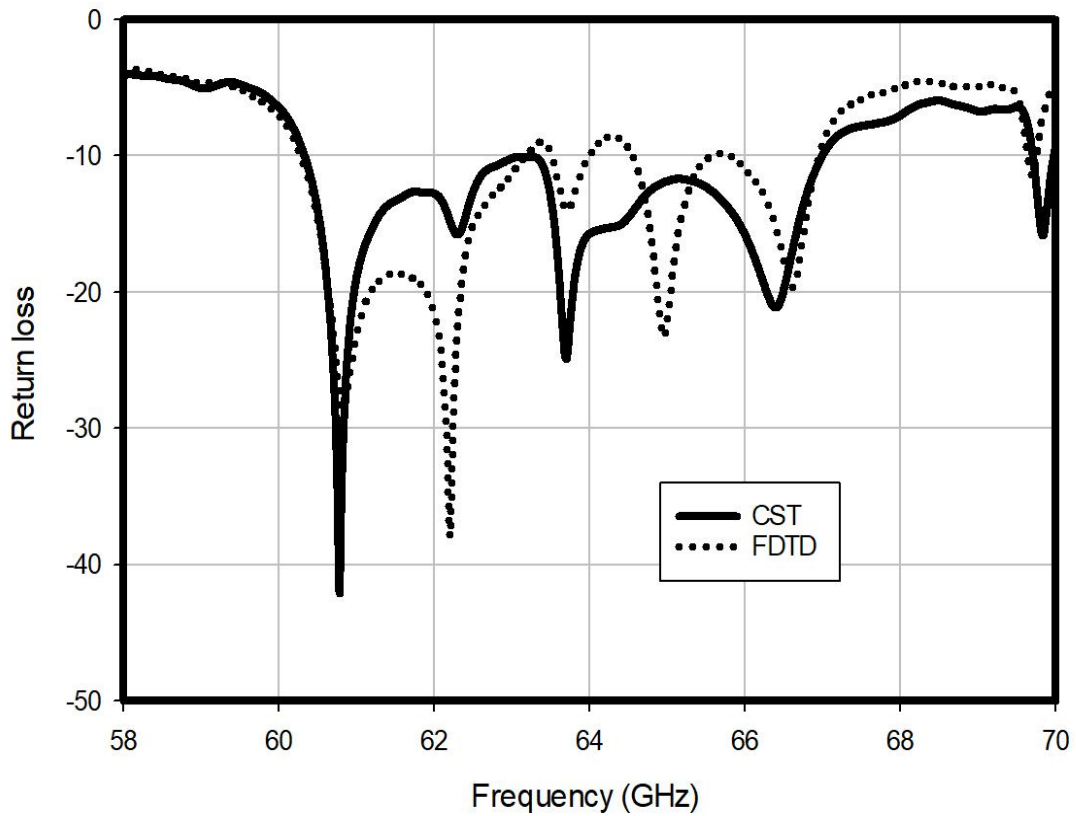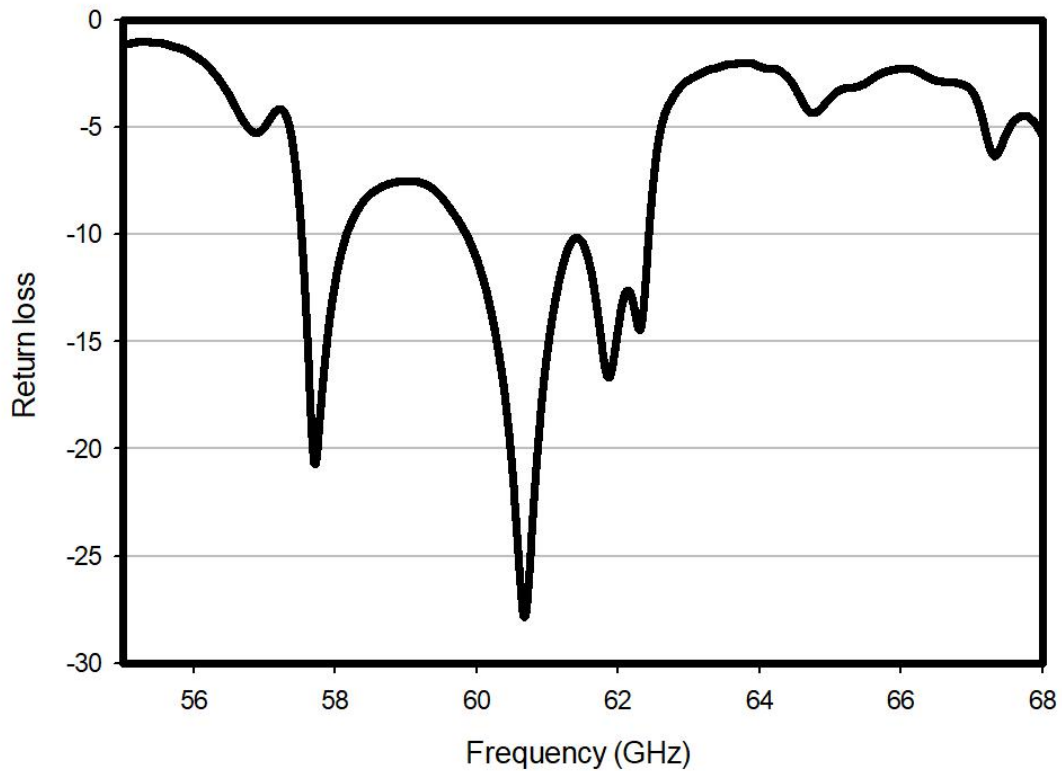

Figure 6.19: Return loss of multi-layered DRA with loop slot width of 0.9mm, open gap of 0.3mm, stub length of 0.3mm and distance from waveguide port of 0.6mm
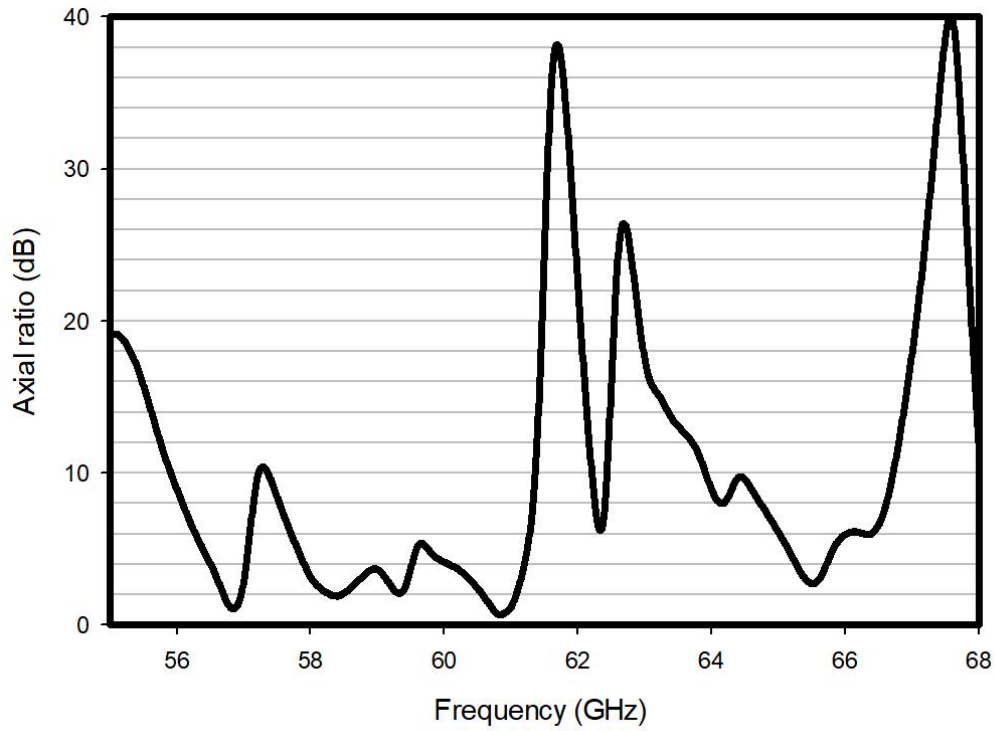
Figure 6.20: Axial ratioof multi-layered DRA with loop slot width of 0.9mm, open gap of 0.3mm, stub length of 0.3mm and distance from waveguide port of 0.6mm
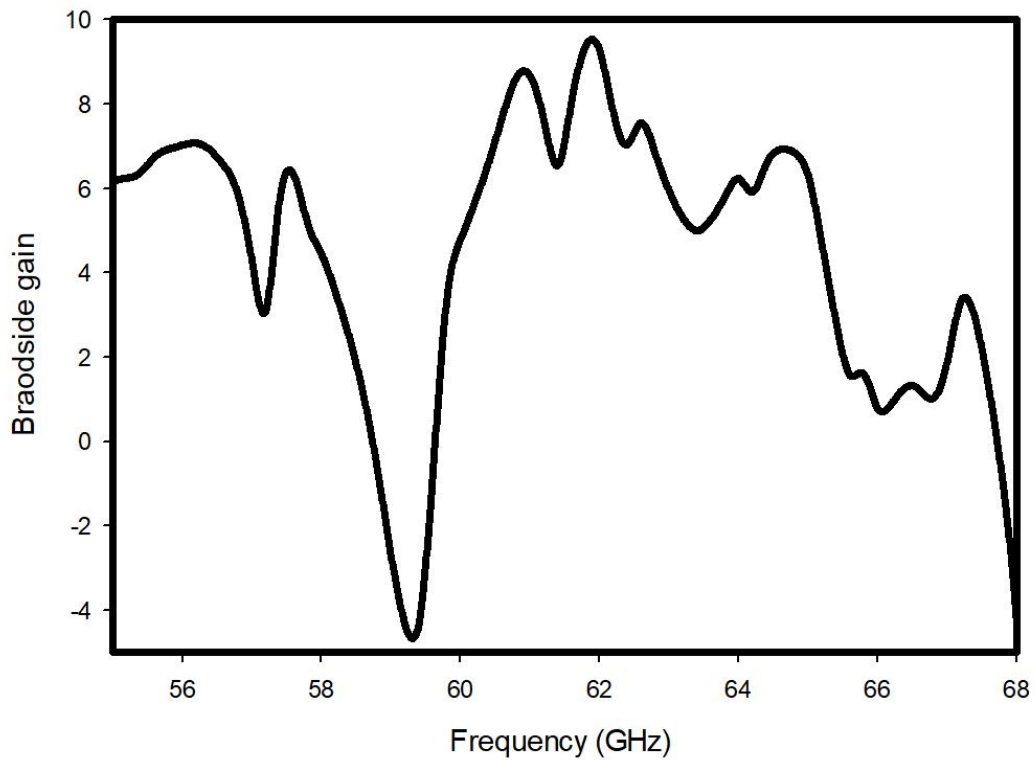
Figure 6.21: Antenna broadside gain of multi-layered DRA with loop slot width of 0.9mm, open gap of 0.3mm, stub length of 0.3mm and distance from waveguide port of 0.6mm
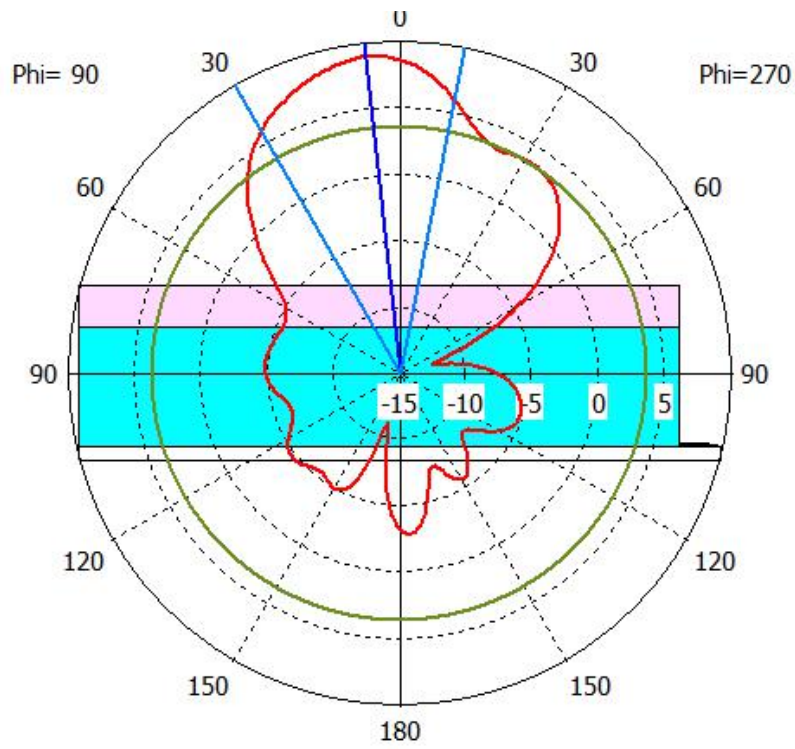
(a)
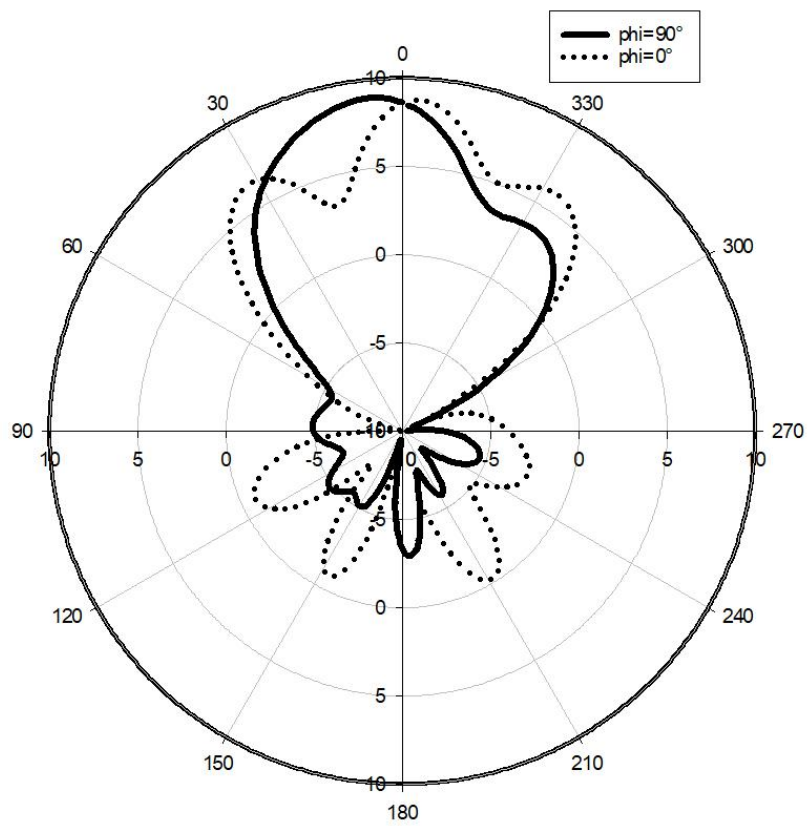
(b)
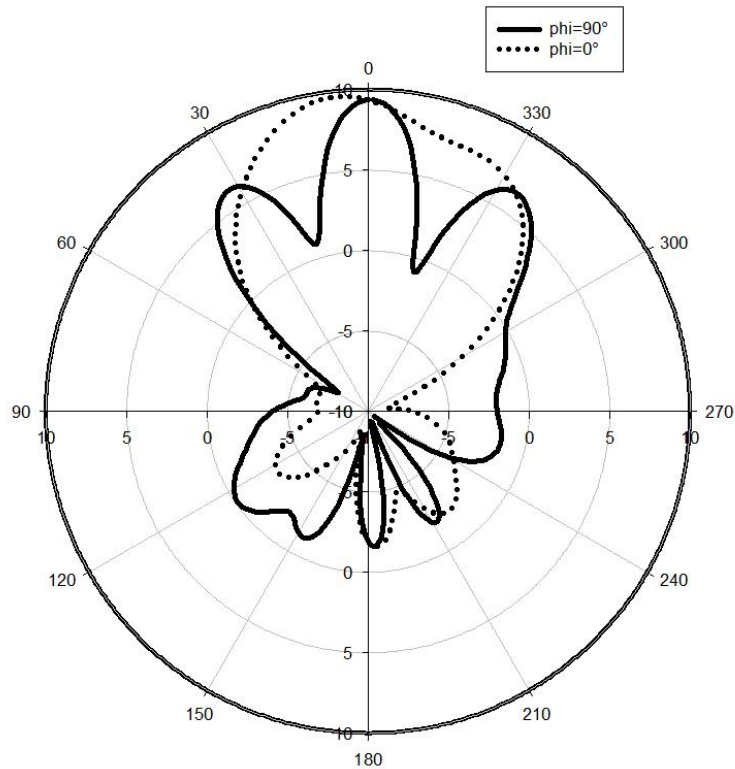
(c)

Figure 6.22 Far field radiation pattern (a) with the structure at 60.8GHz (a) at

60.8GHz (b) at 61.8GHz

The return loss shown in Figure 6.19 demonstrate a resonance band from 59.85GHz to 62.43GHz, and axial ratio shown in Figure 6.20 indicate that the proposed antenna offers two polarisation within this resonance band. It can be seen that from 60.36GHz to 61.13GHz the axial ratio is below 3 which means the circular polarisation is achieved. The axial ratio is more than 30dB has been achieved at 61.8GHz, which can be considered as linear polarisation. Moreover, The broadside gain as a function of frequency shown in Figure 6.21 and the far field radiation pattern shown in Figure 6.22 depict that the antenna gain of 8.9dBi and 9.5dBi can be achieved by circular polarisation and linear polarisation, respectively.

6.5 Summary

The design of DRA truncated from photoconductive substrate introduced in last chapter haven't consider the physical support of dielectric superstrate and feeding network. Therefore, the design of multi-layered DRA that employing a supporting coating layer that covers the DRA and provide physical support to superstrate is

introduced in this chapter. Firstly, the multi-layered DRA resonant at 0.461THz with broadside gain of 14.2dBi is presented. Then, for the fabrication and measurement purposes, the DRA introduced in section 6.2 is down-converted to operate at 65GHz, the ideal slot feed is replaced by coplanar waveguide fed slot, low loss dielectric substrate is involved to provide physical support to the ground plane as well as feeding network and the thickness of metal ground plane and metal plate is considered. As a result of all the changes, the design of DRA proposed in section 6.3 offers 10.2% wideband from 60.4GHz to 66.9GHz with broadside gain of 13.2dBi. Finally, a dual polarised DRA is proposed by employing open loop feeding slot and stub matching. Circular polarisation with 8.9dBi broadside gain have been achieved from 60.36GHz to 61.13GHz. On the other hand, linear polarisation have been achieved at 61.8GHz with 9.5dBi broadside gain. It should be noted that both of the polarisations are achieved within a single resonant band.

Chapter 7: Conclusions and Future Work

7.1 Conclusions

The main focus of this thesis is designing a photomixer based THz antenna with high efficiency.The efficiency of a phtomixer based THz antenna is investigated from three aspects:optical-to-THz conversion efficiency,matching efficiency and radiation efficiency.CST and FDTD Matlab code are used to simulate and validate the proposed configurations.

In chapter 1,various types of THz source have been reviewed,by comparing the performance and limitation of them,THz photomixer becomes a promising solution of compact THz devices at room temperature with high data rate.Higher THz frequency can be achieved by THz photmixer antenna than the THz solid state component.Unlike QCLs,THz photomixer antenna can work at room temperature without cryogenic cooling system. Furthermore, THz photomixer antenna is much smaller than vacuum tube sources.Though,these advantages highlighted THz

photomixer antenna from other THz sources,the limitation of low output power obstructs the development of THz photomixer antenna based technologies.In this case,the necessity of improving the efficiency of THz photomixer antenna has been highlighted and improving such efficiency becomes a subject of great interest.

In chapter 2, the differences between THz photomixer antenna and RF/MW antenna have been reviewed from 6 different aspects: excitation source, feed and biasing; substrate material; antenna electrode material; type of current; fabrication and measurement; and computer aided design. These difference emphasis the necessity of having a new analysis and design process for THz photomixer antenna as the design of THz photomixer antenna can be divided into two part: optoelectronic part that analyses the optical-to-THz conversion efficiency, and electromagnetic part that studies the matching as well as radiation of THz antenna just like what should be done for RF/MW antenna. In accordance with this difference, an equivalent circuit of THz photomixer that combined the large-signal circuit model and physical behaviour of THz photomixer is introduced. Then, a equation that factorised the generated THz power from THz phtomixer have been derived from the equivalent circuit. The time varying characteristic of the equation is caused by the time varying source conductance of photomixer. Moreover, the parameter analysis of time varying source conductance of THz photomixer imply that improving the matching efficiency of phtomixer based THz antenna was required.

In chapter 3, according to the equation of generated THz power that derived from the equivalent circuit, a new design process that simulating both optoelectronic design and electromagnetic design of THz photomixer based antenna in a single full-wave electromagnetic solver is introduced. Furthermore, for the reason of cross validation, finite difference time domain method in company with an overview of Maxwell's equations have been explained.

In chapter 4, various methods of improving the optical-to-THz conversion efficiency have been explained. Firstly, 4 designs of photomixer electrodes reported in literature have been re-simulated and analysed, where it has been noted the improvement are limited. The change of photomixer electrodes lead to a changing in the source capacitance which further complicate the problem. Then, plasmonic THz photomixer electrode proposed in literature has been re-simulated and the result proved that it can improve the optical-to-THz conversion efficiency without changing the structure of electrode. This is because of the surface plasmon resonance offered by

plasmonic material, from which the localised electric field can be enhanced. Next, distributed bragg reflector coupled photomixer that published previously has been studied. 30% more generated THz power has been achieved by reflecting the unabsorbed laser power back to photoconductive region. In accordance with the idea of reflecting unabsorbed power, firstly, two dimensional photonic crystal with central air hole has been implemented with photomixer electrode. Since 2D-PhC not only reflecting unabsorbed incident laser power, but also reflecting scattering surface plasmon resonance in transverse plane, the generated THz power have been enhanced by a factor of 6.87. After that, since plasmonic material can be used to improve the localised electric field, a design of 2D-PhC with central plasmonic rods has been proposed. Due to the extra plasmonic interaction between plasmonic rods and plasmonic electrodes as well as between adjacent plasmonic rods, an enhancement factor of 18.4 have been achieved . Furthermore, a design that utilizing dielectric superstrate above the photomixer in company with the 2D-PhC with plasmonic rod as reflector underneath the photomixer have been presented. The generated THz power has been improved by 256 times due to the cavity created by the dielectric superstrate and 2D-PhC reflector. Finally, the 2D-PhC is used as a frequency selective surface superstrate when the THz photomixer is surrounded by metal ground plane. As a consequence, the proposed configuration offers an enhancement factor of 494, which represent a significantly improvement of optical-to-THz conversion efficiency.

In chapter 5, the photoconductive substrate has been truncated into a dielectric resonator antenna to eliminate substrate effect and avoid using bulky lens. Two dielectric resonator antenna with different feeding method which based upon the photomixer designed in section 4.41 and 4.42 have been described. In order to optimize the matching efficiency, the choke filter network has been implemented to enhance the antenna resistance. Besides, choke filter network can eliminate the power leakage through the DC bias pad and provide inductive capacitance which can be used to compensate the source capacitance. As a result, matching efficiency of dipole fed DRA has improved from 0.16% to 16%, and the matching efficiency of slot fed DRA has improved from 15.8% to 24.5%. However, the drawback of ohmic losses accompanied by choke filter network reduce the radiation efficiency. Hence, dielectric superstrate has been employed. Consequently, the broadside gains of proposed dipole fed DRA and slot fed DRA have been improved to 10.18dBi and 9dBi.

By considering the enhancement factor of photomixer, the total efficiency of the dipole fed DRA based upon dielectric superstrate and 2D-PhC reflector coupled photomixer has an enhancement factor of approximately 51k. On the other hand, the total efficiency of the slot fed DRA based upon 2D-PhC FSS superstrate coupled photomixer has an enhancement factor of approximately 1532. Both of them represents a significant enhancement in the efficiency of THz photomixer based antenna, especially the former one.

In chapter 6, in order to realize the dielectric superstrate coupled DRA by providing physical support to the dielectric superstrate. A central slot fed multi-layered DRA has been introduced at 0.46THz with 14.2dBi Gain. The proposed multi-layered DRA used a dielectric coating to cover the DRA, and the dielectric superstrate is placed on the coating layer. Then, for the fabrication and measurement purpose, the proposed multi-layered DRA was down-converted to resonant at 65GHz. The ideal central slot feeding is replaced by a coplanar waveguide incorporated slot, since then, a dielectric substrate has been implemented to physically support the coplanar waveguide feeding network. The proposed multi-layered DRA offers a 10.2% resonance band with 13.2dBi gain. Finally, a open loop slot has been used to excite the multi-layered DRA. With the stub matching technique, the multi-layered DRA offers dual polarisation in a single resonant band. Circular polarisation has been achieved from 60.36GHz to 61.13GHz with antenna gain of 8.9dBi, and linear polarisation has been achieved at 61.8GHz with antenna gain of 9.5dBi.

7.2 Future work

The efficiency of THz photomixer can be divided into three different efficiencies, since then, the future work can be predicted from three different aspects.

As mentioned in this thesis, the optical-to-THz conversion efficiency depends on many factors, such as properties of suitable photoconductive materials, configurations of photomixer electrode, source conductance and illuminating laser power, etc.. In this thesis, the main focus of improving the optical-to-THz conversion efficiency is enhancing the illuminating power. Several other parameters are waiting to be studied.

Plenty of the methods like PBG isolation layer, has been proposed in the literature to improve the matching efficiency of THz antenna. However, most of them

are planar antenna. As introduced in this thesis, DRA offers higher radiation efficiency over a smaller size, therefore, further investigation on improving the matching efficiency of DRA is necessary.

Dielectric superstrate is intensively used to improve the radiation in this thesis. The radiation enhancement technique like meta-surface has been well developed in the last decades, therefore, extending the operation frequency of meta-surface to THz frequency can be a promising research topic.

All the studies in this thesis is based upon THz photomixer antenna which is used for the continuous wave system. There is another type of THz antenna called THz photoconductive antenna. Though, the working principles of them are identical, only one incident laser beams is required for the THz photoconductive antenna. Therefore, the minor difference in the generation of THz power and the difference in the operation system could lead to another new path that contribute to the future communication system.

Reference

[1] Y. Lee, Principles of terahertz science and technology, 1st ed. New York, NY: Springer, 2008.

[2] B. Ferguson and X. Zhang, "Materials for terahertz science and technology," Nat Mater, vol. 1, pp. 26-33, 2002.

[3] R. Kohler, A. Tredicucci, F. Beltram, H. E. Beere, E. H. Linfield, A. G. Davies, D. A. Ritchie, R. C. Iotti, and F. Rossi, "Terahertz semiconductor-heterostructure laser," Nature, vol. 417, pp. 156-159, 2002.

[4] B. S. Williams, "Terahertz quantum-cascade lasers," Nat Photon, vol. 1, pp. 517-525, 2007.

[5] C. M. Armstrong, "The truth about terahertz," IEEE Spectrum, vol. 49, pp. 36-41, 2012.

[6] T. Kürner, S. Priebe "Towards THz communications - status in research, standardization and regulation," J. Infrared Millim. Terahertz Waves, 35, 2014, pp. 53–62.

[7] M. Tonouchi, "Cutting-edge terahertz technology," Nat Photon, vol. 1, pp. 97-105, 2007.

[8] D. M. Pozar, Microwave engineering, 4th ed. Hoboken, NJ: Wiley, 2012.

[9] T. W. Crowe, W. L. Bishop, D. W. Porterfield, J. L. Hesler, and R. M. Weikle, II, "Opening the terahertz window with integrated diode circuits," IEEE Journal of SolidState Circuits,, vol. 40, pp. 2104-2110, 2005.

[10] R. J. Trew, "High-frequency solid-state electronic devices," IEEE Transactions on Electron Devices, , vol. 52, pp. 638-649, 2005.

[11] H. Eisele, "InP Gunn devices for 400-425 GHz," Electronics Letters, vol. 42, pp. 358- 359, 2006.

[12] H. Eisele and R. Kamoua, "Submillimeter-wave InP Gunn devices," IEEE Transactions on Microwave Theory and Techniques,, vol. 52, pp. 2371-2378, 2004.

[13] N. Orihashi, S. Suzuki, and M. Asada, "One THz harmonic oscillation of resonant tunneling diodes," Applied Physics Letters, vol. 87, p. 233501, 2005.

[14] A. Maestrini, J. Bruston, D. Pukala, S. Martin, and I. Mehdi, "Performance of a 1.2 THz frequency tripler using a GaAs frameless membrane monolithic circuit," in

2001 IEEE MTT-S International Microwave Symposium Digest, , 2001, pp. 1657-1660 vol.3.

[15] J. Tucek, D. Gallagher, K. Kreischer, and R. Mihailovich, "A compact, high power, 0.65 THz source," in IEEE International Vacuum Electronics Conference, 2008. IVEC 2008. , pp. 16-17.

[16] P. H. Siegel, "Terahertz technology," IEEE Transactions on Microwave Theory and Techniques, , vol. 50, pp. 910-928, 2002.

[17] A. G. Davies, E. H. Linfield, and M. B. Johnston, "The development of terahertz sources and their applications," Physics in Medicine and Biology, vol. 47, p. 3679, 2002.

[18] B. S. Williams, S. Kumar, H. Qing, and J. L. Reno, "High-power terahertz quantum cascade lasers," in Conference on Lasers and Electro-Optics and Quantum Electronics and Laser Science Conference. CLEO/QELS 2006. , 2006, pp. 1-2.

[19] S. Kumar, B. S. Williams, S. Kohen, Q. Hu, and J. L. Reno, "Continuous-wave operation of terahertz quantum-cascade lasers above liquid-nitrogen temperature," Applied Physics Letters, vol. 84, pp. 2494-2496, 2004.

[20] C. Worrall, J. Alton, M. Houghton, S. Barbieri, H. E. Beere, D. Ritchie, and C. Sirtori, 192 "Continuous wave operation of a superlattice quantum cascade laser emitting at 2 THz," Opt. Express, vol. 14, pp. 171-181, 2006.

[21] C. Walther, M. Fischer, G. Scalari, R. Terazzi, N. Hoyler, and J. Faist, "Quantum cascade lasers operating from 1.2 to 1.6 THz," Applied Physics Letters, vol. 91, p. 131122, 2007.

[22] Q. Y. Lu, N. Bandyopadhyay, S. Slivken, Y. Bai, and M. Razeghi, "Room temperature single-mode terahertz sources based on intracavity difference-frequency generation in quantum cascade lasers," Applied Physics Letters, vol. 99, p. 131106, 2011.

[23] M. Tonouchi, "Cutting-edge terahertz technology," Nat Photon, vol. 1, pp. 97-105, 2007.

[24] K. Suizu and K. Kawase, "Monochromatic-Tunable Terahertz-Wave Sources Based on Nonlinear Frequency Conversion Using Lithium Niobate Crystal," in IEEE Journal of Selected Topics in Quantum Electronics, vol. 14, no. 2, pp. 295-306, March-april 2008, doi: 10.1109/JSTQE.2007.911306.

[25] A. Eshaghi, M. Shahabadi, and L. Chrostowski, "Radiation characteristics of large-area photomixer used for generation of CW THz radiation," J. Opt. Soc. Am. B, vol. 29, pp.813-817, 2012.

[26] P. Kordoš, M. Marso, and M. Mikulics, "Performance optimization of GaAs-based photomixers as sources of THz radiation," Applied Physics A, vol. 87, pp. 563-567, 2007.

[27] E. Peytavit, A. Beck, T. Akalin, J.-F. Lampin, F. Hindle, C. Yang, and G. Mouret, "Continuous terahertz-wave generation using a monolithically integrated horn antenna," Applied Physics Letters, vol. 93, p. 111108, 2008.

[28] E. Nichols and J. Tear, " Joining the infra-red and electric wave spectra," Astrophysical Journal, vol. 61, pp. 17-37, 1925.

[29] J. Federici, L. Moeller, "Review of terahertz and subterahertz wireless communications," J. Appl. Phys. 107 (11) (2010) 111101.

[30] K. C. Huang, Z. Wang, "Terahertz terabit wireless communication," IEEE Microw. Mag. 12 (4) (2011) 108–116.

[31] T. Kleine-Ostmann, T. Nagatsuma, "A review on terahertz communications research, J. Infrared Millim," Terahertz Waves 32 (2011) 143–171.

[32] R. Piesiewicz, T. Kleine-Ostmann, N. Krumbholz, D. Mittleman, M. Koch, J. Schoebel, T. Kürner: "Short-Range Ultra-Broadband Terahertz Communications: Concepts and Perspectives," IEEE Antennas and Propagation Magazine, vol. 49, no. 6, pp. 24–39, 2007.

[33] C. A. Balanis, "Antenna Theory: Analysis and design", (Wiley, USA), pp. 94-96. 2005.

[34] H. Song, and T. Nagatsuma, "Present and future of terahertz communications," Trans. THz Sci. Technol, 2011, 1, (1), pp. 256–263.

[35] I. F. Akyildiz, J.M. Jornet, C. Han, "Terahertz band: Next frontier for wireless communications," Phys. Commun., 12 (2014), pp. 16–32.

[36] R. Appleby and H. B. Wallace, "Standoff Detection of Weapons and Contraband in the 100 GHz to 1 THz Region," in IEEE Transactions on Antennas and Propagation, vol. 55, no. 11, pp. 2944-2956, Nov. 2007.

[37] P. U. Jepsen, D. G. Cooke, and M. Koch, "Terahertz spectroscopy and imaging – Modern techniques and applications," Laser & Photonics Reviews, vol. 5, pp. 124-166, 2011.

[38] D. L. Woolard, R. Brown, M. Pepper, and M. Kemp, "Terahertz Frequency Sensing and Imaging: A Time of Reckoning Future Applications?," Proceedings of the IEEE, vol. 93, pp. 1722-1743, 2005.

[39] https://teraview.com/

[40] https://www.advancedphotonix.com/

[41] https://www.toptica.com/

[42] V. P. Wallace, A. J. Fitzgerald, S. Shankar, N. Flanagan, R. Pye, J. Cluff, and D. D. Arnone, "Terahertz pulsed imaging of basal cell carcinoma ex vivo and in vivo," British Journal of Dermatology, vol. 151, pp. 424-432, 2004.

[43] A. J. Fitzgerald, V. P. Wallace, M. Jimenez-Linan, L. Bobrow, R. J. Pye, A. D. Purushotham, and D. D. Arnone, "Terahertz Pulsed Imaging of Human Breast Tumors," Radiology, vol. 239, pp. 533-540, 2006.

[44] D. Crawley, C. Longbottom, V. P. Wallace, B. Cole, D. Arnone, and M. Pepper, "Threedimensional terahertz pulse imaging of dental tissue," Journal of Biomedical Optics, vol. 8, pp. 303-307, 2003.

[45] K. Fukunaga, Y. Ogawa, S. i. Hayashi, and I. Hosako, "Terahertz spectroscopy for art conservation," IEICE Electronics Express, vol. 4, pp. 258-263, 2007.

[46] J. B. Jackson, M. Mourou, J. F. Whitaker, I. N. Duling Iii, S. L. Williamson, M. Menu, and G. A. Mourou, "Terahertz imaging for non-destructive evaluation of mural paintings," Optics Communications, vol. 281, pp. 527-532, 2008.

[47] A. J. L. Adam, P. C. M. Planken, S. Meloni, and J. Dik, "TeraHertz imaging of hidden paintlayers on canvas," Opt. Express, vol. 17, pp. 3407-3416, 2009.

[48] N. Krumbholz, T. Hochrein, N. Vieweg, T. Hasek, K. Kretschmer, M. Bastian, M. Mikulics, and M. Koch, "Monitoring polymeric compounding processes inline with THz time-domain spectroscopy," Polymer Testing, vol. 28, pp. 30-35, 2009.

[49] D. H. Auston, K. P. Cheung, and P. R. Smith, "Picosecond photoconducting Hertzian dipoles," Applied Physics Letters, vol. 45, pp. 284-286, 1984.

[50] V. Pacebutas, et al, "THz time-domain-spectroscopy system based on femtosecond Yb:fiber laser and GaBiAs photoconucting components," Applied Physics Letters, vol. 97, 031111, 2010.

[51] E. R. Brown, F. W. Auston, and M. C. Nuss, "Sub-picosecond photoconducting dipole antennas", IEEE, J. Quantum electron., vol 24, no 2, pp. 255-260, 1988.

[52] https://www.synopsys.com/silicon/tcad/device-simulation/sentaurus-device.html

[53] J. Y. Suen, W. Li, Z. D. Taylor, and E. R. Brown, "Characterization and modeling of a terahertz photoconductive switch," Applied Physics Letters, vol. 96, p. 141103, 2010.

[54] G. C. Loata, M. D. Thomson, T. Loffler, and H. G. Roskos, "Radiation field screening in photoconductive antennae studied via pulsed terahertz emission spectroscopy," Applied Physics Letters, vol. 91, p. 232506, 2007.

[55] P. Hale, J. Madeo, C. Chin, S. Dhillon, J. Mangeney, J. Tignon, and K. Dani, "20 THz broadband generation using semi-insulating GaAs interdigitated photoconductive antennas," Opt. Express 22, p. 26358-26364, 2014.

[56] F. Ellrich, T. Weinland, D. Molter, J. Jonuscheit, and R. Beigang, "Compact fibercoupled terahertz spectroscopy system pumped at 800 nm wavelength," Review of Scientific Instruments, vol. 82, p. 053102, 2011.

[57] B. Sartorius, H. Roehle, H. Künzel, J. Böttcher, M. Schlak, D. Stanze, H. Venghaus, and M. Schell, "All-fiber terahertz time-domain spectrometer operating at 1.5 um telecom wavelengths," Opt. Express, vol. 16, pp. 9565-9570, 2008.

[58] S. Han, H. Ko, N. Kim, H. Ryu, C. Wook Lee, Y. Ahn Leem, D. Lee, M. Yong Jeon, S. Kyu Noh, H. Sook Chun, and K. Hyun Park, "Optical fiber-coupled InGaAs-based terahertz time-domain spectroscopy system," Opt. Lett., vol. 36, pp. 3094-3096, 2011.

[59] D. Singh, C. Kalialakis, P. Gardner, and P. S. Hall, "Small H-shaped antennas for MMIC applications," IEEE Transactions on Antennas and Propagation, , vol. 48, pp. 1134- 1141, 2000.

[60] S. Gupta, J. F. Whitaker, and G. A. Mourou, "Ultrafast carrier dynamics in III-V semiconductors grown by molecular-beam epitaxy at very low substrate temperatures," IEEE Journal of Quantum Electronics, , vol. 28, pp. 2464-2472, 1992.

[61] S. Gupta, M. Y. Frankel, J. A. Valdmanis, J. F. Whitaker, G. A. Mourou, F. W. Smith, and A. R. Calawa, "Subpicosecond carrier lifetime in GaAs grown by molecular beam epitaxy at low temperatures," Applied Physics Letters, vol. 59, pp. 3276-3278, 1991.

[62] M. Martin and E. R. Brown, "Critical comparison of GaAs and InGaAs THz photoconductors," Proc. of SPIE, vol. 8261, pp. 826102-826102, 2012.

[63] S. M. Sze and K. K. Ng, Physics of semiconductor devices, 3rd ed. Hoboken, N.J.: Wiley-Interscience, 2007.

[64] L. Hrivank, "Semi-insulating GaAs," Czech. J. Phys. B, vol. 34, pp. 436-444, 1984.

[65] J. Colinge and C. A. Colinge, Physics of semiconductor devices. Boston: Kluwer Academic Publishers, 2002.

[66] A. W. Jackson, J. P. Ibbetson, A. C. Gossard, and U. K. Mishra, "Reduced thermal conductivity in low-temperature-grown GaAs," Applied Physics Letters, vol. 74, pp. 2325-2327, 1999.

[67] F. W. Smith, H. Q. Le, V. Diadiuk, M. A. Hollis, A. R. Calawa, S. Gupta, M. Frankel, D. R. Dykaar, G. A. Mourou, and T. Y. Hsiang, "Picosecond GaAs-based photoconductive optoelectronic detectors," Applied Physics Letters, vol. 54, pp. 890-892, 1989.

[68] I. S. Gregory, C. Baker, W. R. Tribe, M. J. Evans, H. E. Beere, E. H. Linfield, A. G. Davies, and M. Missous, "High resistivity annealed low-temperature GaAs with 100 fs lifetimes," Applied Physics Letters, vol. 83, pp. 4199-4201, 2003.

[69] J. K. Luo, H. Thomas, D. V. Morgan, D. Westwood, and R. H. Williams, "The electrical breakdown properties of GaAs layers grown by molecular beam epitaxy at low temperature," Semiconductor Science and Technology, vol. 9, p. 2199, 1994.

[70] R. Yano, Y. Hirayama, S. Miyashita, H. Sasabu, N. Uesugi, and S. Uehara, "Pump–probe spectroscopy of low-temperature grown GaAs for carrier lifetime estimation: arsenic pressure dependence of carrier lifetime during MBE crystal growth," Physics Letters A, vol. 289, pp. 93-98, 2001.

[71] M. Missous, "Stoichiometric low temperature (SLT) GaAs and AlGaAs grown by molecular beam epitaxy," Microelectronics Journal, vol. 27, pp. 393-409, 1996.

[72] H. Nemec, A. Pashkin, P. Kuzel, M. Khazan, S. Schnull, and I. Wilke, "Carrier dynamics in low-temperature grown GaAs studied by terahertz emission spectroscopy," Journal of Applied Physics, vol. 90, pp. 1303-1306, 2001.

[73] C. Kadowa and e. al, "Self-assembled ErAs islands in GaAs for THz applications," Physica E vol. 7, pp. 97-100, 2000.

[74] P. A. Loukakos, C. Kalpouzos, I. E. Perakis, Z. Hatzopoulos, M. Logaki, and C. Fotakis, "Ultrafast electron trapping times in low-temperature-grown gallium arsenide: The effect of the arsenic precipitate spacing and size," Applied Physics Letters, vol. 79, pp. 2883- 2885, 2001.

[75] J. E. Bjarnason, T. L. J. Chan, A. W. M. Lee, E. R. Brown, D. C. Driscoll, M. Hanson, A. C. Gossard, and R. E. Muller, "ErAs:GaAs photomixer with two-decade

tunability and 12 mu W peak output power," Applied Physics Letters, vol. 85, pp. 3983-3985, 2004.

[76] T. Liu, M. Tani, M. Nakajima, M. Hangyo, and C. Pan, "Ultrabroadband terahertz field detection by photoconductive antennas based on multi-energy arsenic-ion-implanted GaAs and semi-insulating GaAs," Applied Physics Letters, vol. 83, pp. 1322-1324, 2003.

[77] S. Kono, M. Tani, P. Gu, and K. Sakai, "Detection of up to 20 THz with a lowtemperature-grown GaAs photoconductive antenna gated with 15 fs light pulses," Applied Physics Letters, vol. 77, pp. 4104-4106, 2000.

[78] M. Martin and E. R. Brown, "Critical comparison of GaAs and InGaAs THz photoconductors," Proc. of SPIE, vol. 8261, pp. 826102-826102, 2012.

[79] M. Tani, S. Matsuura, K. Sakai, and S.-i. Nakashima, "Emission characteristics of photoconductive antennas based on low-temperature-grown GaAs and semi-insulating GaAs," Appl. Opt., vol. 36, pp. 7853-7859, 1997.

[80] M. R. Stone, M. Naftaly, R. E. Miles, J. R. Fletcher, and D. P. Steenson, "Electrical and radiation characteristics of semilarge photoconductive terahertz emitters," IEEE Transactions on Microwave Theory and Techniques, , vol. 52, pp. 2420-2429, 2004.

[81] R. Stibal, J. Windscheif, and W. Jantz, "Contactless evaluation of semi-insulating GaAs wafer resistivity using the time-dependent charge measurement," Semiconductor Science and Technology, vol. 6, p. 995, 1991.

[82] M. C. Beard, G. M. Turner, and C. A. Schmuttenmaer, "Subpicosecond carrier dynamics in low-temperature grown GaAs as measured by time-resolved terahertz spectroscopy," Journal of Applied Physics, vol. 90, pp. 5915-5923, 2001.

[83] S. J. Jo and e. al, "Carrier dynamics of low-temperature-grown In0.53Ga0.47As on GaAs using an InGaAlAs metamorphic buffer," Applied Phyasics Letter, vol. 86, p. 111903, 2005.

[84] A. Takazato, M. Kamakura, T. Matsui, J. Kitagawa, and Y. Kadoya, "Terahertz wave emission and detection using photoconductive antennas made on low-temperature-grown InGaAs with 1.56 mu m pulse excitation," Applied Physics Letters, vol. 91, p. 011102, 2007.

[85] N. Vieweg, M. Mikulics, M. Scheller, K. Ezdi, R. Wilk, H. W. Hübers, and M. Koch, "Impact of the contact metallization on the performance of photoconductive THz antennas," Opt. Express, vol. 16, pp. 19695-19705, 2008.

[86] Y. C. Shen, P. C. Upadhya, H. E. Beere, E. H. Linfield, A. G. Davies, I. S. Gregory, C. Baker, W. R. Tribe, and M. J. Evans, "Generation and detection of ultrabroadband terahertz radiation using photoconductive emitters and receivers," Applied Physics Letters, vol. 85, pp. 164-166, 2004.

[87] Y. Gao, M. Chen, S. Yin, P. Ruffin, C. Brantley, and E. Edwards, "Terahertz enhancement from terahertz-radiation-assisted large aperture photoconductive antenna," Journal of Applied Physics, vol. 109, p. 033108, 2011.

[88] S. Verghese, K. A. McIntosh, S. Calawa, W. F. Dinatale, E. K. Duerr, and K. A. Molvar, "Generation and detection of coherent terahertz waves using two photomixers," Applied Physics Letters, vol. 73, pp. 3824-3826, 1998.

[89] I. S. Gregory, C. Baker, W. R. Tribe, I. V. Bradley, M. J. Evans, E. H. Linfield, A. G. Davies, and M. Missous, "Optimization of photomixers and antennas for continuouswave terahertz emission," IEEE Journal of Quantum Electronics,, vol. 41, pp. 717-728, 2005.

[90] N. Vieweg, M. Mikulics, M. Scheller, K. Ezdi, R. Wilk, H. W. Hübers, and M. Koch, "Impact of the contact metallization on the performance of photoconductive THz antennas," Opt. Express, vol. 16, pp. 19695-19705, 2008.

[91] M. Tamagnone, J. S. Gomez-Diaz, J. R. Mosig, and J. Perruisseau-Carrier, "Analysis and design of terahertz antennas based on plasmonic resonant graphene sheets," Journal of Applied Physics, vol. 112, p. 114915, 2012.

[92] M. Dragoman, A. A. Muller, D. Dragoman, F. Coccetti, and R. Plana, "Terahertz antenna based on graphene," Journal of Applied Physics, vol. 107, p. 104313, 2010.

[93] B. Heshmat, H. Pahlevaninezhad, T. E. Darcie, and C. Papadopoulos, "Evaluation of carbon nanotubes for THz photomixing," in 2010 IEEE Radar Conference, , 2010, pp. 1176-1179.

[94] M. Tamagnone, J. S. G mez-D az, J. R. Mosig, and J. Perruisseau-Carrier, "Reconfigurable terahertz plasmonic antenna concept using a graphene stack," Applied Physics Letters, vol. 101, p. 214102, 2012.

[95] P. U. Jepsen, R. H. Jacobsen, and S. R. Keiding, "Generation and detection of terahertz pulses from biased semiconductor antennas," J. Opt. Soc. Am. B, vol. 13, pp. 2424-2436, 1996.

[96] B. B. Hu, A. S. Weling, D. H. Auston, A. V. Kuznetsov, and C. J. Stanton, "dc-electric-field dependence of THz radiation induced by femtosecond optical excitation of bulk GaAs," Physical Review B, vol. 49, pp. 2234-2237, 1994.

[97] J. Klier, S. Wohnsiedler, W. Zouaghi, E. Peytavit, J. Lampin, J. Jonuscheit, and R. Beigang, "Far-field THz radiation pattern from photoconductive emitters on different substrates," in 36th International Conference on Infrared, Millimeter and Terahertz Waves (IRMMW-THz), 2011 2011, pp. 1-2.

[98] J. Van Rudd and D. M. Mittleman, "Influence of substrate-lens design in terahertz timedomain spectroscopy," J. Opt. Soc. Am. B, vol. 19, pp. 319-329, 2002.

[99] E. R. Brown, F. W. Smith, and K. A. McIntosh, "Coherent millimeter-wave generation by heterodyne conversion in low-temperature-grown GaAs photoconductors," Journal of Applied Physics, vol. 73, pp. 1480-1484, 1993.

[100] Zangeneh-Nejad, F.; Barani, N.; Safian, R. Temperature dependance of electromagnetic radiation from terahertz photoconductive antennas. *Microw. Opt. Technol. Lett.* 2015, 57, 2475–2479.

[101] Thim, H.W. Computer study of bulky GaAs Devices with random one-dimensional doping fluctuations. *J. Appl. Phys.* 1968, *39*, 3897–3904.

[102] E. R. Brown, "THz Generation by Photomixing in Ultrafast Photoconductors," International Journal of High Speed Electronics and Systems, vol. 13, pp. 497-545, 2003.

[103] https://www.3ds.com/products-services/simulia/products/cst-studio-suite/

[104] E. Peytavit and e. al, "Terahertz frequency difference from vertically integrated lowtemperature-grown GaAs photodetector," Applied Physics Letters, vol. 81, pp. 1174- 1176, 2002.

[105] M. Mikulics and e. al, "Traveling-wave photomixer with recessed interdigitated contacts on low-temperature-grown GaAs," Applied Physics Letters, vol. 88, p. 041118, 2006.

[106] H. Tanoto, J. H. Teng, Q. Y. Wu, M. Sun, Z. N. Chen, S. A. Maier, WangB, C. C. Chum, G. Y. Si, A. J. Danner, and S. J. Chua, "Greatly enhanced continuous-wave terahertz emission by nano-electrodes in a photoconductive photomixer," Nat Photon, vol. 6, pp. 121-126, 2012.

[107] De Murcia, M.; Gasquet, D.; Elamri, A.; Nougier, J.P.; Vanbremeersch, J. Diffusion and noise in GaAs material and devices. *IEEE Trans. Electron Devices* 1991, *38*, 2534–2539.

[108] Zamdmer, N.; Hu, Q.; McIntosh, K.A.; Verghese, S. Increase in response time of low-temperature-grown GaAs photoconductive switches at high voltage bias. *Appl. Phys. Lett.* 1999, *75*, 2313–2315.

[109] M. Mikulics, M. Marso, M. Lepsa, D. Grutzmacher, and P. Kordos, "Output Power Improvement in MSM Photomixers by Modified Finger Contacts Configuration," IEEE Photonics Technology Letters,, vol. 21, pp. 146-148, 2009.

[110] K. Yee, "Numerical solution of initial boundary value problems involving Maxwell's equations in isotropic media," Antennas and Propagation, IEEE Transactions on, vol. 14, pp. 302-307, 1966.

[111] O. P. Gandhi, B.-Q. Gao, and J.-Y. Chen. A frequency-dependent finite-difference timedomain formulation for general dispersive media. IEEE Trans. Microwave Theory Tech., 41:658–665, 1993.

[112] J. B. Pendry, A. J. Holden, D. J. Robbins, and W. J. Stewart. Magnetism from conductors and enhanced nonlinear phenomena. IEEE Trans. Microwave Theory Tech., 47(11):2075– 2084, 1999.

[113] F. B. Hildebrand. Introduction to Numerical Analysis. New York, McGraw-Hill, 1956.

[114] Seeds, A.J.; Williams, K.J. Microwaves photonics. *J. Lightw. Technol.* 2006, *24*, 4628–4641.

[115] N. Khiabani et al., "A Novel Sub-THz Photomixer With Nano-Trapezoidal Electrodes," IEEE Trans. Terahertz Sci. Technol. vol. 4, pp. 501-508, 2014.

[116] Y. Cai, I. Brener, J. Lopata, J. Wynn, L. Pfeiffer, and J. Federici, "Design and performance of singular electric field terahertz photoconducting antennas," Appl. Phys. Lett., vol. 71, pp. 2076–2078, 1997.

[117] Jiang L, Sun YH, Nowak C et al (2011) "Patterning of plasmonic nanoparticles into multiplexed one-dimensional arrays based on spatially modulated electrostatic potential". ACS Nano 5: pp. 8288–8294.

[118] C. W. Berry, M Jarrahi, "Terahertz generation using plasmonic photoconductive gratings," New Journal of Physics, Vol. 14 pp 105029, 2012.

[119] C. W. Berry, N. Wang, M. R. Hashemi, M. Unlu, M. Jarrahi, "Significant Performance Enhancement in Photoconductive Terahertz Optoelectronics by Incorporating Plasmonic Contact Electrodes", Nature Communications, 4, pp1622, 2013.

[120] E. D. Palik, Handbook of Optical Constants of Solids, Academic Press, 1998.

[121] R. Faulks *et al*., "Enhanced Terahertz Receiver Using a Distributed Bragg Reflector Coupled to a Photoconductive Antenna," in *IEEE Photonics Technology Letters*, vol. 21, no. 21, pp. 1603-1605, Nov.1, 2009.

[122] Jiři Homola, Sinclair S. Yee, Günter Gauglitz, "Surface plasmon resonance sensors: review," Sensors and Actuators B: Chemical, Vol. 54, Issues 1–2, pp. 3-15, 1999.

[123] X. Huang, M. A. El-Sayed, "Gold nanoparticles: Optical properties and implementations in cancer diagnosis and photothermal therapy," Journal of Advanced Research, Volume 1, Issue 1, Pp. 13-28, 2010.

[124] McCall, S.L., Platzman, P.M., Dalichaouch, R. et al, 'Microwave Propagation in Two-Dimensional Dielectric Lattices,' Physical Review Letters, 1991, 67, pp.2017-2020.

[125] G. V. Trentini, "Partially reflecting sheet arrays," IRE Trans. Antennas Propag., vol. AP-4, pp. 666-671, Oct. 1956.

[126] A. Foroozesh and L. Shafai, "Investigation into the effects of the patch-type fss superstrate on the high-gain cavity resonance antenna design," IEEE Trans. Antennas Propag., vol. 58, no. 2, pp. 258-270. 2010.

[127] N. Engheta, C. H. Papas, and C. Elachi, "Radiation patterns of interfacial dipole antennas," Radio Science, vol. 17, pp. 1557-1566, 1982.

[128] D. B. Rutledge, D. P. Niekirk, and D. P. Kasilingam, "Integrated circuit antennas," Infrared and Millimeter-Waves Series, vol. 11, New York: Academic, 1983.

[129] P. U. Jepsen and S. R. Keiding, "Radiation patterns from lens-coupled terahertz antennas," Opt. Lett., vol. 20, pp. 807-809, 1995.

[130] Khamas, S.K.; Starke, P.L.; Cook, G.G. Design of a printed spiral antenna with a dielectric superstrate using an efficient curved segment moment method with optimisation using marginal distribution. *IEE Proc. Microw. Antenn. Propagat.* **2004**, *151*, 315–320.

[131] S. M. Duffy, S. Verghese, A. McIntosh, A. Jackson, A. C. Gossard, and S. Matsuura, "Accurate modeling of dual dipole and slot elements used with photomixers for coherent terahertz output power," IEEE Transactions on Microwave Theory and Techniques, , vol. 49, pp. 1032-1038, 2001.

[132] I. Woo, T. K. Nguyen, H. Han, H. Lim, and I. Park, "Four-leaf-clover-shaped antenna for a THz photomixer," Opt. Express, vol. 18, pp. 18532-18542, 2010.

[133] K. Han, T. K. Nguyen, I. Park, and H. Han, "Terahertz Yagi-Uda Antenna for High Input Resistance," Journal of Infrared, Millimeter, and Terahertz Waves, 2009.

[134] J. Frydrych, J. Petrzela and K. Pitra, " Dual slot-superstrate terahertz antenna without Si-lens," 2017 Conference on Microwave Techniques (COMITE), Brno, Czech Republicpp.1-5, 2017.

[135] Jha, K.R.; Singh, G. "Ring resonator-intergrated hemi-elliptical lens antenna at terahertz frequency." In Proceedings of the International Conference on Communication Systems and Network Technologies, Katra, India, 3–5 June 2011.

[136] Sun, M.; Chen, N.; Teng, J.H.; Tanoto, H. "A membrane supported photomixer driven antenna with increased continuous-wave Terahertz output power." In the Proceedings of 2011 International Topical Meeting on Microwave Photonics Jointly held wiht the 2011 Asia-Pacific Microwave Photonics Conference, Singapore, Singapore, 18–21 October 2011.

[137] Hou, D.; Xiong, Y.-Z.; Goh, W.-L.; Hu, S.; Hong, W.; Madihian, M. "130-GHz on-chip meander slot antennas with stacked dielectric resonators in standard CMOS technology." *IEEE Tans. Antenn. Propag.* **2012**, *60*, 4102–4109.

[138] Li, C.; Chiu, T. "340-GHz low-cost and high-gain on-chip higher order mode dielectric resonator antenna for THz applications." *IEEE T. THz Sci. Techn.* **2017**, *7*, 284–294.

[139] A. Petosa and A. Ittipiboon, "Dielectric resonator antennas: A historical review and the current state of the art," IEEE Antennas Propag. Mag., vol. 52, pp. 91–116, 2010.

[140] B.B. Pal, Compositional dependence of permittivity in quarternary III–V semiconductor compounds, Solid-State Electronics, Volume 28, Issue 12, Pages 1235-1239,19.

[141] Kimura, W.D. What are electromagnetic waves? In *Electromagnetic Waves and Lasers,* Morgan & Claypool Publishers: San Rafael, CA, USA, 2017.